Continuum Mechanics Studies on Glass-Forming Liquids

Inaugural Dissertation

for the attainment of the title of doctor
in the Faculty of Mathematics and Natural Sciences
at the Heinrich-Heine-Universität Düsseldorf

presented by

Heliana Cárdenas
from Caracas, Venezuela

Köln, May 2018

from the Institute for Theoretische Physik II, der weichen Materie
at the Heinrich-Heine-Universität Düsseldorf

Published by permission of the
Faculty of Mathematics and Natural Sciences at
Heinrich-Heine-Universität Düsseldorf

Supervisor: Prof. Dr. Thomas Voigtmann

Co-supervisor: Prof. Dr. Jürgen Horbach

Date of the oral examination: 24.09.2018

Eidesstattliche Versicherung

Ich, Frau Heliana Cárdenas Bello, versichere an Eides statt, dass die vorliegende Dissertation von mir selbstständig und ohne unzulässige fremde Hilfe unter Beachtung der „Grundsätze zur Sicherung guter wissenschaftlicher Praxis an der Heinrich-Heine-Universität Düsseldorf" erstellt worden ist.

Köln, 01. Mai 2018

Unterschrift

Publications

The following publication, based on this thesis, show results covered in chapter 2, section 2.4, regarding the effect of the advection term in describing viscoelastic flow.

Nonlinear mechanical response of supercooled melts under applied forces. Cárdenas H., Frahsa, F., Fritschi, S., Nicolas, A., Papenkort, S., Voigtmann, Th., Fuchs, M. The European Physical Journal Special Topics; 226:3039 (2017), 14.

Abstract

Glass forming liquids show relaxation on a timescale that is many orders of magnitude higher than that of single particle motion: their dynamics depends on slow collective structural relaxation processes that cause viscoelasticity. Consequently, their rheology is highly non-linear and, under strong driving, the flow becomes non-Newtonian; it is characterized by a yield stress and by shear thinning [1]. Microscopic yielding can produce heterogeneous flow patterns like shear bands and cooperativity in the flow: active areas will induce stress to their neighbors up to a length scale called "cooperativity length"; hence the stress is non-local and diffuses at a rate defined by plastic activity [2–4]. We use a phenomenological fluidity model to capture the competition between the quiescent structural relaxation and flow-induced relaxation. This model reproduces typical non-Newtonian effects like plug flow in the center of a pressure-driven flow as a signature of the existence of a yield stress. In simple shear start-up, we observe transient shear bands that disappear when steady state is reached, whereas long-lasting bands can result from wall effects. Memory effects, like residual stresses found in glasses, are also reproduced: after removing the applied shear rate in a non-equilibrium stationary state in simple shear, the fluid velocity drops to zero yet the shear stress remains present. Other non-trivial geometries were probed like lid-driven cavity flow, flow going through an abrupt 4:1 contraction and also through a plate with obstacles. We have studied the sedimentation of non-Brownian particles in the glass-forming fluidity model using a resolved Fictitious Domain Method (FDM) based on Shirgaonkar et al. [5], coupled to a Lagrangian Discrete Element Method (DEM) to track particles [6, 7]. Sedimenting particles will fluidize the neighboring areas up to a scale defined by the cooperativity length around them. Our model can reproduce the so-called drafting-kissing-chaining effect expected when two particles separated by an initial vertical distance start sedimenting on top of each other: the particle on top accelerates when entering the wake of the leading particle until they touch and remain together before reaching the bottom. In shear thinning fluids this effect is more pronounced than in viscoelastic fluids because a corridor with lower viscosity is formed behind the trailing particle accelerating the following one [8]. We used computational fluid dynamics (CFD) package OpenFOAM® and CFD-DEM-coupling by means of the finite volume method to perform all mentioned calculations [9].

Zusammenfassung

Glasbildende Flüssigkeiten weisen um viele Größenordnungen grössere Zeitskalen auf als die Bewegung eines Einzelteilchens: Ihre Dynamik hängt von langsamen, kollektiven, strukturellen Relaxationsprozessen ab, die Viskoelastizität verursachen. Folglich ist ihre Rheologie stark nichtlinear und unter starker Verformung nicht-Newtonsch aufgrund ihrer Fließgrenze und Scherverdünnung [1]. Mikroskopische Verformung kann zu heterogenen Fließmustern wie z.B. Scherbändern oder Kooperativität im Fluss führen: Aktive Bereiche übertragen Spannung auf ihre Nachbarn innerhalb der „Kooperationslänge". Somit ist die Spannung nicht-lokal und diffundiert mit einer durch die plastische Aktivität definierten Rate [2–4]. Ein phänomenologisches Model der Flussfähigkeit wurde benutzt, um die konkurrierenden Prozesse der strukturellen, stationären Relaxation und der flussinduzierten Relaxation zu untersuchen. Das Model reproduziert typische nicht-Newtonsche Effekte wie z.B. Pfropfenströmung im Zentrum einer druckgetriebenen Kanalströmung. Einfache Scherung führt zur Bildung transienter Scherbänder, die sich im stationären Zustand auflösen, während durch Wandeffekte langlebige Bänder entstehen. Memory-Effekte wie z.B. eingefrorene Spannungen nach dem Ausschalten einer einfachen Scherung können ebenfalls reproduziert werden. Die Fließgeschwindigkeit sinkt auf Null, während die Scherspannung weiter besteht. Andere, nicht-triviale Geometrien wie z.B. Strömung in einem Hohlraum, durch einen verjüngenden Kanal und in Anwesenheit von Hindernissen wurden untersucht. Sedimentation von nicht-brownschen Partikeln wurde im Model des glasbildenden Fließverhaltens mit der Methode der fiktiven Domänen (FDM) basierend auf [5] kombiniert mit einer Diskreten-Element Methode (DEM) [6, 7] analysiert. Sedimentierende Teilchen fluidisieren ihre Umgebung in einem Bereich, der durch die Kooperationslänge bestimmt wird. Unser Model kann den Drafting-Kissing-Chaining-Effekt reproduzieren, der erwartet wird, wenn zwei Teilchen, die anfangs vertikal getrennt sind, zusammen sedimentieren: Das obere Teilchen beschleunigt, sobald es in den Einflussbereich des vorderen Teilchens eintritt, die Teilchen berühren sich und sinken so zu Boden. In scherverdünnenden Fluiden ist dieser Effekt stärker ausgeprägt als in viskoelastischen, da ein Bereich mit niedrigerer Viskosität hinter dem führenden Teilchen gebildet wird, wodurch das nachfolgende Teilchen beschleunigt wird [8]. Für alle Berechnungen wurde die Finite-Volumen-Methode (FVM) und eine CFD-DEM-Kombination auf Basis der Software OpenFOAM® eingesetzt [9].

Acknowledgments

I could not submit this thesis without saying how profoundly thankful I am to my professor and supervisor Prof. Thomas Voigtmann. Thank you very much for believing in me, for guiding me, and for giving me the chance and freedom to work with you and share so many memories together. I enjoyed very much being part of your group, which brings me to thank Dr. Simon Papenkort, Dr. Alexander Liluashvili, Dr. Luis Elizondo and Jonathan Onody for our discussions about physics, different perspectives, and programming tips. In fact, Alexander became a good friend of mine and helped me get through the whole project, for that, I am thankful too. Working at DLR was a great experience that allowed me to make really good colleges and friends, who also motivated me to keep going, especially during rough patches. Isabell Jonas, Christian Karrasch, Johanna Wessing and Carolina Kreischer will always be part of this group. Last but not least, I want to thank my family, Vicky, Andrea and Deyly for their transatlantic and local support, friendship and love.

Contents

1 Introduction **1**

2 Continuum Mechanics **5**
2.1 Governing Equations 6
2.2 Constitutive Equations 8
2.2.1 Newtonian Response 8
2.2.2 Non-Newtonian Linear Response 9
2.2.3 Upper Convected Time Derivative 11
2.2.4 Non-Linear Constitutive Equations 13
2.3 Computational Fluid Dynamics 16
2.3.1 Finite Volume Method 16
2.3.2 Domain Discretization 17
2.3.3 Temporal Term Discretization 21
2.3.4 Split-Stress Tensor Approach 24
2.3.5 Pressure-Velocity Coupling 25
2.3.6 Boundary Conditions 27
2.4 Effect of Advection Term in Flow 28
2.4.1 Taylor-Green Vortex 29
2.4.2 Abrupt 4:1 Planar Contraction 35

3 Glass-Forming Liquids **39**
3.1 Glass Transition 39
3.2 Microscopic Theory 42
3.2.1 Schematic MCT 43
3.2.2 Further Simplifications 44
3.3 Fluidity Model 45
3.3.1 Fluidity Model Assessment 47
3.3.2 Fluidity Boundary Conditions 53
3.3.3 Fluidity Model and FVM 54

4 Time Dependent Effects **61**
4.1 Material Parameters 63

4.2 Initial Conditions . . . 63
4.3 Neumann Boundary Condition . . . 64
4.4 Dirichlet Boundary Condition . . . 68
4.4.1 Homogeneous Initial Fluidity Field . . . 68
4.4.2 Heterogeneous Initial Fluidity Field . . . 70
4.4.3 Steady State Banding . . . 72
4.4.4 Wall Effects . . . 74
4.5 Bauschinger Effect . . . 75

5 Residual Stresses 79
5.1 Simple Shear . . . 80
5.2 Lid-Driven Cavity Flow . . . 81
5.2.1 Steady State . . . 82
5.2.2 Flow Cessation . . . 87
5.2.3 Mechanical Transient Effects . . . 93
5.3 Flow Through Abrupt 4:1 Contraction . . . 95
5.3.1 Flow Cessation . . . 97
5.4 Flow Through Obstacles . . . 102

6 Particles in Viscoelastic Fluids 109
6.1 Immersed Boundary Conditions . . . 112
6.1.1 Governing Equations . . . 114
6.1.2 CFDEM®Coupling Algorithm . . . 117
6.2 Particle Sedimentation . . . 118
6.2.1 Oldroyd-B Fluid . . . 118
6.2.2 Shear Thinning Fluid . . . 122
6.3 Two Particle Sedimentation . . . 128
6.3.1 Side by Side Configuration . . . 135

7 Summary and Conclusions 137

A Supplementary Information 141
A.1 Simulation Basics . . . 141
A.2 Code Implementation . . . 141
A.2.1 Material Models . . . 141
A.2.2 Under-relaxation . . . 145
A.2.3 OpenFOAM Case Setup . . . 146
A.2.4 Particles Sedimentation . . . 147
A.3 Mesh Analysis: Abrupt 4:1 Contraction . . . 149
A.4 Supplementary Plots . . . 152

Bibliography 156

Chapter 1

Introduction

As scientists we are very well acquainted with the multiscale paradigm, where the physics we want to study in a material can be decomposed according to the length and timescales one is interested in. There exists a wide spectrum of computational and experimental techniques that have been developed to describe the physical behavior of materials on the pertinent scale. Techniques encompass atomistic methodologies such as quantum mechanics, molecular dynamics, up to the continuum scale, which is disclosed schematically in Fig. 1.1. There, we show typical experimental techniques that have been widely used in material science according to their size and timescales, starting, for example, with high-resolution microscopy at the smaller scales up to optical microscopy for bigger ones. In the upper right corner, continuum mechanics defines the area of study where computational techniques like *finite volume methods* (FVM), *finite element methods* (FEM), and *lattice Boltzmann* (LB) methodologies are powerful tools to describe material behavior from an application point of view.

However, each method has a limit as indicated roughly by the circles in the same figure. Specific theories are used to describe material behavior on specific scales, and somehow they need to enclose the effects that arise from other scales. Typically the information obtained from smaller scales is expressed through model parameters, encapsulating them into empirical functions to work ideally in one scale. This means that, hypothetically, we should be able to use all the microscopic properties of a material obtained with smaller-scales-methods to design and predict its behavior macroscopically using continuum mechanics techniques.

A multiscale technique would be ideal, where we can start from a microscopic theory to design how the material will behave in bigger scales. Traditionally, Hooke's and Newton's laws have been present as common knowledge for a long time as successful ways to describe elastic and viscous materials respectively, even though these laws come from empirical observation. When the material we are dealing with shows

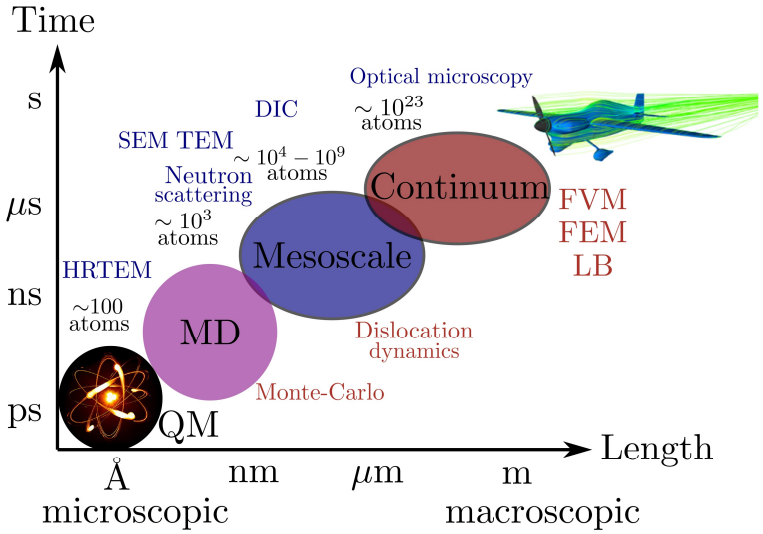


Figure 1.1: Schematic representation of different length and timescales and corresponding used experimental and computational methods.

more complex behavior, i.e. complex flow behavior, we are in need of more detailed theories or models. Rheology of complex flows is our main interest in this thesis, and we aim to be able to describe flow deformation by improved empirical theories that are better rooted in microscopic descriptions. We use the term "complex flows" to include colloidal systems, polymers, and materials with long relaxation times like glass-forming liquids, which can be regarded as viscoelastic fluids. In order to describe flow dynamics, the momentum and mass conservation equations must be fulfilled. The former, also known as the Navier-Stokes equations, is a macroscopic field theory that is closed by a stress tensor which ultimately represents the coupling to smaller scales. One can write this equation generally as

$$\rho \frac{\partial \boldsymbol{u}}{\partial t} + (\nabla \cdot \rho \boldsymbol{u}\boldsymbol{u}) = -(\nabla \cdot \boldsymbol{\pi}). \tag{1.1}$$

The right side of the equation balances the momentum that crosses a control volume in the fluid, and it is determined by hydrostatic pressure p when the fluid is at rest, otherwise it amounts to $\boldsymbol{\pi} = p\mathbf{I} - \boldsymbol{\Sigma}$, where the stress tensor $\boldsymbol{\Sigma}$, by means of a *constitutive equation*, includes microscopic properties like viscosity [10], in terms of variables present in the momentum equations. In Chapter 2 we will explain the general description of fluids, their governing equations, and how to solve them. We will go through methodologies dealing with equations of such nature for our flow of interest, and we introduce some constitutive equations for linear and non-linear flows as examples. There have been various attempts to write constitutive equations in function of microscopic material properties. Entangled polymer behavior has

been successfully described through Doi and Edwards equations starting from first-principles [10, 11]. However, in glass-forming liquids context, we need to understand to an extent what happens close to the glass transition and the applicability of glass theories to describe macroscopic behavior.

We dedicate Chapter 3 to recall relevant facts about glass-forming liquids, where the Mode Coupling Theory of the glass transition (MCT) has been a tool to understand and describe this behavior starting from first principles. In this chapter, we summarize the MCT microscopic model since its applicability, in glass-forming colloidal suspensions and hard spheres systems, has proved to be satisfactory in reproducing complex behavior using molecular dynamics simulations and experiments of similar systems [12–14]. A simplified version of this theory has been used to describe macroscopic systems under simple shear. Complex glass-forming flows depend on material history, therefore, a memory kernel must be included in the material description. This makes numerical calculations cumbersome and not easily applicable to complex geometries required in final applications. To reduce numerical effort, at the end of the same chapter, we introduce a new *fluidity model* as a mesoscopic way to capture the main features observed and described by the microscopic theory, through a simplified differential equation. This equation can be robustly solved using finite volume methodologies that have been implemented in the open source package OpenFOAM®.

Validation of the method and model was done by setting flow going through trivial geometries like simple shear and pressure-driven flow. This allowed us to reproduce shear thinning and yield stress phenomena characteristic of glass-forming liquids. Moreover, in Chapter 4, we describe shear banding phenomenology that is as well observed in complex flows and how, in our fluidity model, it arises through boundary conditions of a "new" material property called fluidity, i.e. a non-local relaxation rate that scales as an inverse viscosity. Fluidity in the flow is modeled through a diffusion equation which includes microscopic effects like cooperativity in the flow. There are constitutive equations available that can describe shear thinning, yield stress, among main complex viscoelastic flow effects, but a striking feature that is reproduced and validated naturally by MCT equations is the existence of persistent stresses after flow cessation. This is a phenomenon that has been observed experimentally and through simulations as well. In Chapter 5 we show how the fluidity model is able to reproduce these phenomena, and how they depend on the flow advection symmetry. Therefore, we did not find residual stresses after flow cessation in symmetric flows like pressure driven flow, but we did find them in more complicated geometries like abrupt contractions, lid-driven cavity flow, and flow passing obstacles. Summarized results in this chapter also cover the influence of material parameters inherent to the fluidity equation.

After having implemented, validated, and assessed the fluidity model and its vari-

ations, and also reproduced complexities of glass-forming liquids in trivial as well as in non-trivial geometries, we move to a more advanced topic, namely to bodies immersed in the flow. This was done thanks to the synergistic relationship between a simplified model and powerful modeling tools. Chapter 6 is devoted to describing the use and implementation of immersed boundary (IB) condition methodology to simulate the interaction between an immersed solid sedimenting in a fluid without using reduced order models as the Stoke's equations. As a side note, it is important to clarify that IB is a name given to methodologies involving immersed bodies, but by being completely pragmatic the method is called Fictitious Domain method, though IB is more widely used to refer to this kind of calculations in the sedimentation field. Validation of the methodology is introduced in this chapter for viscoelastic fluids, and fluidity parameters were varied to study their effect on one and two particle sedimentation in a shear thinning fluid.

Chapter 2

Continuum Mechanics

Matter is composed of atoms stacked together in a specific arrangement. Thus ultimately, on a microscopic scale, makes matter not continuous, meaning that a body does not really fill completely the space it resides. Still, on macroscopic scales, we may assume that matter occupies homogeneously all the space it is in, which can allow us to divide it in an infinite number of elements, larger than molecular distances, so each element contains the physical properties of the body itself. With this assumption in mind, modeling of the mechanic and kinematic behavior of materials is known as continuum mechanics [15, 16].

The flow of materials regarded as a continuous medium can be described by a joined theoretical and experimental approach. Efforts to understand how to transport water and food started in ancient times, like water canals old as 4000 years BC. Fast forward to the beginning of 16th century, before Sir Isaac Newton, Leonardo Da Vinci gave a lot of thought and craft to study how flow develops in tubes, movement of water, flow passing obstacles, flow visualization and streamlines formation, development of vortices, among other phenomena [17]. Some of his drawings are shown in Fig. 2.1.

We must then state that any macroscopic physical property of matter can be described by a continuum function depending on time and space, and that the distribution of

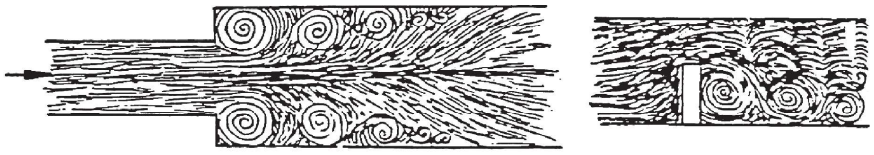


Figure 2.1: Flow separation in duct enlargement and flow behind obstacles with vortex formation sketched by Leonardo da Vinci [18].

the fluid velocity $\boldsymbol{u}(x, y, z, t)$ and two other thermodynamic quantities like pressure p and density ρ must suffice to characterize a flow macroscopically [15, 19].

Continuum mechanics can be used to describe solid and fluid behavior. Solids can withstand static shear forces and respond with a finite deformation. The material can deform and keep its new shape permanently i.e. they show plastic behavior, or go back to its initial state when the force is removed, i.e. they show elastic solid behavior. On the other hand, fluids (gas and liquids) will continuously deform at a certain rate under static shear force. There is a rich phenomenology to describe specific behaviors like:

- elastic: reversible deformation proportional to shear force,
- anelastic: reversible deformation not proportional to shear force,
- plastic: non reversible deformation,
- viscous: fluids that show irreversible deformation which is proportional to the stress,
- creeping: infinite deformation, when shear rate is close to zero,
- viscoelastic: elastic behavior at short times and viscous at longer times.

2.1 Governing Equations

Let us describe a flow with valid equations for continuum media based on universal laws of physics: conservation of mass, momentum, and energy. We shall regard the matter as divided into control volumes focusing on the flow in a certain spatial region, where our main concern is mass and momentum conservation [20]. A control volume, schematically drawn in Fig. 2.2, will have time and length scales larger than the group of molecules it represents, therefore continuum properties like velocity, pressure, and density do not refer to discrete particles in the flow but the whole group of them.

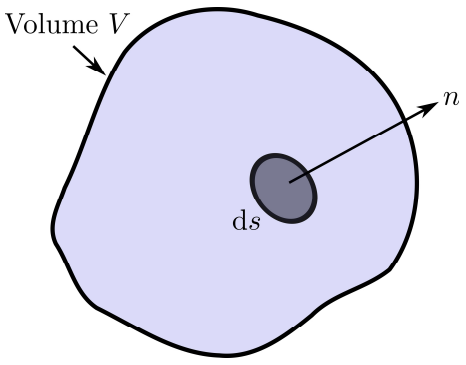


Figure 2.2: Control volume representation with arbitrary shape within the flow.

Conservation equations must be written for the mentioned control volume, starting with the fact that mass cannot be created or destroyed but conserved, thus in a flow element:

$$\frac{\mathrm{d}m}{\mathrm{d}t} = 0, \tag{2.1}$$

where m stands for mass and t time. We must write this down for the elements forming a fluid, hence the rate of mass that enters an element will be equal to the net rate of flow into the element.

Therefore for an element of volume V, the mass of fluid within this volume is $\int_V \rho \mathrm{d}V$. The mass flow rate through an element of surface $\mathrm{d}\boldsymbol{s}$ is given by the product of density, area and the velocity component normal to that face, $\rho\boldsymbol{u} \cdot \mathrm{d}\boldsymbol{s}$. By convention, this quantity is negative when it is flowing into the element, and positive when flowing out of it. The latter will equal the mass decreasing inside the element, which overall could be conveniently written as

$$\oint \rho\boldsymbol{u} \cdot \mathrm{d}\boldsymbol{s} = -\frac{\partial}{\partial t} \int \rho \mathrm{d}V. \tag{2.2}$$

The integrals should hold for any volume, so after rearranging equation 2.2, the continuity equation becomes

$$\frac{\partial \rho}{\partial t} + \nabla \cdot (\rho\boldsymbol{u}) = 0. \tag{2.3}$$

For an incompressible fluid, equation 2.3 turns into

$$\nabla \cdot \boldsymbol{u} = 0. \tag{2.4}$$

The conservation of momentum by the action of forces is based on Newton's second law of motion, stating that the rate of change of momentum must be balanced by the forces f acting on the element (or particle), which might be expressed as

$$\frac{\mathrm{d}(m\boldsymbol{u})}{\mathrm{d}t} = \sum f. \tag{2.5}$$

This means that the total momentum within a volume V will increase because of an increase of momentum across the element surface $\mathrm{d}\boldsymbol{s}$ by bulk flow and molecular motions and gravity acting on the fluid [10]. Forces can be separated in two categories, surface forces like pressure and viscous forces and body forces like centrifugal forces and gravity [21].

The rate at which momentum is transported across the fluid element $(\boldsymbol{n} \cdot \boldsymbol{u})\rho\boldsymbol{u}\mathrm{d}s$, can be also written as $(\boldsymbol{n} \cdot \rho\boldsymbol{u}\boldsymbol{u})\mathrm{d}s$ where $\rho\boldsymbol{u}\boldsymbol{u}$ is the momentum flux or convective

transport, i.e. momentum per unit area and time. The momentum flux from molecular motion and interaction within the fluid is commonly defined as $\boldsymbol{\pi}$ (symmetric stress tensor). $\boldsymbol{\pi}$ enclosures hydrostatic pressure p, which is a normal stress, and the viscous stress denoted by $\boldsymbol{\sigma}$, where $\boldsymbol{\pi} = -p\mathbf{I} + \boldsymbol{\sigma}$ ($\mathbf{I}$ is the unit tensor). This reduces to p when the fluid is at rest, otherwise stress response $\boldsymbol{\sigma}$ to deformation arises [10, 16, 21].

The law of momentum conservation follows:

$$\rho\frac{\partial \boldsymbol{u}}{\partial t} + \rho(\nabla \cdot \boldsymbol{u}\boldsymbol{u}) = (\nabla \cdot \boldsymbol{\pi}) + \rho\boldsymbol{g}. \tag{2.6}$$

Combining governing equations 2.4 and 2.6 contains the unknown mentioned viscous stress tensor $\boldsymbol{\sigma}$. The definition of the viscous stress tensor in terms of microscopic quantities or material parameters is called constitutive equation, and it describes the behavior of specific materials. Most of these relations come from empirical observation based on how macroscopic deformation behaves when forces are applied. Traditional relations between stress and strain are Hooke's law where stress and strain are linearly related by a constant, or Newton's law where stress and shear rate are related through a material property as viscosity, i.e. the resistance of the material to flow.

2.2 Constitutive Equations

Constitutive equations allow us to calculate the viscous stress tensor $\boldsymbol{\sigma}$ by knowing the flow history and idealizing the molecular behavior that produces the stress. Some of them are based on empirical stress measurements that are written in a closed mathematical way which is useful to predict flow behavior. Ideally, these equations can help us understand the relation between microscopic physics and macroscopic response [10].

2.2.1 Newtonian Response

Newtonian fluids are defined by relating stress and deformation linearly through the (dynamic) viscosity of the fluid η which is assumed constant during deformation and has units of $\mathrm{Pa} \cdot \mathrm{s}$ (kinematic viscosity μ is $\mu = \eta/\rho$). It is assumed an instantaneous relation between stress and strain rate. The generalized stress tensor $\boldsymbol{\pi}$ of the Newton's law of viscosity for an incompressible fluid is written as:

$$\boldsymbol{\pi} = -p\mathbf{I} + \mu\mathbf{D}, \tag{2.7}$$

$\mathbf{D}$ is the symmetric deformation rate tensor $\mathbf{D} = (\nabla \boldsymbol{u}) + (\nabla \boldsymbol{u})^T$. From now on, we will define the term $\boldsymbol{\kappa} = (\nabla \boldsymbol{u})^T$. Note that in most mechanical engineering books a factor of (1/2) is used to calculate the symmetric part of the deformation rate tensor.

However, more complex deformation response to applied stress is of our interest, specifically non-Newtonian response. This is characterized by more complex constitutive models which belong to a field called rheology. In general, the deformation of the material is not necessarily related to the stress in a linear fashion like it is for Newtonian fluids.

2.2.2 Non-Newtonian Linear Response

Macromolecular fluids show interesting phenomena like rod climbing, die swell, vortex formation in contraction flows, among others. These should be thoroughly described by an adequate constitutive relation that represents quantitatively and mathematically non-trivial material properties dependence on deformation.

Description of viscoelastic behavior has been mostly oriented to the flow behavior of polymeric melts and solutions. The total stress present in the flow depends on the contribution of all molecules present in the fluid which, following the kinetic theory for polymer solutions and melts, regards polymer molecules as viscous components surrounded by a solvent that follows a Newtonian behavior [22].

Viscosity is a main property used to characterize mentioned melts. It could be defined as a relation between the shear stress and shear rate in a simple shear system, and it is constant for Newtonian fluids. Yet, for non-Newtonian cases, viscosity depends on shear rate and it is characterized by a zero-shear-rate viscosity η_0 that normally decreases with deformation. A strong evidence of viscoelasticity is the presence of the first and second normal stress differences, which are required for their viscometric characterization, and are in function of shear rate. They are defined respectively as:

$$N_1(\dot{\gamma}) \equiv \sigma_{xx} - \sigma_{yy}, \tag{2.8}$$

$$N_2(\dot{\gamma}) \equiv \sigma_{yy} - \sigma_{zz}, \tag{2.9}$$

for a system that is sheared in the x-direction and the flow is along the y-direction. Normal stresses differences are of rheological significance since they can tell us if there is tension or compression in the flow. They are related to strain-induced anisotropy and they are responsible of diverse phenomena as die swell and rod-climbing in polymers.

At smaller shear rates (when viscosity is close to η_0), a viscoelastic system will behave similarly to a Newtonian fluid. However, its departure from this behavior has been found to start when N_1 is proportional to $\dot{\gamma}^2$ for smaller shear rates; the latter is still proportional to the shear stress. This led to the definition of the first and second stress difference coefficients, $\mathcal{N}_1(\dot{\gamma}) \equiv N_1(\dot{\gamma})/\dot{\gamma}^2$ and $\mathcal{N}_2(\dot{\gamma}) \equiv N_2(\dot{\gamma})/\dot{\gamma}^2$ respectively, which are useful since they approach to a constant value at low shear rates allowing characterization of viscoelastic fluids [10, 22]. First normal stress differences and viscosity are usually measured with a rotational rheometer and are referred as viscometric functions.

Construction of viscoelastic models started by assuming a one-dimensional state of stress, i.e. simple shear system. The response of this system would be analogous to linear spring following $\sigma = G\gamma_{xy}$ or to viscous flow as $\sigma_{xy} = \eta\dot{\gamma}_{xy}$ as well, where G is the elastic modulus and γ_{xy} the shear strain.

Maxwell Model

Maxwell in 1867 attempted to describe empirically viscoelasticity as fluids behaving like an elastic solid or viscous fluid depending on the time scale of observation. The mechanical analogous setup of Maxwell's equations is a spring and a dash-pot in series. This can be written as Eq. 2.10. The total general deformation would be dominated by the time derivative for fast stress changes that yield to an elastic solid behavior, and in steady state we will have a Newtonian fluid depending on the shear rate [10, 16].

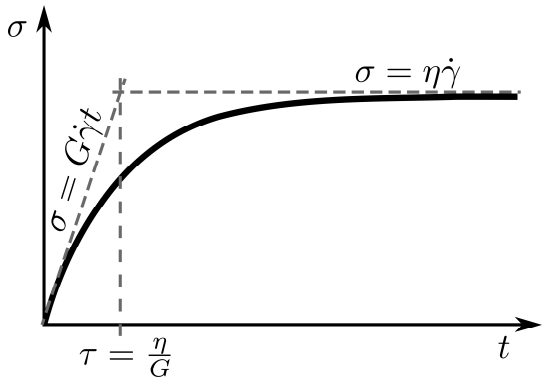


Figure 2.3: Schematic representation of stress evolution in time using the Maxwell equation for constant shear rate $\dot{\gamma}$.

$$\dot{\gamma} = \frac{\dot{\boldsymbol{\sigma}}}{G_\infty} + \frac{\boldsymbol{\sigma}}{\eta}. \tag{2.10}$$

The solution for this expression, if we have sudden onset of constant shear, has the form of:

$$\boldsymbol{\sigma}(t) = \int^t G_\infty e^{\frac{-(t-t')}{\tau}} \dot{\gamma}(t')\, \mathrm{d}t'. \tag{2.11}$$

The Maxwell relation $\eta = G_\infty \tau$ defines the viscosity, where τ is the relaxation time of the fluid, G_∞ is the shear modulus, and the dynamical shear modulus is defined as $G(t-t') = G_\infty \exp[(-(t-t')/\tau]$. The linearity of the model comes by making $G(t)$ independent of $\dot{\gamma}$. Though the assumption made was simple, this model has been a step-stone to describe polymer fluid dynamics [10]. A schematic representation of the stress evolution after startup of shear is shown in Fig. 2.3.

2.2.3 Upper Convected Time Derivative

Non-locality, in time and space, encodes the divergence of the viscosity in the fluid by implementing the upper convected time derivative of the stress instead of the time derivative as the constitutive equation. The upper convected time derivative of the stress tensor enforces the stress to be independent of any frame of reference, translational and rotational motion of the fluid element, and superimposed rotations [10].

This was explained in 1950 by Oldroyd [23], where he introduced a convected coordinate system $(\hat{x}^1, \hat{x}^2, \hat{x}^3)$ embedded in the material and moving continuously with it. A material that is at $\hat{x}^i$ at one instant is at the same point, with respect to $\hat{x}^i$, at every other time, hence, a fluid particle has the same coordinates for all times [24].

By defining a fixed Cartesian coordinate system (x_1, x_2, x_3), a particle P at a final time t in a fluid in motion will have the same convected Cartesian coordinates, but not at a past time t'. As a result we can write the location of this particle P as:

$$x_i' = x_i'(\hat{x}^1, \hat{x}^2, \hat{x}^3, t, t') \quad \text{or} \quad \boldsymbol{r}' = \boldsymbol{r}'(\boldsymbol{r}, t, t'), \tag{2.12}$$

$\boldsymbol{r}'$ is the displacement function.

Convected base vectors $\hat{\boldsymbol{g}}_i$ at each fluid particle are defined as functions of the location in the convected coordinate system and also dependent on time t' since the coordinate system itself is changing with time as the fluid moves along in the Cartesian coordinates. Hence, $\hat{\boldsymbol{g}}_i(\hat{x}^1, \hat{x}^2, \hat{x}^3, t') = \hat{\boldsymbol{g}}_i(\boldsymbol{r}, t, t') = \partial_{\hat{x}^i} \boldsymbol{r}'$. The base vector $\hat{\boldsymbol{g}}_i$ is tangent to the $\hat{x}^i$ coordinate curve, meaning $\hat{\boldsymbol{g}}_i(\boldsymbol{r}, t, t')$ describes how the fluid in the particle's neighborhood is oriented and distorted as it moves through space. Convected reciprocal base vectors $\hat{\boldsymbol{g}}^i(\boldsymbol{r}, t, t')$ are defined as well. They are normal to the surface of the convected coordinate system, so we have information of how the fluid is deformed [10].

If then the stress tensor is expanded in terms of the base vectors and contravariant components, we obtain respectively:

$$\boldsymbol{\sigma}(\boldsymbol{r},t,t') = \sum_i \sum_j \hat{\boldsymbol{g}}_i \hat{\boldsymbol{g}}_j \hat{\sigma}^{ij}(\boldsymbol{r},t,t'), \tag{2.13}$$

$$\boldsymbol{\sigma}(\boldsymbol{r},t,t') = \sum_i \sum_j \hat{\boldsymbol{g}}^i \hat{\boldsymbol{g}}^j \hat{\sigma}_{ij}(\boldsymbol{r},t,t'). \tag{2.14}$$

By setting the base vectors and reciprocal base vectors in terms of the unit vectors, we can express the stress tensor in Cartesian components. We may write the derivative of the stress with respect to time t' when time $t = t'$ following [23] as

$$\overset{\triangle}{\boldsymbol{\sigma}}(\boldsymbol{r},t) = \frac{D\boldsymbol{\sigma}}{Dt} + \left[(\nabla \boldsymbol{u}) \cdot \boldsymbol{\sigma} + \boldsymbol{\sigma} \cdot (\nabla \boldsymbol{u})^T\right] \tag{2.15}$$

and

$$\overset{\triangledown}{\boldsymbol{\sigma}}(\boldsymbol{r},t) = \frac{D\boldsymbol{\sigma}}{Dt} - \left[(\nabla \boldsymbol{u})^T \cdot \boldsymbol{\sigma} + \boldsymbol{\sigma} \cdot (\nabla \boldsymbol{u})\right]. \tag{2.16}$$

Equation 2.15 and 2.16 are called *covariant and contravariant convected derivatives* respectively. They are also known as *lower convected and upper convected time derivatives* of the stress tensor, being the latter the derivative mostly used in constitutive equations.

The operator $D/Dt = \partial/\partial t + (\boldsymbol{u} \cdot \nabla)$ is called "material derivative". It describes time rate of change of the stress tensor seen by an observer who is moving with the fluid [10].

The effect of the different components of the upper convected time derivative of the stress was studied for different constitutive equations in a pressure driven flow going through a abrupt 4:1 planar contraction. This is shown section 2.4.

Upper Convected Maxwell Model

The upper convected time derivative is implemented in linear models like the Maxwell model to make them frame invariant and to turn them into quasi-linear and non-linear models, which allows the construction of more complete and feasible constitutive equations [10].

By changing the time derivative in the Maxwell model in equation 2.10 for the upper convected time derivative 2.16 we obtain the upper convected Maxwell model (UCM) proposed by Oldroyd,

$$\tau \overset{\triangledown}{\boldsymbol{\sigma}} + \boldsymbol{\sigma} = \eta \mathbf{D}. \tag{2.17}$$

This model can predict the first normal stress differences but not the second. It does not account for effects like shear thinning since it assumes the viscosity is shear rate independent and it has a well known deficiency since it predicts infinite extensional viscosity [22].

2.2.4 Non-Linear Constitutive Equations

Linear viscoelastic models are valid for small deformation gradients, but not enough to describe more complex flow phenomenology. There are plenty of experimental data of viscoelastic flow that shows non-linear behavior of the dynamic shear modulus $G(\dot{\gamma})$, which can depend on the shear rate, time, and on the flow history.

For example, a concentrated polystyrene solution under step strain, see Fig. 2.4 (taken from [22]), shows how the shear modulus varies for different strain magnitudes (increasing from top to bottom). These are stress relaxation curves that show that for high strain the relaxation moduli are strain dependent (small strains top circles). In this case the dynamic shear modulus can be expressed together with a damping function that includes strain softening effect (see [25] for more details).

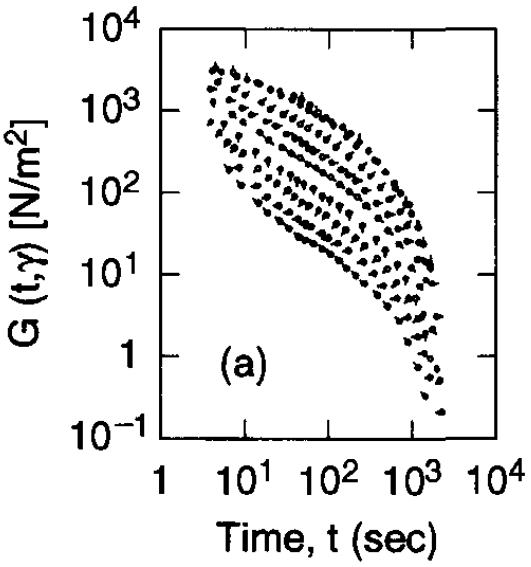


Figure 2.4: Dynamic shear modulus $G(t, \dot{\gamma})$ for a step strain experiment of a polystyrene solution with time [22] [25].

This non-linearity in the stress relaxation can be introduced as a shear rate dependence in the constitutive equation. If the relaxation time or viscosity is then to be made dependent on shear rate, this tensor must be independent of the coordinate system, therefore it is common to use independent combinations as the shear rate invariants.

Quasi and non-linear differential models have been for long time developed and successfully used to describe time-shear-dependent flows. This usually starts by modifying an existent linear model and making certain dependence that fit experimental data. Others are derived from theories like the kinetic theory of polymeric solutions and melts, where the system is represented by spheres connected through springs (which follow Hooke's law). The spheres represent the hydrodynamic interaction between the solvent and the polymer chains, and the spring the restoring effect of the macromolecules [10].

Oldroyd-B Model

A variation of the UCM model that can describe viscoelastic effects is the Jeffrey's model which is a starting point for quasi-linear and non-linear constitutive equations. Originally, this constitutive equation included the time derivative of the shear rate, "relaxation time" τ_1, and "retardation time" τ_2 as explained in [10, 22], thus:

$$\boldsymbol{\sigma} + \tau_1 \frac{\partial \boldsymbol{\sigma}}{\partial t} = -\eta_0 \left(\dot{\boldsymbol{\gamma}} + \tau_2 \frac{\partial \dot{\boldsymbol{\gamma}}}{\partial t} \right). \tag{2.18}$$

By using the upper convected derivative, this equation becomes frame-invariant and turns into the linear viscoelastic Oldroyd-B model, which is more general than the Upper Convected Maxwell model. If we consider a polymer solution (polymer plus solvent), this model will now included the hydrodynamic interaction as a result of the feedback of the polymer in the flow.

$$\tau_1 \overset{\triangledown}{\boldsymbol{\sigma}} + \boldsymbol{\sigma} = \eta(\mathbf{D} + \tau_2 \overset{\triangledown}{\mathbf{D}}). \tag{2.19}$$

This equation follows the assumption that for viscoelastic constitutive equations there is a "polymer" and "solvent" contribution to the stress in a polymer melt, from the molecular point of view. The total stress is:

$$\boldsymbol{\sigma} = \boldsymbol{\sigma}_s + \boldsymbol{\sigma}_p, \tag{2.20}$$

and the polymeric stress $\boldsymbol{\sigma}_p$ follows the relation:

$$\tau \overset{\triangledown}{\boldsymbol{\sigma}_{\boldsymbol{p}}} + \boldsymbol{\sigma}_p = \eta_p \mathbf{D}. \tag{2.21}$$

The stress contribution from the solvent component follows a Newtonian relation as $\boldsymbol{\sigma}_s = \eta_s \mathbf{D}$. The total viscosity η is then the sum of the polymeric and solvent viscosity contribution, i.e. $\eta = \eta_p + \eta_s$, and the retardation time for the Oldroyd-B model is defined as described by:

$$\tau_2 = \frac{\eta_s \tau_1}{\eta_s + \eta_p} \tag{2.22}$$

From now on, we will refer to the relaxation time simply as τ (which encapsulates the polymer relaxation time), and discuss its meaning in the next chapter. The Oldroyd-B model reduces to the Upper Convected Maxwell model if $\tau_2 = 0$, and to a

Newtonian fluid when $\tau = \tau_2$ [10]. It can estimate the first normal stress differences whereas for the second one it goes zero as result.

There is also an Oldroyd-A model, where the lower convected time derivative is used instead but it fails to predict the observed normal stress differences ratio.

White-Metzner Model

The White-Metzner model is a modification of the UCM where the relaxation time and viscosity are dependent on the second invariant of the symmetric velocity gradient tensor $\mathrm{II}_D = (1/2)\mathbf{D} : \mathbf{D}$ [26]. The model follows next relation:

$$\tau(\mathrm{II}_D)\overset{\nabla}{\boldsymbol{\sigma}}_p + \boldsymbol{\sigma}_p = \eta_p(\mathrm{II}_D)\mathbf{D}. \tag{2.23}$$

The dependence of τ and η_p on II_D captures shear thinning effects and normal stress differences. The relaxation time was defined in [27] as:

$$\tau(\mathrm{II}_D) = \frac{\tau}{1 + a\tau\sqrt{\mathbf{D} : \mathbf{D}}}, \tag{2.24}$$

and viscosity will follow

$$\eta_p(\mathrm{II}_D) = G\tau(\mathrm{II}_D). \tag{2.25}$$

The problem of the UCM that leads to infinite elongational viscosities in steady state elongation is avoided by using the empirical parameter $a > 2/\sqrt{3}$. This parameter tunes the viscosity and relaxation time dependence on the shear rate [10, 22, 27].

There are plenty of other models that are currently being used to describe viscoelastic behavior, where other forms of the non-linearity of the stress tensor have been introduced. Among the popular ones are Giesekus model where the product of the stress tensor is used, and different versions of the Phan-Thien-Tanner models in which the relaxation time depends on the trace of the stress tensor.

2.3 Computational Fluid Dynamics

In this section, we will describe the tools that can be used to solve viscoelastic flows using (mainly) differential constitutive equations. There is a widely established diversity of computational tools used in engineering to design, manufacture, test, and optimize many products which not only depend on structural properties, but on heat transfer, fluid flow, fluid-solid behavior, among other phenomena [19].

Computational Fluid Dynamics, or CFD, is a branch of fluid dynamics that allow to solve numerically the non-analytically-possible or impractical solutions of the different fluids and their governing equations. Mostly all CFD codes contain three main components. First, a pre-processor where the computational domain is defined together with grid generation, model selection, and material properties. Second, a solver that depends on what numerical technique is to be used: finite differences, finite volume, or spectral methods. We will use finite volume methodology, which will be explained in the next section. And last, the post-processor which includes grid display, contour plots, vector plots, and view manipulation among other user-friendly interface [21].

2.3.1 Finite Volume Method

Finite volume method is a special finite difference formulation that has been found reliable and central to most of the CFD codes. With this method, the solution domain is divided into a finite number of control volumes (CV) or cells that do not overlap and that cover the whole computational domain. For transient calculations, time is also divided in time-steps. The integral form of the conservation of mass and momentum is applied to each CV, which means that for each cell relevant properties and/or variables are conserved. Variables must be calculated at the CV central node, consequently, these values are interpolated to obtain their values at the surface in terms of nodal values.

Surface and volume integrals are approximated as an algebraic system of balance equations for each CV which then are discretized. Attention shall be put on the fluxes at the CV boundaries since they must be conserved and consistent. An important FVM feature is its suitability for any type of grid, which means that the control volumes can be of general polyhedral shape creating unstructured meshes [19–21].

In the next subsections we will describe the methodology followed by FVM widely used in different commercial CFD packages. There is well documented literature about FVM that started in the 1970s by McDonald in 1971 [28], MacCormack

and Paullay in 1972 [29]. Though the available information and development are extensive, our bibliographic base resides mainly on [19–21, 30, 31].

OpenFOAM®

OpenFOAM is an open-source software that is written in C++ language and allows the development of numerical solvers and diverse utilities, models, objects, thanks to a vast library needed to solve continuum mechanics problems [32]. This tool has helped us to study flow going through diverse geometries like pressure driven flow in planar channels, simple shear, cavities, and more complicated geometries like pressure-driven planar flow with obstacles and abrupt contractions. Meshing is one important capability of OpenFOAM, where refinement is easily done for more accuracy, for example, close to abrupt contractions where high velocity and stress gradients are expected, see Fig. 2.5.

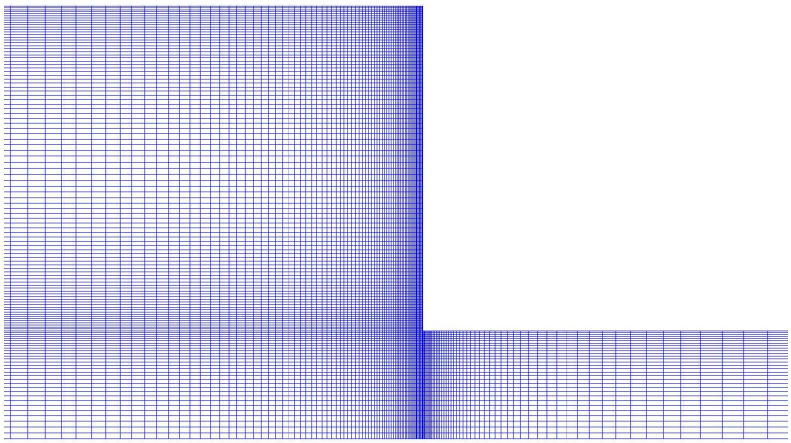


Figure 2.5: Mesh used for abrupt 4:1 contraction flow where a refinement is done close to the contraction.

OpenFOAM is versatile enough to use the finite volume method on unstructured grids with any kind of grid elements using a co-located methodology, where the quantities of interest are located in the center of the control volume, allowing each of them being discretized individually with the preferred scheme [33].

2.3.2 Domain Discretization

The starting point is the discretization of the solution domain in time and space. Time discretization requires a time-step size to be defined where forward marching is done by starting from a prescribed initial condition [19, 30]. Space discretization,

on the other hand, utilizes the subdivisions of the domain, where boundaries are defined instead of the computational nodes like in other finite difference methods. This means that the nodal value represents the mean over the CV for higher accuracy (second order) [20], and also avoids the need to calculate the stress at geometrical singular points [34].

Based on the conservation of mass and momentum, the general equation used in finite volume method for a variable ϕ, which can be as well $\boldsymbol{u}$, is written as:

$$\frac{\partial(\rho\phi)}{\partial t} + \nabla \cdot (\rho\phi\boldsymbol{u}) = \nabla \cdot (\Gamma\nabla\phi) + S_\phi. \tag{2.26}$$

On the left side of the equation we have first the rate of change of ϕ, then a convective term; on the right-hand side we have first a diffusive term and then a source term.

Equation 2.26 must be integrated over the control volume surface and rearranged using the Gauss' theorem, where vector $\boldsymbol{n}$ is normal to surface $\mathrm{d}A$, therefore it must be expressed as:

$$\begin{aligned}\int_{\Delta t} \frac{\partial}{\partial t} \left(\int_{\mathrm{CV}} \rho\phi \mathrm{d}V \right) \mathrm{d}t + \int_{\Delta t} \int_A \boldsymbol{n} \cdot (\rho\phi\boldsymbol{u}) \mathrm{d}A \mathrm{d}t = \\ \int_{\Delta t} \int_A \boldsymbol{n} \cdot (\Gamma\nabla\phi) \mathrm{d}A \mathrm{d}t + \int_{\Delta t} \int_{\mathrm{CV}} S_\phi \mathrm{d}V \mathrm{d}t.\end{aligned} \tag{2.27}$$

Since there is a time dependence of property ϕ, the latter must be integrated over small time interval Δt up to $t+\Delta t$. Convective and diffusive terms are first integrated over the entire bounding surface A and the source term over the CV.

A discretization equation is derived from a differential equation governing ϕ turned into algebraic relations depending on how ϕ varies between grid points, hence influencing its distribution across the immediate neighbors. This means, the larger the number of grid points the closer we get to the exact solution of the differential equation. FVM is attractive because the integral conservation equations are satisfied over any group of control volumes, hence by summing the equations for all CVs, a global conservation equation is finally obtained. The surface and volume integrals must be approximated by interpolation schemes to then obtain the algebraic equations needed to solve the flow [20, 30]

Interpolation Schemes

There are many ways of solving the convective, diffusive, and source terms in the global transport equation by means of interpolation in a grid.

Let us assume we have the next control volume (grey area), of area A, surrounding the central node P, where flow goes from left to right. Neighbor nodes are W and E, and boundaries of the CV are at w (west) and e (east) like it is shown in Fig. 2.6 [21].

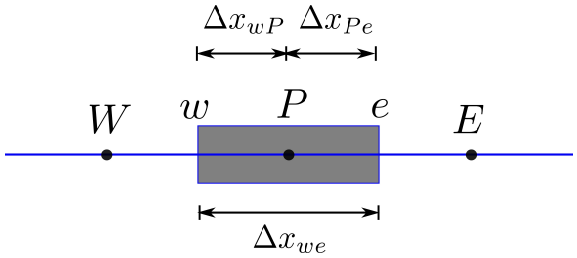


Figure 2.6: Control volume representation with centroid P.

If we assume that the variation of the flux ϕ in space and time around P is linear, the space linearization of $\phi(x)$ should be [19]:

$$\phi(x) = \phi_P + (x - x_P)(\nabla\phi)_P \tag{2.28}$$

where $\phi_P = \phi(x_p)$, and its time linearization will be:

$$\phi(t + \Delta\mathrm{t}) = \phi^t + \Delta t \left(\frac{\partial\phi}{\partial t}\right)^t. \tag{2.29}$$

A second-order accurate discretized form of Gauss' theorem is used to rewrite the convection part of the transport equation 2.27, for the control volume shown in previous figure (f refers to CV faces), which leads us to:

$$\int_A \boldsymbol{n} \cdot (\rho\phi\boldsymbol{u})\mathrm{d}A = \sum_f A(\rho\boldsymbol{u}\phi)_f. \tag{2.30}$$

We can generalize $F = A(\rho\boldsymbol{u})_f$ as the convective mass flux per unit area (or surface). Applying this to Fig. 2.6 in the CV, the discretized diffusion process would be $(\rho u A\phi)_e - (\rho u A\phi)_w$.

For the diffusion term, a similar procedure can be used. It is noted that the diffusive flux ϕ leaving the east face e minus the diffusive flux of ϕ entering the west face w is equal to the generation of ϕ in the control volume. Therefore, we can write it as:

$$\int_A \boldsymbol{n} \cdot (\Gamma\nabla\phi)\mathrm{d}A = \sum_f A(\Gamma_\phi\nabla\phi)_f, \tag{2.31}$$

such that the convection process in the CV can be written as:

$$\left(\Gamma A \frac{\phi_E - \phi_P}{\Delta x_{PE}}\right)_e - \left(\Gamma A \frac{\phi_P - \phi_W}{\Delta x_{WP}}\right)_w . \tag{2.32}$$

It could be seen the value of ϕ and its gradient normal to the cell face are needed to calculate the convective and diffusive fluxes. The simplest approximation used to calculate ϕ values for the **convective term** is the linear interpolation between the neighboring nodes: "Central Differencing Scheme" (CDS). It is a second-order scheme and may produce solutions that seem to oscillate around analytic solutions when available, since it depends on the grid uniformity [20]. The problem with this scheme is that it fails at identifying flow direction. It is written as:

$$\phi_e = \phi_E f_x + \phi_P (1 - f_x), \tag{2.33}$$

where f_x is an interpolation factor:

$$f_x = \frac{\Delta x_{Pe}}{\Delta x_{PE}}. \tag{2.34}$$

When a flow is strongly convective, this linear interpolation might fail. "Upwind Differencing Scheme" (UDS) considers the flow direction since it approximates the ϕ value, for example ϕ_e, to the next node upstream, ϕ_E. If the flow goes from left to right in Fig. 2.6 and $u_w > 0$ and $u_e > 0$, then $\phi_w = \phi_W$ and $\phi_e = \phi_P$. Even though it is a first-order scheme, it yields no oscillating solution, but it might numerically diffusive [20]. This scheme was ultimately used in all our calculations.

There are plenty of other alternative interpolation schemes, such as hybrid schemes between UDS and CDS, higher order ones like "QUICK", which converges to more accurate results when using more number of nodes, "Skew Upwind Schemes", and high order schemes like "Total Variation Schemes" (TVD). The main goal of schemes development is to ultimately retain solution stability. Hence, it is important that the schemes have: conservativeness of ϕ through CV, boundedness i.e. solutions must be bounded by its own boundaries, and transportiveness whereas the direction of the flow is correctly related to the Peclet number [20, 21].

Regarding boundedness, as mentioned before, a system of algebraic equations is formed which can be written in function of the coefficients for each node of the discretized equations. There is a criteria for convergence that enforces diagonal dominance over the resulting matrix, meaning that the coefficient value at a node must be bounded by its neighboring nodes (coefficients) values, and that source terms must be added positively to it. Usually, all coefficients must have the same

sign (positive) to fulfill the convergence criteria, which means that an increase of ϕ at P should increase ϕ at its neighbors too.

For the **diffusion term**, linear approximations are the simplest way of calculating interface values and gradients, which is similarly defined as CDS. The gradient in Eq. 2.31 is discretized at face f (which can be e in Fig. 2.6), as:

$$(\nabla\phi)_e = f_x(\nabla\phi)_P + (1 - f_x)(\nabla\phi)_E. \tag{2.35}$$

The **source term** can be any function of ϕ, and involves terms that are not written as convection, diffusion or time dependent terms. It must be expressed as a linear dependence on ϕ to enter the equations framework, henceforth the linearized source, following [21, 30], will be:

$$\int_{\mathrm{V_P}} S_\phi \mathrm{d}V = S_u V_P + S_p V_P \phi_P, \tag{2.36}$$

S_u and S_p arise form the source term linearization [30].

2.3.3 Temporal Term Discretization

Transport equation 2.27 not only must be discretized in space through surface and volume integrals but also in time, hence the importance of knowing at which time the fluxes must be evaluated: either explicitly where the terms are evaluated at times where the solution is already known, or implicitly, where the discretization happens at a time where the solution is not known yet. The first term of the transport equation might be rewritten for the CV as:

$$\int_t^{t+\Delta t} \frac{\partial}{\partial t} \left(\rho\phi V_P\right) \mathrm{d}t. \tag{2.37}$$

We can write the time derivative of ϕ for point P in Fig 2.6 depending on old time (index o) and new time (index n) as:

$$\frac{\partial \rho\phi}{\partial t} = \frac{\rho_P^o \phi_P^o - \rho_P^n \phi_P^n}{\Delta t} \tag{2.38}$$

in which $\phi^n = \phi(t + \Delta t)$ and $\phi^o = \phi(t)$.

For the rest of the transport equation, ϕ values and $\nabla\phi$ at the faces must be defined (see Eq. 2.30 and 2.31 respectively). The Explicit Euler method is the simplest

discretization, where the fluxes and gradients are evaluated at known times. We will write them at the face e considering the center of the control volume as P and the next node as E, see Fig. 2.6. Therefore following Eq. 2.33 and 2.35, we can obtain:

$$\phi_e = f_x \phi_P^o + (1 - f_x)\phi_E^o. \tag{2.39}$$

And, for the flux gradient

$$(\nabla\phi)_e = f_x (\nabla\phi)_P^o + (1 - f_x)(\nabla\phi)_E^o. \tag{2.40}$$

When the system of algebraic equations is written for all nodes using this method a maximum limit of time-step size is needed so the convergence criteria is fulfilled, which makes it limited and expensive, especially for transient problems.

The Implicit Euler method expresses the flux at face values depending on the new-time values, therefore flux and gradient are:

$$\phi_e = f_x \phi_P^n + (1 - f_x)\phi_E^n \tag{2.41}$$

$$(\nabla\phi)_e = f_x (\nabla\phi)_P^n + (1 - f_x)(\nabla\phi)_E^n. \tag{2.42}$$

Only first order accuracy is obtained with this method, and the system of algebraic equations obtained will contain "new" ϕ values on both sides of the equations. Convergence criteria here is fulfilled because all coefficients are positive, which makes it stable. Small steps are desired to improve accuracy.

However, the Crank-Nicolson was the method we used along this work though no differences were found when the implicit method was probed as well. It is second-order accurate in time and requires cell flux values at old and new times. It is written as:

$$\int_t^{t+\Delta t} \phi(t)\mathrm{d}t = \frac{1}{2}(\phi^o + \phi^n)\Delta t. \tag{2.43}$$

Transport equation 2.27 simplified by Eq. 2.30, 2.31 and 2.36, and using the Crank-Nicolson assumption ends up being [19]:

$$\begin{aligned}\frac{\rho_P^o\phi_P^o - \rho_P^n\phi_P^n}{\Delta t}V_P + \frac{1}{2}\sum_e F\phi_e^n + \frac{1}{2}\sum_e F\phi_e^o \\ -\frac{1}{2}\sum_e A(\Gamma_\phi\nabla\phi)_e^n - \frac{1}{2}\sum_e A(\Gamma_\phi\nabla\phi)_e^o = \\ S_u V_P + \frac{1}{2}S_P V_P\left(\phi_P^n + \phi_P^o\right),\end{aligned} \tag{2.44}$$

where F was previously defined as $F = A(\rho u)$ at the face.

This is a implicit method since unknown values of ϕ are ultimately present in the system of algebraic equations, but the positive sign of all coefficients must be ensured so the solution is realistic as mentioned in the explicit case. Therefore, there is not so strong time-step limitation but otherwise the method is suitable for transient calculations where great accuracy has been found [21].

After using the appropriate discretization methods for the convection and diffusion terms, a final equation must be written for each CV. For CVs that are adjacent to boundaries, the discretized equation must take into account boundary conditions. As mentioned, by summing all approximations for all nodes, a system of algebraic equations is obtained for all CVs that must be solved to find the flux distribution at nodal points. This has a general form of Eq. 2.45 [19–21].

$$a_P\phi_P^n + \sum_E a_E\phi_E^n = R_P. \tag{2.45}$$

The system of algebraic equations is composed by a sparse matrix $[A]$, a vector of ϕ, and a source term vector $[R]$ as in $[A][\phi] = [R]$ and can be solved directly or iteratively. Direct methods have higher computational cost and are only recommended for small systems. Iterative methods are more flexible regarding handling large equation sets. They proceed by guessing ϕ distribution, and update its value until the solution tolerance is met [19, 21].

The sparsity of matrix $[A]$ means that almost all coefficients are zero. a_P coefficients are on the matrix diagonal, and they correspond to ϕ_P^n, and a_E coefficients are off-diagonal and correspond to neighboring points. Sparsity reduces computational cost, hence solvers have been developed and used to preserve this matrix property and to achieve diagonal dominance. The latter is an important feature to preserve boundedness as well: the values of ϕ must be bounded by its boundaries [21]. When calculations are done in steady state ($\phi_P^o = \phi_P^n$), this diagonal dominance might be

enhanced by the use of under-relaxation factors. An artificial term is added to both sides of equation 2.45 in function of a factor $0 < \alpha < 1$, like for example [19]:

$$a_P \phi_P^n + \frac{1-\alpha}{\alpha} a_P \phi_P^n + \sum_E a_E \phi_E^n = R_P + \frac{1-\alpha}{\alpha} a_P \phi_P^o. \tag{2.46}$$

This technique allows to reach steady state solutions without instabilities of transient computation [20, 30]. When $\alpha = 1$ there is no under-relaxation, and $\alpha = 0$ means that the solution will not change with subsequent iterations [35].

Conjugated solvers included in all CFD packages are able to iteratively solve the algebraic equations. They are able to increase the diagonal dominance by means of equation preconditioners like for example: PCG (preconditioned conjugate gradient solver for symmetric matrices), DIC (diagonal incomplete-Cholesky) pre-conditioner, PBiCG (preconditioned bi-conjugate gradient solver for asymmetric matrices), DILU (diagonal incomplete lower upper) pre-conditioner, are very common in the field.

2.3.4 Split-Stress Tensor Approach

Viscoelastic computations have a well-established reputation of being challenging and unstable, in particular for high Weissenberg or Deborah number. These two terms indeed are sometimes used interchangeably, however the first one, usually abbreviated a Wi, refers to the ratio between elastic and viscous forces, and the second one, De, is the relation between the relaxation time of a material and the time of observation given to such material to flow.

As mentioned in section 2.1, the momentum equation for incompressible viscoelastic flows includes a constitutive law that should be able to describe different non-Newtonian phenomena found experimentally. The constitutive law defines a stress tensor $\boldsymbol{\sigma}$, that depends on the velocity gradient, and will be coupled to the momentum and mass conservation equation. Henceforth, we will have to solve the conservation equations simultaneously with a hyperbolic set of quasi-linear-non-linear differential equations for the stress tensor (with new unknown variables) [36].

There is a diverse number of methodologies that can make viscoelastic simulations more stable and less costly, nonetheless, we have decided to use a solver that is encoded in OpenFOAM 3.0® and OpenFOAM-extend® called “viscoelasticFluidFoam”. It uses a split-tensor approach that stabilizes viscoelastic solutions, especially at high Weissenberg numbers [9, 37]. This approach is called “Discrete Elastic Viscous Split-Stress” (DEVSS) and can be applied to steady-state and transient problems. It consists of introducing the rate of deformation tensor as an additional unknown,

which is proved to stabilize the discretization of the equations, mainly for rheological models where changing variables in the constitutive equations is cumbersome [38].

As it was mentioned earlier the stress tensor for viscoelastic fluids can be modeled as the sum of a Newtonian and non-Newtonian contribution as if we had a polymeric solution (polymer and solvent) (See Eq. 2.20).

Thus, by rewriting and rearranging the momentum equation 2.6 (omitting gravitational effects) we obtain:

$$\rho\frac{\partial \boldsymbol{u}}{\partial t} + \rho(\nabla \cdot \boldsymbol{uu}) = -\nabla p + \nabla \cdot \boldsymbol{\sigma}_p + \eta_s \nabla \cdot (\nabla \boldsymbol{u}). \tag{2.47}$$

The DEVSS approach adds a new diffusive term to both sides of the momentum equation to stabilize the calculations, with a pre-factor λ that should be positive. Thus, the new momentum equation to be solved is:

$$\rho\frac{\partial \boldsymbol{u}}{\partial t} + \rho(\nabla \cdot \boldsymbol{uu}) - (\eta_s + \lambda)\nabla \cdot (\nabla \boldsymbol{u}) = -\nabla p + \nabla \cdot \boldsymbol{\sigma}_p - \lambda \nabla \cdot (\nabla \boldsymbol{u}). \tag{2.48}$$

According to [38], a good choice for λ would be η_P. In CFD calculations the left side of the equation will be solved implicitly and the right side explicitly. The way this equation is solved will be explained in the next section. Among DEVSS advantages we find that it can be extended to complicated rheological models, and also easy to implement since the constitutive equation does not change. This method is highly versatile regarding Weissenberg numbers in the flow, since reliable results are found even at high values, which has been a problem that has puzzled the community for a long time [37, 38].

2.3.5 Pressure-Velocity Coupling

A pressure-velocity treatment is used to solve iteratively the linearized partial differential equations one at a time (segregated way). This means that while solving the equations for velocity components, or pressure correction, others variables are treated as known [20]. This algorithm is called PISO algorithm (*Pressure Implicit with Splitting of Operator*), and it is used for solving time-dependent flow equations [39].

The transport equation must be discretized before being solved since non-linearity arises from the convective term $\rho(\nabla \cdot \boldsymbol{uu})$. This can be linearized by the procedures explained in previous sections. However, pressure is the most complex issue to resolve and define (if it is unknown) since there is no equation for it. Incompressibility (and isothermal systems) can make the issue a bit more complicated because pressure comes

from an equation of state depending on density and temperature, i.e. $p = p(\rho, T)$. Pressure, should be then derived from the discretized form of the momentum and continuity equation, in order to assure consistency [19].

A semi-discretized form of the momentum equation can be written as:

$$a_P \boldsymbol{u}_P = \boldsymbol{H}(\boldsymbol{u}) - \nabla p, \tag{2.49}$$

where the pressure gradient is not discretized just yet. $\boldsymbol{H}(\boldsymbol{u})$ corresponds to all coefficients for all neighbors of node P (neighboring nodes N) multiplied by their velocities, transient and source terms (stress tensor), besides pressure. This means $\boldsymbol{H}(\boldsymbol{u})$ is:

$$\boldsymbol{H}(\boldsymbol{u}) = -\sum_N a_N \boldsymbol{u}_N + \frac{\boldsymbol{u}^o}{\Delta t}. \tag{2.50}$$

At a generic face f, we can write the velocity $\boldsymbol{u}_f$ following equation 2.49 as:

$$\boldsymbol{u}_f = \left(\frac{\boldsymbol{H}(\boldsymbol{u})}{a_P}\right)_f - \left(\frac{1}{a_P}\right) \nabla p_f. \tag{2.51}$$

The mass conservation equation should be fulfilled, and its linearization is:

$$\nabla \cdot \boldsymbol{u} = \sum_f S \boldsymbol{u}_f = 0. \tag{2.52}$$

Henceforth, from equation 2.51 we can obtain:

$$\nabla \cdot \left(\frac{\boldsymbol{H}(\boldsymbol{u})}{a_P}\right)_f = \nabla \cdot \left(\frac{1}{a_P}\right) \nabla p_f \tag{2.53}$$

By linearizing the pressure gradient in the transport equation 2.49 as 2.54, and combining with Eq. 2.53, an expression for pressure is defined as 2.55 [19].

$$a_P \boldsymbol{u}_P = \boldsymbol{H}(\boldsymbol{u}) - \sum_f S(p)_f, \tag{2.54}$$

$$\sum_f S \left[\left(\frac{1}{a_P}\right)_f (\nabla p)_f\right] = \sum_f S \left(\frac{\boldsymbol{H}(\boldsymbol{u})}{a_p}\right)_f. \tag{2.55}$$

The PISO algorithm is used to solve this discrete set of equations. The algorithm was developed by Issa in 1986 [39] and it is commonly used in transient calculations where all the high-order terms dependent on time are included in the calculations.

It follows mainly three main steps: first, a pressure is guessed and used explicitly to solve the momentum equation giving an approximated velocity field. Second, $\boldsymbol{H}(\boldsymbol{u})$ is assembled using the velocity field and a new value of pressure is obtained. Third, the flux is calculated as $F = S\boldsymbol{u}_f$, and a new velocity field is obtained with the new pressure field reached in the second step. A minimum of two corrector steps is required to obtain legitimate velocity and pressure solutions, which are pre-determined by the solution tolerance set by the user [19, 39].

2.3.6 Boundary Conditions

The flow geometry will determine how the boundaries must be defined. The main boundary conditions set in OpenFOAM used along this work are summarized next (see [19, 33, 35]).

- Dirichlet: a fixed value ϕ at a face e as ϕ_e is set at the boundary for a variable. In OpenFOAM this is called '`fixedValue`'.

  Following Eq. 2.30, the convection term will be then discretized depending on the already fixed value as $\sum_f A(\rho\boldsymbol{u}\phi)_f = F_f\phi_f$ at the face e i.e. $F_e\phi_e$.

  The diffusion term will be discretized following Eq. 2.31, where the face gradient at the face e will be calculated between that face and the centroid P of the CV, hence

$$\Gamma A \cdot (\nabla\phi)_e = \Gamma A \frac{\phi_e - \phi_P}{\Delta \mathrm{x}_{\mathrm{PE}}}. \tag{2.56}$$

- Neumann: the gradient of a variable is fixed normal to a boundary, called in OpenFOAM as '`fixedGradient`'. If the gradient at a boundary is G_e whose surface area is A_e, then

$$G_e = \left(\frac{A_e}{|A_e|} \cdot \phi_e\right)_e. \tag{2.57}$$

  At a boundary face ϕ is calculated as $\phi_e = \phi_P + \mathbf{d} \cdot (\nabla\phi)_e$. Here the vector separating the e and P is $\mathbf{d}$. If the discretization requires the face gradient $A_e \cdot (\nabla\phi)_e = |A_e|G_e$.

For incompressible flows, we utilize inlet boundary conditions where the velocity fields are prescribed, and the pressure is prescribed as '`zeroGradient`'. Nonetheless, for pressure driven flow we do set a pressure at the inlet and outlet, and '`zeroGradient`' for the velocity. At the outlet boundary condition the mass balance must be satisfied, either by setting a fixed value for the pressure with zero-gradient for the velocity field, or the velocity distribution is scaled to satisfy continuity at the outlet [19].

No-slip boundary conditions are set at the walls to guarantee that the velocity of the fluid on the wall is the same as the velocity of the wall. This means that a fixed value at the wall is needed and the pressure must be specified as zero-gradient condition [33]. Symmetry planes are set to reduce computational time by setting the normal component of the velocity gradient to zero at the boundary.

2.4 Effect of Advection Term in Flow

As it was mentioned previously in Section 2.2.3, the upper convected time derivative of the stress tensor follows the relation

$$\overset{\triangledown}{\boldsymbol{\sigma}}(t) = \underbrace{\frac{\partial \boldsymbol{\sigma}}{\partial t}}_{\text{a}} + \underbrace{(\boldsymbol{u} \cdot \nabla \boldsymbol{\sigma})}_{\text{b}} - \underbrace{[\boldsymbol{\sigma} \cdot \nabla \boldsymbol{u}]^T - [\boldsymbol{\sigma} \cdot \nabla \boldsymbol{u}]}_{\text{c}}. \tag{2.58}$$

Each one of the components has an effect on the how the flow is described, which could be summarized as:

- a: Euler time derivative of the stress tensor $\partial \boldsymbol{\sigma}/\partial t$,
- b: spatial term involving the streamline tensor derivative of the field $(\boldsymbol{u} \cdot \nabla \boldsymbol{\sigma})$ (stress advection). This term becomes relevant when the streamlines of the flow are curved,
- c: rotation of the stress tensor that makes it frame invariant (material objectivity).

When Newtonian fluids are described, inertial effects become important at high Reynolds number which usually indicates turbulence in the flow. In the case of viscoelastic fluids, instabilities have been found as well at low Reynolds number. They are referred as "elastic turbulence" [40]. For example, a elastic polymer solution can become irregular a low velocities even for high viscosities, showing turbulent features like secondary and vortex flows [41]. These features have been a challenge when one wants to develop more complicated constitutive models for complex flows that are not necessarily differential equations. In the next chapter we will talk

about how the Mode-Coupling Theory has been used as base to develop materials models starting from first-principles. Extensions of this microscopic theory become cumbersome when heterogeneous flows must be described and the advection term inclusion becomes relevant [42].

We studied the effect of the stress advection in heterogeneous flows by using the Upper Convected Maxwell model (section 2.2.3) as a basis to define the non-Newtonian component of the stress tensor. The Newtonian contribution will follow a linear relationship between stress and deformation $\boldsymbol{\sigma}_s = \eta_s \mathbf{D}$, therefore the system at rest will have a total viscosity as the sum of the Newtonian (solvent) and non-Newtonian (polymer) components $\eta = \eta_s + \eta_p$. The definition of the non-Newtonian stress is:

$$\overset{\triangledown}{\boldsymbol{\sigma}}_p(t) = G_\infty \boldsymbol{D} - \frac{\boldsymbol{\sigma}_p(t)}{\tau_M}, \tag{2.59}$$

where G_∞ is the elastic modulus, and τ_M is the relaxation time. The definition of the relaxation time establishes the linearity of the model, i.e. if the relaxation time is constant we will have a linear model (we called it LMM). On the other hand, if we make it dependent on the shear rate we enforce non-linear response and can introduce, for example, shear thinning effects. For this case, we use a definition of τ_M that comes from a detailed microscopic theory that will be explained in the next chapter, nonetheless, let us write it down for the following discussion as

$$\frac{1}{\tau_M} = \frac{1}{\tau} + \frac{\sqrt{\mathrm{II}_D}}{\gamma_c}. \tag{2.60}$$

This equation follows closely the form of the White-Metzner model previously presented (we called it NLMM). We might refer to results obtained with models missing advection term as model-ac.

2.4.1 Taylor-Green Vortex

To get deeper insight into the advection-term effect in viscoelastic flows we studied its influence on a decaying Taylor-Green vortex. This is a typical scenario to study the momentum equations and to validate numerical schemes. It was originally developed by Taylor [43] and resembled four-roll mills located at the edge of a square domain. This vortex has been used to simulate a wide range of flows subjected to simple shear and extensional flow at an extent that could be varied at a given velocity gradient [44]. The setup was made in a cavity of size $l = l_x = l_y = 2\pi$ with periodic boundary conditions at the walls. The Deborah number De was varied and defined as D$e = \tau u_0 / l$ were u_0 is the characteristic velocity of the system. At time $t = 0$ initial

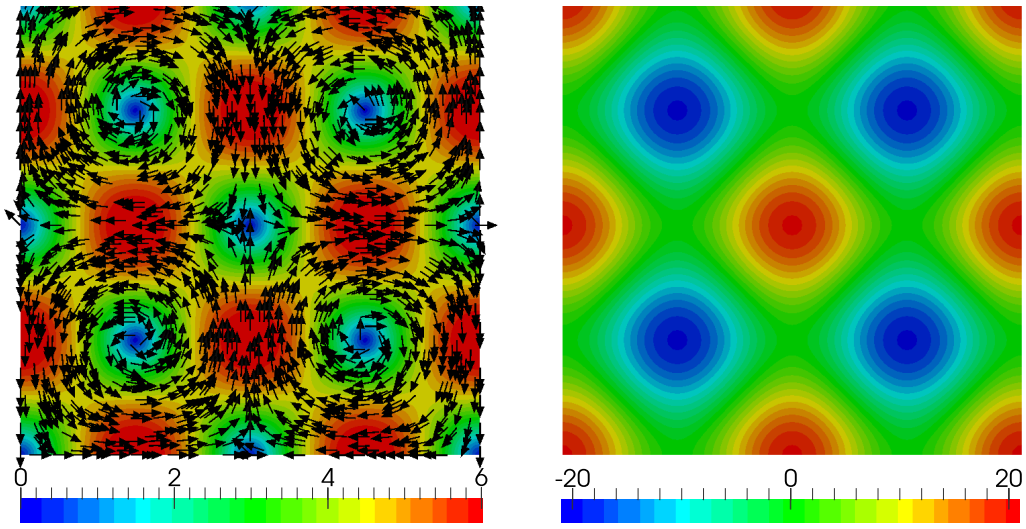


Figure 2.7: Schematic representation of the Taylor-Green multiple-roll mills set-up. Left side shows velocity magnitude contours at time $t = 0$ (arrows show flow direction), and right side shows pressure contours (case D$e = 100$).

fields for velocity and pressure were implemented following the analytical solutions of the Newtonian flow in a Taylor-Green vortex [45]. Vortices are formed creating a stagnation point in the center, which we set-up as shown in Fig. 2.7.

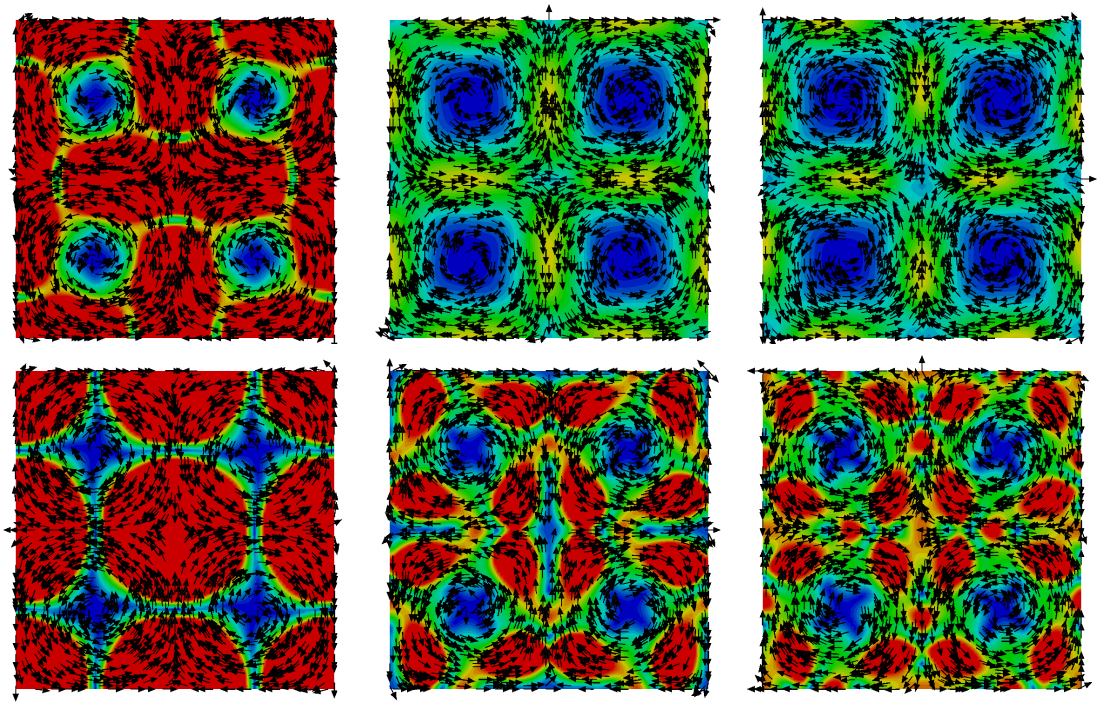
$$u_x(x,y) = u_0 \sin\left(\frac{2\pi x}{L}\right)\cos\left(\frac{2\pi y}{L}\right), \tag{2.61}$$

$$u_y(x,y) = -u_0 \cos\left(\frac{2\pi x}{L}\right)\sin\left(\frac{2\pi y}{L}\right), \tag{2.62}$$

$$p(x,y) = \frac{\rho}{4}{u_0}^2\left(\cos\left(\frac{4\pi x}{L}\right) + \cos\left(\frac{4\pi y}{L}\right)\right). \tag{2.63}$$

First, we solved the flow using the LMM and studied the differences observed during the decay of the non-Newtonian stress. We made comparisons between flows obtained using D$e = 10$, 100 and studied the influence of including the stress advection term at a stress distribution level in the system. Second, for D$e = 100$, we studied the decay using both LMM and NLMM and assessed the influence of the advection term inclusion. For both analyses, we focused on studying the transient behavior of the stress magnitude starting at around the overshoot found at earlier times. We also compared first normal stress differences and shear stress patterns at intermediate times. Relaxation time was set to $\tau/\tau_0 = 100$, where τ_0 corresponds to the Newtonian (solvent) fast time scale $\eta_s = G_\infty \tau_0$.

Linear Maxwell Model



$t/t_0 = 0.5$ $t/t_0 = 2.5$ $t/t_0 = 5$

Figure 2.8: Magnitude of the non-Newtonian stress at indicated times for relaxation time $\tau/\tau_0 = 100$ using full LMM (top row) and solution without the stress advection term (bottom row), case $De = 100$. Arrows represent direction of the flow. Red is for high values, $\|\boldsymbol{\sigma}\| = 1$, blue for low ones, $\|\boldsymbol{\sigma}\| = 0$.

Fig. 2.8 shows color maps of the stress magnitude at different points in time when the full linear Maxwell model is used including the advection term (top) and without it (bottom). For small De number, differences induced by the stress advection are negligible. However, at higher De, stress magnitude patterns develop differences at earlier times. It is noticeable that for the times shown, structures and stress distribution differ in shape. When the advection term is missing, structures around the vortices are star-shaped with higher stress values than those obtained with the full model (top row) where lower stresses seemed to cover more of the vortices area. Overall higher stresses are predicted without the stress advection, mainly around the center of vortices and stagnation points, where the inclusion of the term relaxes and carries the stress faster along the flow lines.

Regarding normal stress difference distribution, similar discrepancies were found for higher De at earlier times before stress relaxes to zero. Fig. 2.9 shows color maps obtained using the full linear Maxwell model (left) and same model without the

advection term (right) at intermediate time $t/\tau_0 = 2.5$. The absence of the advection term resulted in similar distribution tendency of N_1 but did not capture completely the mix of compression and tension expected around the stagnation points and between the vortices.

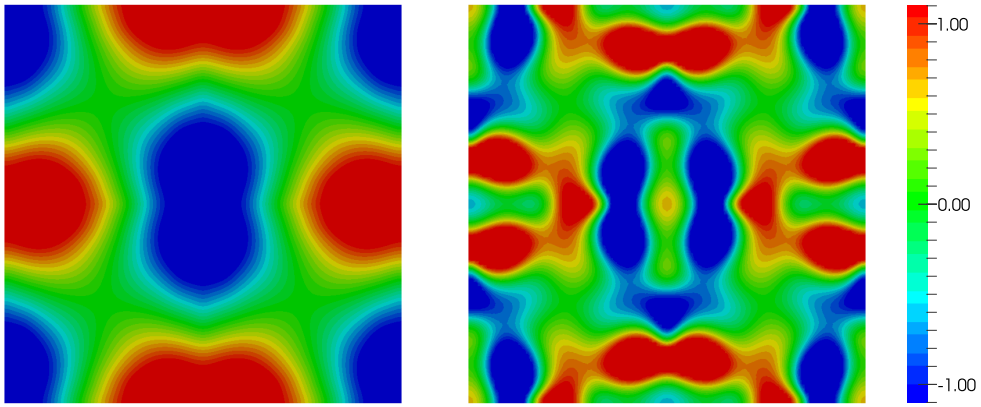


Figure 2.9: Normal stress difference N_1/G_∞ color maps at $t/\tau_0 = 2.5$ for D$e = 100$. Left: full LMM, right: model without advection term.

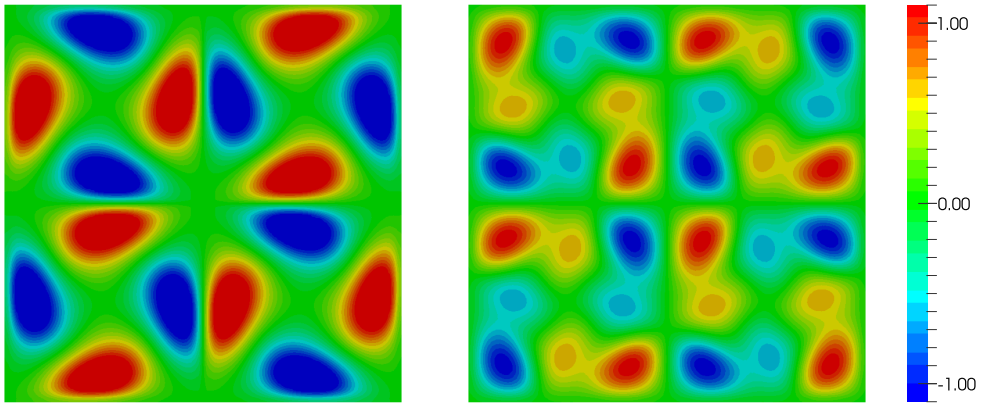
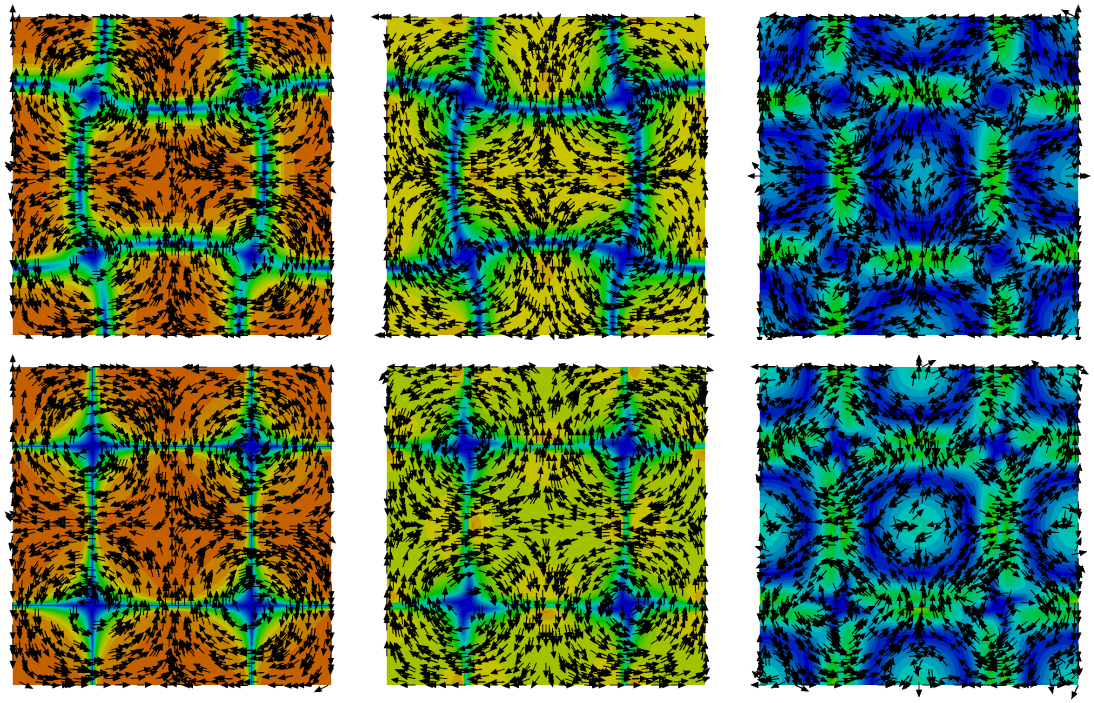


Figure 2.10: Shear stress σ_{xy}/G_∞ color maps at $t/\tau_0 = 1$ for D$e = 100$. Left: full LMM, right: model without advection term.

Fig.2.10 illustrates the shear stress case comparison. Areas with higher shear are not captured completely without the stress advection, which in fact seemed to have turned clockwise next to the expected sheared areas obtained with the full model (left).

Non-Linear Maxwell model

A shear dependent relaxation time was used like it was exemplified by Eq. 2.60. Same parameters were used using De = 100. Shear thinning reduces the effect of the advection: stress magnitude patterns, shown in Fig. 2.11, differ in less extent to results obtained using the advection term. Including the advection term (top row) causes a visible dependence on the flow direction as shown by the star-shaped patterns at each vortex which appear more "rigid" when the term is not present (bottom row).



$t/t_0 = 0.5$ $t/t_0 = 2.5$ $t/t_0 = 5$

Figure 2.11: Magnitude of the non-Newtonian stress at indicated times for relaxation time $\tau/\tau_0 = 100$ and De= 100 using NLMM (top row) and solution without the stress advection term (bottom row). Arrows represent direction of the flow. Red is for high values, $\|\boldsymbol{\sigma}\| = 0.17$, blue for low ones, $\|\boldsymbol{\sigma}\| = 0$.

Fig. 2.12 shows the evolution of stress magnitude of the non-Newtonian stress tensor at position $\vec{r} = (0.1, 0.1)$. This quantity relaxes faster at this position to the zero-steady-state value when the model is non-linear than when linearity is enforced for higher De number case. Shear thinning effect fastens the stress relaxation. Stress magnitude is wrongly estimated at early times where disparities are higher with LMM. Normal stress, in the NLMM case, shows a rather squared-shape distribution around the central stagnation point for the case

of a high De number when NLMM missed the advection term, which does not capture the elongated and highly tensional subjected areas around that point as obtained with the full NLMM. This comparison is shown in Fig. 2.13. Shear stress patterns obtained without stress advection followed more closely the results obtained with the full model, see Fig. 2.14. It seems that the shear thinning effect reduces the differences obtained when the model has or not the stress advection in the material derivative, even for higher De number. The advection operator in the upper convected time derivative of the stress tensor describes how the stress is transported along the streamlines which is not seen in the color plots obtained when the advection term is missing. Typically the stress advection is stronger in regions that also have a stronger local shear rate, where flow-induced stress relaxation becomes more effective when the shear thinning model is used.

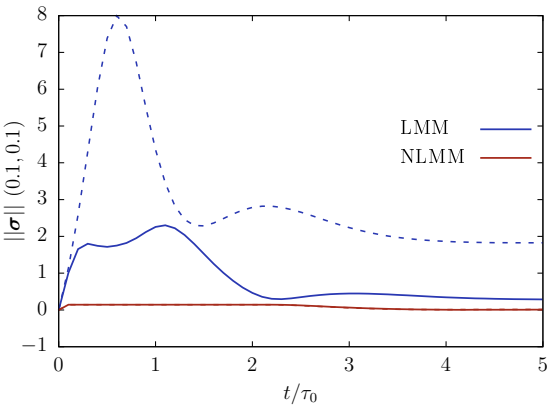


Figure 2.12: Transient behavior of non-Newtonian stress tensor magnitude at position $\vec{r} = (0.1, 0.1)$. Full models (solid lines) and model-ac (dashed lines) (De=100).

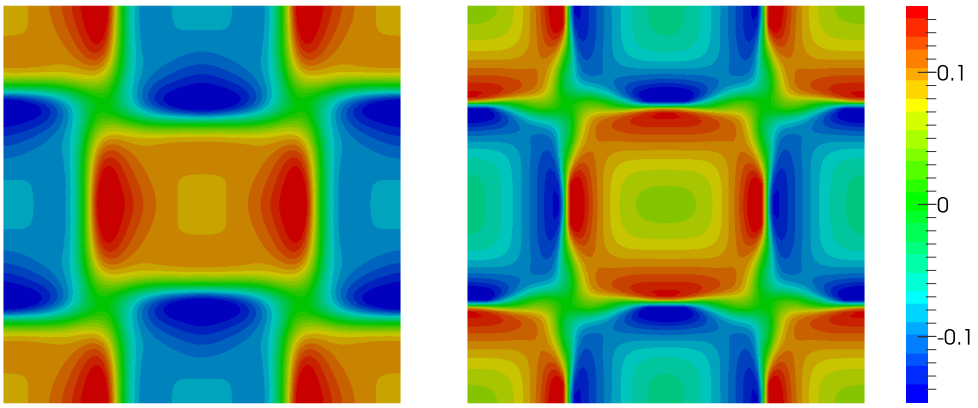


Figure 2.13: Normal stress difference N_1/G_∞ color maps at $t/\tau_0 = 2.5$ for De $= 100$. Left: full NLMM, right: model without advection term.

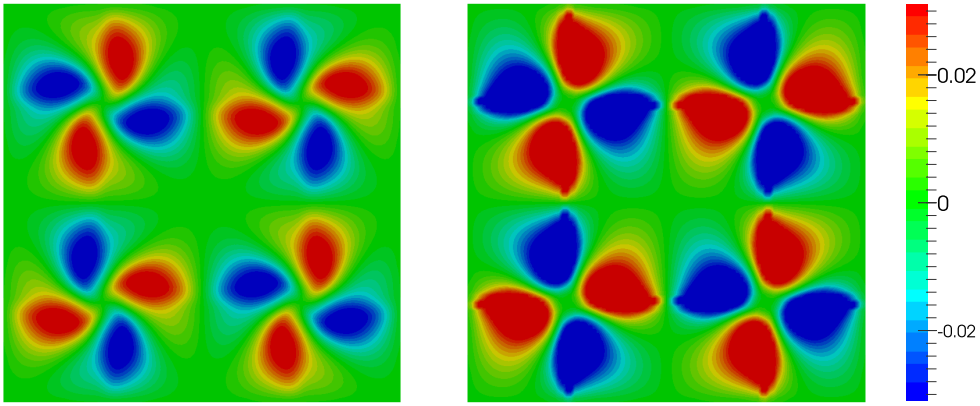


Figure 2.14: Shear stress σ_{xy}/G_∞ color maps at $t/\tau_0 = 2.5$ for $De = 100$. Left: full NLMM, right: model without advection term.

2.4.2 Abrupt 4:1 Planar Contraction

We studied the effect of the stress advection in an abrupt 4:1 contraction geometry as well, which was further used along this work. This geometry has been a benchmark problem for at least the last 30 years [46, 47], where flow features like lip vortex or corner vortex became relevant [48]. Many industrial applications deal with contracting flows, for example, polymer injection, film blowing, molding, extrusion, which makes its challenging for experimental and numerical descriptions [49].

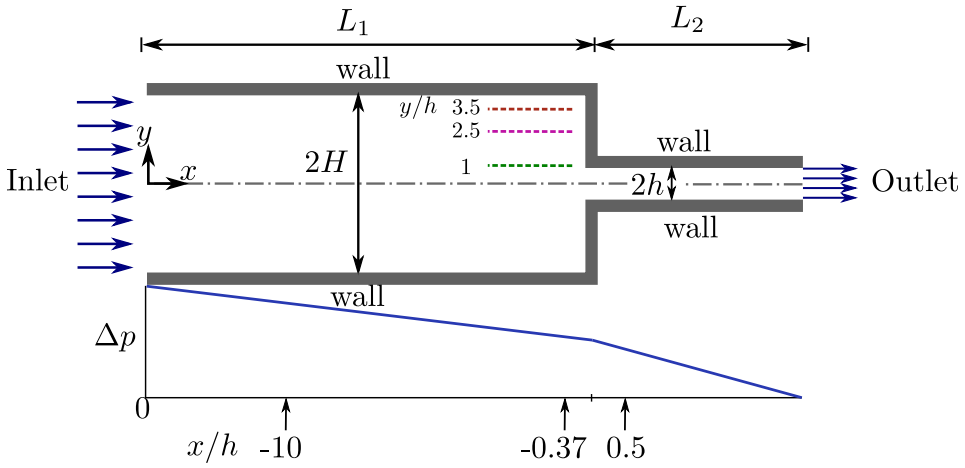


Figure 2.15: Schematic representation of the abrupt 4:1 contraction geometry.

A schematic representation of the contraction geometry we used in our research is shown in Fig. 2.15. The upstream length $L_1 = 80h$ is chosen to ensure that the flow is completely developed before the contraction, and $L_2 = 50h$ is the downstream

length used to avoid outlet effects as suggested and assessed in [9]. We did a mesh analysis where a compromise was made regarding the effects we wanted to study and computational time/cost. For the current analysis, we used Mesh 1, whose details are described in Appendix A.3. A fixed pressure was set up at the inlet to create a gradient down to the outlet where pressure was set to zero. In order to vary the De number the inlet pressure was varied. The relaxation time was set to $\tau/\tau_0 = 10$. No-slip boundary conditions were used for the velocity at the walls, and Neumann conditions at the inlet and outlet which sets the velocity gradient at these locations to zero.

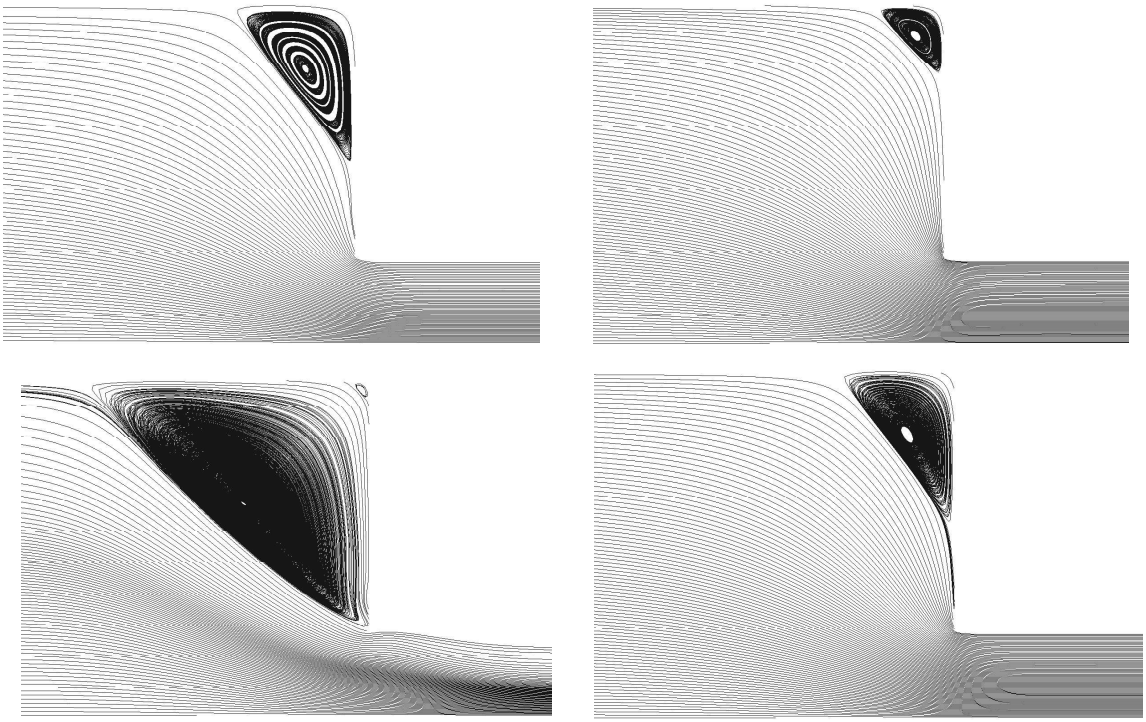


Figure 2.16: Flow streamlines in steady state for low De number (top row) and high De number (bottom row). Left side: LMM (De = 0.2, 27), and right side: NLMM (De = 1.4, 190).

For contraction flows the characteristic time can be calculated as a function of characteristic shear rate downstream the channel which is computed as the ratio of the average velocity downstream, $\langle u_d \rangle$, and the downstream channel width h. The flow relaxation time, as suggested by [50], is taken as the "longest" relaxation time of the system. Therefore, we used De $\equiv \tau \langle u_d \rangle / h$. Complex flow patterns are generally observed when viscoelastic flows go through sudden contractions, mainly including regions of strong shearing near the walls and non-homogeneous extension along the centerline upstream and downstream the channel [51, 52]. The formation of a recircu-

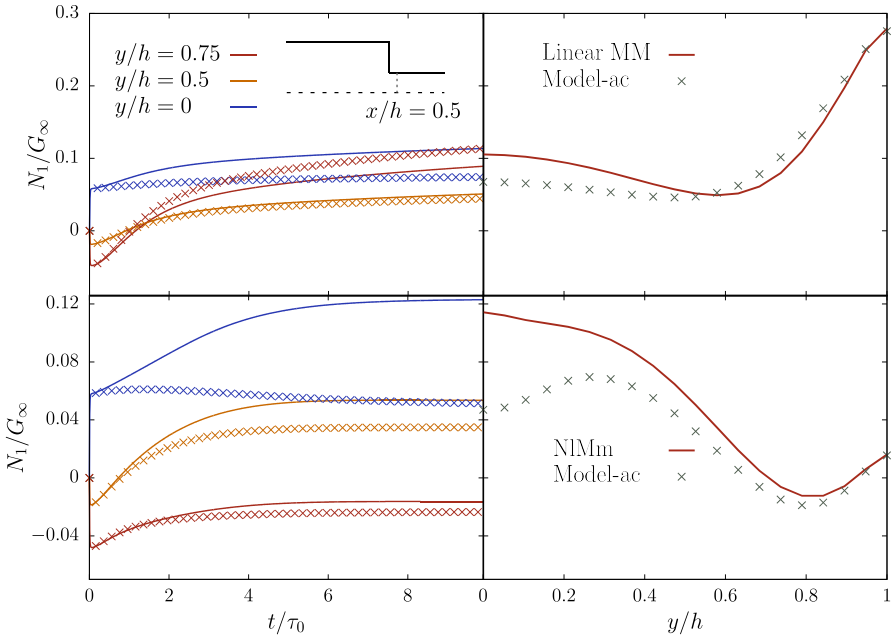


Figure 2.17: Left: transient evolution of N_1 for full models (lines) and no advection (model-ac) (symbols) probed downstream at $x/h = 0.5$. Right: corresponding steady state profiles. Top row: LMM using De = 0.21, bottom row: NLMM using De = 1.37.

lating area on the upper corner upstream of the contraction, resembling a vortex, is an observed phenomenon that might be associated to the extensional viscosity [50–52]. These features make this geometry in principle interesting regarding the influence of the advection term in the stress derivative. Fig. 2.16 shows the vortices obtained in steady state for both LMM and NLMM for low and high Deborah numbers. In the case of low De, both models show negligible differences between resulting velocity and stress distribution when the stress advection term was or not present upstream the contraction. However, we must say that downstream the channel, the first normal stress differences profiles were slightly different from the expected full model prediction, which is summarized in Fig. 2.17 as profiles right after the contraction. When the Deborah number was increased, the LMM without the advection term diverged. Streamlines in this case showed stronger curvature, which lead to the subsequent instability of the advection-less model. When shear thinning effects were included, divergences were avoided and in fact suppressed. We found virtually

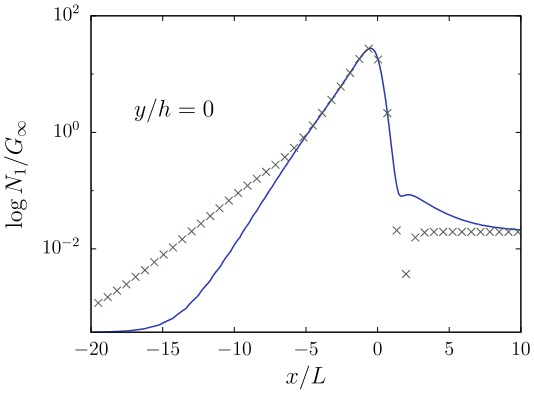


Figure 2.18: N_1 x-profile at $y/h = 0$ for NLMM with stress advection (line) and without (symbols) for high De number.

no difference across the channel for any of the variables studied, in fact, higher De numbers stabilized the NLMM without stress advection faster than when low De numbers were studied. One can say though, that the first normal stress difference is slightly affected by the absence of the advection term in the centerline of the geometry, as shown in Fig. 2.18.

Chapter 3

Glass-Forming Liquids

In this chapter, we will briefly introduce glass-forming liquids and how they are described within the mode-coupling theory (MCT). There is abundant literature regarding the details of this theory, nonetheless, it is important for us to consider its background and its resulting schematic model used to describe glass rheology from a microscopic point of view. As we discuss in the following, some features of the schematic model provided the basis to develop a "fluidity model" that we will use to describe how glass-forming liquids flow in complex geometries.

3.1 Glass Transition

It is an empirical fact that when we heat up minerals they melt into a liquid state and then they start flowing. If we subject this system to an undercooling process below its melting point, crystallization is expected to occur. Nonetheless, there are certain conditions when highly viscous liquids cooled down rapidly might not undergo crystallization, but instead, a rather steep increase in their viscosity occurs, which might give the material solid-like properties yet a liquid-like microscopic structure. The protocol followed to produce a glass might define its intrinsic properties making them history dependent. When this phenomenon happens it is said the material is going through a *glass transition*, thus these materials are called glasses [53]. In fact, it has been virtually accepted that all fluids that go through an undercooling (or compression) faster (or greater) than the intrinsic structural relaxation can go through glass transition. Sometimes this behavior can only be attained by computer simulations since faster cooling rates are required [54, 55]

The viscosity increase is related to a dramatic slowing down of the system dynamics, frequently following an abrupt temperature quench. However, this is not the only

way of obtaining a glass. For instance, an increase in pressure, volume fraction, or cross-linking density could produce a glassy system. Glass transition has been empirically defined as the temperature or density when the viscosity of the system reaches about $10^{11}\text{Pa}\cdot\text{s}$ [55].

Macroscopic quantities like viscosity and diffusion coefficients can be written in terms of microscopic correlation functions which can be measured experimentally using methods like dynamic light scattering [55–60] and neutron scattering [61]. The density-density correlation function, $\Phi(t)$, is a typical physical observable object suitable to study glassy behavior since it allows to analyze disordered (or ordered) structures in a system of N particles by being directly related to the scattering-intensity of a sample [58]. Density fluctuations as a function of wave vector $\mathbf{k}$ are defined by $\delta\rho(\mathbf{k},t) = \sum_{j=1}^{N} e^{i\mathbf{k}\cdot[\mathbf{r}_j(t)]}$. The dynamics of density fluctuations is described by the so-called density correlator:

$$\Phi(\mathbf{k},t) = \frac{1}{N}\big\langle \delta\rho(\mathbf{k},t)^{*}\delta\rho(\mathbf{k},0)\big\rangle \tag{3.1}$$

Connecting macroscopical behavior of a glassy system to the slowing down of the dynamic of its constituent particles have been subject of much research, involving experimental characterization, simulation analysis, and theoretical descriptions. The time dependence of the correlation function provides important information regarding what happens during the slowing down of the dynamics, either by undercooling or increasing the volume fraction of the system.

Figure 3.1 is a schematic representation of the relaxation of $\Phi(t)$ with time for two quiescent systems: one is at higher temperature (red line), and the other one at lower temperatures (blue line) [62]. The former relaxes faster than the latter since at lower temperatures the interaction between the particles in the system increases. The motion of particles in the system is hindered, i.e. they cannot move freely because they are trapped by their nearest-neighboring particles forming a cage. This is referred to as the "cage effect", when $\Phi(t)$ remains almost constant during the β-relaxation plateau. For longer times particles will be able to leave the nearest-neighbor cages at a time called α-relaxation time. For a glassy state $\tau^{\alpha} \to \infty$ since particles are unable to break the cage and a dynamically arrested system is formed [14, 63].

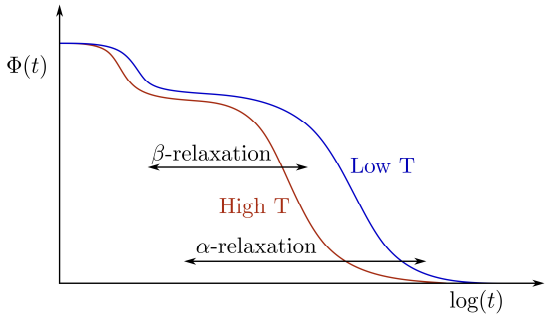


Figure 3.1: Schematic representation of a generic microscopic density correlator $\Phi(t)$ versus correlator time and regimes of interest.

If an external force is applied to the system during the α-relaxation, the cage breaking phenomena might be enhanced. Hence, there will be a competition with the relaxation mechanism where finally the system is taken out of equilibrium. In other words, the inherent relaxation time τ of the system will compete with the deformation imposed, giving rise to non-linear rheological effects when the deformation rate $\dot{\gamma}$ is bigger than the relaxation rate $1/\tau$. The relation between $\dot{\gamma}$ and τ is called "dressed" Péclet number (also known as Weissenberg number) as $\mathrm{Pe} = \dot{\gamma}\tau$ [1].

Measurements in diverse glass formers, like colloidal suspensions close to glass transition, have shown that forces can induce a decrease in the viscosity or thinning of the system. Breaking the cages makes the system go from elastic deformations to irreversible plastic deformations, which have been found to happen when cages are deformed at around 10 %. This process melts the glass by overcoming a force threshold, which is another feature of these systems called yield stress [1,14,64]. Fig. 3.2 exemplifies the correlator decay in time for glass-forming liquids (blue lines) and how steady shear rate drives the system into a non-equilibrium state. Red lines correspond to fluid phase correlator where the quiescent system exhibits a decay as a stretched exponential to zero [65]. The distance to the glass transition is quantified by ϵ as a measure of volume fraction: $\epsilon = 0$ defines the point of the glass transition, $\epsilon < 0$ the fluid state, $\epsilon > 0$ the glassy state. For more information about these expressions refer to [12, 66]. Glassy state systems appear mechanically as solids, nonetheless, a rather intermediate behavior has been documented. Their structure is similar to a liquid since their molecules are close to each other but not free to move like it is the case of a fluid. From the point of view of mechanical response, they share properties found in solids (elastic modulus), but could behave either as a solid or liquid, as it is for the case of viscoelastic materials [53]. At high concentration, glass formers like silica, metallic liquid alloys, and colloidal suspensions show similar complex flow properties. A first-principles approach as the MCT, under certain assumptions, has been able to characterize the observed slowing down of the dynamics and to predict the viscosity-temperature dependence as well.

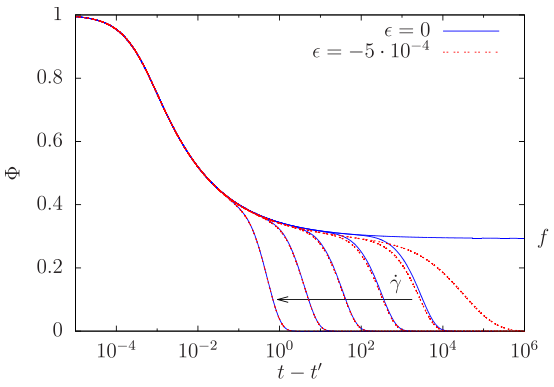


Figure 3.2: Φ correlator for glass state (blue line) (plateau at f), and the shear rate effect. Red lines correspond to the liquid phase (taken from [65]).

This theory has the ability to describe microscopically what happens during glass transition, which has allowed the development of models where external forces are introduced into the system to get a closer understanding of glass rheology [3,12,14,66]. Although the scope of our research does not involve the detailed discussion of how

the MCT was developed, we have used a schematic model derived from this theory as a basis to write down a constitutive equation used to study glass-forming liquids rheology. The specific details of the MCT approach can be found in many references like [13, 67, 68].

3.2 Microscopic Theory

Fuchs and Cates [67] and Brader, Cates, and Fuchs [12,13,69] developed an extension of MCT to describe what happens when a quiescent state is under (simple) flow through the Integration Through Transients (ITT) formalism. Through Green-Kubo relations one is able to express the stress tensor of a homogeneous system that is initially at rest and then switched on, by integrating in time the transport coefficients which, in MCT context, are density correlators. The approximation results in the time integral of the stress tensor encompassing strain history via the Finger tensor, static structure factor S_k, and the square of a transient density correlator [12, 64].

$$\boldsymbol{\sigma}(t) = -\int_{-\infty}^{t} \mathrm{d}t' \int \frac{\mathrm{d}\mathbf{k}}{32\pi^3} \left[\frac{\partial}{\partial t'} \left(\mathbf{k} \cdot \mathbf{B}(t,t') \cdot \mathbf{k} \right) \mathbf{k}\mathbf{k} \right] \mathscr{G}_k(t,t'). \tag{3.2}$$

The finger tensor is defined as $\mathbf{B}(t,t') = \mathbf{E}(t,t') \cdot \mathbf{E}^T(t,t')$, where $\mathbf{E}(t,t')$ is the deformation gradient tensor between time t' and t. The wave vector-dependent kernel involves time derivatives of the structure factor and density correlator:

$$\mathscr{G}_k(t,t') = \frac{S'_k S'_{k(t,t')}}{kk(t,t')S_k^2} \Phi^2_{\mathbf{k}(t,t')}(t,t'). \tag{3.3}$$

$\Phi(t,t')$ is a transient density correlator that amounts how much the density fluctuation at a wave vector $\mathbf{k}$ at time t overlaps with the one at past time t'. The transient density correlator is written as [64]:

$$\partial_t \Phi_{\mathbf{q}}(t,t_0) + \Gamma_{\mathbf{q}}(t,t_0) \left(\Phi_{\mathbf{q}}(t,t_0) + \int_{t_0}^{t} dt' m_{\mathbf{q}}(t,t',t_0) \partial_{t'} \Phi_{\mathbf{q}}(t',t_0) \right) = 0, \tag{3.4}$$

where the initial decay of the correlator, $\Gamma_{\mathbf{q}}(t,t_0)$, is related to short time motion [1]. The three-time dependent memory kernel $m_{\mathbf{q}}(t,t',t_0)$ is a rather non-trivial function that depends on the accumulated strain between the three arguments and quadratically on the density correlator [65]. These equations have been feasibly used, after some approximations, to describe simple flows. These approximations comprise the exclusion of the angular dependence of the correlator so then the system

is assumed isotropic, which lead to the development of the isotropically sheared hard sphere model.

3.2.1 Schematic MCT

Solving the MCT-ITT equations is cumbersome and computationally expensive, even after simplifications, for simple flows like simple shear. With this premise, Brader et al. [64] simplified and described a more practical model starting form the the MCT-ITT equations 3.2, assuming isotropy and no dependence on wavelength [14]. The resulting expression is:

$$\boldsymbol{\sigma}(t) = \int_{-\infty}^{t} \mathrm{d}t' \left[-\frac{\partial}{\partial t'} \mathbf{B}(t, t') \right] G(t, t'). \tag{3.5}$$

By discarding wave dependence, one can write a generalized modulus as:

$$G(t, t') = \nu_\sigma \Phi^2(t, t'), \tag{3.6}$$

where ν_σ determines the initial height of the shear modulus.

The remaining correlator will evolve then as the next equation of motion:

$$\partial_t \Phi(t, t_0) + \Gamma \left(\Phi(t, t_0) + \int_{t_0}^{t} dt' m(t, t', t_0) \partial_{t'} \Phi(t', t_0) \right) = 0, \tag{3.7}$$

where only one initial decay Γ is present to set the microscopic scale. The memory kernel $m(t, t', t_0)$ has been simplified by mentioned authors where strain dependence is kept and many aspects of the glass transition contained in MCT are quantitatively captured. Next ansatz is set:

$$m(t, t', t_0) = h(t, t_0) h(t, t') \left[\nu_1 \Phi(t, t') + \nu_2 \Phi^2(t, t') \right] \tag{3.8}$$

In this equation $h(t, t')$ will account for the memory decay due to strain. In steady shear, when setting $h = 1/(1 + (\gamma/\gamma_c)^2)$, one can get results close to the suggested by MCT-ITT. However, this expression was generalized to different flows and to preserve material objectivity by using the first and second invariant, I_1 and I_2, of the finger tensor $\mathbf{B}$ respectively, thus:

$$h(t, t_0) = \frac{{\gamma_c}^2}{{\gamma_c}^2 + [\nu I_1(t, t_0) + (1 - \nu) I_2(t, t_0) - 3]} \tag{3.9}$$

γ_c is a fit parameter that scales the recoverable elastic strain and can accurately account for structural distortions, it is usually set to 0.1, and $\nu = 0.5$ is a mixing parameter. Further simplification of this model sets $\nu_1 = 2(\sqrt{2}-1) + \epsilon/(\sqrt{2}-1)$ and $\nu_2 = 2$. As previously mentioned, ϵ is a separation parameter related to density, where $\epsilon < 0$ corresponds to fluid state and $\epsilon > 0$ to glass state. This schematic model results in similar behavior as the microscopic model [64].

3.2.2 Further Simplifications

The decay of the dynamic shear modulus might be further simplified as an exponential decay [63, 66, 70], as it is usually done for the Maxwell model:

$$G(t, t') = G_\infty e^{-(t-t')/\tau_M}. \tag{3.10}$$

The analogy to MCT in this expression is that the shear modulus shows a slow exponential relaxation that starts from G_∞, which corresponds to the β-relaxation plateau. This decay accounts for the competition between slow structural relaxation defined by τ and shear-induced deformation $\dot{\gamma}$ (see Fig. 3.2) [63, 66, 70]. This gave rise to an ad-hoc expression for a relaxation time τ_M that decays with shear, more specifically on the second invariant of the velocity gradient tensor, or it is just constant when no shear is present. Thus, inspired by the solution of MCT, the shear dependent relaxation time is written as:

$$\frac{1}{\tau_M} = \frac{1}{\tau} + \frac{\sqrt{\mathrm{II}_D}}{\gamma_c}. \tag{3.11}$$

Note that when τ_M in equation 3.10 is constant, the shear modulus reduces to the linear Maxwell model expression (section 2.2.2).

The shear modulus $G(t, t')$ is the sum of a slow structural part $G_{struc}(t, t') = G_\infty$ and a short-time contribution $G_{micr}(t, t')$. The short-time contribution $G_{micr}(t, t') \approx (G_0 - G_\infty)\Theta(\epsilon - (t - t'))$ is modeled by the Heaviside function. When $\epsilon \to 0$ the short-time Newtonian viscosity is defined as $\eta_\infty = G_\infty \tau_0$. G_0 is the high-frequency shear modulus for $t \ll \tau_0$, and G_∞ is the low-frequency shear modulus. A Newtonian-background viscosity is present to account what happens when $\sigma > \sigma_Y$ i.e. yield stress.

By combining equations 3.5 and 3.10 one can obtain a "memory dependent" integral constitutive equation, relying on the deformation history defined by τ_M, which can as well be called generalized non-linear Maxwell model [63]:

$$\boldsymbol{\sigma}(t) = \eta_\infty \mathbf{D}(t) + \int_{-\infty}^{t} \mathrm{d}t' \left[-\frac{\partial}{\partial t'} \mathbf{B}(t,t') \right] G_\infty e^{-(t-t')/\tau_M(t')} \tag{3.12}$$

In this model, a Newtonian background viscosity is added manually as the first term to set a minimum in the viscosity. This is also introduced in the schematic model as a lower bound in the correlator decay ($\eta_\infty = G_\infty \tau_0$ and τ_0 is the fast-relaxation time). Note that this model accounts for memory dependence sort of similar to the MCT model since the relaxation time is in function of $\dot{\gamma}(t)$ in order to capture MCT effects [63, 65].

However, if Eq. 3.12 loses the shear rate time dependence, we arrive to a differential constitutive equation similar to the White-Metzner model introduced earlier (section 2.2.4).

$$\overset{\triangledown}{\boldsymbol{\sigma}} = G_\infty \mathbf{D}(t) - \frac{\boldsymbol{\sigma}(t)}{\tau_M} \tag{3.13}$$

The generalized non-linear Maxwell model has been used in the past to reproduce important and central features predicted by MCT since it is able to mimic the physics of glass-forming liquids rheology [65, 71, 72]. We used its differential form, Eq. 3.13 to compare methodologies for steady state flow behavior.

However, transient behavior depends not only on the memory of a previously deformed material but also on how the time dependence of shear shear rate. For this reason, a material property called "fluidity" will be next introduced and developed, which will describe the relaxation time τ_M by means of its own differential equation hence the shear rate time dependence is more involved in the material deformation solution.

3.3 Fluidity Model

As if it was previously stated, a single differential equation for the stress tensor $\boldsymbol{\sigma}(t)$ is not sufficient to accurately describe non-linear glass-forming liquids rheology. The simplification, done to obtain the stress tensor expression shown by Eq. 3.13, makes it lose the history dependence well known in glassy systems since the shear rate is taken to be instantaneous in its effect on relaxation time.

Derec et al. [73] defined a term called "fluidity" as an inverse mechanical relaxation time in order to describe the memory of a glassy system that shows yielding behavior. In their paper, they defined the stress tensor related to this new term fluidity, which at the same time depends on the shear rate, aging, and rejuvenation of the system. These authors mention that the model has no reference to microscopic mechanisms.

However, its simplicity has helped to understand the relation between non-linear rheology and yield stress (glass-forming) liquids. Picard et al. [74] followed the same concept to develop a fluidity model that depended on aging and rejuvenation in pasty systems, by using a monotonic and non-monotonic steady state flow curve where spatial heterogeneities are introduced.

Yielding in glassy systems have been found to be dependent on the interplay between slow structural relaxation and local flow induced rearrangements [2]. Rearrangement in the flow is a concept that has been used to develop schematic models for glassy materials, like emulsions. The yield stress, in this case, is regarded as the stress needed to make an irreversible change within neighbors [2]. This has been studied experimentally in emulsions through diffusing-wave spectroscopy by [75]. Interestingly, it has been demonstrated that in colloidal glasses, while approaching from the liquid phase to the glass transition, there is a cooperativity zone between particles that allow rearrangements due to microscopic yielding as a response to an externally applied shear. After the glass transition is reached those rearrangements become more restricted [76]. The cooperativity phenomenon results in finite-size effects that could deviate the expected final flow behavior of glass-forming systems. For example, it could lead to the formation of heterogeneous flow patterns like shear bands and/or peculiar spatial features in the flow [3].

Localized plastic events generate non-local long-ranged elastic relaxation of the stress within the system, hence the constitutive relation that defines the flow behavior should be non-local [4]. Predictions of non-local models involving fluidity are successfully used to capture yield stress fluid behavior and to describe cooperativity in the flow where the term "fluidity" started gaining notoriety.

With this premise, we modified Eq. 3.13 by using this new term called fluidity as an inverse relaxation time following [2–4, 74]. Our fluidity definition indeed has a microscopic background since we include the relaxation time dependence on the shear rate that is related to the cage-breaking phenomenon, explained by the MCT, in glass-forming systems under shear.

The new expression for the deviatoric stress tensor is:

$$\overset{\triangledown}{\boldsymbol{\sigma}}(t) = G_{\infty}\boldsymbol{D}(t) - f(\mathbf{r},t)\boldsymbol{\sigma}(t), \tag{3.14}$$

$$\tau_f \frac{D}{Dt} f(\mathbf{r},t) = -\left(f(\mathbf{r},t) - \frac{1}{\tau_M(\mathrm{II}_D)}\right) + \xi^2 \nabla^2 f(\mathbf{r},t). \tag{3.15}$$

This form captures the competition between the quiescent structural relaxation rate $1/\tau$ and flow-induced relaxation since τ_M is defined by equation 3.11. In absence of

flow the fluidity will be an inverse relaxation time $f = 1/\tau$, that will have a steady state value $f = 1/\tau_M$. We model the fluidity as a diffusion-relaxation process, whose diffusion coefficient is $D_f = \xi^2/\tau_f$. The diffusion term is linked to stress diffusion since it defines how plastic events are interacting and spreading [4]. A term called cooperativity length ξ is introduced, and τ_f defines the fluidity timescale.

The cooperativity length ξ tells to what extent a fluidized region triggers local relaxations to its neighbors during flow, taking into account spatial heterogeneities that are present in the system [2, 4, 74, 77]. In fact, flow cooperativity is already known in rheology of a confined jammed emulsion in microchannels, and it has been said that it is in the order of droplet diameters [4]. The cooperativity length presence in confined emulsions and yield stress fluids is one of the causes of why flow profiles experimentally look different from predictions in confinements (microchannels). When the cooperativity length reached a fraction of the confinement, flow curves tend to be different from bulk predictions. Stress gradients or boundary effects can cause these differences, especially if the former is at a scale comparable with ξ [2, 4]. However, we approach the cooperativity length as a material property that is not dependent on the confinement as mentioned authors in their specific set-up suggest. Along this thesis we used ξ values that range from small fractions of the channel up to the channel width studied. Anyways, we considered Goyon et al. [4] suggested values as $\xi/h^* \approx 0.5$.

3.3.1 Fluidity Model Assessment

The stationary solution using the fluidity model for a homogeneous flow converges to $f = 1/\tau_M$, therefore Eq. 3.14 becomes:

$$-\boldsymbol{\kappa}\cdot\boldsymbol{\sigma} - \boldsymbol{\sigma}\cdot\boldsymbol{\kappa}^T = G_\infty\left[\boldsymbol{\kappa} + \boldsymbol{\kappa}^T\right] - \frac{1}{\tau_M}\boldsymbol{\sigma} \tag{3.16}$$

The resulting expression for the stress in steady state homogeneous flow follows:

$$\boldsymbol{\sigma} = \sum_{n=1}^{\infty} G_\infty \tau_M^n \boldsymbol{d}^n, \tag{3.17}$$

$$\boldsymbol{d}^n = \sum_{m=0}^{n} \begin{pmatrix} n \\ m \end{pmatrix} \boldsymbol{\kappa}^m (\boldsymbol{\kappa}^{\mathrm{T}})^{n-m}. \tag{3.18}$$

τ_M and the flow conditions will determine if $\boldsymbol{d}^n$ converges. In simple shear $\boldsymbol{\sigma} = G_\infty\tau_M\boldsymbol{D} + 2G_\infty\tau_M^2\left[\boldsymbol{\kappa}\cdot\boldsymbol{\kappa}^T\right]$ and shear stress is $\sigma_{xy} = G_\infty\dot{\gamma}\tau_M$. The first normal

difference is $N_1 = \sigma_{xx} - \sigma_{yy} = 2G_\infty \dot{\gamma}^2 \tau_M^2$. Yield stress is defined as the stress needed to start the flow, which in our model for simple shear would be $\sigma_Y = G_\infty \gamma_c$.

Following previous expressions, we can determine the viscosity in a simple shear system and verify its dependence on shear rate. This is shown in Fig. 3.3. Corresponding normal stress coefficients ($\mathcal{N}_1 = N_1/\dot{\gamma}$) are plotted for different relaxation times ($\tau/\tau_0 = 10^3$, 10^5, and 10^9). $\mathcal{N}_1$ is remarkably higher than σ_{xy} when $\tau \to \infty$, and it is always positive, which means the flow exerts a force pushing apart the containing walls. The higher the relaxation time, $\mathcal{N}_1$ and η diverge for $\dot{\gamma} \to 0$ which mimics the presence of a finite yield stress characteristic of glass-forming liquids [64].

Start up flow

Assume now that we have a time-dependent homogeneous simple shear system, so that $\kappa_{xy} = \dot{\gamma}(t)$. The fluidity equation 3.15 turns then into:

$$\tau_f \frac{\partial f(t)}{\partial t} + f(t) = \frac{1}{\tau} + \frac{\dot{\gamma}(t)}{\gamma_c}, \tag{3.19}$$

whose solution is:

$$f(t) = f(0)e^{-t/\tau_f} + \int_0^t dt' e^{-(t-t')/\tau_f} \frac{1 + \dot{\gamma}(t')\tau/\gamma_c}{\tau\tau_f}. \tag{3.20}$$

The shear stress equation reduces to:

$$\frac{\partial \sigma(t)}{\partial t} + f(t)\sigma(t) = G_\infty \dot{\gamma}(t), \tag{3.21}$$

which is solved as:

$$\sigma(t) = \sigma(0)e^{-\int_0^t f(s)ds} + \int_0^t dt' e^{-\int_{t'}^t f(s)ds} G_\infty \dot{\gamma}(t'). \tag{3.22}$$

For start-up shear, with initial conditions $\sigma(0) = 0$ and $f(0) = 1/\tau$, and $\dot{\gamma}(t) = \dot{\gamma}$ for $t > 0$, the fluidity will be:

$$f(t) = \frac{1}{\tau} + \frac{\dot{\gamma}}{\gamma_c}\big(1 - e^{-t/\tau_f}\big). \tag{3.23}$$

The shear stress is then solved as:

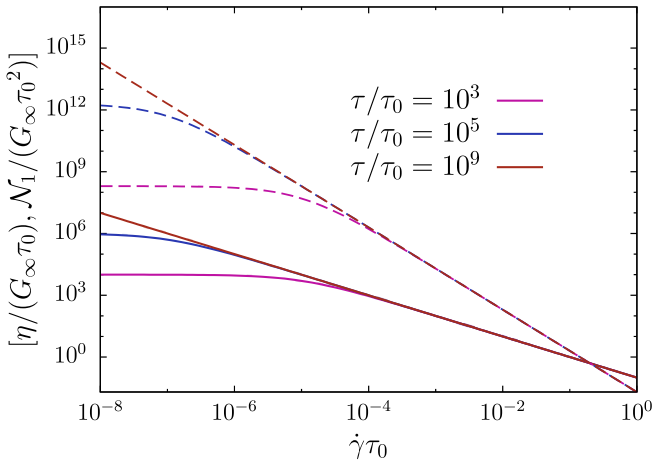


Figure 3.3: Shear viscosity $\eta = \sigma_{xy}/\dot{\gamma}$ (solid lines) and normal stress coefficient $\mathcal{N}_1 = N_1/\dot{\gamma}^2$ (dashed lines) as function of the shear rate $\dot{\gamma}$ for homogeneous simple shear flow for different relaxation times.

$$\sigma(t) = G_\infty \dot{\gamma} \int_0^t dt' e^{-(t-t')/\tau_M(\dot{\gamma})} e^{-(\dot{\gamma}\tau_f/\gamma_c)[e^{-(t/\tau_f)} - e^{(-t'/\tau_f)}]}. \tag{3.24}$$

The shear stress derivative is therefore:

$$\frac{\partial \sigma(t)}{\partial t} = G_\infty \dot{\gamma} - \sigma(t) \left(\frac{1}{\tau} + \frac{\dot{\gamma}}{\gamma_c} \left(1 - e^{-t/\tau_f}\right) \right). \tag{3.25}$$

Stress admits at intermediate times an overshoot whose size increases with shear rate and fluidity time scale τ_f. These overshoots are an effect of the fluidity model which are not obtained with the non-linear Maxwell model. They are shown in Fig. 3.4 together with the effect of the shear rate (left side) and fluidity relaxation time (right side). For convenience we set up $\tau \to \infty$. At short times, the stress converges to $\sigma = G_\infty \dot{\gamma} t = G_\infty \gamma$, where γ is the accumulated strain, i.e. the system behaves as an elastic solid.

The cooperativity length does not influence the transient stress behavior of the flow in this case. The steady state shear stress obtained from the constitutive equation plus the Newtonian contribution $\sigma_N = \eta_s \dot{\gamma}$ is $\sigma = \eta_s \dot{\gamma} + G_\infty \dot{\gamma}/f_{ss}$, where steady fluidity is $f_{ss} = 1/\tau + \sqrt{\text{II}_D}/\gamma_c$.

The final shear stress σ_{xy} values observed in mentioned figures are different and increase with the initial shear rate. Obtained overshoots and maximums found in the transient stress are known in dense glass forming systems, and they are related to the elastic energy storage capacity which increases the higher the shear rate [78]. The fluidity timescale τ_f delays the steady state and presumably gives more time

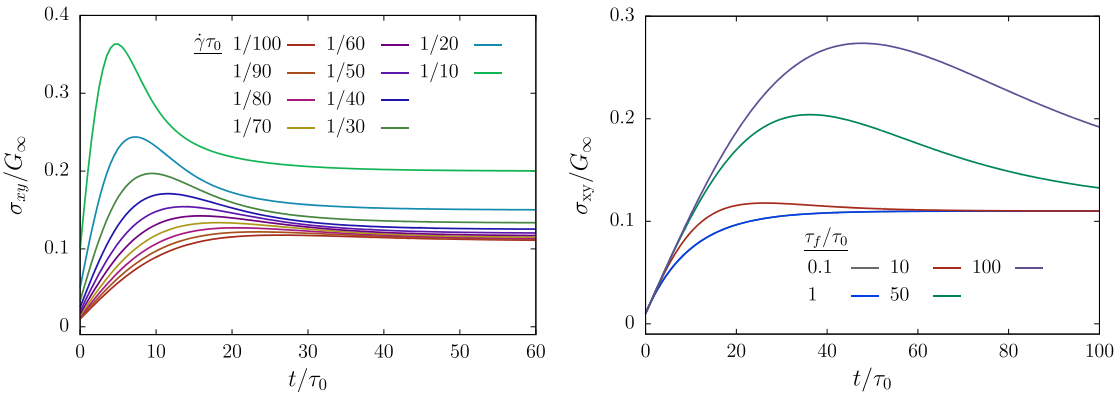


Figure 3.4: Shear stress during start-up for different $\dot{\gamma}$ using $\tau_f/\tau_0 = 10$ and $\xi = 0$ (left), and different τ_f using $\dot{\gamma} = 1/100$ and $\xi = 0$ (right, $\tau_f/\tau_0 = 0.1$ line hindered by $\tau_f/\tau_0 = 1$ line).

to elastic energy to be stored, therefore the overshoot increases for higher τ_f, like it is illustrated on the right side of Fig. 3.4 (the line corresponding to $\tau_f/\tau_0 = 0.1$ is hindered by the line obtained using $\tau_f/\tau_0 = 1$). As a reference, Koumakis et al. [79] performed experiments in hard-sphere glassy systems and, together with theory and simulations, could find and assess stress overshoots during simple shear set-ups. They related the overshoots to the inability of the system to recover after deformation, where experimentally Brownian motion cannot relax the structured otherwise distorted. Tendency says that the peak size increases with Peclét number $Pe = \dot{\gamma}\tau$, which we can reproduce with our model as well.

Cessation of flow

After the system reaches homogeneous steady state, the applied shear could be turned off and cessation of the flow attained. The fluidity model is able to reproduce residual stresses, which is another characteristic phenomenon in glass rheology.

Starting from a homogeneous stationary state after simple shear, where $\boldsymbol{\sigma}(0) = \boldsymbol{\sigma}_{ss}$ and $f(0) = 1/\tau + \dot{\gamma}/\gamma_c$, the fluidity will relax as

$$f(t) = \frac{\dot{\gamma}}{\gamma_c} e^{-t/\tau_f} + \frac{1}{\tau}, \tag{3.26}$$

and the shear stress will decay following:

$$\sigma(t) = \sigma_{ss} e^{-(\dot{\gamma}/\gamma_c)\tau_f(1-e^{-t/\tau_f})} e^{-t/\tau}. \tag{3.27}$$

Therefore, for $t \to \infty$, the model can reproduce residual stresses after flow cessation. For a glassy system when $\tau = \infty$ the stress will become:

$$\sigma_\infty = G_\infty \gamma_c e^{-\dot{\gamma}\tau_f/\gamma_c}, \tag{3.28}$$

where the yield stress is defined as $\sigma_Y = G_\infty \gamma_c$. As observed in the previous equation the remaining stress after flow cessation will scale initially with $\dot{\gamma}t$, by decreasing with the shear rate initially imposed. We will refer to the residual stresses phenomenon in Chapter 5, where the corresponding solution of Eq. 3.28 is shown in 5.2.

Extensional Flow

In planar extensional flow, the equation 3.18 will be $\boldsymbol{d}(t)^n = 2^n \boldsymbol{\kappa}^n$, hence the normal stresses are:

$$\sigma_{xx} = \frac{2G_\infty \tau_M \dot{\gamma}}{1 - 2\dot{\gamma}\tau_M}, \qquad \sigma_{yy} = -\frac{2G_\infty \tau_M \dot{\gamma}}{1 + 2\dot{\gamma}\tau_M}. \tag{3.29}$$

For a constant relaxation time the upper-convected Maxwell model is recovered, which will converge only for small Péclet numbers, i.e. $\dot{\gamma}\tau < 1/2$. Otherwise, the results become unrealistic. This issue is solved by using a relaxation time τ_M that depends on the shear rate, as it was previously stated.

To study the tensorial capabilities of the fluidity model we tested the Trouton ratio. This is usually obtained as the ratio of the extensional viscosity (first normal stress differences) and shear viscosity in 3D-uniaxial extensional flow. With $\boldsymbol{\kappa} = \mathrm{diag}(\dot{\gamma}, -\dot{\gamma}/2, -\dot{\gamma}/2)$, we obtain the Trouton ratio as:

$$Tr = \frac{3(\gamma_c + \dot{\gamma}\tau)(\gamma_c + \sqrt{3}\dot{\gamma}\tau)}{(\gamma_c + (\sqrt{3} - 2\gamma_c)\dot{\gamma}\tau)(\gamma_c + (\sqrt{3} + \gamma_c)\dot{\gamma}\tau)}. \tag{3.30}$$

By adding a Newtonian high-shear background viscosity as $\boldsymbol{\sigma}_N = G_\infty \tau_0 \boldsymbol{D}$ ($\tau_0 = 1$ is the Newtonian relaxation time), the Trouton ratio as a function of shear rate decreases with the latter down to a minimum to then increase again, as seen in Fig. 3.5a. The Newtonian limit is recovered for constant τ_M as $Tr = 3$ [80], and at the glass limit when $\tau \to \infty$ and $\dot{\gamma} = 0$, the value tends to $Tr \approx \sqrt{3}(1 + {\gamma_c}^2) + \gamma_c \approx 1.85$. Trouton ratio can also be defined as the ratio of two-dimensional extensional flow to simple shear flow. In this case $\boldsymbol{\kappa} = \mathrm{diag}(\dot{\gamma}, -\dot{\gamma})$, and a $Tr = 4$ is expected for a Newtonian flow behavior. For this set-up (see Eq. 3.29), the Newtonian limit is recovered, and like for Brader et al. in [64], a value of $Tr \approx 2 + 2{\gamma_c}^2 \approx 2.02$ is

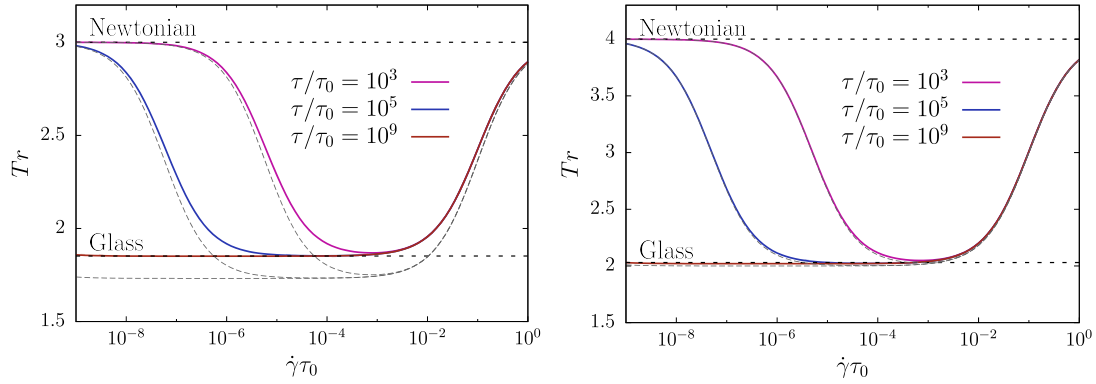


Figure 3.5: Trouton ratio obtained as function of the shear rate for a) 3D-uniaxial flow $\boldsymbol{\kappa} = \mathrm{diag}(\dot{\gamma}, -\dot{\gamma}/2, -\dot{\gamma}/2)$ where Newtonian limit converges to $Tr = 3$ and glass limit to $Tr \approx 1.85$, and for b) planar 2D-extensional flow $\boldsymbol{\kappa} = \mathrm{diag}(\dot{\gamma}, -\dot{\gamma})$, where Newtonian limit is at $Tr = 4$ and glass limit at $Tr \approx 2.02$. Dashed lines represent Tr when only time derivative is used in the upper convected time derivative of the stress tensor (see Eq. 2.58).

obtained for the glass limit. Mentioned authors call it "numerically indistinguishable" from 2 for the rheological schematic MCT model they use to describe the glassy state, see Fig. 3.5b. The Trouton ratio values obtained with the fluidity model for both 2D and 3D extensional cases, are comparable to what is obtained in the schematic MCT model derived by [64] and a similar glass model called ISHSM (isotropically sheared hard sphere model), see ref. [66], where the Trouton ratio for the 2D case converges to $Tr \approx 1.6$.

The tensorial properties of the model are linked to how relevant the components of the upper convected time derivative of the stress tensor really are. When only the time derivative of the stress tensor is used in 3D and 2D extensional flow (instead of the full upper convected derivative) the Trouton ratio is shown as the grey dashed lines in figures 3.5a and 3.5b respectively. This means that the model reduces to a low-extension-rate approximation, where, the 2D-extensional flow shows bigger differences than in the 3D-case, even though the tendencies are clearly followed. The impact of the upper convected time derivative components was studied in not-so-trivial geometries in section 2.4.

Analytical Comparison

Figure 3.6 shows viscosity curves obtained with the fluidity model for different relaxation times (τ/τ_0), and when $\tau = \infty$. We call the latter's case "fluidity glass

model". Curves obtained with the analytical expressions are obtained using the schematic MCT model and used for comparison [71].

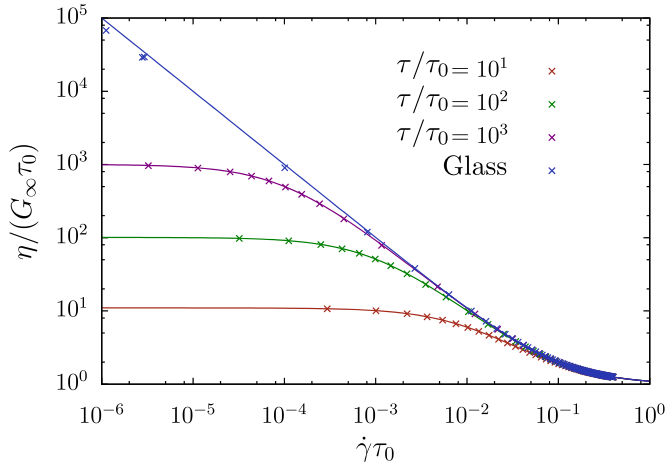


Figure 3.6: Viscosity curves for different τ/τ_0 used in the fluidity Maxwell model and fluidity glass model ($\tau/\tau_0 = \infty$) compared to flow curves obtained analytically (solid lines) [65].

3.3.2 Fluidity Boundary Conditions

Boundary conditions must be defined to solve the fluidity equation. It has been observed that, in emulsions context [2], surface properties can affect flow profiles, i.e. rougher surface will induce bigger wall fluidity than a smoother surface. According to these authors, in certain emulsions, spreading of the fluidity can soften the flow profiles in confinement, suppressing yield stress (see [3]). However, this argument is not straightforward, since a rough surface could also be interpreted as low fluidity areas, where fluid close to the walls cannot flow or move easily [81].

In all our simulations we use Neumann boundary conditions at the walls unless it is specified differently. This means that the fluidity is set as a material property and it is defined across the whole channel, i.e. not changing at the walls. This is expressed as:

$$\left.\frac{\partial f}{\partial y}\right|_{y=0,H} = 0 \tag{3.31}$$

In [74], a similar fluidity model is used where they study two boundary conditions for the fluidity at the walls: a fixed fluidity value at the walls and no flux at the wall for different start-up regimes. This approach was done to assess transient effects like shear banding and surface roughness influence in ve-

locity profiles and fluid rheology. Chapter 4 is dedicated to this topic, where we study the effect of these two boundary conditions in a simple shear set-up. In order to find consistent values for the fluidity at the wall we implemented the Dirichlet boundary condition and followed [74] and [2] approach. The fluidity value at the wall was set as:

$$f_w = \frac{G_\infty \dot{\gamma}_w}{\sigma_w}. \tag{3.32}$$

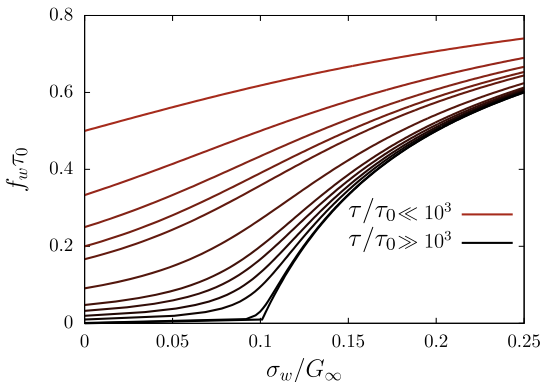


Figure 3.7: Fluidity at the wall versus shear stress at the wall for different τ/τ_0 (increasing from top to bottom) obtained with the fluidity model

σ_w is the shear stress at the wall (in steady state) $\sigma_w = \sigma_{xy} = \tau_M G_\infty \dot{\gamma}_w$ plus the Newtonian stress contribution, and $\dot{\gamma}_w$ is the shear rate at the wall. Goyon et al. [2] found the latter value as the slope of the velocity profile at the walls recovered from experimental data. With this in mind, we could sketch how the fluidity at the wall looked like for different wall-stress in a simple shear scenario. Our model reproduces was in alignment with what was found experimentally by [2] where for higher viscosity the fluidity at the wall decreased and the stress at the wall increased. Following rather simple relation 3.32 one could foresee directly the relationship between the fluidity, shear stress, and shear rate at the wall by increasing relaxation time in the system. Fig. 3.7 shows the predicted fluidity at the wall for different shear stress at the wall and a relaxation time range. Here it is easily seen when there is no stress present at the wall the wall fluidity will start from low values or even closer to zero for systems with higher relaxation times. This wall fluidity increases with shear stress while the system fluidizes, whereas for higher relaxation time cases (black lines) there is more poignant threshold that indicates the yield stress present in the system below which the wall fluidity is zero otherwise it increases with shear.

3.3.3 Fluidity Model and FVM

In the previous section, we could assess analytically how the fluidity model in set-ups like simple shear, 2D-, and 3D-extensional homogeneous flow, could describe glass-forming liquids rheology by attaining important features like flow curves and Trouton ratio. Moreover, we wanted to use the fluidity model to describe flow with possible heterogeneities going through not-so-trivial geometries that are otherwise troublesome to describe analytically. To test the capabilities of the model we made qualitative comparisons between steady state results obtained with the fluidity glass model in an

abrupt 4:1 planar contraction and experimental data obtained by Quinzani et al. [82] using a non-Newtonian fluid in a similar set-up. The latter followed a viscosity versus shear rate curve shown in Fig. 3.8.

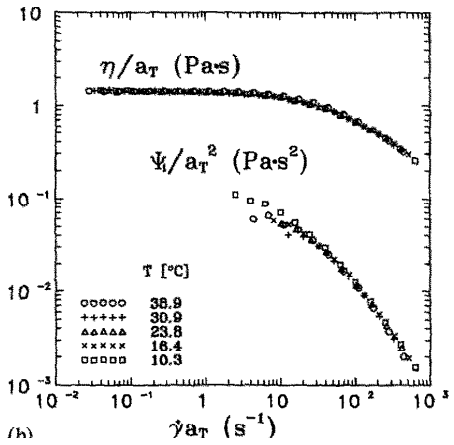


Figure 3.8: Master curve of 5% PIB/C14 solution of viscosity $\eta(\dot{\gamma})$ used by [82] in abrupt 4:1 contraction.

Note that by using the fluidity glass model, we setup the relaxation time of our fluid as $\tau = \infty$, hence the system has a higher viscosity that follows the behavior shown in Fig. 3.6 (symbols), which is in very different range as in the experimental results we are comparing with. Even though we used a fluid with different material properties, we pursued to assess qualitative features with this comparison. A schematic representation of the contraction geometry we use along our research has been already shown in Fig. 2.15, section 2.4.2. A pressure step was setup proportional to the elastic modulus of the material as $\Delta p/L = G_\infty/h*$, where L is the total length of the channel and $h*$ is a characteristic width of the contraction channel (we chose it to be bigger than the smaller channel width as $h* = 5h$ hence complete flow development is assured). The fluidity model parameters used were $\xi/4h = 0.2$ and $\tau_f/\tau_0 = 0.1$. Tendencies between resulting velocity, shear stress, and normal stress differences profiles obtained after the implementation of our model and the experimental data obtained by [82] are illustrated for areas upstream the channel in figures 3.9, 3.10, 3.11. Downstream the channel same quantities were compared in figures 3.12, 3.13 and 3.14. To remain consistent with the common way of plotting contraction flow profiles, we normalized positions using half of the small channel length ($h = 0.0032$ m). These plots show experimental results on the right axis denoted by symbols, and simulation results on the left axis denoted by solid lines. Experimental ranges are adjusted to be consistent with our resulting data, since one must take into account the different viscosity ranges we are comparing and the experimental conditions used. We found in this comparison that the best fit between shear stress profiles obtained with our model and the experiments was done by setting $G_{\infty exp} \approx 140\ G_{\infty sim}$.

In general, we can say that the tendencies found with our model followed the experimental ones, where the assessment velocity profiles follows closely the data. However, stress development showed more disparities with data, especially normal stresses development close to the contraction edge and downstream the contraction. In the latter case, the model results differ notably, especially regarding the previously set shear modulus. Downstream the channel, the normal stresses seem to not develop

completely across the y-axis to maintain the accord imposed by the shear modulus, however, the profile shape tendency seemed to be slightly followed. We must also remember, that obtaining experimental data close to edges can be cumbersome, which in our simulations are mathematically defined where wall irregularities, usually seen experimentally, are not present. It is important to notice as well that Reynolds number and flow curve for Quinzani et al. fluid and our flow set-up are in different ranges. The former used a dynamic viscosity of 1.424 Pa · s, relaxation time of 0.06 s, and they set $\mathrm{Re}_0 = 0.56$ by imposing a fixed flow rate. In our simulations we are in the $Re \approx 0$ range since the relaxation time $\tau/\tau_0 = \infty$ is set-up in the model. Favero et al. in [9] did comparisons with the same solver and more suitable models, fluid parameters and experimental set-up close enough to reproduce same experimental data.

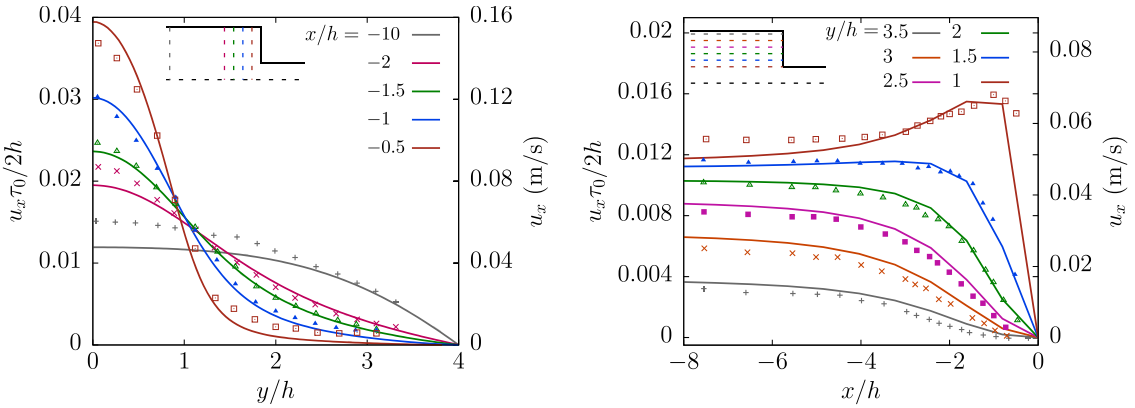


Figure 3.9: Steady state velocity y-profiles (left) and x-profiles (right) obtained using fluidity model ($\xi/4h = 0.2$ and $\tau_f/\tau_0 = 0.1$) (solid lines) and experimental results obtained by Quinzani et al. [82] for a viscoelastic flow with $\mathrm{Re}_0 = 0.56$ (symbols).

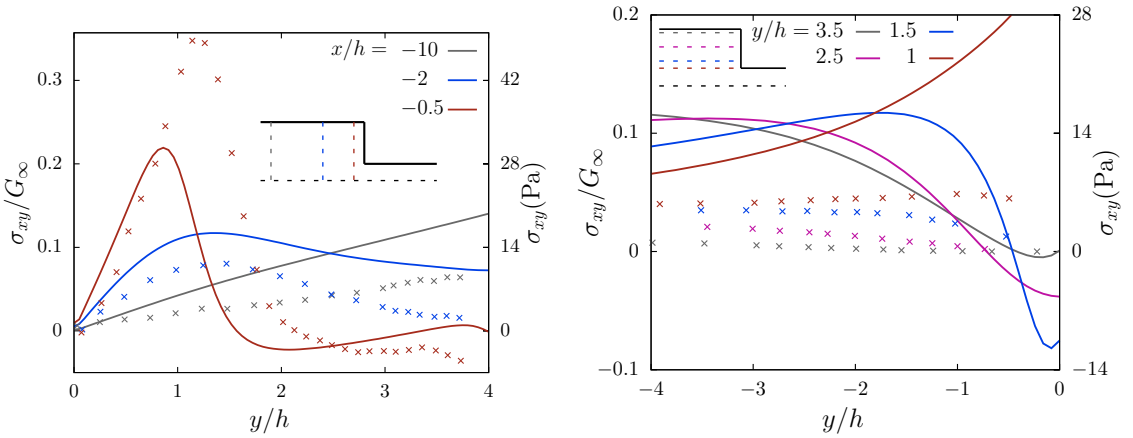


Figure 3.10: Shear stress σ_{xy}/G_∞ y-profiles (left) and x-profiles (right) obtained using fluidity model ($\xi/4h = 0.2$ and $\tau_f/\tau_0 = 0.1$) (solid lines) and experimental results (symbols) by Quinzani et al. [82] for viscoelastic flow with $\mathrm{Re}_0 = 0.56$.

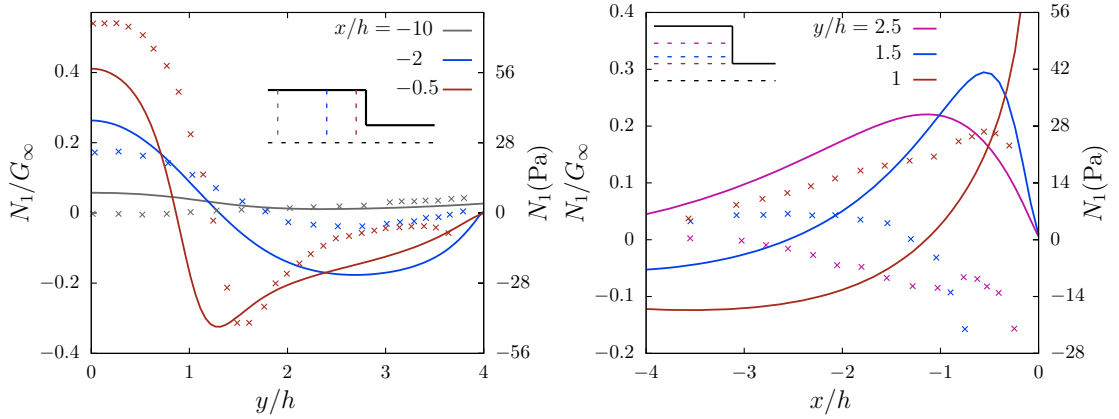


Figure 3.11: Normal stress differences N_1/G_∞ y-profiles (left) and x-profiles (right) obtained using fluidity model ($\xi/4h = 0.2$ and $\tau_f/\tau_0 = 0.1$) (solid lines) and experimental results (symbols) by Quinzani et al. [82] for viscoelastic flow with $\mathrm{Re}_0 = 0.56$ (symbols).

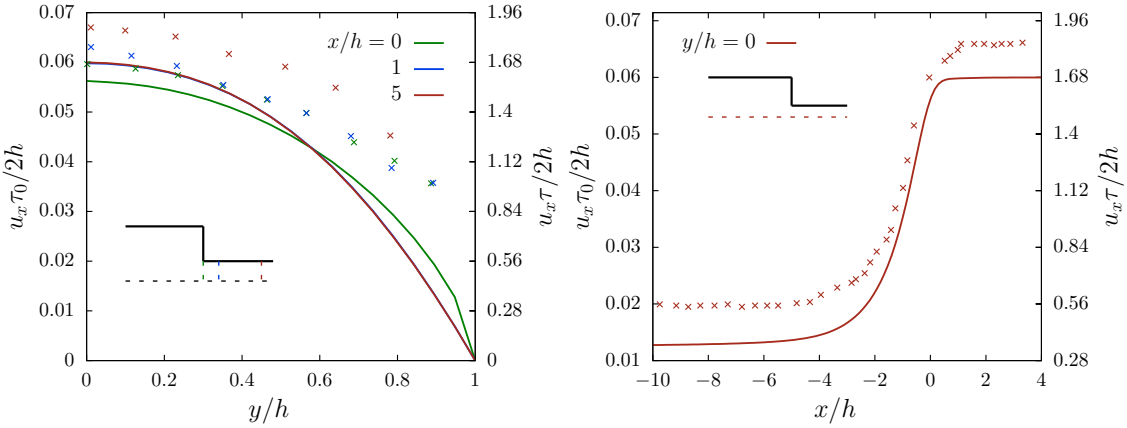


Figure 3.12: Downstream velocity $u_x\tau_0/2h$ profiles along y-axis (left) and x-centerline (right) obtained using fluidity model ($\xi/4h = 0.2$ and $\tau_f/\tau_0 = 0.1$) (solid lines) and experimental results (symbols) by Quinzani et al. [82] for viscoelastic flow with $\mathrm{Re}_0 = 0.56$.

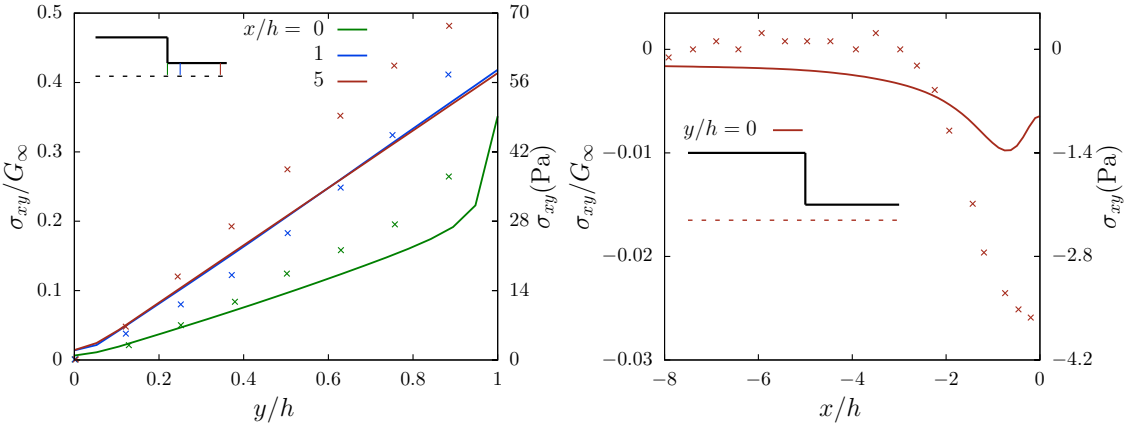


Figure 3.13: Downstream shear stress σ_{xy}/G_∞ profiles along y-axis (left) and x-centerline (right) obtained using fluidity model ($\xi/4h = 0.2$ and $\tau_f/\tau_0 = 0.1$) (solid lines) and experimental results (symbols) by Quinzani et al. [82] for a viscoelastic flow with $\mathrm{Re}_0 = 0.56$.

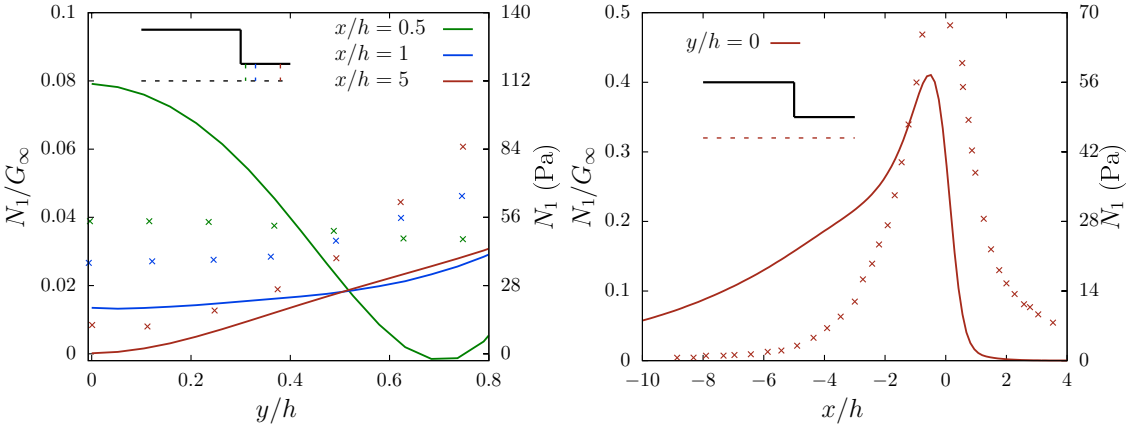


Figure 3.14: Normal stress differences N_1/G_∞ profiles along y-axis (left) and x-centerline (right) obtained using fluidity model ($\xi/4h = 0.2$ and $\tau_f/\tau_0 = 0.1$) (solid lines) and experimental results (symbols) by Quinzani et al. [82] for a viscoelastic flow with $\mathrm{Re}_0 = 0.56$.

2D-Pressure Driven Planar Flow

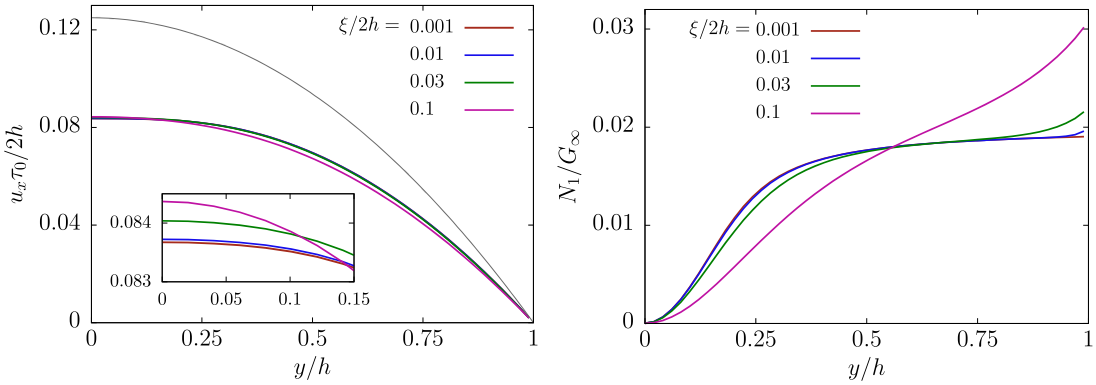


Figure 3.15: Steady state velocity half-channel-profiles (left) and normal stress difference profiles (right) using the fluidity model for different $\xi/2h$. Grey line in the velocity profile plot shows the Newtonian parabolic profile.

The influence of cooperativity length ξ was studied in a pressure-driven 2D-planar channel. The channel had a length $L/2h = 4$ where $2h$ is the width, and a pressure gradient imposed between inlet and outlet was proportional to the elastic modulus as $\Delta p/L = G_\infty/2h$. Details about the set-up are in the Appendix section A.1. Left side of Fig. 3.15 shows the velocity half-profiles obtained in steady state for a relaxation time $\tau/\tau_0 = 10$. Velocity profiles can go from a typical non-Newtonian plug-like profile (red line) to a parabolic-like profile when the cooperativity length increases (magenta line). This means that fluidized areas will spread across the channel with ξ. Normal stress profiles are strongly affected by the cooperativity length as shown

on the right side of in Fig. 3.15, since they lose the typical shoulder to become more linear. In this case, we are not taking into account fluidity wall effects like roughness or smoothness [3], but a Neumann boundary condition for the fluidity. We define the fluidity as a material property across the channel that should not change at the walls. Nevertheless, the possible influence of fluidity boundary conditions will be explained in the next section. Analytical flow curves were compared with these simulation results and have been previously shown as viscosity versus shear rate curves in Fig. 3.6.

Chapter 4

Time Dependent Effects

Spatial heterogeneities are not only part of nonlinear glass rheology at a microscopic level but can determine materials final mechanical behavior. As matter of fact, due to the yield stress phenomena present in glasses forming liquids, strain might be induced in particular regions of the flow more than others causing eventually inhomogeneous flow patterns [83] which have been extensively studied through experiments and simulations [83, 84]. Banding phenomena is a sign of heterogeneities in the flow and perceived as a nearly planar region with large deformation where two areas are displaced relative to each other, however, the material retains full physical continuity [85]. Bands might be present in metal alloys, metallic glasses and in complex fluids including colloidal dispersions, polymer solutions, melts, emulsions, surfactant solutions, microgels, among others which ultimately belong to the soft matter field [86, 87]. Their universal presence in mentioned materials makes them important in parts design at a macroscopic level because of their impact on their mechanical properties and failure [88].

Shear banding might appear transiently during steady imposed strain applied to the flow, or permanently in steady state. Transient banding might be triggered during startup shearing and disappear when steady state is reached. When only transient and not permanent banding occurs in a system, it is fair to say that the material had a monotonic flow curve. As an example, Fielding et al. [89] induced heterogeneity in the flow by means of a small perturbation to the imposed stress using a similar fluidity model. This lead to instabilities in the stress versus shear rate curve showing transient banding in the velocity profiles even though the initial flow curve was monotonic. They also used a soft glassy rheology model that showed similarities to their fluidity model which led to thing that transient shear banding might be generic for soft glasses.

For bands to form and prevail in steady state of complex fluids, a non-monotonic

flow curve is needed. This means that a region of negative slope shall be present for yield stress fluids when the stress is plotted versus the shear rate. On this regard, Fielding in [90] extended mentioned Letter, by using the soft glassy rheology (SGR) model and a similar mesoscopic fluidity model (as a simplification of their SGR model), where they both have monotonic flow curves, to describe non-local effects in soft glass materials. SGR model could reproduce transient banding using different start-up protocols. However, with a change in the model definition, they obtained viscosity bifurcating curves which allow them to attain permanent shear banding. Curves are displayed in [91]. In the same line, and as introduced in past chapter, Derec et al. [73] introduced a fluidity model that is able to describe monotonic flow curves. This model was modified by Picard et al. [74] into a similar (simpler) model that could characterize monotonic and nonmonotonic curves, which is aligned to what we did in this chapter. They evaluated the effect of fixing the fluidity at the wall for imposed stress and shear rate, obtaining banding for the latter as frozen and fluidized regions in the system, which might lead to specific surface rheology effect [2]. The nature of fluidity boundary conditions at the wall is not trivial since fluidity can be seen as a material property independent of walls. In this chapter, we describe how we attain shear banding using the fluidity model that was previously introduced, and how material parameters influence the ultimate velocity profiles obtained. Initially, we studied how to induce transient banding by following mentioned research, which secondly led us to assess and study the influence of fluidity boundary conditions on permanent steady state banding. Fig. 4.1 shows the monotonic flow curve (line) we used to obtain transient banding. This curve was in fact obtained by plotting the stress versus shear rate obtained in a pressure-driven flow. However, a flow curve could also be obtained by plotting the shear stress obtained in a simple shear set up for various imposed shear rates, since the final stress is constant according to the Navier Stokes equation. We can appreciate in same figure, denoted by symbols, that when we fixed the fluidity at the wall and shear the system, instead of obtaining a constant value, we get a span of stress for one applied shear rate, since the latter would not reach a constant value because of the fixed fluidity value at the wall. Therefore, the shear rate and shear stress vary across the domain as a system response to the fixed condition at the walls. As a remark, fixing the fluidity at the wall might be an indication of

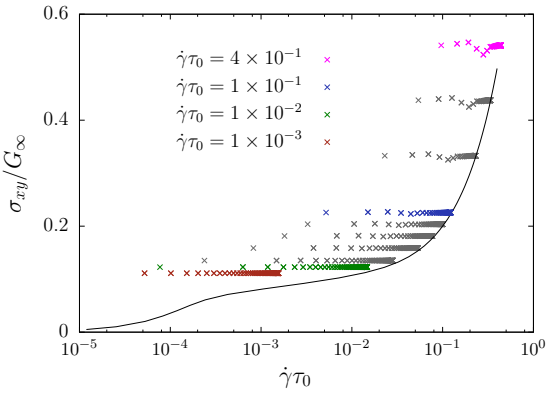


Figure 4.1: Monotonic flow curve obtained in a pressure-driven setup ($\tau_f/\tau_0 = 0.1$ and $\xi = 0.01$) (line), and stress versus shear rate curves (symbols) obtained using wall fluidity $f_w = 0$ and $\xi/h = 0.01$ in simple shear system for different shear rates.

roughness/smoothness according to [2], even though it is important to remember that our initial fluidity model definition describes the fluidity as a material parameter that changes with shear rate locally, i.e. shear rate dependent inverse relaxation time. These stress distributions with shear rates were obtained for a fixed cooperativity length ξ. This parameter is used in our fluidity model to describe the diffusion of the fluidity property along the domain, and could promote material fluidization and yield stress suppression in confinement [2].

4.1 Material Parameters

Shear banding was studied in different simple shear setups. Several model parameters had to be defined to solve this using the fluidity model as: relaxation time τ, zero-shear-rate viscosity η, background Newtonian viscosity η_N (solvent viscosity), density ρ, cooperativity length ξ, and fluidity timescale τ_f. Since we are dealing with a viscoelastic fluid, we chose $\tau = 10$ s, $\eta_0 = 10\text{Pa}\cdot\text{s}$, $\eta_N = 1\text{Pa}\cdot\text{s}$, and $\rho = 1360\ \text{kg}\,\text{cm}^{-3}$ as general properties of our material. We defined as elastic modulus $G_\infty = 1\,\text{Pa}$ which sets the Newtonian limit as $\eta_N = G_\infty \tau_0$, where $\tau_0 = 1$ s. Regarding the cooperativity length, Goyon et al. in [2, 4] suggest that this value could be related to confinement size and/or in the order of nanometers. In fact, they state that in microfluidic configurations non-local effects affect "jammed" state behavior when ξ is comparable to the confinement width, i.e. effects arise from fluidity gradients that might come from stress gradients or boundary conditions (wall roughness or smoothness). Thus, for microfluidic configurations they state that a relation of $\xi/h \approx 0.5$ should hold (h is the width of the channel), and that in wider configurations the effects might weaken down to $\xi/h \approx 10^{-3}$. As mentioned, we define ξ as a material property independent on confinement. However, we used different values in the order of μm as kept a relation of $0 \leq \xi/h \leq 1$. Regarding how fast the fluidity reaches its neighbors, we must define a characteristic time scale for the fluidity equation: we define a diffusion coefficient as ξ^2/τ_f, where τ_f sets the fluidity time scale. The effect of changing this parameters was assessed as well.

4.2 Initial Conditions

We defined a simple shear system where a fluid is placed between two walls. The top wall is defined as a moving wall where we imposed a constant velocity $u_{\max}$. The top wall is fixed. The initial fluidity field was defined across the material as a non-local inverse relaxation time, which initially should be $f_0 = 1/\tau$. However, we induced a perturbation in the latter to study its effect on the transient behavior of

the fluid. Parameters as $\dot{\gamma}$, ξ and τ_f were varied. Startup shear rate was implemented accordingly so that the Reynolds number remained below 0.1.

A fluidity boundary condition has to be set at the walls to solve the fluidity equation. This will be an important point to study shear banding. We will use Neumann and Dirichlet boundary conditions for fluidity at the wall and study their effects on transient and steady state behavior. In summary, we studied the following:

First, we set up the fluidity as a homogeneous field across the channel as $f_0 = 1/\tau$. At the wall, we set a Neumann boundary condition for the fluidity (Eq. 3.31). In this case, we can already say shear banding is not triggered neither transiently nor in steady state.

Second, we define a Neumann boundary condition for the fluidity at the wall and a heterogeneous initial fluidity field is set across the channel. In this case transient shear banding was triggered. Heterogeneities are induced by adding a small perturbation to the initial fluidity. We did this by implementing an initial fluidity field that followed Eq. 4.1 with $a = 0.1$, from $y = 0$ at the fixed wall and $y = h$ at the moving wall.

$$f_0(y) = \frac{1}{\tau}\left(1 - a \cdot \cos\left(\frac{\pi y}{h}\right)\right) \tag{4.1}$$

This defined qualitative how transient banding was shaped. However, we also induced random initial perturbations that triggered similar transient banding with diverse shapes that was still reminiscent of the initial field.

Third, the Dirichlet boundary condition is set for the fluidity at the wall and a homogeneous fluidity field $f_0 = 1/\tau$ was set across the domain. We evaluated different cases using the fluidity wall relation suggested in past chapter, but also evaluated the influence of more extreme case as smoother (large fluidity) or rougher (low fluidity) wall (section 4.4.4). For these cases, long-lasting shear banding was obtained in steady state.

Fourth, the Dirichlet boundary condition is set again for the fluidity at the wall but with a heterogeneous initial fluidity field following 4.1. In this case, we obtained transient and long-lasting shear banding, whose size increased with the timescale of the fluidity model τ_f and depended on ξ/h.

4.3 Neumann Boundary Condition

In this case the fluidity is set as a material parameters that should show no difference between the cell value next to the wall and at the wall. If a homogeneous fluidity

field is set across a system that is sheared, no transient or long lasting-banding was observed. This system was used as control system to compare with further field variations. However, by including a perturbation in the initial fluidity field across the channel, transient banding is triggered, which is what we show in this section. Model parameters τ_f and ξ are varied and their influence on the size and band behavior were studied.

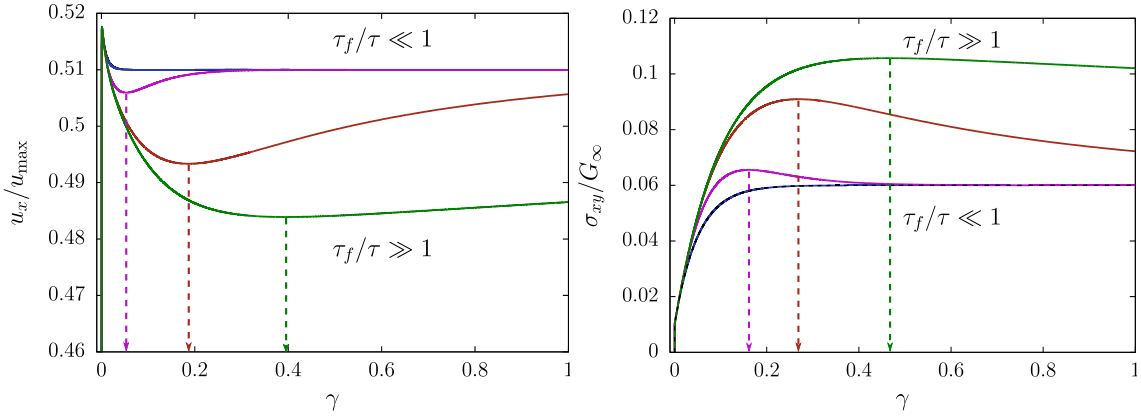


Figure 4.2: Transient evolution of velocity (left) and shear stress (right) using an initial heterogeneous fluidity field and different $\tau_f/\tau = 0.01, 1, 10, 100$ at $y/h = 0.51$ using $\dot{\gamma}\tau_0 = 10^{-2}$ (black line corresponds to no perturbation, hindered by $\tau_f/\tau = 0.01$).

Transient banding appears for different τ_f in time where velocity versus strain reaches an undershoot or overshoot, depending where it is measured, before relaxing back to its steady-state values, see left side of Fig. 4.2. In this figure we used a $\dot{\gamma}\tau_0 = 10^{-2}$, and measured the velocity evolution in time close to the center of the channel (position $y/h = 0.51$) for different τ_f/τ_0. In steady state, profiles are linear as expected, but during the mentioned undershoot (overshoot) a deviation from a linear velocity profile is obtained. We refer to these bent profiles as bands because there are areas across the channel with higher viscosities than others. Since the induced perturbation was cosine-shaped, transient band profiles followed the same shape. Therefore, biggest bands were attained at the velocity undershoot in the middle of the channel. Random perturbations were used as well, where transient banding was also triggered whose shapes were seemly related to the initial fluidity field shape. Increasing τ_f will promote bigger banding denoted by undershoot size in transient velocity in same figure. The influence of this parameter in the total shear stress (Newtonian plus non-Newtonian contribution) is observed on the right side. τ_f determines how fast heterogeneities in the fluid will spread along their neighbors before fluidity reaches its steady state value. The strain value where the undershoot in transient velocity happens (maximum banding) is smaller than the strain value for the stress overshoot observed, meaning that the stress lags behind the deformation which does not exactly correspond with other findings as in [90],

since they found that banding happens at similar strain when the overshoot in the shear stress takes place. Shear stress overshoot is enhanced when τ_f increases as well, before relaxing to corresponding steady state value. In fact, overshoots in shear stress versus deformation in complex dense fluids are related to the microscopic effect of cages being more deformed by imposed shear. When τ_f increases the system will take longer to thin and actually be deformed, thus generally it will have a higher "instantaneous" viscosity (lower fluidity). This effect decreases the shear thinning process in the system. Since our system had initially heterogeneities in the flow that must be deformed, overshoots might be related to the necessary energy to bring back the system to a homogeneous state.

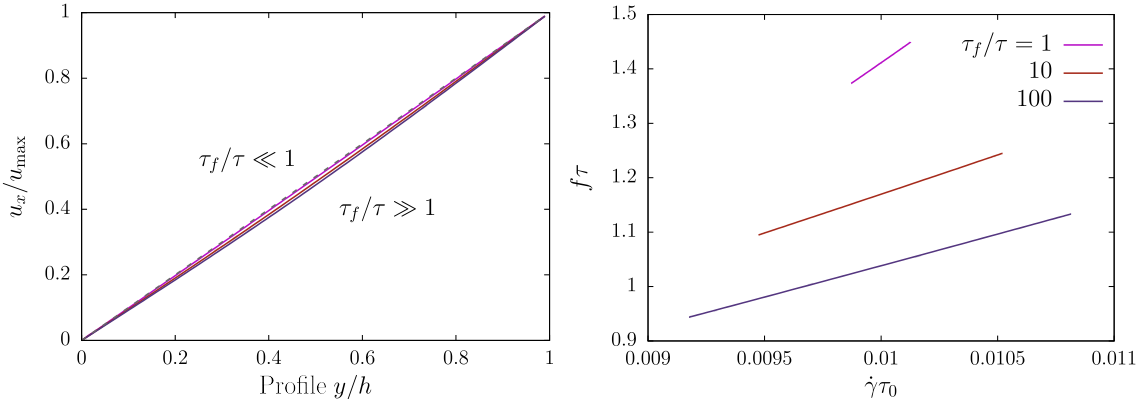


Figure 4.3: Velocity profiles (left) and fluidity versus shear rate (right) during maximum transient banding for different τ_f/τ_0 using an initial heterogeneous fluidity field and $\dot{\gamma}\tau_0 = 10^{-2}$. Dashed lines in left figure corresponds to steady state.

Velocity profiles at maximum transient banding are shown on the left side of Fig. 4.3. As mentioned, for bigger τ_f more bent and deviated profiles from linearity are obtained. The induced perturbation in the fluidity field was rather small hence smaller bands are ultimately generated. On the right side of same figure, fluidity versus shear rate is shown. These profiles correspond to maximum banding for different τ_f, and show how fluidity is lower but wider at banding as the fluidity timescale increases and how for faster scales the fluidity is higher and closer to its final constant steady state value. Additionally, the latter case corresponds to smaller bands where fluidization is more localized, which explains the small band size.

Cooperativity length affects the banding size during transient behavior which is seen as a size change in the velocity undershoots displayed on the left side of Fig. 4.4: velocity undershoots increase for smaller ξ. For $\xi/h \approx 1$ bands are virtually non-detectable however, when $0 < \xi/h < 0.3$ transient bands are visible which makes smaller ξ trigger bigger bands. In fact, the smaller the cooperativity length is, fluidization along perturbation neighbors is more localized. This promotes bigger bands before the fluidity spreads more along the fluid as it does for bigger ξ. Actually,

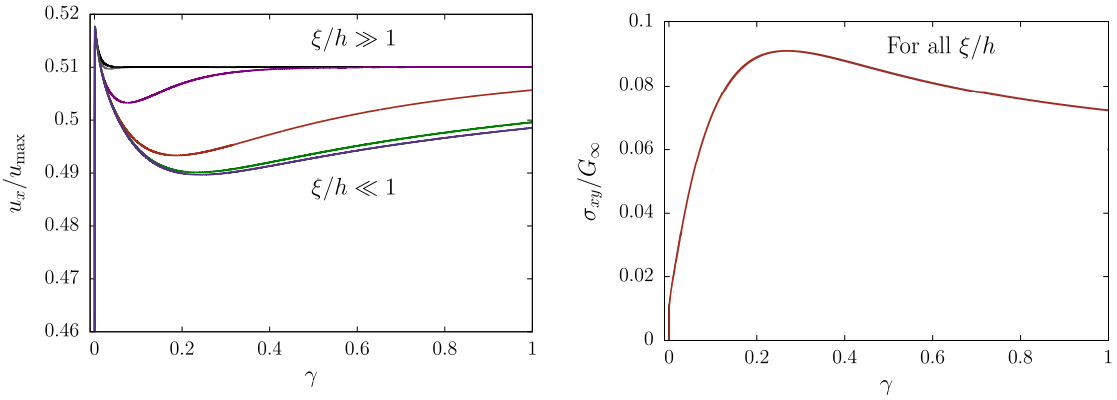


Figure 4.4: Transient evolution of velocity (left) and shear stress (right) using an initial heterogeneous fluidity field for different ξ/h (including $\xi = 0$) at $y/h = 0.51$ using $\dot{\gamma}\tau_0 = 10^{-2}$ and $\tau_f/\tau = 10$.

we find that for $\xi/h < 0.1$, differences between band sizes are virtually undetectable: there is an optimal ξ value for detecting bigger bands in our configuration. Shear stress, on the other hand, is hardly affected by varying cooperativity length as observed on the right side of Fig. 4.4, since same overshoot was found for different ξ when the initial flow is heterogeneous or homogeneous. In summary, when this condition is used, the stress overshoot size depends on τ_f as a model parameter. Overshoots in shear stress are actually an effect of the fluidity model.

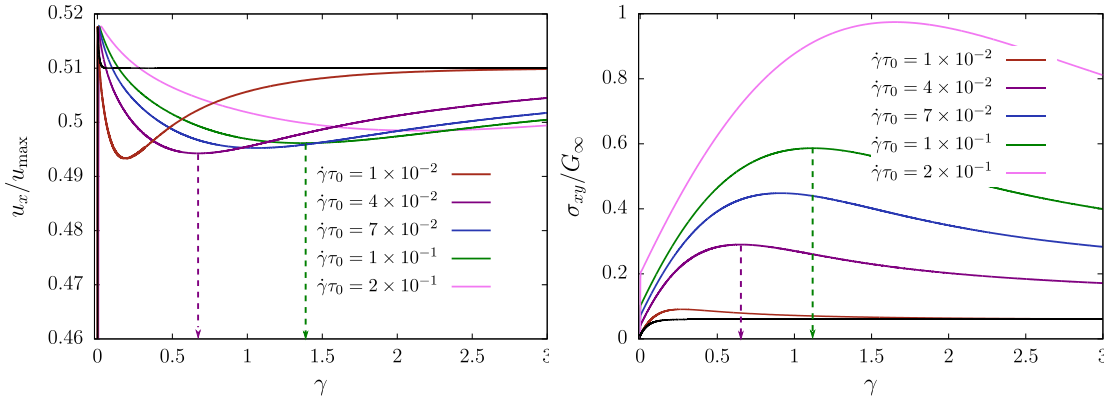


Figure 4.5: Transient evolution of velocity (left) and shear stress (right) measured at $y/h = 0.51$ using an initial heterogeneous fluidity field for different shear rates (black line corresponds to no-perturbation), fixed $\xi/h = 0.3$ and $\tau_f/\tau = 10$.

Imposed shear rate has an effect on the transient banding obtained as well. We varied the top wall velocity to start, and found that increasing the velocity reduces the transient band size down to a point where bands are no longer present, as shown on left side of Fig. 4.5. Also, for higher shear rates the strain needed to form a band will be higher, since the material is been "forced" to be deformed faster. Therefore,

the lower the shear rate the bigger the induced transient band when there is a heterogeneous initial fluidity field: more time is also given to the material to deform "unevenly". On the right side of the same figure, we observe that corresponding stress overshoots increase with shear rate as suggested by numerous papers as for example [79], where they show through Brownian dynamic simulations of start-up of hard-sphere glasses, the same tendency. We can also notice that contrary to the case when τ_f was varied for a fixed shear rate, the maximum banding strain (where velocity undershoot happens) is higher than when the stress happens for each case. In fact, differences between the position of both strains increase with shear rate. When we increase the shear rate, not only the stress overshoot increases in size but also its corresponding strain moves to the right. The strain for corresponding maximum banding will happen also at higher strains for higher shear rates, though smaller bands size. For smaller shear rates, differences between strain when under(over)shoots happen are minimal.

4.4 Dirichlet Boundary Condition

Setting a fixed value as a boundary condition for the fluidity at the wall (Eq. 3.32) was also studied. This condition induced long lasting banding in steady state. First we studied the transient banding that is also induced by this condition even though the initial fluidity field is homogeneous. Biggest bands will appear at the velocity overshoot (transients measured in the first quarter of the channel, close to the non-moving wall) or undershoot (transients measured closer to the moving wall): their size will be directly related to τ_f, ξ and shear rate $\dot{\gamma}$, as it was mentioned in previous section. Values of $\tau_f/\tau \gg 10$ are needed to see the s-shaped transient banding. Transient bands turn into smaller long-lasting bands in steady state when enough time is given to the system to relax. In fact, the s-shape transient profiles flips sides to the steady state ones.

4.4.1 Homogeneous Initial Fluidity Field

Banding occurs transiently when a fixed fluidity value is used at the wall and the initial fluidity field is homogeneous (and heterogeneous, next section). Close to the non-moving wall, the profiles are slightly more bent than in the upper part of the channel, but we measure transients in the latter to appreciate better the undershoots in velocity. Evolution of velocity with deformation is shown on the left side of Fig. 4.6 for different fluidity timescales τ_f. As mentioned earlier, increasing τ_f promotes bigger transient banding. On the right side, corresponding shear stress in function of deformation is displayed, where bigger overshoots will be triggered by higher τ_f.

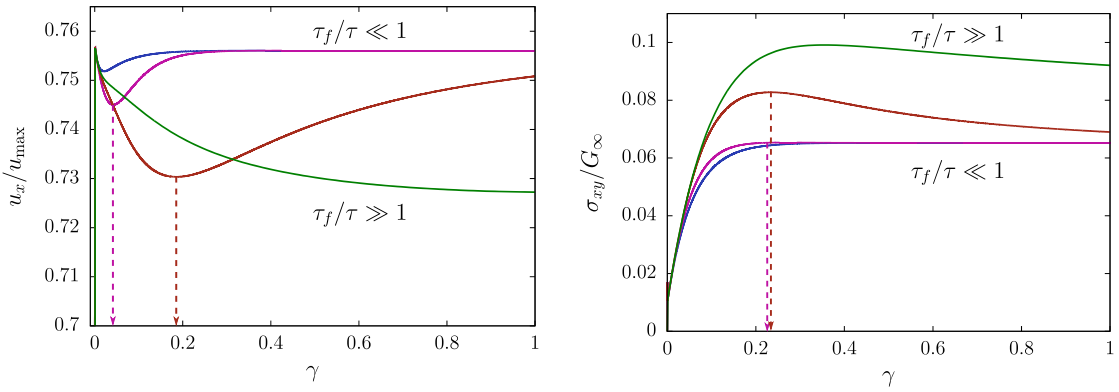


Figure 4.6: Transient evolution of velocity (left) and shear stress (right) using initial homogeneous fluidity field and fixed wall fluidity values for different $\tau_f/\tau = 0.01, 1, 10, 100$, $\xi/h = 0.3$, at $y/h = 0.751$ using $\dot{\gamma}\tau_0 = 10^{-2}$.

In this case though, curves tend to be smaller than transient stress curves obtained with a heterogeneous initial fluidity field and Neumann boundary condition (for same specific model parameters). Biggest transient banding for this case is displayed as velocity profile on the left side of Fig. 4.7. As noted, a rather symmetric s-shaped profile was obtained where two branches are located close to each wall. Close to the moving wall ($y/h = 1$) the velocity seems to be lower than the expected one in steady state since this area has a smaller fluidity or higher viscosity. Fluidity profiles are plotted versus the shear rate for this case on the right side of the same figure, pointing out where the biggest transient banding happened (crosses) and the final fluidity behavior in steady state. We see in this figure, as mentioned before, that transient bands are bigger than the ones obtained in steady state which can be deduced by the size of this particular fluidity profile.

When the cooperativity length was varied under these conditions, we found contrary effects than when the Neumann condition was used for the fluidity at the walls. First, smaller or null cooperativity lengths reduce the size of the transient bands significantly (see left side of Fig. 4.8 for transient velocity). However, shear stress overshoots seem to be in this case largely affected by ξ, which did not happen when Neumann condition was used. The overshoots are bigger for smaller ξ, as observed on the right side of same figure which, in fact, produces minor banding. Hence, when fluidization is more spread out, the stress overshoots reduces its size.

In our case no banding was found in this set-up for lower or zero ξ and yet the maximum stress overshoot was present. In summary, when a homogeneous flow is initially sheared no bands are formed but a stress overshoot is always present, which is enhanced by τ_f, shear rate γ, and ξ depending on the boundary condition. In the present case, as the cooperativity length increases, the transient band size increases

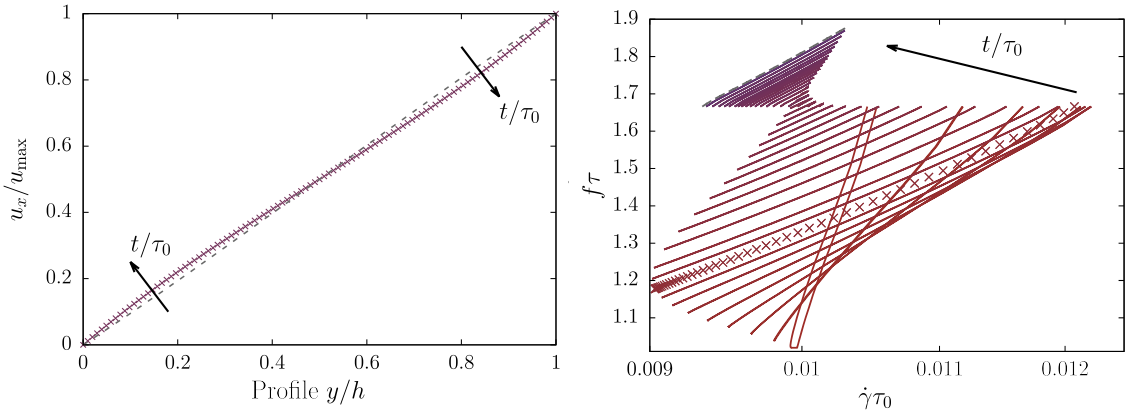


Figure 4.7: Left: maximum banding for fixed wall fluidity ($\tau_f/\tau = 10$ and $\xi/h = 0.3$). Right: evolution in time of fluidity profile. Dashed lines are steady state profiles, crosses are profiles at biggest banding.

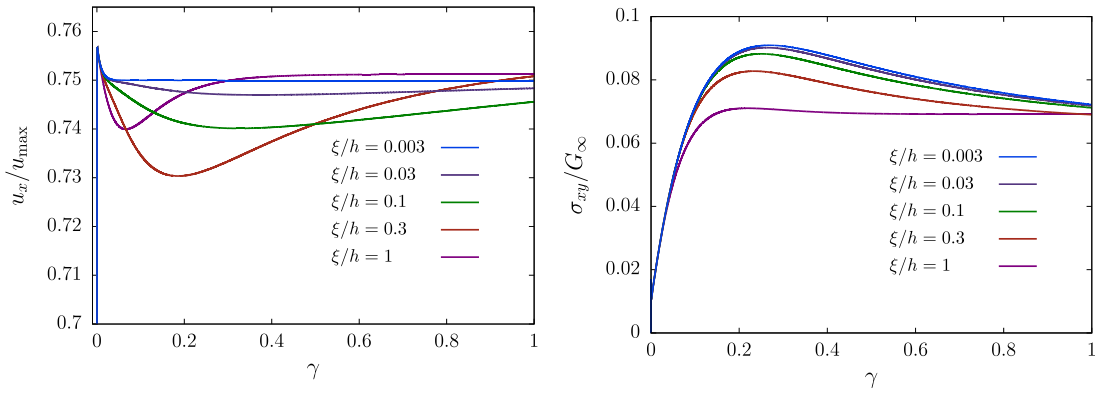


Figure 4.8: Transient evolution of velocity (left) and shear stress (right) using an initial homogeneous fluidity field and fixed wall fluidity values for different ξ/h using $\tau_f/\tau = 10$ at $y/h = 0.751$ (black line corresponds to no-perturbation).

as well up to a value where its size saturates and then decreases for even higher ξ. For this set-up, $\xi/h = 0.3$ seems to be the value where the biggest transient bands are found. By increasing the shear rate, we found opposite tendencies as in the previous section. For higher shear rates we found bigger transient banding size, which is shown on left side of Fig. 4.9. Shear stress shows again a bigger overshoot for higher velocities which is displayed on right side of same figure.

4.4.2 Heterogeneous Initial Fluidity Field

We used a heterogeneous initial fluidity field with this condition, using Eq. 4.1. In this case, transient banding is observed with similar shapes as the ones obtained

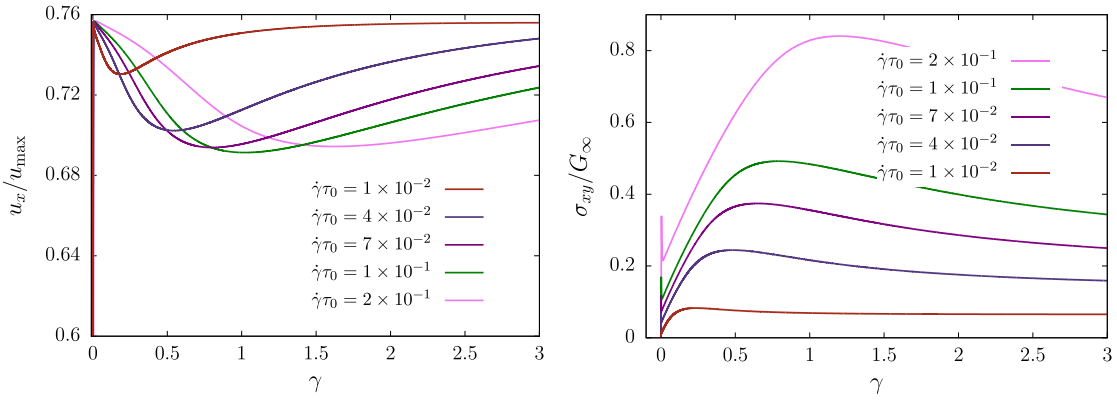


Figure 4.9: Transient evolution of velocity (left) and shear stress (right) using an initial homogeneous fluidity field and fixed wall fluidity values for different shear rates $\dot{\gamma}$ measured in the middle of the channel.

when Neumann boundary condition was used, but slightly more bent by the moving wall (left side of Fig. 4.10). Fluidity behavior versus shear rate in time is shown on the right side of same figure, where the fluidity profile is wider with deformation when the biggest transient band occurs. In both figures, we showed profiles that were obtained using $\tau_f/\tau \gg 10$ to enhance bigger banding. Moreover, transient bands are formed faster than when the fluidity field is homogeneous across the fluid but fixed at the walls.

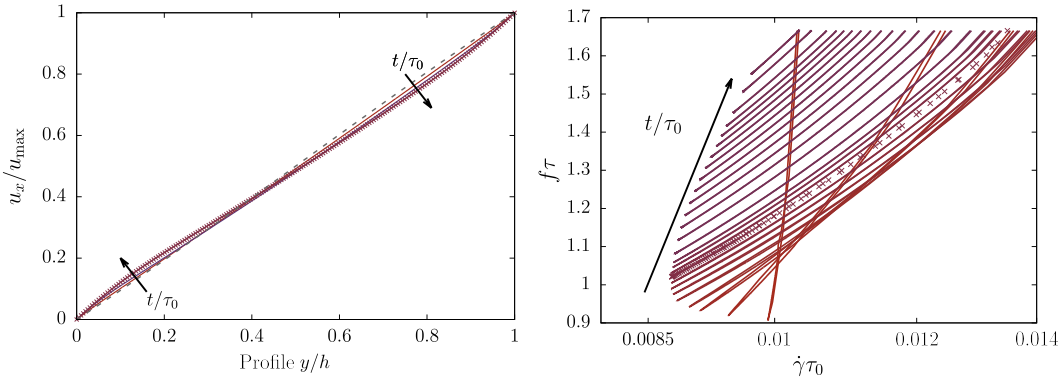


Figure 4.10: Velocity profiles (left) and fluidity profile (right) during transient banding for fluidity fixed at the wall boundary condition and cosine initial fluidity field ($\tau_f/\tau_0 \gg 10$). Dashed line steady state, crosses are biggest banding.

A comparison between bent velocity profiles found for three different initial fluidity conditions during maximum transient banding and corresponding fluidity profiles is shown in Fig. 4.11. As a reference, a dotted line represents the expected linear velocity profile on the left figure. Fluidity in function of shear rate (right side) allows

to discern between band sizing. Smaller transient bands are found when fluidity does not change greatly with shear rate, this means by using a Neumann boundary condition and a heterogeneous initial fluidity field.

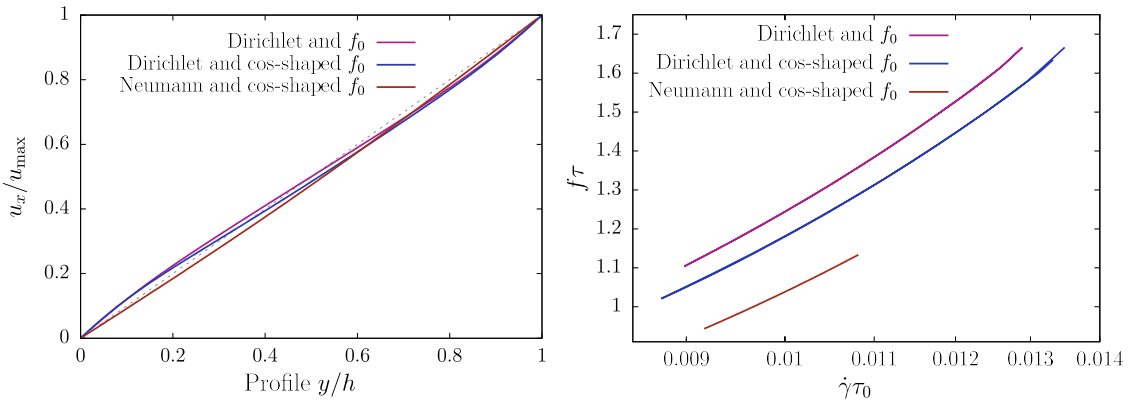


Figure 4.11: Velocity (left) and fluidity (right) profiles at maximum banding for different fluidity boundary conditions at the wall ($\tau_f/\tau_0 \gg 10$). Dashed line in left figure is expected linear steady state profile.

By enforcing a fluidity value at the wall and a heterogeneous initial fluidity field we reached yet bigger bands but similar in size as when a homogeneous field is setup initially without perturbations but a fixed fluidity value at the wall is defined. As a summary, biggest transient bands are obtained when the Dirichlet boundary condition for fluidity and an initial perturbation along the fluid. Next in size will be same perturbation but Neumann boundary condition at the walls, and lastly no bands were observed when no-perturbations were included.

4.4.3 Steady State Banding

When we set a fixed fluidity value at the wall and either a homogeneous or heterogeneous fluidity field at the rest is set for the fluid, we find that the steady state velocity profile is different from the expected linear profile for a simple shear experiment. This means, this boundary condition can reproduce long-lasting effects in steady state. Following Eq. 3.32 we found remaining bands as observed in Fig. 4.12 for different imposed shear rates. Increasing shear rate increases bands size up to a maximum

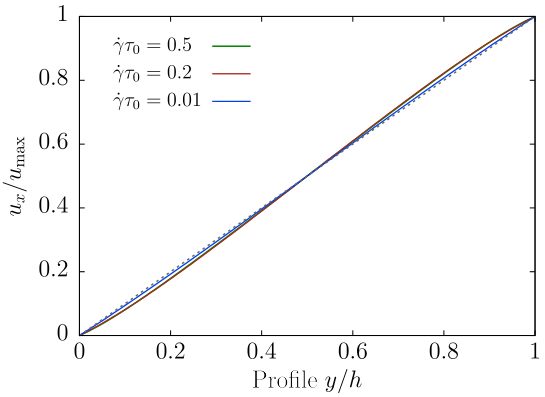


Figure 4.12: Shear bands in steady state after setting fluidity at the wall for different shear rates during simple shear.

size as shown on left side Fig. 4.13. There, we plotted band size as the difference between the velocity at the maximum band u_b found at position $y/h = 0.125$ and the expected value for a linear profile u_t. In fact, we chose to plot the velocity found at the $y/h = 0.125$ position because this side of the channel showed biggest bent in the velocity profile due to its closeness to the non-moving wall. The shear rate was varied up to $\dot{\gamma}\tau_0 = 1$, but still a Reynolds number below or around 0.1 was maintained. We found that if $\dot{\gamma}\tau_0 > 0.3$, bands started decreasing their size and eventually vanish. This leads us to conclude that there is a point where the velocity is so high that, even though a fixed fluidity is set at the wall, the fluid has not enough time to be fluidized and forms directly small or no bands.

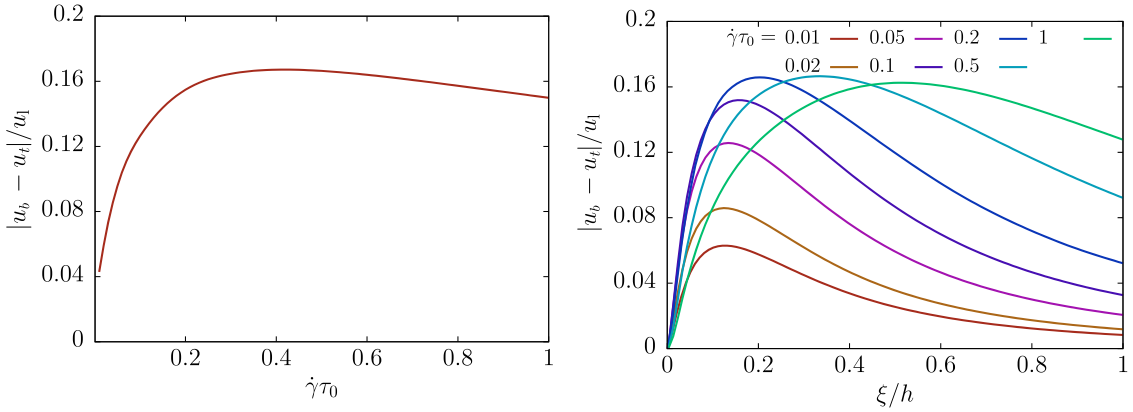


Figure 4.13: Normalized velocity difference with expected value at position $y/h = 0.125$ in steady state for different shear rates and fixed $\xi/h = 0.3$ (left) and different ξ/h and shear rates (right).

The cooperativity length has a fluidizing effect on the velocity profiles, which in this case, when ξ increases, the boundary effect is not strong enough to deviate the flow profile from its expected linear steady state shape. However, for each shear rate used, there seemed to be a optimal ξ that trigger the bigger banding. This effect is displayed on right side of Fig. 4.13 where we plotted again band size at $y/h = 0.125$ for each cooperativity length probed and different shear rates. We observe a tendency regarding shear rate, where there is a maximum banding size obtained when imposed shear rate increases, but after $\dot{\gamma}\tau_0 \sim 0.3$ band size starts to decrease. We can note as well that there is an "optimal value" for cooperativity length for each shear rate run, where the biggest band in steady state is found. For small cooperativity length, in the order of 10 μm, band size is barely visible since profiles differ by around 5% from the linear profile. However, increasing ξ increases the band size up to where the fluidity diffusion and/or cooperativity is so big that the bands fluidize and reduce their size: when ξ/h is bigger or smaller than approximately 0.2 the bands become again smaller.

4.4.4 Wall Effects

As we mentioned at the beginning of this chapter, by setting a fixed fluidity value at the wall we enforce a flow curve that shows same stress values for different shear rates. This particularity allows bands to remain in the flow. Fluidity values at the wall were initially chosen following what Goyon et al. [2] did for shear profiles obtained experimentally. For them, these values coupled surface rheology (considering roughness and smoothness) to fluid rheology. Moreover, they say that smooth surfaces show fluidity values close to the bulk values of the fluid and rough surfaces higher values: rough surfaces in their context fluidize the system, which is not a trivial concept and it is related to corresponding emulsions context. Rough surfaces might also be seen as sticky walls that will not let material to actually flow, which is a concept we take from now on, following [81], i.e. rough surfaces will have a low fluidity as $f_w \approx 0$ and smooth surfaces will show higher values than bulk fluidity $f_w \geq f_0$. By setting $f_w\tau_0 = 0$ and $f_w\tau_0 = 1$, we used the fluidity glass model ($\tau \approx \infty$) to exemplify rough and smooth surfaces respectively. In this case, we obtained more extreme bent velocity profiles in steady state as it is exposed on top of Fig. 4.14. When the wall has lower fluidity than the final steady state value, fluidity in the center of the channel will increase to reach to the expected value whereas in the rest of the channel the system tries to get to it while being hindered by the walls. This causes the curved fluidity profile, as shown at the bottom of same figure. Close to the moving wall, higher velocities than expected are developed (than linear profile). Moving the wall will induce fluidization in the system, which is not present when close to the fixed wall. In this case, areas with higher fluidity are present as well, but the opposite velocity s-shape flank is formed with lower velocity values than expected as in the linear profile.

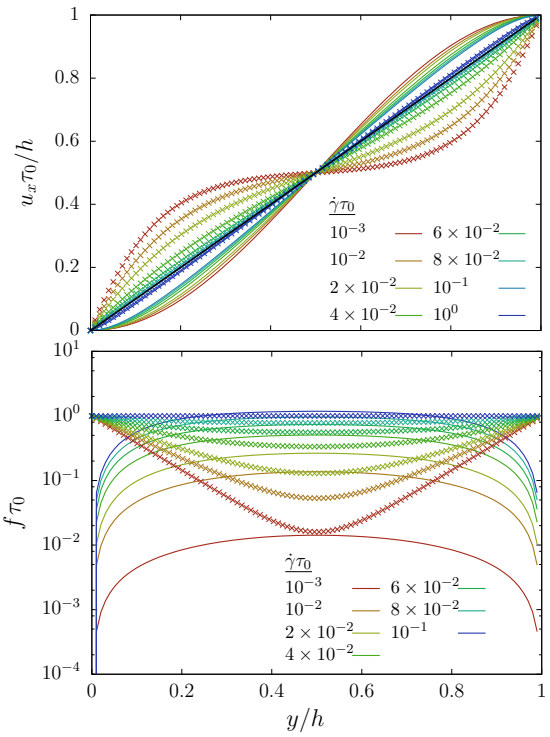


Figure 4.14: Top: steady state velocity profiles and bottom: fluidity profiles, for different $\dot{\gamma}\tau_0$. $f_w\tau_0 = 0$ (lines) and $f_w\tau_0 = 1$ (symbols).

The opposite shape was found for higher fluidity wall values and shear rate velocities studied, where profiles looked bent inwards pointing to the final corresponding steady state value (center of the channel). This fluidity shape flipped the shape of the velocity profiles, where two flanks are

observed: close to the moving wall velocities are under the linear profile, and close to the fixed wall higher velocities than expected values were obtained, however still in a lower range than the upper section of the channel. The first case corresponds to a system that must decrease its fluidity down to the final steady state value, hence lower velocities. In the second case, close to the fixed wall, the counter flank is formed where lower velocities are obtained for same fluidity value.

4.5 Bauschinger Effect

Material history has been proved to influence the mechanical macroscopic final response of a system. As previously shown a stress-strain overshoot is found when we start shearing a system starting from equilibrium state using the fluidity model. This overshoot is enhanced by τ_f and appears in homogeneous and heterogeneous flows. As already mentioned, this overshoot might be related to the dynamics of cages breakage in glass forming liquids, which is a non-linear response phenomenon. The maximum stress has been named as the stress that separates elastic and plastic deformation [92].

As previously introduced there is a relation between material history and this overshoot. For example, after an amorphous solid has been deformed into steady state and from there a reverse deformation is applied, the stress-strain curve is not fully recovered. The stress overshoot is susceptible to the protocol used to deform the sample, where the phenomenon observed is that by reversal the overshoot decreases. Differences between the stress-strain curves show what is called Bauschinger effect. This phenomenon tells us that there is a strain reversal point that contains enough material information to change the new start-up curve to ultimately change the mechanical properties of a system [93]. This is a phenomenon that can be measured in a rheometer though it is not necessarily a mathematical concept.

This means that for homogeneous fluids, the fluidity model, in principle, should not reproduce a Bauschinger effect. However, when we reverse homogeneous flow after steady state, the curvature of the curve is larger than without pre-strain. Let us assume we have a simple shear setup where $\dot{\gamma}(t) = \dot{\gamma}$ for $t \in [0, t_r]$ and then the flow is reversed as $\dot{\gamma}(t) = -\dot{\gamma}$ at $t = t_r$ for $t > t_r$. The solution for $\sigma(t)$ using the fluidity model for $t > t_r$ is:

$$\sigma(t) = G_\infty \dot{\gamma} \left(\int_0^{t_r} dt' e^{-(t-t')/\tau_M(\dot{\gamma})} e^{-\left(\dot{\gamma}\tau_f/\gamma_c\right)\left(\exp[-t/\tau_f]-\exp[-t'/\tau_f]\right)} - \int_0^{t_r} dt' e^{-(t-t')/\tau_M(\dot{\gamma})} e^{-\left(\dot{\gamma}\tau_f/\gamma_c\right)\left(\exp[-t/\tau_f]-\exp[-t'/\tau_f]\right)} \right). \tag{4.2}$$

This equation yields to the reversed stress-strain curve for smaller t_r, but when t_r increases the overshoot vanishes which is similar to what is known as Bauschinger effect. The time derivative of the stress for $\dot{\gamma} = \dot{\gamma}(t)$ at flow reversal, knowing that $d\sigma/d\gamma = \sigma/(-\gamma)$, is:

$$\frac{d\sigma}{d\gamma} = G_\infty + \sigma(t) \left(\frac{1}{\dot{\gamma}t} + \frac{1}{\gamma_c} \left(1 - e^{-t/\tau_f}\right) \right). \tag{4.3}$$

This is larger than G_∞ at time reversal. In fact, at the point of reversal $d\sigma/d\gamma = 2G_\infty$ is obtained when we insert the steady state stress in Eq. 4.3, which is not dependent on shear thinning effects. However, the shear modulus is usually measured at the point of reversal where $\sigma(t)$ crosses zero at time t_*. From then on the slope of the curve converges to G_∞ as implied by the fluidity model definition. However, one can measure the curvature of the reversed stress-strain curve which shows to be larger at around $\sigma = 0$. In same curve $\ddot{\sigma} = \mp G_\infty \dot{\gamma}(1/\tau + (\dot{\gamma}/\gamma_c))(-\exp(-t/\tau_f))$, where upper sign is for $t = 0$ and lower for $t_* > t_r$. For t_* at $t_r \to \infty$ the curvature is $\ddot{\sigma} = G_\infty \dot{\gamma}/\tau_M(\dot{\gamma})$, which means that $\mid \ddot{\sigma}(t_*) \mid > \mid \ddot{\sigma}(0) \mid$. Therefore, one could measure an effective shear modulus G_{eff} which is indeed lower than G_∞ at around $\sigma(0)$. Second derivatives have been used by [93] to determine the order parameter that changes the shape of stress-strain curves when flow is reversed, since they converge to a value due to asymmetry of the reversed stress-strain function. Same authors establish a relation between this non-vanishing derivative to plastic deformation that breaks the isotropic system in amorphous solids. This is an effect of the fluidity model since the Maxwell model does not show overshoots during start-ups. We checked the hysteresis behavior of heterogeneous flows when transient shear banding is present, see Fig. 4.15. By using a heterogeneous initial fluidity field, we started same simple shear system until steady

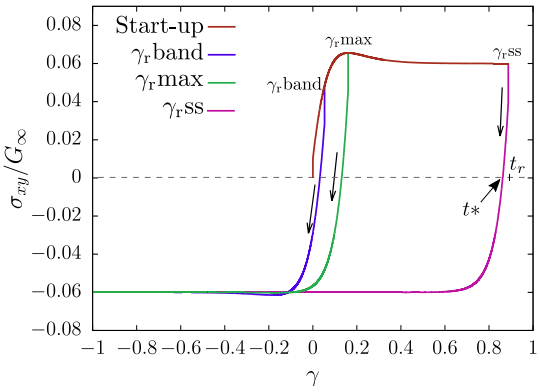


Figure 4.15: Hysteresis loops after start-up is reversed from steady state, maximum stress, and biggest band strain location.

state is reached, i.e. $\sigma_{xy}(\dot{\gamma} \to \infty) = \sigma_{ss}$, to then reverse the direction of the flow at different points of the stress-vs-strain curve with the same initial imposed shear rate. This setup can be summarized with next relation:

$$\gamma(t) = \begin{cases} |\dot{\gamma}|t & \text{for } t < t_{rev} \\ 2|\dot{\gamma}|t_{rev} - |\dot{\gamma}|t & \text{for } t > t_{rev}. \end{cases} \tag{4.4}$$

First, we started moving the top wall at a constant shear rate, which resulted in a fairly linear stress versus strain relation defining an elastic regime at small deformations, i.e. $\sigma_{xy} \approx G_\infty \gamma$. Second, a transient overshoot appeared characterized by a σ_{max} at $\gamma_{max} \approx 0.16$. This deformation comes from a model constant γ_c. Third, steady state is reached where stress does not change greatly with deformation anymore at higher times. We reversed the flow at three different points of this resulting shear stress versus strain curve. First, from steady state stress where $\gamma_{ss} = 1$ was chosen as sufficient deformation, second from maximum stress σ_{max} at overshoot, and third where the biggest transient band occurs σ_{band}, which happens in the linear regime before the overshoot at $\gamma_{\text{band}} \approx 0.053$. This was chosen, as it was mentioned before, where an overshoot in the transient velocity occurs, which corresponds to the biggest transient banding as it was previously observed for example in Fig. 4.2. By plotting the previous curves versus $|\gamma - \gamma_0|$, we can have all the curves shifted, inverted, and starting from the same point to easily compare behaviors, see Fig. 4.16. The stress overshoot decreases the closer to steady state we reverse the flow from. When we reversed the flow from where the biggest band happens, the overshoot is bigger than when we reverse from the other states. The curvature of each curve changes as well: it will decrease the further in steady state we start reversing the flow from. As stated earlier these curvatures are related to an elastic modulus, since their measurement is done after the reversing the stress crosses zero. We found an effective decrease of the curvature the closer the time of reversal is to steady state. Even though, Bauschinger's initial idea was more focused on the vanishing stress overshoot and its relation to material strength, mentioned authors [92] and [93] have attempted to re-define the Bauschinger effect by calculating an effective decreasing shear modulus depending on the time of reversal where material properties could also be assessed and characterized.

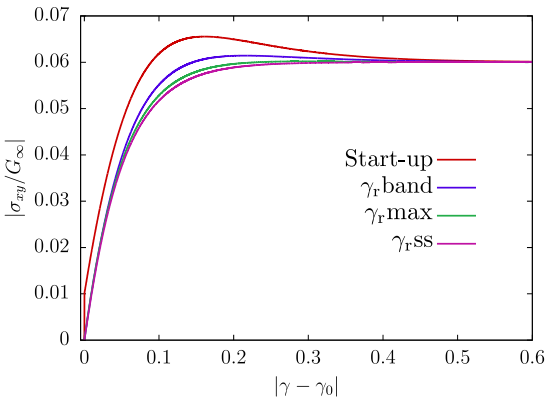


Figure 4.16: Shear stress evolution during start up and after reversing from different points in the middle of the channel.

Chapter 5

Residual Stresses

Prince Rupert's drops have been a curiosity since they were introduced in the early 17th century to the science community. They are tadpole-shape drops with a characteristic fine tail that are obtained from molten glass: usually, the end of a molten glass-rod is dropped in cold water, where the separation of the melt from the rod forms a thin tail. During the sudden solidification process, the drop surface cools down faster than the center creating compressive stresses on the former and tensional in the latter. A drop is shown Fig 5.1. Extraordinary strength is one of the most important mechanical properties of these drops since they are able to withstand hammering, indentation, compression even of up to load of 15 kN for a 6 mm diameter drop without failure [94]. However, they behave incredible fragile when the tail is damaged where same compressive (surface) and tensional (center) stresses are present in a tube-shaped ensemble: as soon as the latter is released disintegration travels in both directions like a wave of stress which is responsible for the drop's well known rapid explosion, i.e. a residual stress network created during the sudden-cooling process is released [95].

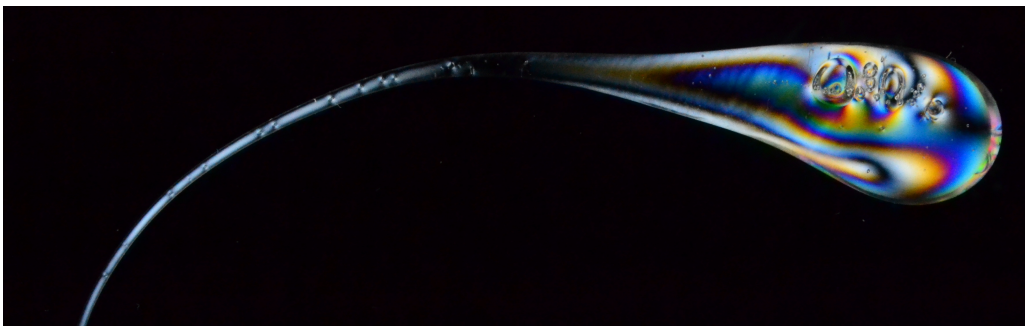


Figure 5.1: Prince Rupert's drop photograph.

Residual stresses are defined as persistent remaining stress at larger times after solidification either by cessation of the flow, quenching, or chemical reactions [96, 97]. If the quenched system forms a glass, its structure is not able to reach a state of equilibrium since part of the stress coming from the liquid phase stays present in the solid. Many manufacturing processes involve solidification of amorphous materials by one of the mentioned methods, and the presence of residual stresses in the final product can be a burden, e.g. leading to material failure, or it might also be used as an advantage for improving the mechanical performance. When considering quenching, strong temperature gradients are created along the material where some areas might deform plastically creating misfits of permanently stressed areas that remain until the system reaches equilibrium, where a typical example is safety glass [98]. Recently, cover and displays glasses for electronic devices, like Gorilla® Glass, are produced by an ion-exchange process that strengthens the surface by imposing compressive stresses that ultimately prevent flaws, cracking, or failure [99].

Mode coupling theory has given a theoretical framework to understand the mechanisms involved in the emergence of residual stresses in glass formers, going beyond of what tensorial constitutive models like soft-glassy rheology predicts where stresses in stopping flow go to zero [97, 100]. MCT within ITT formalism can qualitatively reproduce residual stresses found in colloidal glasses after cessation of flow in simple shear, which was supported by experiments and molecular dynamics simulations by Ballauff et al. including the strong dependence on deformation history [97].

We used the fluidity model to reproduce residual stresses found during cessation of the flow of glass forming liquids after having reached a non-equilibrium steady state. We started by implementing the model in a simple shear setup and the influence of the model parameters was understood. This allowed the results to be validated analytically, however, the versatility of the model implementation on the FVM package allowed us to assess residual stresses in lid-driven cavities, and not-so-trivial geometries like pressure-driven flow with obstacles and abrupt 4:1 contractions. We will discuss how the cooperativity length and fluidity timescale play a determining role in the residual stress patterns obtained. From now on we will use the fluidity glass model that was introduced in 3.3.1 unless it is said otherwise.

5.1 Simple Shear

A simple shear system was set up like it was previously explained in Section 4. We used a homogeneous initial fluidity field, $f = 1/\tau = 0$ since we use the fluidity glass model. A shear rate $\dot{\gamma}$ was imposed as a top-wall constant velocity. After steady state is reached, the top-wall velocity was set to zero making the flow enter into cessation state where system velocity decays (almost immediately) to zero together

with the Newtonian contribution to the stress. Nonetheless, the non-Newtonian contribution to the stress will decay from its steady state value to a finite residual stress that depends on past shear rate $\dot{\gamma}$ and a timescale set by the fluidity relaxation time τ_f.

Left side of Fig. 5.2 shows how the relaxation of the stress decays in cessation with time for different pre-shear rates following the analytic solution of Eq. 3.28. The higher the previous deformation more stress is relaxed resulting in lower residual values. As it was mentioned before, MCT predicts the existence of residual stresses during cessation of flow, where for higher pre-shear rates the residual stresses found in the system were lower [1,78,97]. This also concurs with the increase of the fluidity relaxation time τ_f, see right side of same figure, where the more time is given to the fluidity to spread in the system during cessation, less stress remains afterwards, a tendency we validate in next sections for the other geometries studied.

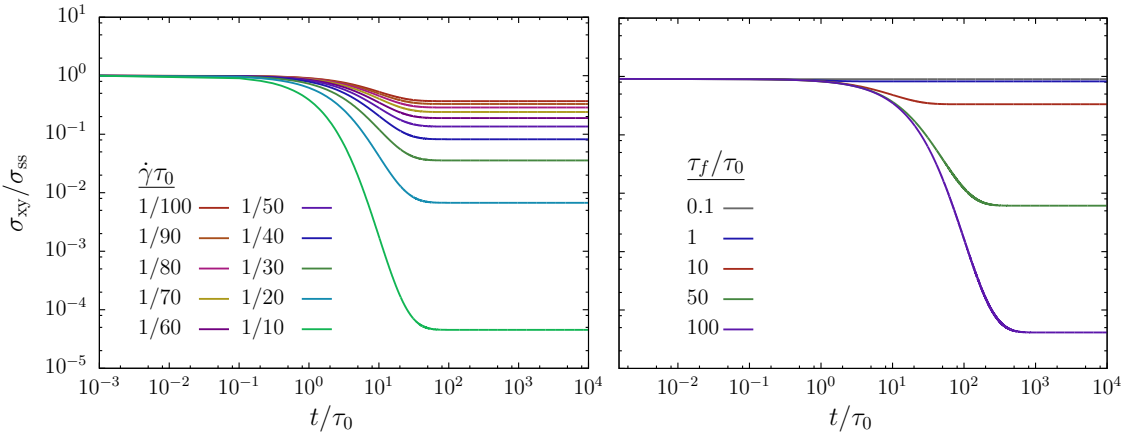


Figure 5.2: Left: shear stress in time during cessation for different $\dot{\gamma}$ using $\tau_f/\tau_0 = 10$ and $\xi = 0$. Right: shear stress in time during cessation for different τ_f/τ_0 and $\dot{\gamma}\tau_0 = 10^{-2}$ and $\xi = 0$.

5.2 Lid-Driven Cavity Flow

A classical two-dimensional cavity was set-up with a fluid that follows the fluidity glass model. This geometry is one of the most used in continuum mechanic and refers to a recirculating flow confined between walls and driven by the top wall at a constant velocity while rest of walls are fixed. A vortex is formed in the center of the cavity, though other vortices might be found in the cavity bottom corners [101, 102].

First, we studied the influence of model parameters as τ_f and ξ in steady state, to then verify their role in flow cessation where, similarly to the simple shear case, residual stresses were also present. Schematically, a lid-driven cavity flow looks like in Fig. 5.3.

The cavity geometry is a square $h \times h = 0.1\,\mathrm{m}$, and the velocity of the top-lid was varied as $u_x\tau_0/h = 0.01,\ 0.1,\ 1$. Reynolds number was ensured as $\mathrm{Re} < 0.1$. This number was calculated locally as $\mathrm{Re}_L = hu_x/\eta_L$. Its distribution is shown as a color map in Fig. 5.4, where we display side-by-side the resulting values using the fluidity model for a viscoelastic fluid (left column) and a Newtonian fluid (right column) with similar viscosity as the final viscosity obtained with corresponding fluidity model results. Note that our model considers a viscosity dependent on shear, hence it is defined locally as:

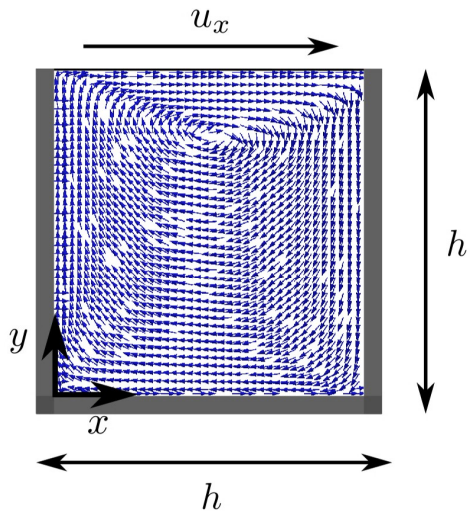


Figure 5.3: Schematic representation of the lid-driven cavity flow set-up.

$$\eta_L = \frac{\sigma_{xy}}{\sqrt{\mathrm{II}_\mathrm{D}}}. \tag{5.1}$$

In fact, for this geometry and fluid a Reynolds number of 0.1 already induced symmetry breaking, which for a Newtonian fluid is not observed. This is shown by bottom left figure in Fig. 5.4, by resulting Reynolds number distribution for a high lid-velocity that promotes turbulent flow even though Re is still under 0.1. Note that in the case of Newtonian flows for $\mathrm{Re} = 0.1$ the symmetry is still conserved (see right panel second figure). We used a non-dimensional velocity normalized by the top wall velocity as $u_L = u_x/u_{\max}$ for profile probing, and $u_l = u_{\max}\tau_0/h$ as top-lid-velocity.

5.2.1 Steady State

We studied flow symmetry breaking by means of the Reynolds number distribution along the cavity for different lid-velocities, as it is shown in Fig. 5.4. As already mentioned, we found that symmetry starts breaking at around $\mathrm{Re} \approx 0.1$, which one might see as a "low" Re value if we compare this to what is obtained for Newtonian fluids. For Reynolds numbers close to zero, the convection terms vanish in the momentum equation leading to symmetric patterns. Symmetry is broken as soon as the convection term becomes more relevant in the momentum equation for Newtonian fluids [103, 104].

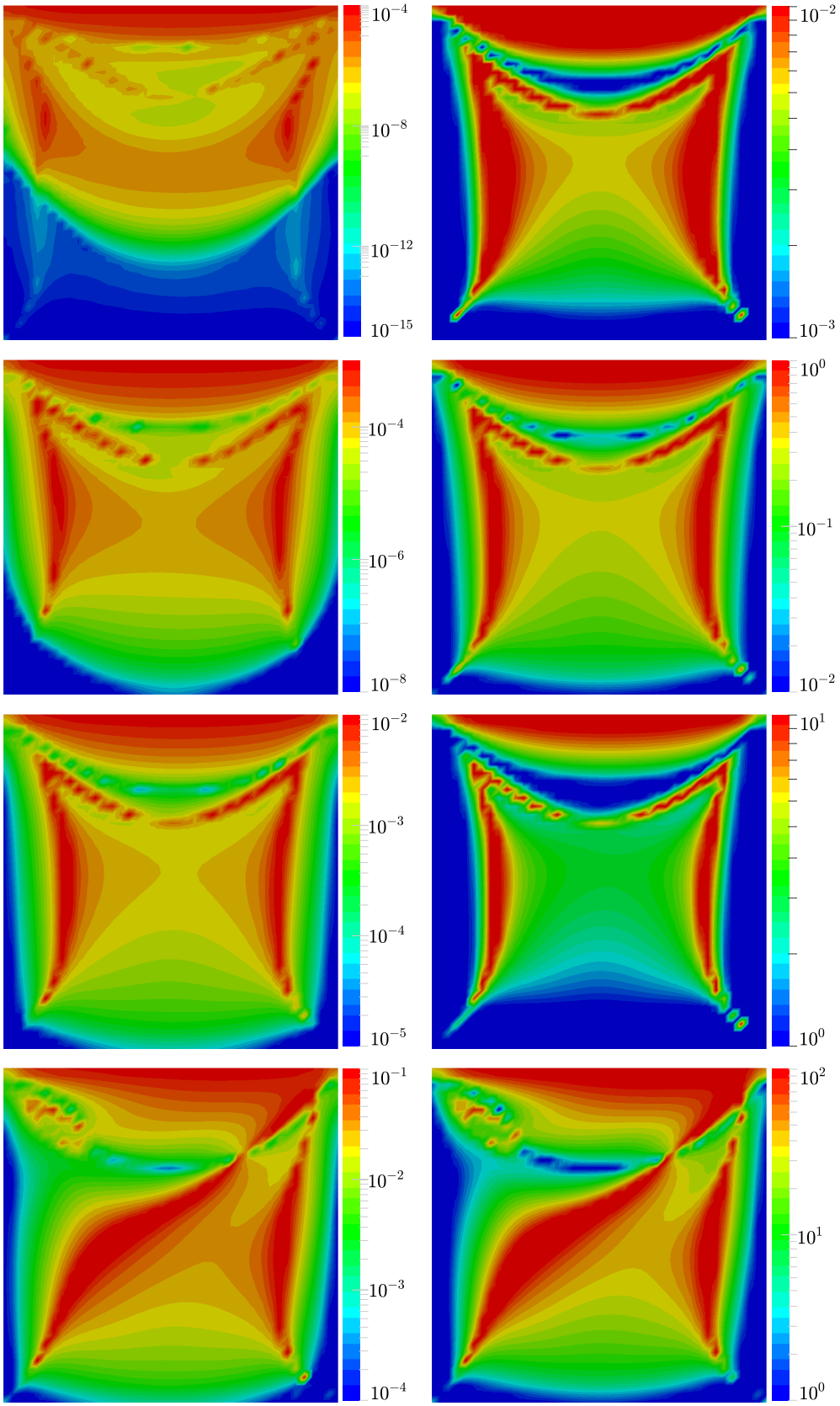


Figure 5.4: Local Reynolds number color maps in logarithmic scale using, from top to bottom, $u_x\tau_0/h = 0.01, 0.1, 1, 10$. Left side: $\tau_f/\tau_0 = 0.1$ and $\xi/h = 0$. Right side: Newtonian cases using $\eta = 5$ Pa $\cdot$ s for $u_x\tau_0/h = 0.01$ and $\eta = 1$ Pa $\cdot$ s for rest velocities.

However, in the fluidity model cases, symmetry seems to be broken by viscoelasticity. Consequently, changing the lid-velocity affected flow streamlines in steady state as well. For example, we found that the vortex formed close to the top-wall was shifted down and to the right when velocity increased (see Fig. 5.5). Two bottom-corner vortices are also observed when the velocity increases. For the case of highest velocity one bottom vortex remains of a considerable size. Bottom corner vortices presence is mostly expected for higher Reynolds numbers [101], where also the center vortex becomes inviscid [104]. For these streamline figures we used cooperativity length zero and $\tau_f/\tau_0 = 0.1$. The effect of mentioned model parameters will be pointed out in the following sections.

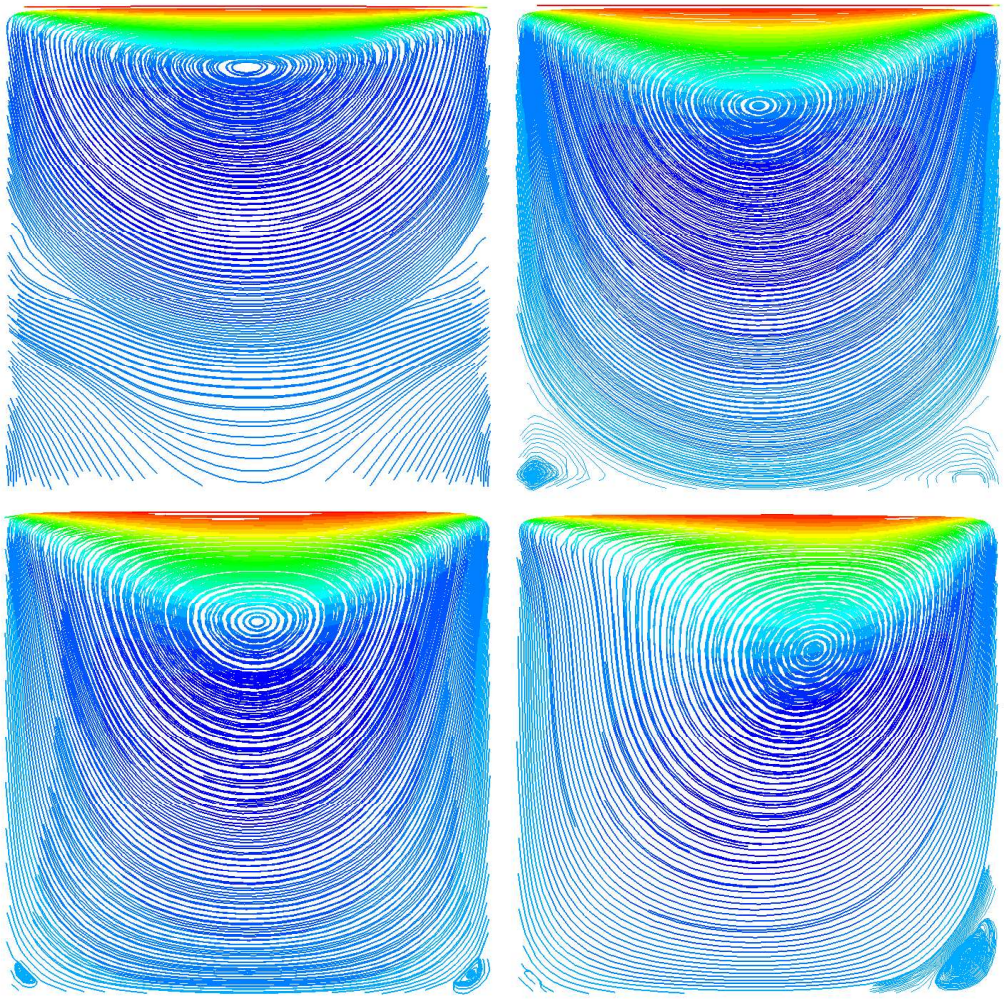


Figure 5.5: Steady state streamlines using u_l: 0.01 (top left), 0.1 (top right), 1 (bottom left), and 10 (bottom right). Red for high values, blue for low values.

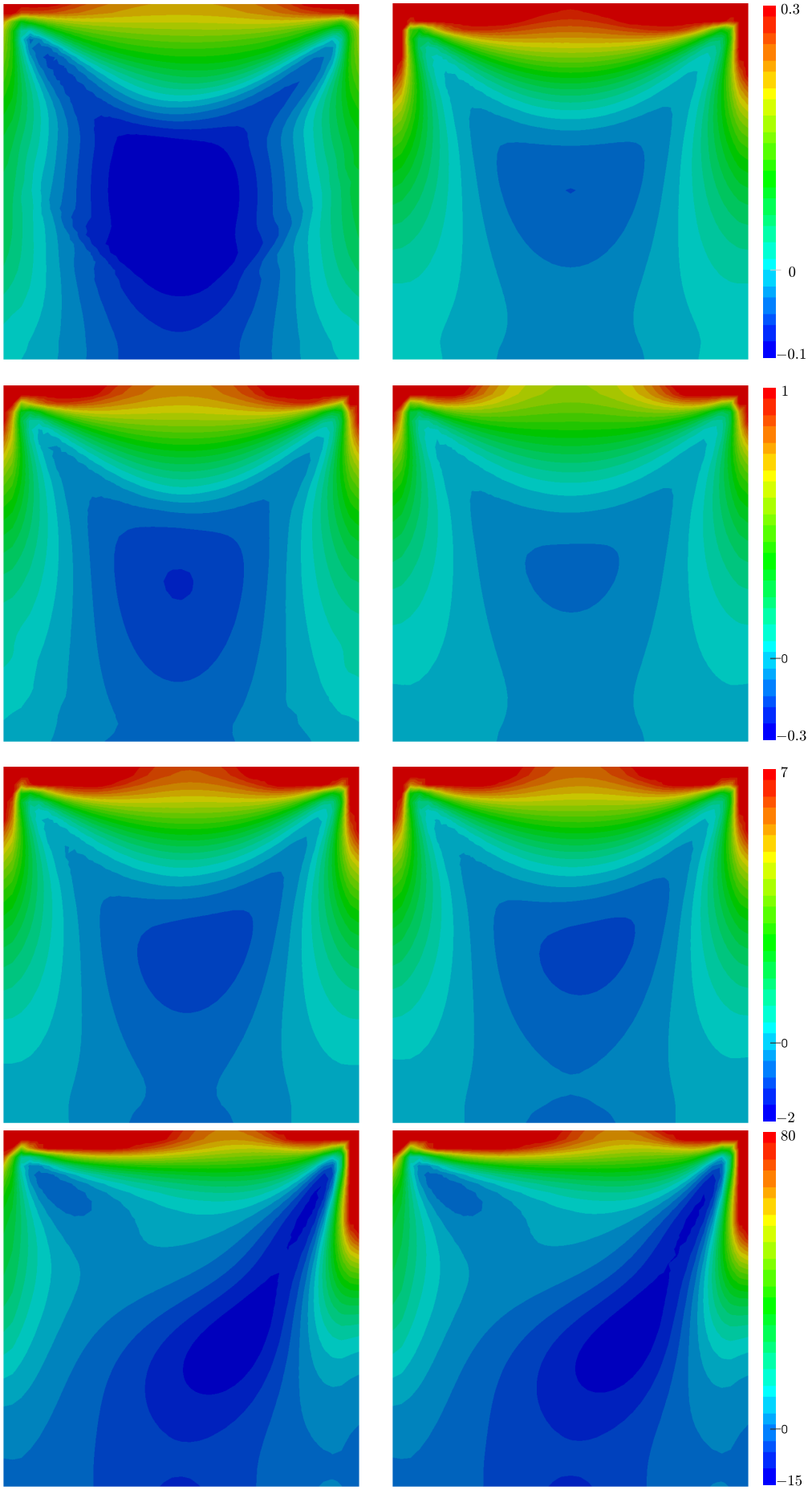


Figure 5.6: Left panel: shear stress in steady state using $\xi/h = 0.03$ and $\tau_f/\tau_0 = 0.1$. Right panel: Newtonian fluid. Top row $u_l = 0.01$ and Newtonian fluid $\eta = 5$ Pa $\cdot$ s. Second $u_l = 0.1$, Third $u_l = 1$, Bottom $u_l = 10$ and Newtonian fluid with $\eta = 1$ Pa $\cdot$ s.

Increasing the lid-velocity modifies the shear stress distribution as well. This is displayed using color maps in Fig. 5.6. These figures show side by side resulting patterns in steady state using low, intermediate, and high lid-velocity ($u_x\tau_0/h = 0.01, 0.1, 1$) for a fixed cooperativity length of $\xi/h = 0.03$. Velocity distribution was affected by the initial conditions of the system, yet shear stress was altered in a bigger extent by the cooperativity length.

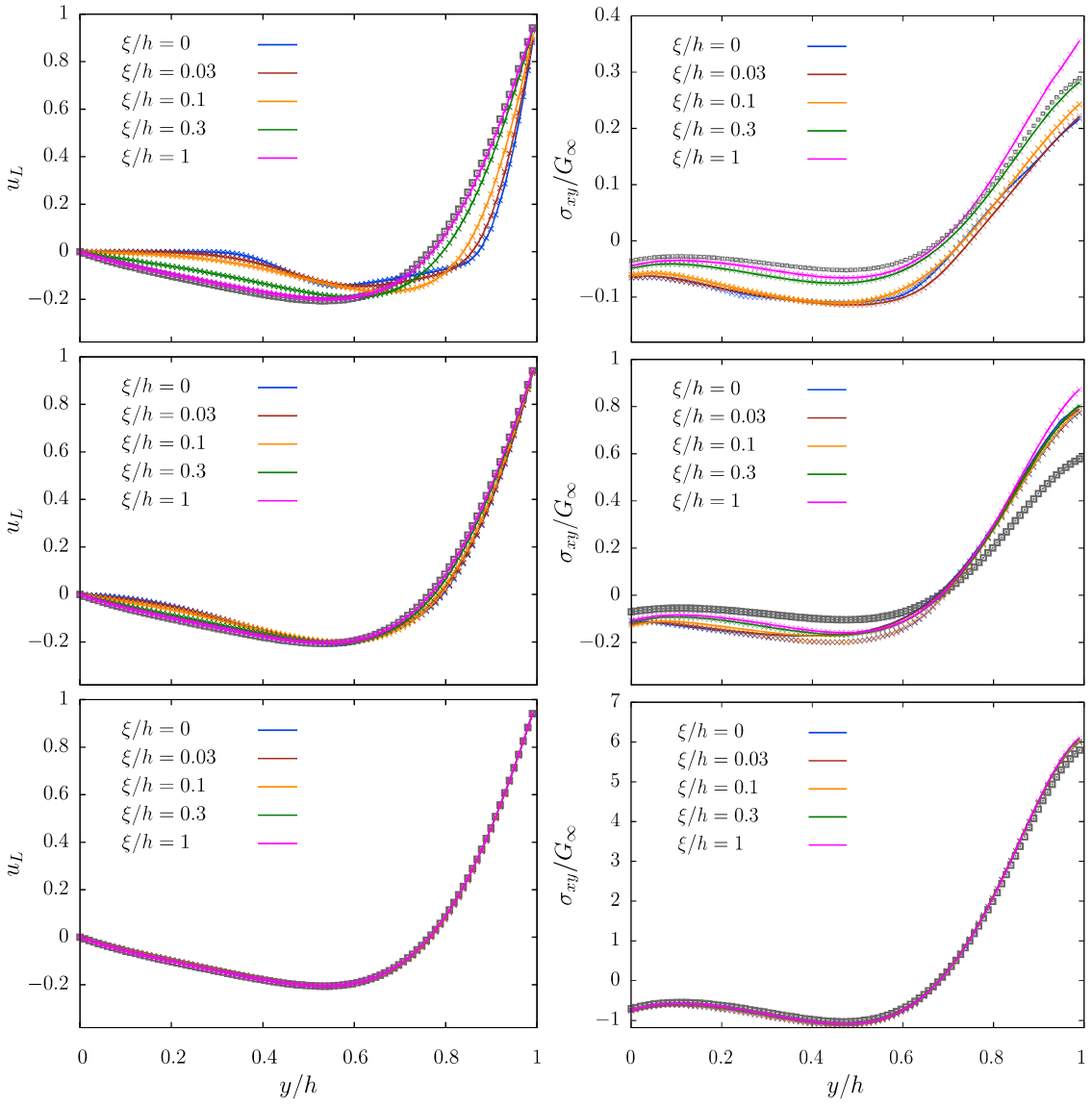


Figure 5.7: Velocity y-profiles (left panel), and shear stress y-profiles (right panel) in steady state for different ξ/h values and $\tau_f/\tau_0 \in \{0.1, 10\}$ (cross and solid lines respectively). Newtonian cases marked with squares. First row: $u_x\tau_0/h = 0.01$ (Newtonian viscosity $\eta = 5$ Pa $\cdot$ s). Second row: $u_x\tau_0/h = 0.1$ (Newtonian viscosity $\eta = 1$ Pa $\cdot$ s). Third row: $u_x\tau_0/h = 1$ (Newtonian viscosity $\eta = 1$ Pa $\cdot$ s).

Fluidity timescale τ_f has no effect in the steady state velocity and shear stress profiles as exemplified in each one of the profiles shown in Fig. 5.7. The cooperativity length on the other hand, changes the velocity profiles for different lid-velocities, being its effect stronger for lower ones. When u_l is increased all profiles collapse for different ξ. The higher ξ value the closer we get to a Newtonian velocity profile. To produce the latter we used viscosities that yield similar profiles as comparison. In summary, the effect of ξ is stronger for smaller lid-velocities. On the right side of the same figure, the corresponding shear stress profiles are displayed for same probed ξ, where similar tendencies were found as in for the velocity profiles. Note that when the lid-velocities are smaller the shear stress profiles differ importantly for the ξs studied and do not exactly match the corresponding Newtonian profile. For higher lid-velocities the Newtonian profiles that fit closely the model results were obtained with lower viscosity, which arises from the shear thinning effect of the viscoelastic fluid at higher shear rates.

The central vortex position is affected by the cooperativity length in steady state to some extent. This effect is more noticeable for lower lid-velocities since, when the Reynolds number was increased, ξ effect faded. For lower velocity, streamlines showed symmetry around the y-axis for every ξ studied. However, it is observed that increasing ξ moved the central vortex slightly downwards enhancing the emergence of bottom-corners smaller vortices. This is illustrated in Fig. A.5.

5.2.2 Flow Cessation

Shear stress profiles already gave us a hint of how cooperativity length within the flow affects steady state. By comparing profiles to a Newtonian expected behavior we found: for lower velocities, the highly cooperative flow follows a higher Newtonian viscosity tendency and, for higher lid-velocity, the Newtonian-like behavior corresponds to a lower viscosity instead.

When the top-lid is stopped and the velocity of the flow decays to zero, residual stresses remain "alive" in the cavity, like in the simple shear case. We mentioned before that fluidity timescale does not affect steady state behavior, but when the flow ceases, the remaining shear stress is not only affected by ξ but also by τ_f. Fig. 5.8 encompasses all the resulting shear stress patterns in steady state (first column), and the residual stresses found for $\tau_f/\tau_0 = 0.1$ (second column) and $\tau_f/\tau_0 = 10$ (third column) for cooperativity length values from top to bottom $\xi/h = 0$, 0.03, 0.1, 0.3. The final state patterns were obtained at large enough times when stress did not change notably with time anymore. This large time depended on τ_f, so we found that a fair final time was around $t_f \approx 500\tau_f$.

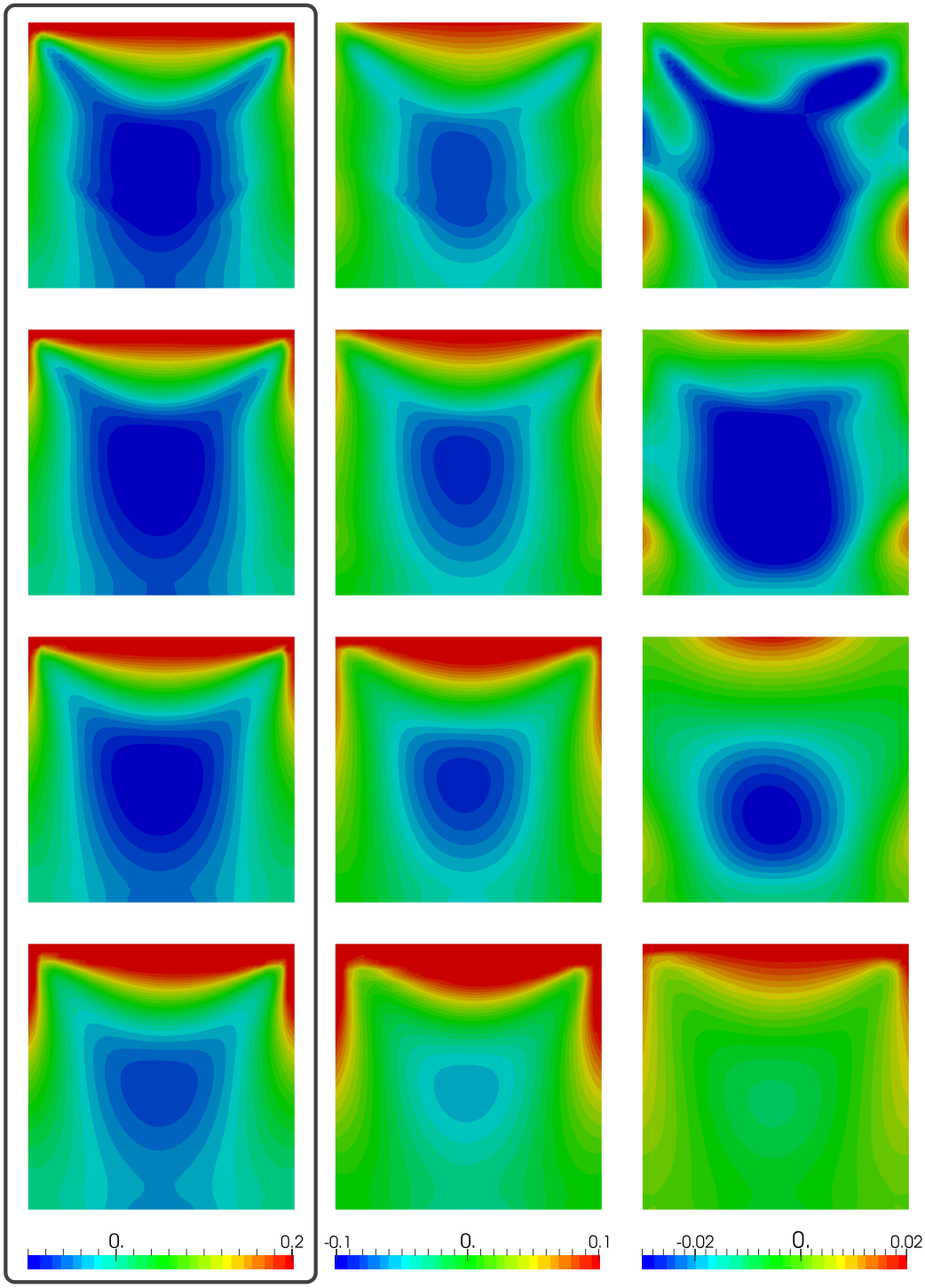


Figure 5.8: Shear stress patterns for: first column steady state using $u_x\tau_0/h = 0.01$. Second column ($\tau_f/\tau_0 = 0.1$) and third column ($\tau_f/\tau_0 = 10$) are residual stresses obtained after flow cessation. From top to bottom: $\xi/h = 0, 0.03, 0.1, 0.3$.

It should be noted that higher residual stresses are located both in the center of the

cavity, resembling a bundle, and close to the top wall forming a lip-shaped curved area pointing downwards. Central stress bundle shape and size are altered by both cooperativity length and fluidity timescale, since increasing the former decreases the bundle size and increases the top-lid shear stress. On the other hand, τ_f decreases the overall residual shear stress and the central stress bundle area as well: the system has more time to be fluidized and the stress relaxes which will eventually cause the stress to become zero. On the other hand ξ/h modifies the shear stress patterns and their symmetry: for lower values the pattern symmetry is modified mainly for higher τ_f (top right snapshot) which seems distinct than the immediate next ξ values studied just right below it, where the central stress bundle changes shape and moves slightly downwards until it disappears at higher ξ.

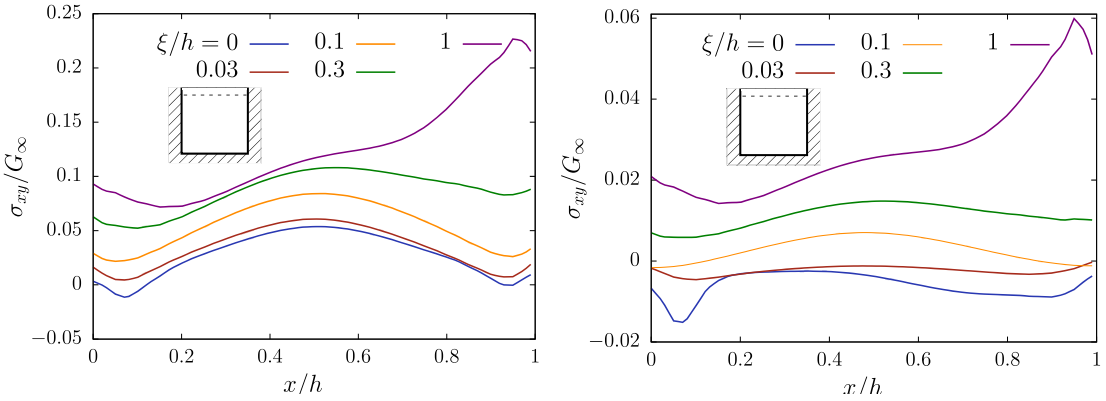


Figure 5.9: Shear stress x-profile after flow cessation at $y/h = 0.9$ (lid-velocity $u_x\tau_0/h = 0.01$) for $\tau_f/\tau_0 = 0.1$ (left) and $\tau_f/\tau_0 = 10$ (right) for different ξ/h.

Fig. 5.10 illustrates the shear stress profiles after flow cessation using same variations of ξ and τ_f. These profiles are obtained in the middle of the cavity along the y-axis, where the residual shear stress follows the same tendency obtained in the start-up of the flow regarding shape, though certainly smaller stress values. It is also noticeable how in the center of the cavity, the shear stress increases for lower ξ values up to around $\xi/h = 0.03$ to then decrease for ξ. Close to the top wall, at $y/h = 0.9$, x-profiles were measured and displayed in Fig. 5.9 for $\tau_f/\tau_0 = 0.1$ and 10. In both cases, symmetric patterns are somehow conserved for lower ξ, however higher ξ values bend the profiles closer to the top right side of the wall. It is therefore evident that even when the top-lid has already stopped and

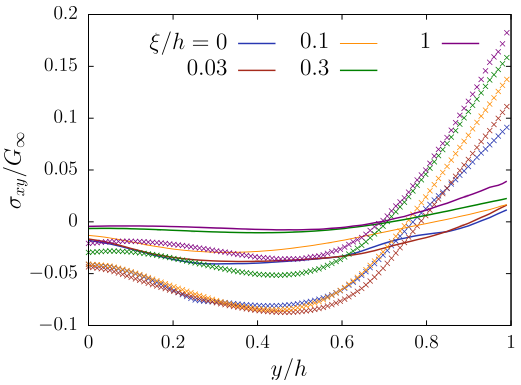


Figure 5.10: Shear stress y-profile after cessation ($u_l = 0.01$) for different ξ/h and $\tau_f/\tau_0 \in \{0.1, 10\}$ crosses and lines respectively.

velocity reached zero, there is a remnant shear stress nearby whose patterns is less symmetric for high cooperativity length and enhanced by τ_f. However, when the latter increased full-patterns softened mainly for higher cooperativity length values, even though close to the top-wall the asymmetry remained.

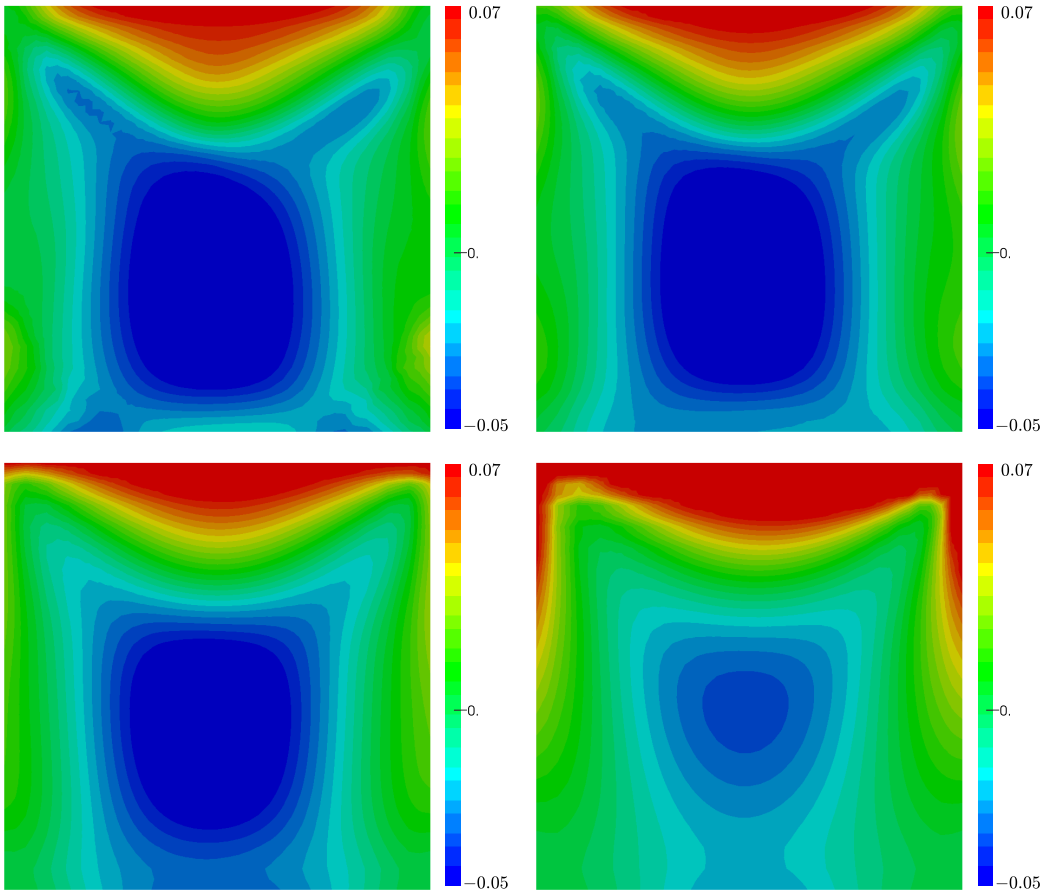


Figure 5.11: Residual shear stresses found after flow cessation (lid-velocity $u_l = 0.1$ and $\tau_f/\tau_0 = 0.1$) for: $\xi/h = 0$ (top left), 0.03 (top right), 0.1 (bottom left), and 0.3 (bottom right).

When we use intermediate velocities like $u_l = 0.1$, we obtain a symmetric shear stress pattern in steady state, see Fig. 5.6 middle row. The symmetry along x remains after flow cessation as shown by the stress color patterns in Fig.5.11. In fact, for the next higher lid-velocity $u_l = 1$, which still produced symmetric steady state patterns, shear stress after flow cessation showed reasonable symmetry along x-axis even though patterns were affected by ξ as shown in Fig. 5.12. The stress bundle is not localized in the center like for lower lid-velocities but closer to the bottom wall, and is where higher remaining stress is localized. Its size is affected by ξ (note different scales). Close to the the top wall an area with high residual shear stresses is also present, which is affected by ξ. Higher ξ in this case tends to produce uneven stress distributions, where small bundles of stress remain close to the side walls.

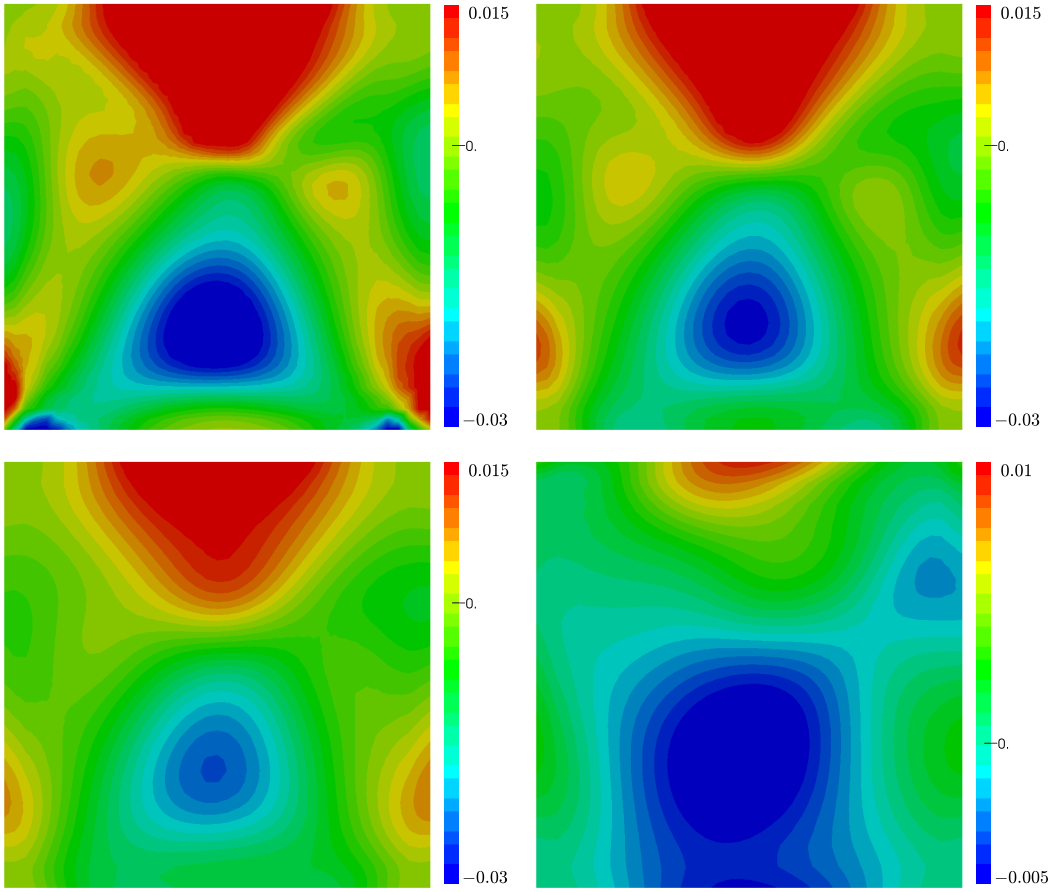


Figure 5.12: Residual shear stress after flow cessation ($u_l = 1$ and $\tau_f/\tau_0 = 0.1$) for: $\xi/h = 0$ (top left), 0.03 (top right), 0.1 (bottom left), and 0.3 (bottom right).

Fig. 5.13 shows shear stress profiles on the x-axis in the middle of the channel. Across the x-axis, symmetry is affected by higher cooperativity length values. They shift the profile towards the right side of the cavity and decrease the overall shear stress along that line. For yet higher lid-velocity as $u_l = 10$, there is a clear symmetry breaking in steady state along the x-axis for stress distribution as shown in bottom of Fig. 5.6. In that case, lid velocity is increased but neither cooperativity length nor fluidity timescale changes the velocity and shear stress profiles in steady state. Residual shear stress pattern distribution is shown as color maps in Fig. 5.14. Here we see scattered remaining stress centers across the cavity mainly close to

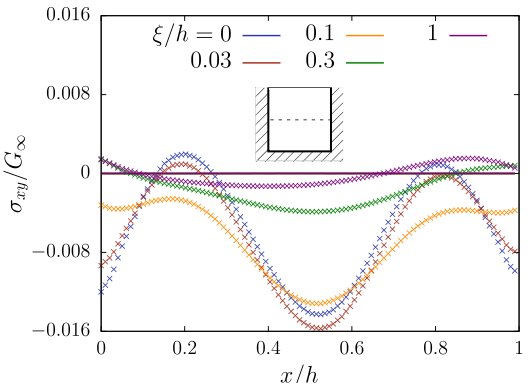


Figure 5.13: Shear stress x-profiles after flow cessation ($u_l = 1$) for $\tau_f/\tau_0 \in \{0.1, 10\}$ cross and lines respectively.

the walls. They seem to then fuse into bigger and elongated shaped areas when the cooperativity length increases. Increasing the cooperativity in the flow induces symmetry breaking along the x-axis in the remaining stresses after cessation.

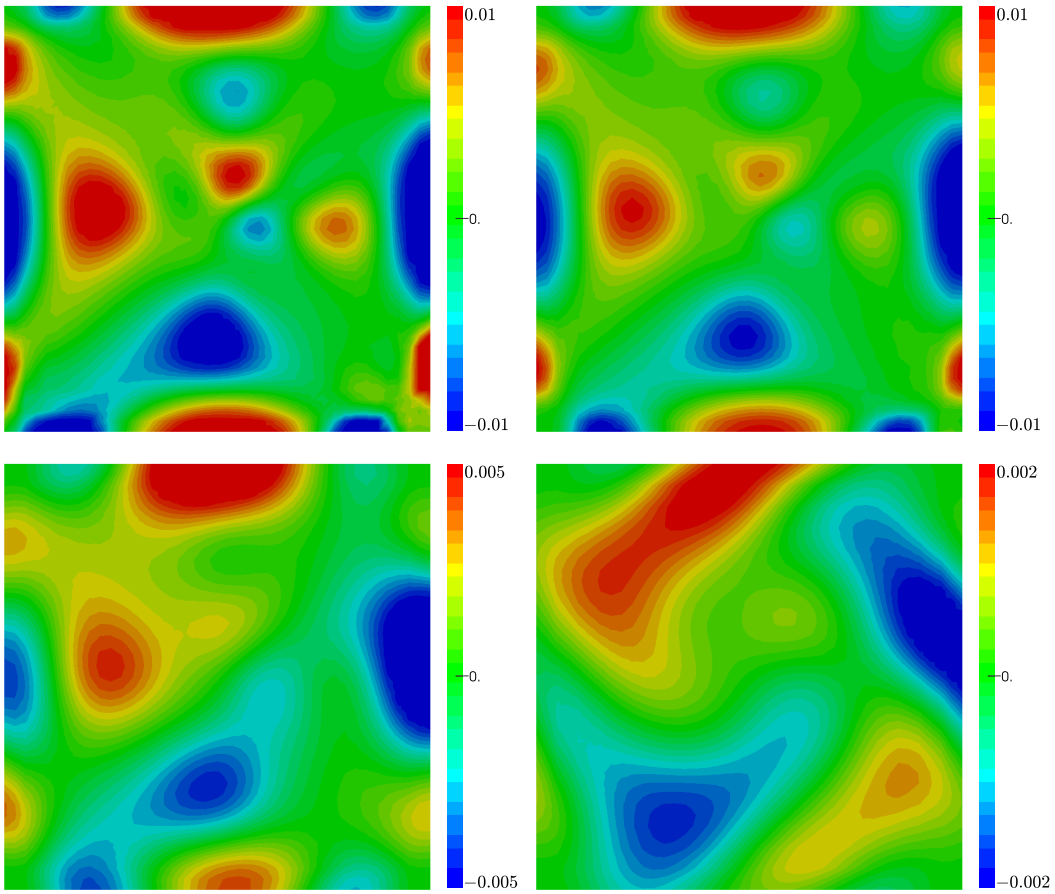


Figure 5.14: Residual shear stress after flow cessation ($u_l = 10$ and $\tau_f/\tau_0 = 0.1$) for: $\xi/h = 0$ (top left), 0.03 (top right), 0.1 (bottom left), and 0.3 (bottom right).

5.2.3 Mechanical Transient Effects

Previous sections demonstrated us qualitatively and quantitatively how residual stresses emerge from a non-equilibrium steady state after a previously imposed deformation is released. The fluidity model cannot only reproduce residual stresses found after flow cessation but its parameters can tailor their shape, magnitude, and distribution along the remaining system. It is important to point out that during start-up, for all lid-velocities, Reynolds numbers remained below 0.1 as it was previously shown in Fig. 5.4 to avoid turbulent effects.

An interesting feature to investigate is the mechanical response of a system with residual stresses present. Therefore, we measured how the shear modulus was affected by the presence of residual stresses by restarting the flow of a pre-stressed system. Different velocities were used as restarting driving force and, as before, the influence of cooperativity length was acknowledge for transient start-up stress behavior with deformation.

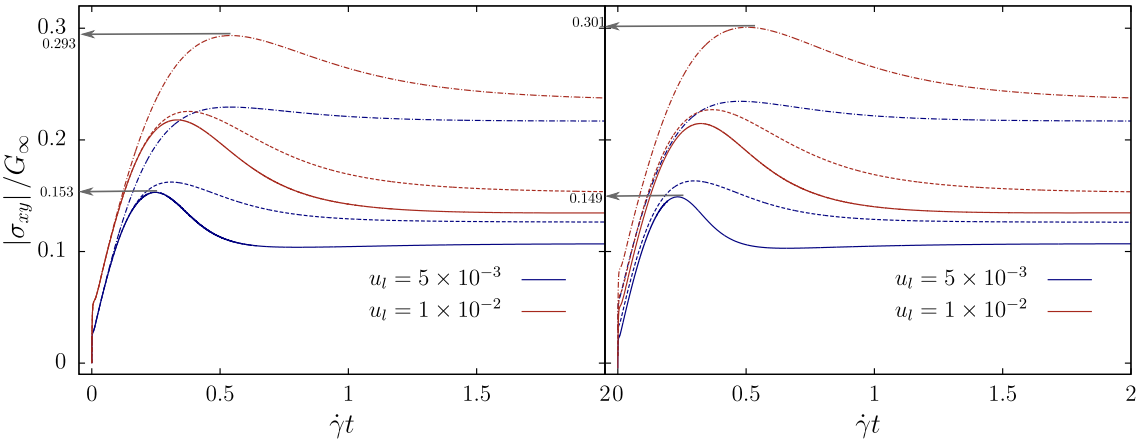


Figure 5.15: Transient shear stress versus deformation for different lid-velocities, for different $\xi/h = 0$ (—), $\xi/h = 0.03$ (- - -), and $\xi/h = 0$ (-·-·-). Right side shows behavior without residual stresses present and left side shows behavior with residual stresses present. Transients were measured at $y/h = 0.9$ using $\tau_f/\tau_0 = 0.1$.

Firstly, we show on the left side of Fig. 5.15 how varying the cooperativity length affected the start-up behavior of shear stress evolution with deformation close to the upper wall at the center of the channel (position $y/h = 0.9$). Here, the final shear stress is higher for bigger cooperativity length values, which is also seen in previous steady state profiles (Fig. 5.7). These start-up curves were obtained using noted lid-velocities with no stresses already present in the system but just different cooperativity length scales. We observe that stress overshoots values increase as the cooperativity length increases and also these overshoots happen at later deformations with ξ as well, they are shifted. After these systems go into flow cessation, residual

stresses remain as it was discussed earlier. Restarting the system again with residual stresses present either with same lid-velocity or different one, showed a similar transient stress tendency. Resulting transients are shown on the right side of same figure, where the same pre-stressed system was re-started with the same initial lid-velocity $u_l = 10^{-2}$ and a lower one as well $u_l = 5 \times 10^{-3}$. In this plot we also show again the startup curves obtained using different ξ, as noted. The overshoot value when flow is restarted changes slightly its value and position when there are stresses present in the flow by means of cooperativity length. In fact, for lower ξ we found these overshoots at slightly lower values than the original startup curve. However, this changes when ξ increases, since the overshoots reached higher shear stress values when residual stresses are present in the flow than when they are not. It is important to note, that from the start-up of the flow (at around $\gamma = 0.005$) there seems to be a slight change of slope. This corresponds to the Newtonian contribution to the deformation due to the sudden startup. Effective shear moduli were measured

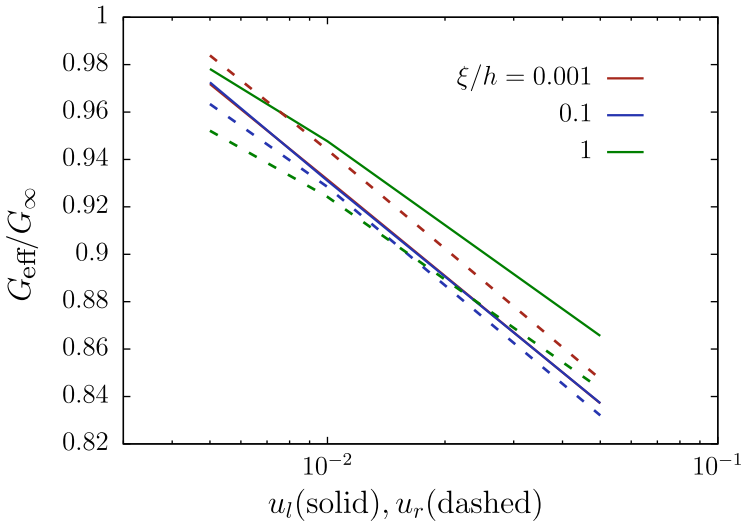


Figure 5.16: Shear moduli for different ξ and u_l starting with no residual stress present (solid lines), and with residual stress as initial condition (dashed lines). Residual stressed state was obtained with $u_l = 10^{-2}$.

after the Newtonian start-up for low deformation values as the slope of the stress versus deformation curve ($0.005 < \gamma < 0.1$). Combining previous results, we can display in Fig. 5.16 the shear moduli values obtained during start-up without and with residual stresses present. For the latter case they were induced by a lid-velocity of $u_l = 10^{-2}$ that was led into flow cessation, and then the system was re-started with different velocities. We found that for low ξ the presence of residual stresses produces an increase in the shear modulus of around 6% when smaller velocities were used to drive the system. For higher re-start velocities the shear modulus was sent to smaller values in presence of residual stresses. When the system had more

cooperativity along the flow, the shear modulus was lower when residual stresses were present as well.

5.3 Flow Through Abrupt 4:1 Contraction

Having studied flow through well-known geometries and resulting residual stresses after flow cessation, we now implement more complicated geometries thanks to the FVM package versatility. As it was introduced in section 2.4.2, abrupt 4:1 contraction is a geometry where curved streamlines are developed within the flow together with features like vortices. Factors like contraction ratio, Reynolds number, and flow nature influence directly the enhancement and presence of mentioned phenomena. We implemented the fluidity glass model for a flow going through this geometry, same way it was shown in section 3.3.3. A pressure step was setup as $\Delta p/L = G_\infty/h*$, where L is the total length of the channel and $h*$ is a characteristic width of the contraction channel ($h* = 5h$). This was done with the purpose of illustrating how

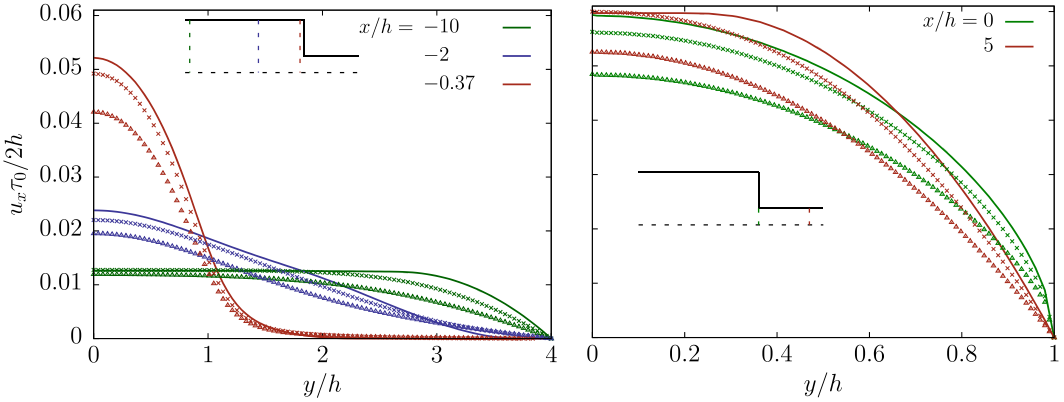


Figure 5.17: Velocity y-profiles upstream (left) and downstream (right) obtained using $\tau_f/\tau_0 = 0.1$. $\xi/4h = 0.001$ (solid lines), 0.01 ($\times$), 0.2 ($\triangle$).

model parameters affect first, the steady state behavior and second, the final shear stress state after flow cessation. In the latter, we examine persistent residual stresses from a profile point of view across main areas and general distribution along the geometry. Fig. 5.17 shows the effect of increasing the cooperativity length in the fluid on the steady state velocity profile shapes obtained upstream (left side) and downstream (right side). Differences are more pronounced upstream the channel since downstream the overall velocity is higher. Fluidization of velocity profiles was already introduced for 2D-planar channels (see section 3.3.3) which we explained as "softening" of profiles in steady state, i.e. smoothing the expected central plug expected for yield stress fluids by making profiles more parabolic-like as it would be expected for a Newtonian fluid.

Shear stress profiles are shown in Fig. 5.18, upstream (left side) and downstream the channel (right side). Cooperativity length again modifies the steady state profiles, mainly upstream close to the contraction area, by inducing higher shear stresses when ξ increases. Downstream the channel, shear stress undergoes same behavior where the most shifted profile is again by the contraction area (position $x/h = 0$) for higher ξ.

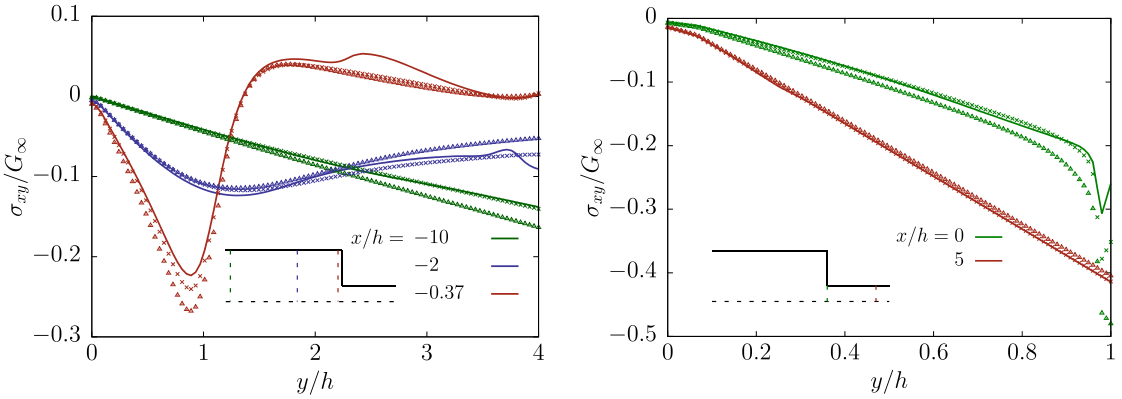


Figure 5.18: Shear stress y-profiles upstream (left) and downstream (right) obtained using $\tau_f/\tau_0 = 0.1$. $\xi/4h = 0.001$ (solid lines), 0.01 ($\times$), 0.2 ($\triangle$).

Vortex formation is linked to the cooperativity length to some extent since their size increases with ξ. Fig. 5.19 shows a comparison between the corner vortices and corresponding streamlines obtained in steady state, using $\tau_f/\tau_0 = 0.1$. We include the vortex obtained for a Newtonian flow case where viscosity is set equal to the zero-shear-rate viscosity in the fluidity model i.e. $\eta = 11\,\mathrm{Pa}\cdot\mathrm{s}$. It is evident how the fluidity spreads further across the domain since, as soon as ξ values increase, the vortex size increases mimicking the one obtained with a Newtonian flow, therefore the system is said to be fluidized. As a side note, the vortex size obtained using a pure Newtonian flow does not depend on the viscosity but on the pressure used at the inlet of the channel. Increasing the fluidity timescale did not produce a noticeable change in the vortex size and shape. Next, we will compare steady state and cessation of the flow profiles for different fluidity timescales where a dependence is found.

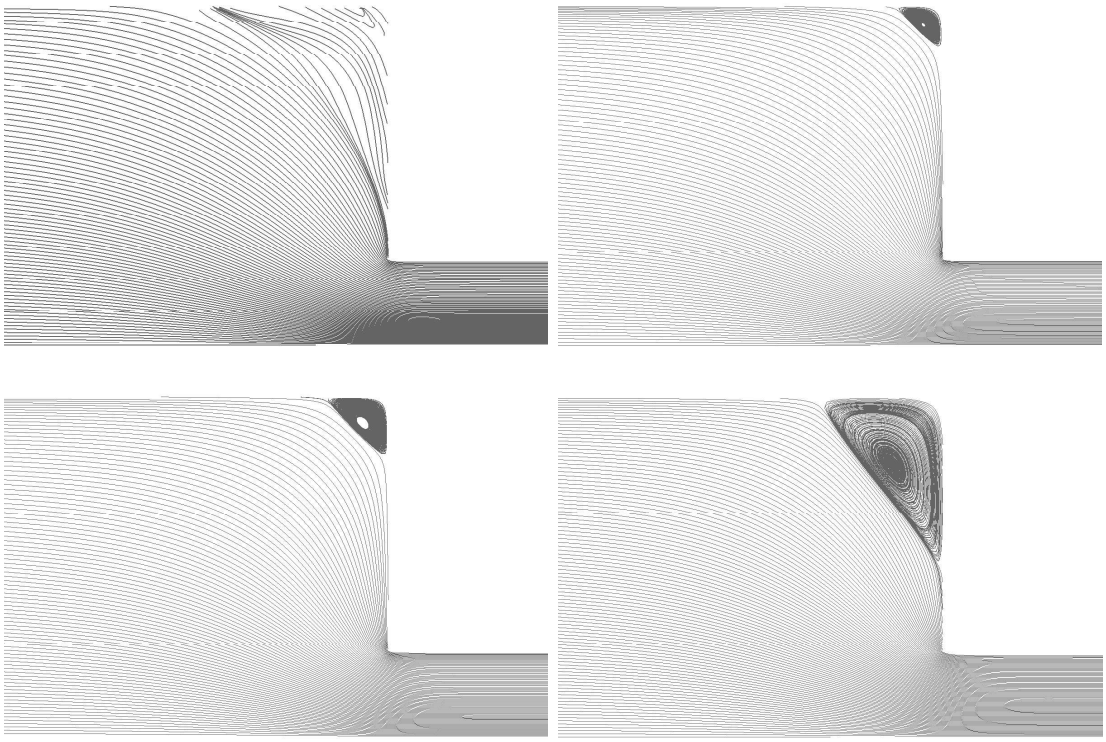


Figure 5.19: Steady state vortices found in abrupt 4:1 contraction flow using $\tau_f/\tau_0 = 0.1$ for $\xi/4h$: 0 (top left), 0.08 (top right), 0.2 (bottom left) and Newtonian case using $\eta = 11\,\mathrm{Pa}\cdot\mathrm{s}$ (bottom right).

5.3.1 Flow Cessation

Different ξ and τ_f have been studied and their effects on the shear stress were compared after the flow has stopped. Shear stress profiles become our interest since we find them persistent when the fluid is not flowing anymore. After the pressure is removed in steady state, velocity drops immediately to zero in the channel. Left side of Fig. 5.20 shows how, close and upstream the contraction, velocity decays to an undershoot with time which is bigger in the middle of the channel, and then relaxes to zero. We observe as well on the right side of same figure how shear stress relaxes, starting from corresponding steady state values across the channel, to constant values.

Moreover, color maps gave us an insight into the distribution of the stresses along the channel both in steady state and after flow cessation. Highest residual stresses are found close to the contraction area and next to the upper wall before approaching the upper corner, making those areas critical ones. Fig. 5.21 shows color maps comparisons for shear stress in steady state (left panel) and residual shear stress

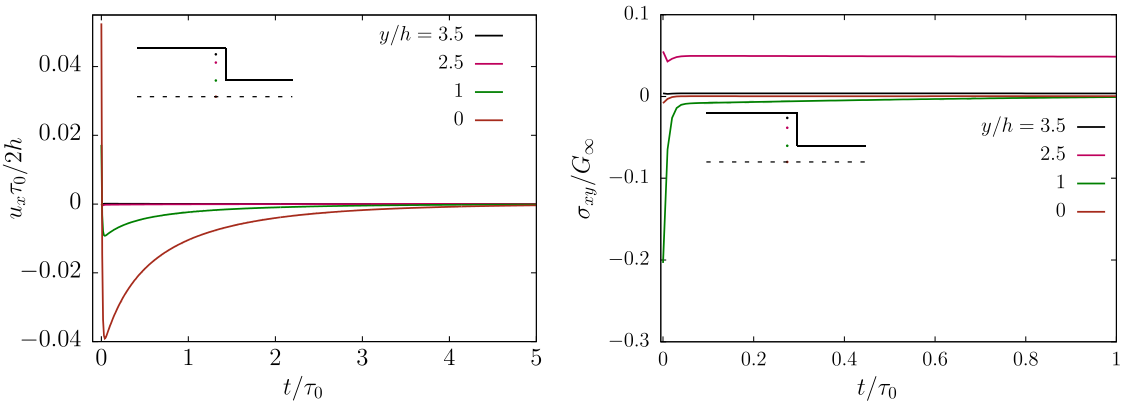


Figure 5.20: Transient velocity (left) and shear stress (right) at different positions of the channel before the contraction during cessation.

(right panel) found by increasing the cooperativity length from top to bottom.

Fluidity timescale was kept constant as $\tau_f/\tau_0 = 0.1$. Resulting color maps for $\tau_f/\tau_0 = 10$ are shown in Fig. A.6, where residual stresses are lower. We observe that close to the contraction area, stress relaxes and as if a higher stress front coming from upstream the channel stopped before reaching the contraction area. Close to the side-wall before the contraction, remaining stress show similar values and same sign for different ξ in flow cessation. However, downstream around and after the contraction we found opposite stress signs than in steady state. In lid-driven cavity and simple shear setup we did not observe this sign reversal of shear stress after flow cessation. This could be related to the velocity undershoot characteristic of pressure-driven flow during cessation where the velocity decays to negative values, i.e. it goes in the opposite flow direction, before relaxing to zero. In next section we will comment about this again since same behavior is found in pressure-driven flow through obstacles.

After having a brief idea about how non-vanishing shear stress looks like during flow cessation we can state the model parameters influence, τ_f and ξ, on the actual remaining shear stress profiles. As we analyze the profiles from far upstream the channel to areas close to the contraction, we find shear stress profiles spread more in the channel when a higher fluidity timescale and smaller cooperativity length are set in the system, which means that fluidization happens in a more localized way though it takes longer. Left panel of Fig. 5.22 illustrates this effect on the shear stress profiles in steady state upstream the channel before the contraction.

Near the contraction model parameters influence becomes relevant. However, by the contraction, as in position $x/h = -0.37$, differences become tighter. On the right panel of the same figure, shear stress profiles after flow cessation are shown where mostly an opposite tendency to what happened in steady state was found. As it is

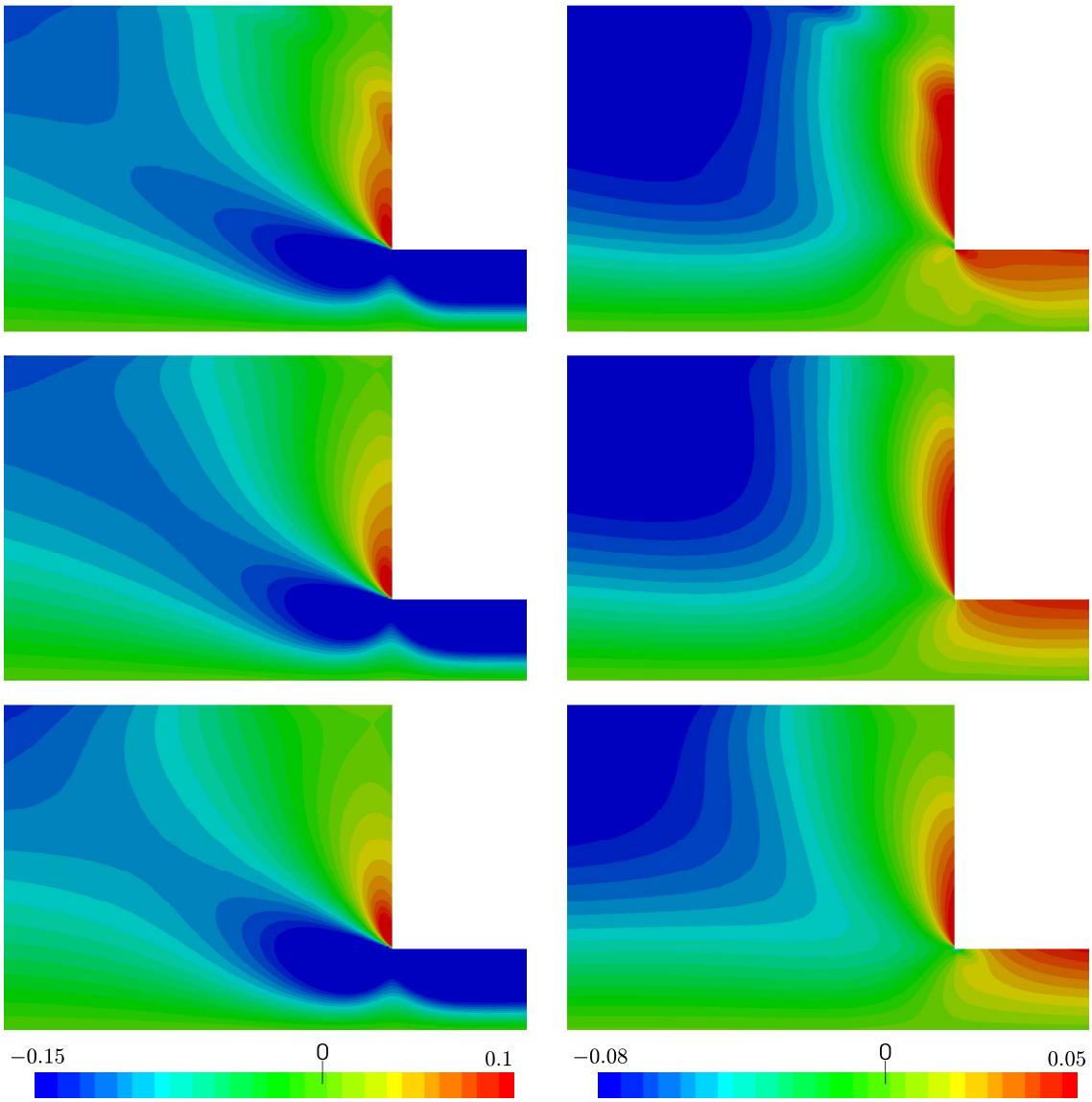


Figure 5.21: Shear stress color maps found in steady state (left panel) and after cessation of flow (right panel) for $\tau_f/\tau_0 = 0.1$ and cooperativity length $\xi/4h$ values from top to bottom of 0.001, 0.01 and 0.2.

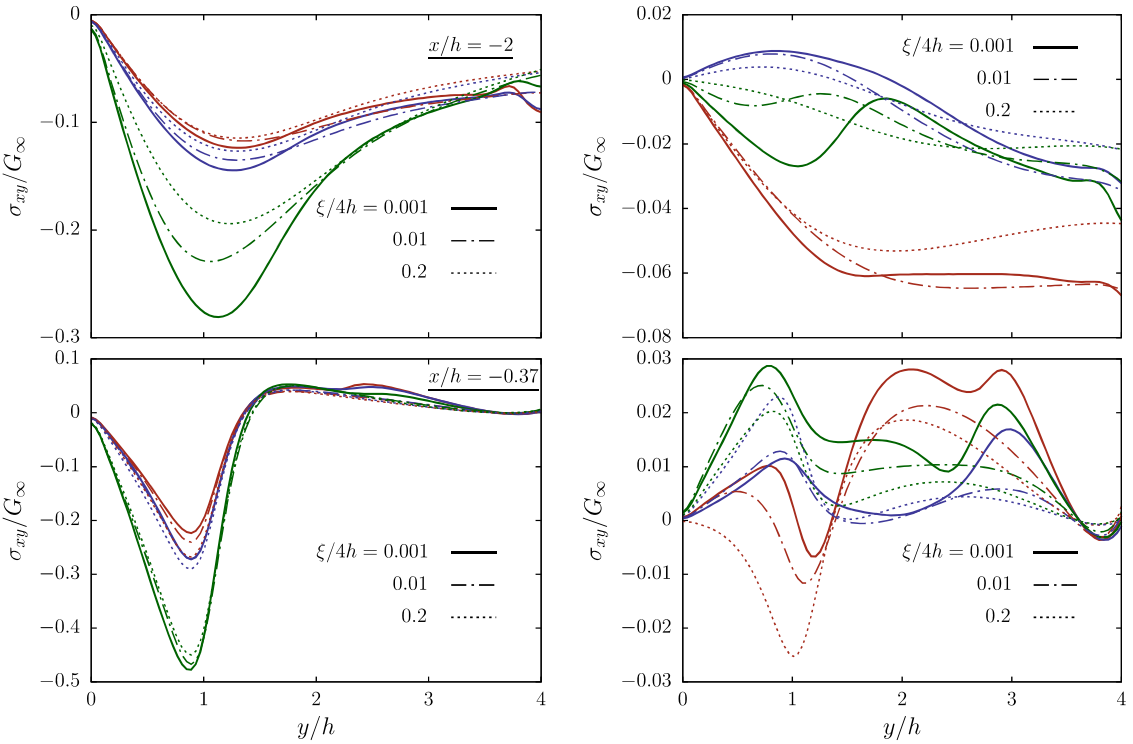


Figure 5.22: Upstream shear stress profiles found in steady state (left panel) and after flow cessation (right panel) for $\tau_f/\tau_0 = 0.1$ (red lines), $\tau_f/\tau_0 = 10$ (blue lines), and $\tau_f/\tau_0 = 100$ (green lines). Profiles from top to bottom measured at $x/h = -2$, -0.37 and indicated ξ values.

seen in the corresponding color maps lower fluidity timescale "freezes" the remaining shear stress that comes from the flow to a bigger extent. Higher cooperativity length spreads the stress further in the channel. Downstream the channel, as it is exhibited in Fig. 5.23, linearity of shear stress profile in steady state is perturbed just right after the contraction (position $x/h = 0.5$) by means of τ_f. However, it is recovered as soon as the profile is measured further downstream in steady state. In flow cessation (right panel), we show the already mentioned flipped signs, meaning that instead of negative shear stress profiles, positives arose. One more time, when τ_f is increased in flow cessation (e.g. green lines) shear stress across the channel tends to be smaller and closer to zero. This tendency is seen far upstream and downstream the channel where planar flow occurs, where no residual stresses should be expected by the symmetry of the channel. However, stresses still persisted in our setup probably due to the presence of the far contraction.

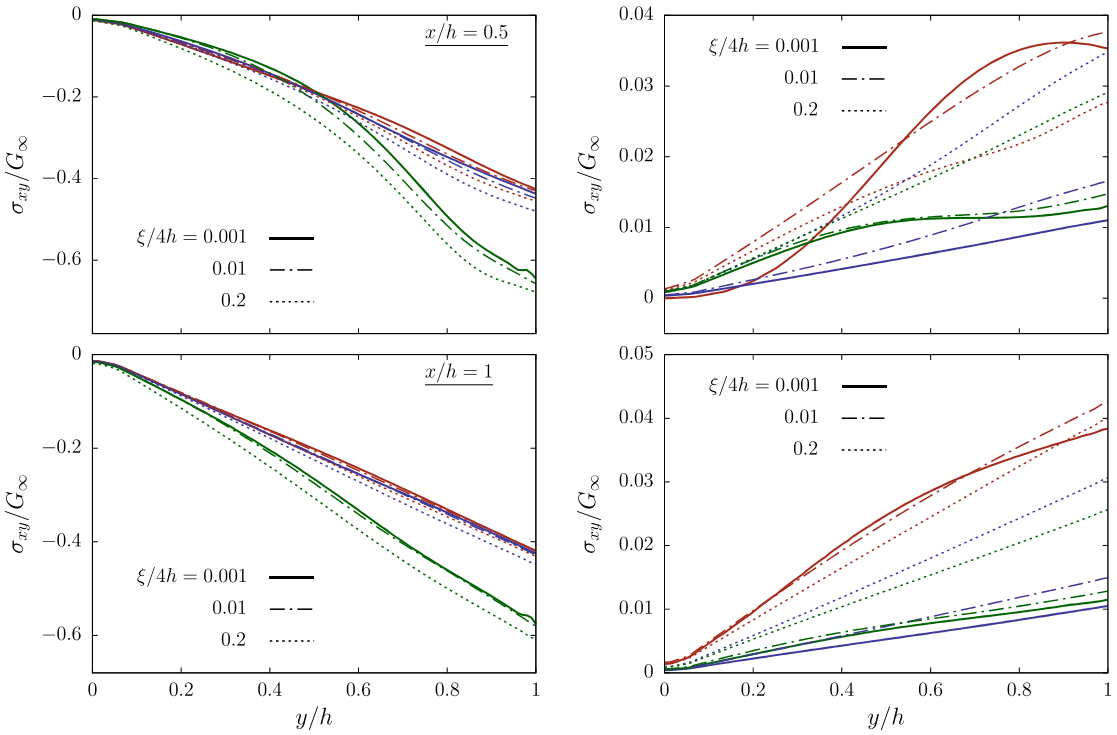


Figure 5.23: Downstream shear stress profiles found in steady state (left panel) and after flow cessation (right panel) for fluidity timescale variations as $\tau_f/\tau_0 = 0.1$ (red lines), $\tau_f/\tau_0 = 10$ (blue lines) and $\tau_f/\tau_0 = 100$ (green lines). Profiles from top to bottom measured at $x/h = 0.5$, 1 and $\xi/4h$ values indicated in figures.

5.4 Flow Through Obstacles

Disrupting the flow is certainly attractive regarding remaining residual stresses distribution. A planar flow that goes through an abrupt contraction already showed us different tendencies produced by model parameters and changes of flow direction. We modified this geometry by introducing obstacles on the walls which resembles a plate with dents. A schematic representation of the geometry is shown in Fig 5.24. A pressure step was applied at the inlet as $\Delta P/L = G_\infty/h^*$ (similarly to the contraction case), where h^* was probed to be slightly smaller than the width of the channel so the flow was completely developed.

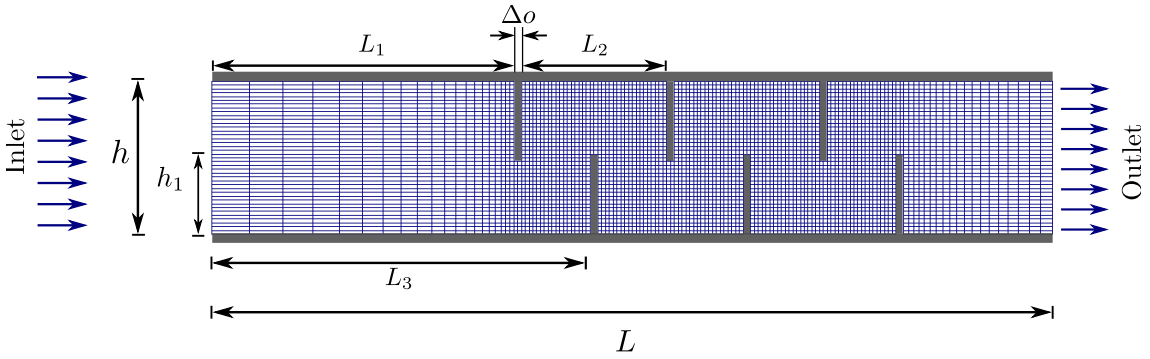


Figure 5.24: Mesh and design details used for the flow going through obstacles set-up. Details: $L = 5.5 \times 10^{-2}$ m, $L_1 = 1.975 \times 10^{-2}$ m, $L_2 = 9.5 \times 10^{-3}$ m, $L_3 = 2.475 \times 10^{-2}$ m, $\Delta o = 5 \times 10^{-4}$ m, $h = 1 \times 10^{-2}$ m, $h_1 = 5.25 \times 10^{-3}$ m. Pressure gradient was set as $\Delta p = 8.16$ Pa.

Including obstacles evidently changed the regular flow direction since curved streamlines in series are now present, as exemplified in Fig. 5.25, however, the Reynolds number was kept close to zero as it is shown at the bottom of same figure. It is important to note that the channel was not necessarily long enough before the obstacles for the stresses far upstream the channel to decay completely to zero in cessation. Residual stresses are not present, as mentioned already, in symmetric flow but rather remain when flow is not. In fact, the expected linear profile in a planar flow upstream the channel was not obtained in this particular geometry because the upstream length was not enough to allow planar flow to develop. We can observe in Fig. 5.26 the shear stress profiles obtained far upstream

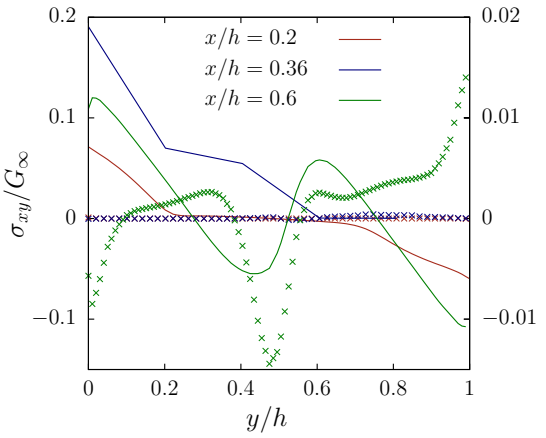


Figure 5.26: Shear stress y-profiles in steady state (left axis) and after cessation (right axis) at different x-positions upstream the channel.

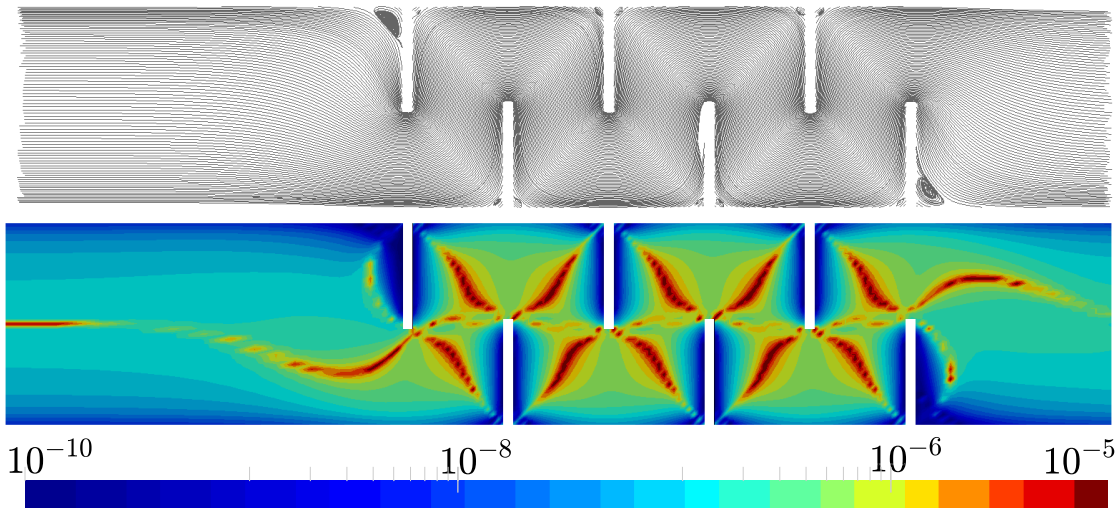


Figure 5.25: Streamlines of flow going through a planar channel with top/bottom obstacles. Bottom figure shows local Reynolds number distribution.

the channel before the obstacles ($x/h = 0.2$), and two other locations closer to the obstacles as well. Profiles show shear stress in steady state (lines, left axis) and the shear stress found after cessation (symbols, right axis). Far upstream, the stress profiles were already affected by the obstacles presence since the linearity is not fulfilled. However, in steady state same area show profiles with values close to zero as denoted by red and blue symbols. Like for the abrupt 4:1 contraction, model parameters, like cooperativity length and fluidity timescale, affect greatly the steady state behavior of stress along the geometry. When obstacles are present in the flow we found similar tendencies, and also high symmetry along the channel regarding stress distribution as shown in top part of Fig. 5.27. In this case, the cooperativity length was increased from top to bottom and a fast diffusion of the fluidity was enforced by setting a small $\tau_f/\tau_0 = 0.1$ (see corresponding Fig. A.7 for higher τ_f). Close to inlet and outlet shear stress seemed to decrease with ξ. After the flow ceased, stresses along the flow relaxed and decayed to finite values. The three bottom color maps shown in same figure show the resulting shear stress spreading along the geometry when there is no flow present. Colors are biased in order to show stress distribution more focused on the center of the geometry and close to the obstacles area. In general, we see according to the color scale, that values decreased greatly, nonetheless stress persisted.

There is however a loss of symmetry around the central obstacles, which is enhanced by lower ξ. Here we observe a more localized and edgy distribution of the stress around obstacles walls and between them. This localization decreased by increasing ξ, which implies more fluidization of the system as it is observed in bottom figures. Higher remaining stresses fill the areas in between obstacles and on their side walls

close to their top as well. Top and bottom corners in the obstacles area seemed to show higher overall stress. In this case, as in previous section, sign reversal is observed from the steady state configuration towards cessation of flow. This effect is shown in time in Fig. 5.28, where top two figures show velocity color maps in steady state (top) and right after cessation started (bottom) at $t/\tau_0 = 0.5$, before the complete decay to zero. In this case velocity decays in an undershoot where there is a sign-reversal and the fluid flows back. The corresponding shear stress behavior at earlier cessation times ($t/\tau_0 = 0$, 0.1, 0.5, 30) is shown in bottom four figures. Top of the four figures shows the shear stress at steady state, and last figure at flow cessation. Intermediate figures show decay of shear stress and almost immediate sign-reversal within the obstacles area. A loss of symmetry is also visible in same area where features repeat in series around obstacles but are not symmetrical distributed in between as they were in steady state.

Stress magnitude was also used to describe the remaining stresses by including the effect of normal stresses. Fig. 5.29 shows patterns obtained in steady state (top part of figure) and after flow cessation (bottom part of figure) for different ξ. In steady state, we can see an overall concentration of stress in the area between the first and last obstacle, along with the fact that the inlet and outlet show less stress concentration which still decreases with ξ. Symmetry is clearly seen in the steady state distribution as well. After flow cessation, as seen in the bottom three figures, we noted small symmetry breaking for small ξ regarding features between set of obstacles. Higher stress areas are found before and after the obstacles. In the area that is between the first and last obstacle, we observe high remaining stress around the tip of each obstacle and around the top and bottom corners. By increasing the cooperativity in the flow overall stress decreases along the geometry, especially close to the inlet and outlet. Asymmetry is induced in those areas as well and before and after each obstacle.

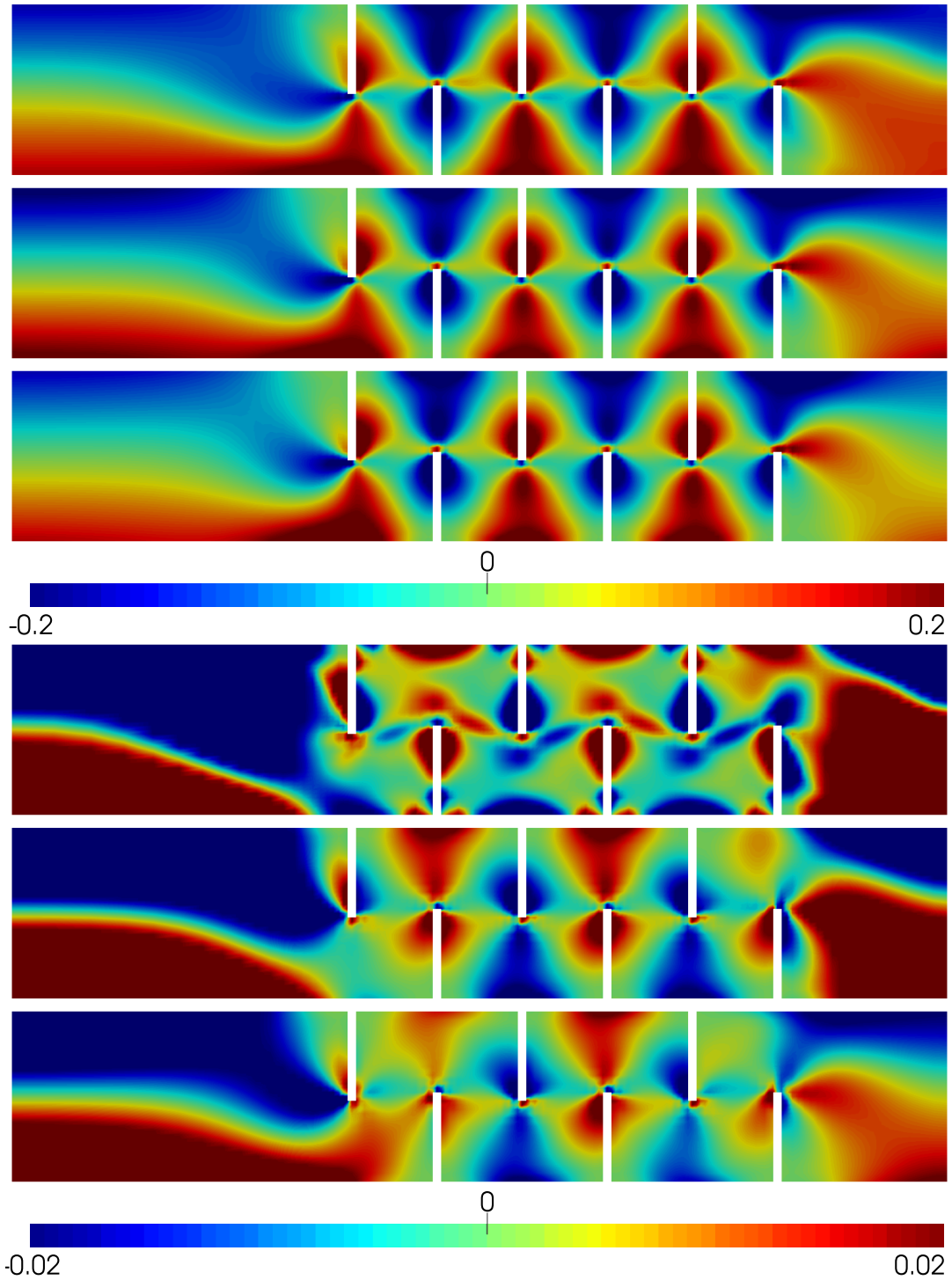


Figure 5.27: Top three figures: steady state shear stress color maps obtained using $\xi/h = 0$, 0.3, 1 from top to bottom and $\tau_f/\tau_0 = 0.1$. Bottom three figures: residual shear stress color maps obtained using $\xi/h = 0$, 0.3, 1 from top to bottom.

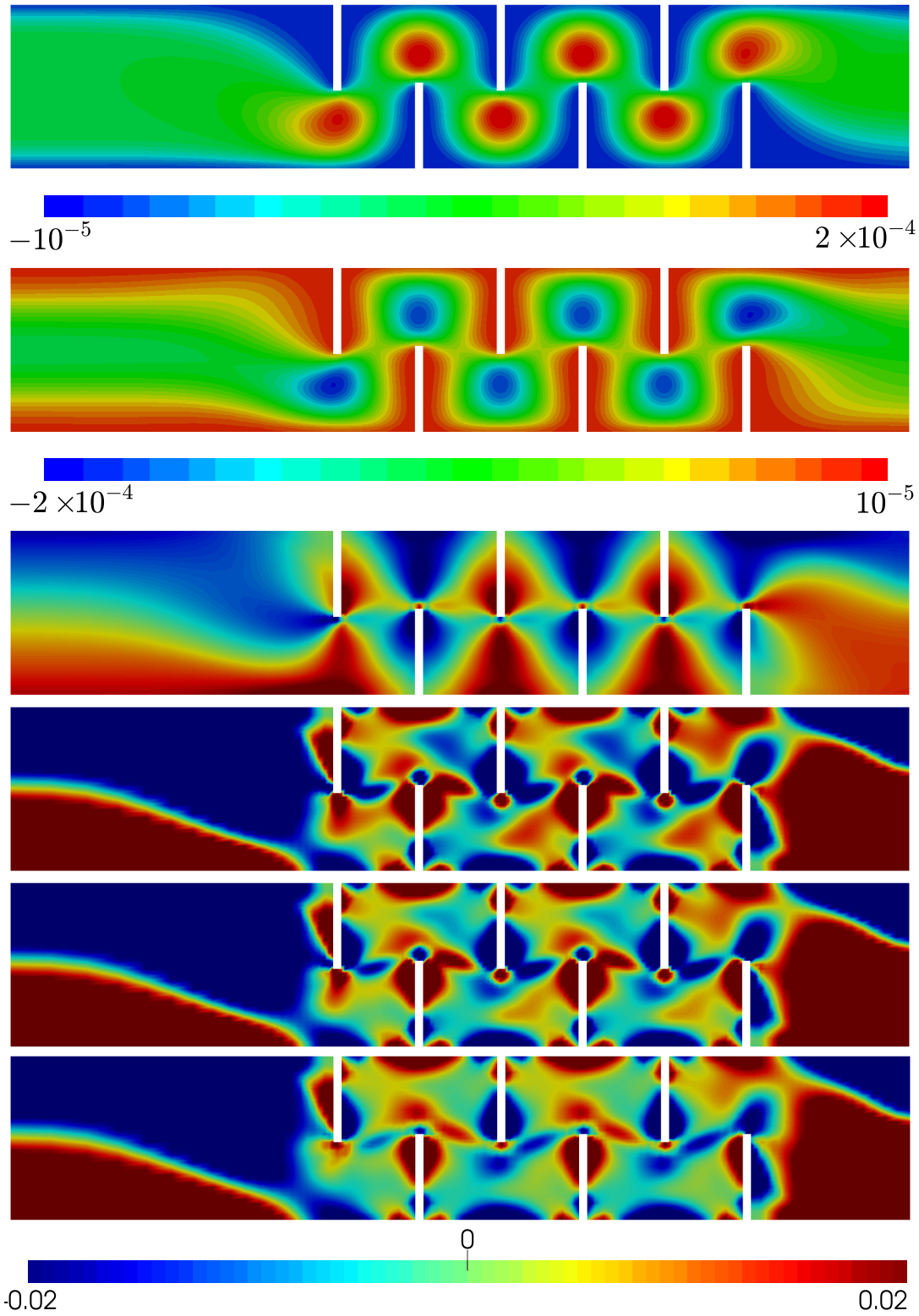


Figure 5.28: Top foremost: velocity in steady state using $\xi/h = 0$ and $\tau_f/\tau_0 = 0.1$, next velocity during cessation $t/\tau_0 = 0.5$. Bottom four figures: shear stress at steady state (top), next three: during flow cessation at $t/\tau_0 = 0.1$, 0.5, 30.

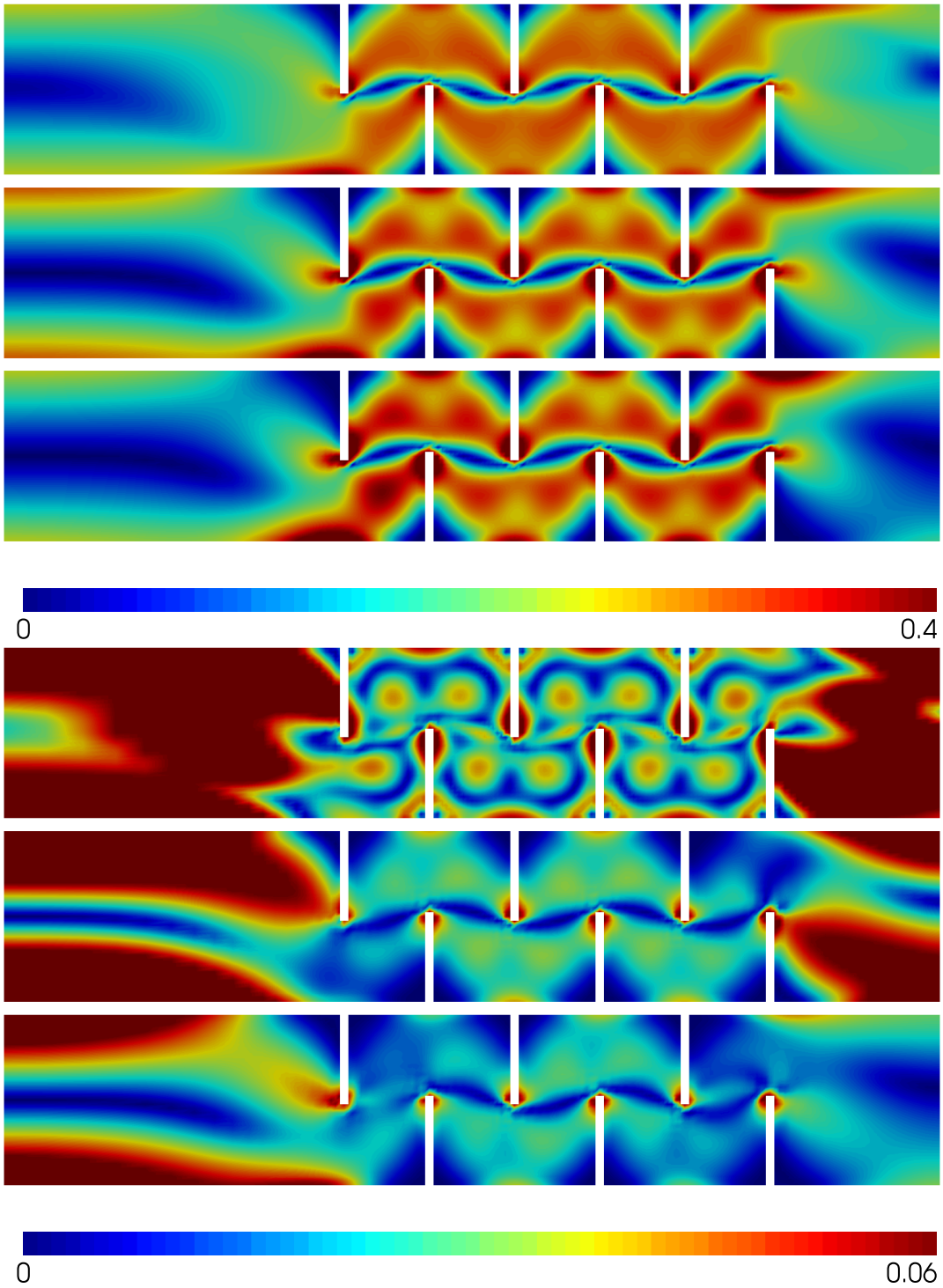


Figure 5.29: Top three figures: steady state stress magnitude color maps obtained using $\xi/h = 0$, 0.3, 1 from top to bottom and $\tau_f/\tau_0 = 0.1$. Bottom three figures: residual stress magnitude color maps obtained using $\xi/h = 0$, 0.3, 1 from top to bottom.

Chapter 6

Particles in Viscoelastic Fluids

Sedimentation of particles in liquids is a benchmark problem in rheology, where broad interest has been devoted to particles sedimentation in Newtonian systems [46]. In this case, the Stoke's law could sufficiently describe at low Reynolds number, or so-called "creeping flow", the dynamics of a system in which the drag forces are proportional to the particles and fluid properties by disregarding inertial effects [10]. This assessment could be modified by correction factors obtained mostly through experiments and/or system simplifications when Reynolds number increases [105]. However, as previously mentioned, we are interested in sedimentation of particles in a viscoelastic fluid that shows shear thinning and yield stress as key behavior.

We dedicate this chapter to study the sedimentation of a single and pair of particles in a non-Newtonian fluid, as an application of our fluidity model, and how particles interact in such fluid. This model has been already used to describe the rheology of non-Newtonian systems, either for infinite relaxation times (fluidity glass model) or for a viscoelastic fluid with finite relaxation times (fluidity Maxwell model). We used the latter to describe the fluid behavior inside a container when a particle or a couple of particles sediment by the action of gravity. Sedimentation of particles in non-Newtonian fluids has a broad range of applications at an industry level like describing filled polymer nanocomposites processing, use of polymer additives, sedimentation in mud, the pharmaceutical industry, among others [46, 106, 107].

When a particle, initially at rest, of radius r and density ρ_s starts sedimenting by the action of gravity in a fluid of density ρ and viscosity η, the Stokes' law results in a terminal velocity of $u_\infty = 2(\rho_s - \rho)gr^2/9\eta$ if inertial terms are neglected. As the particle moves in the fluid a drag force due to friction between particle and fluid will act in the opposite direction which is expressed as

$$F_D = 6\pi\eta r u_\infty \tag{6.1}$$

for Newtonian fluids with Reynolds number $\mathrm{Re} = 2ru_\infty\rho/\eta \leq 0.1$ (creeping flow). The total force exerted on the particle parallel to the gravity including gravitational acceleration will be $F = -F_D + (4/3)\pi r^3(\rho_s - \rho)g$ [10, 108].

Drag correction factors must be added to correct the drag force depending on the fluid properties and the shape of the object when the regime we study is not Stokesian. These coefficients are mostly obtained by mathematical derivations and experimental data. In fact, this law has been modified and expanded using diverse sedimentation experiments and analytical approximations considering different set-ups like particle shapes, drops, non-Newtonian fluids, high Reynolds numbers, wall effects, particle interactions, among others [109].

For an Oldroyd-B fluid with τ as relaxation time and zero-shear-rate viscosity defined as $\eta = \eta_p + \eta_s$: η_s solvent viscosity and η_p polymeric contribution to the viscosity, the drag coefficient can be expressed, for small Reynolds and Deborah number $\mathrm{Re} \ll \mathrm{De} \ll 1$ using $\mathrm{De} = \tau u_\infty/r$, as [10, 106]

$$X(\mathrm{C_D})_{\mathrm{th}} = \left[1 - \frac{1}{2275}\left(\frac{401}{11} - \frac{39\eta_s}{\eta}\right)\left(1 - \frac{\eta_s}{\eta}\right)\mathrm{De}^2\right]. \tag{6.2}$$

Multiple investigations have been done to declare tendencies expected when particles are sedimenting either in Newtonian or non-Newtonian fluids. These tendencies do not only depend on the fluid inherent properties but also on the particle or particles initial configuration, size, shape, distance separation, initial location, and wall effects of the container. Joseph et al. [110] have been one of the experimental pioneers in describing particle sedimentation in diverse initial positions using single, pair, or fluidized bed of spherical particles [111–113] and long bodies like cylinders in diverse fluids as well [114]. Interesting and plenty of reviews of ongoing investigations are available, however, we might suggest authors in reference [8] for punctual information. As a general statement we must say that inertia partly determines the orientation of particles sedimenting in either Newtonian or non-Newtonian fluids. Consequently, when inertial effects are smaller, viscoelasticity will dominate the system and particles will sediment with the broadside parallel to streamlines, but when inertia increases objects will accommodate perpendicular to flow lines.

Two spheres sedimenting on top of each other (see Fig. 6.10) in non-Newtonian fluids have shown a dependence on the initial critical separation since particles will attract and chain when the distance is below a critical value or repel for larger separations as shown experimentally by Riddle et al. [115]. However, the distance between sedimenting spheres has been a subject of debate, whereas it has been found by many others authors through theoretical analysis that no critical separation was necessary since aligned particles tend to attract and fall along with their line of centers [116]. Experiments performed by Bot et al. show attraction of particles

separated by large distances in Boger fluids but repulsion for smaller distances [117]. Recent experiments done by [118] have found a critical separation between spheres sedimenting in power-law fluids, where beyond, particles behave like isolated spheres. A negative wake has been considered as a possible reason for this repulsion which is an upstream-directed flow that appears behind the leading sphere that might push up the trailing sphere [8, 119]. This effect might be enhanced by the presence of normal stresses in the fluid since the particles encounter unbalanced compressive stresses at the bottom and top of the tandem which could even promote chaining. This has been shown in an Oldroyd-B fluid numerically by [120]. There is presumably a dependence on the viscoelastic characteristics of the fluid where particles sediment, since the experimental tendency still dictates mostly attraction during sedimentation like in more recent experiments performed by [121], and numerical analyses where particle-particle interactions are calculated in presence of a viscoelastic FENE-liquid, attraction was mostly the case between leading and trailing spherical particles sedimenting [122].

Shear thinning has been found to induce attraction in sedimenting spheres and even chaining. There is a dependence on how strong the shear thinning effect and memory associated with the fluid is present in the system. Therefore, it is thought that persisting corridors of lower viscosity are formed behind the leading sphere while sedimenting which might accelerate the following sphere. This has been seen experimentally with falling ball viscometer by [123] who could measure the drag velocities of falling spheres after time intervals. The latter determined how much the system had recovered after deformation by accelerating the following falling sphere when this one was dropped right after the first one, therefore, increasing the settling velocity. Mentioned velocity decreased if the second particle was dropped long after the first one sedimented. This phenomenon has also been found experimentally by [124] and numerically in shear thinning fluids by [125], where regions of sheared fluid with lower viscosity values (regions size was relaxation time-dependent) were found behind of the settling sphere for a highly viscous fluid. Drag, kissing, and chaining effect has been ultimately observed when two particles sediment on top of each other in non-Newtonian fluids. Drag happens when the trailing particle enters the wake of the leading one, kissing refers to the moment when particles touch, and chaining is said to be when the particles remain together while sedimenting. In the latter, they form a stable doublet whose centers are parallel to the streamlines and fall with gravity in the fluid. The mentioned low viscosity corridor formed behind the leading sphere can enhance this effect, therefore it is safe to say that shear thinning and memory of shear thinning play an important role in aggregation and chaining formation. However similar effects have also been found in constant viscosity fluids or when shear thinning effects are not so pronounced [8, 112]. It is also believed that the formation of aggregates and their subsequent stability is augmented by the streamlines formed around the particles doublet to avoid the gap between them. This

effect is enlarged by the normal stress differences from the fluid that push the particles together [8]. As a reference, in the case of two particles sedimenting in a Newtonian fluid, they show a phenomenon called drafting, kissing, and tumbling. In this case, as soon as particles start to sediment, dragging happens as well until particles touch (kiss) and tumble (separate), making their trajectory unpredictable until they reach the bottom of the container. This a well-known effect described experimentally in earlier times by [110]. The formed doublet, whose centers are parallel to the stream, is unstable in the streamline direction, therefore, they turn perpendicular to the stream to then tumble and get thrown apart: an unsymmetrical wake is formed when there is a misalignment of the centers which causes the destabilization.

Since a shear-dependent viscosity in the fluid is in our interest, the drag force should be adapted by introducing correction factors that include deformation rate dependence. Some models have been developed to assess settling of particles in shear thinning fluids, which are mostly based on numerical methods, experiments, and empirical relations, like for example the work done by Rodrigue et al. [126]. Besides the availability of drag models, we chose to use a fully resolved simulation method where the particle size and the fluid are in the same scale, therefore the interaction of particles and fluid is assessed. We used an open source package called CFDEM®coupling that can couple OpenFOAM for the computational fluid dynamics problem and a discrete element method (DEM) called LIGGGHTS that is able to track particles present in fluids. The coupling between CFD and DEM and corresponding parallelization was done by Hager et al. [127]. The power of the DEM lies in its ability to resolve the granular medium at the particle scale: particle geometry and particle motion. It needs small time step sizes because contact force has a stiff behavior (it must be around 10^{-6} s.)

6.1 Immersed Boundary Conditions

Conventionally, to study immersed bodies the approach entails a body-conformal structured or unstructured grid to define them in the fluid through a boundary condition on the solid where grid resolution could be adapted for complex geometries. The discretization of the governing equations can be done through finite-differences, finite-elements, or finite volume methods where coordinate transformations must be adapted to grid-alignment and therefore to geometries whose complexity depends on the shape and orientation of the body. This procedure can become cumbersome for flows with moving boundaries where a new grid must be generated with each time step. Navier-Stokes equations have to be solved to describe the fluid and Newton's equations to describe particle dynamics. The coupling between two scenarios has been assessed using diverse methodologies like for example lattice-Boltzmann methods [128], finite

element methods [129], and immersed boundary methods [130] where hydrodynamic forces at the boundary between both systems must be obtained [131].

We decided to study the interaction between a fluid and sedimenting particles using a fully resolved method. As mentioned before, fully resolved methods do resolve the interaction between particles and surrounding fluid, therefore, there is no need of using drag models. This methodology is in the category of fictitious domain methods where the use of a boundary condition between the particles and fluid gives rise to a force introduced in the momentum equations of the system. Immersed boundary (IB) method is based on a methodology initially developed to study flow patterns around heart valves, however, it has been extended and generalized to fluid-solid interactions. The fluid is solved in a Eulerian frame on a fixed mesh and the solid in a Lagrangian one that can move around the Cartesian mesh freely [132]. This method uses non-body conformal meshes since a mesh is generated initially disregarding the presence of the immersed solid. A boundary condition is introduced where the solid should be that will require the modification of the governing equations close to it. Diverse methods can be used to discretize mentioned equations, like finite volume method, without complicated coordinate transformations. Acknowledging the presence of a solid by imposing the immersed boundary condition can be done usually by continuous or direct forcing methods. The continuous approach is mainly used for biological systems where immersed elastic boundaries are present. A force term is added to the governing equations before discretization. In this case, using rigid bodies needs more assumptions since force terms become unstable. Hence, simplified models must be used to imitate solid boundaries behavior, which consequently is a trade-off with accuracy and stability. On the other hand, the direct forcing approach is done by introducing the boundary conditions in the already discretized equations, making the method depending on discretization schemes to satisfy the velocity boundary condition imposed in the immersed solid face [131, 133].

Shirgaonkar et al. [5] have developed an algorithm based on assumptions made by Patankar et al. [134] that could take into account body deformations of swimming organisms in a fluid and resolve the dynamics of the system using an immersed boundary method. This method could be used to simulate free-swimming organisms using a hydrodynamic approach that includes a body constraint formulation, therefore the flow field, body velocity, and forces acting on the body can be calculated. Generally speaking the presence of a particle in a fluid is seen as another fluid with a specific deformation rate tensor, that would be determined by the body characteristics, i.e. swimming organisms. However, if we are dealing with immersed solids they might be seen as a fluid with an infinite viscosity and compressibility, hence the deformation rate tensor for the stress field inside the solid must be zero which is added as a rigidity constraint. This constraint is introduced in the momentum equation formulation as a Lagrange multiplier, analogous to when pressure is used

in fluid momentum equations to assure incompressibility [135].

CFDEM®coupling has adapted mentioned algorithms and ideas [5,135] as a fictitious domain method to solve the interactions of solid particles with fluids. This methodology has been tested and validated in Newtonian fluids and reported by Hager et al. in [127] for different set-ups including sedimentation of spherical particles. They have validated a typical set-up of two settling particles aligned vertically and separated by a particle distance in a container filled with a Newtonian liquid that are released to fall by the action of gravity. They reproduced the drag, kissing, and tumble phenomenon. These calculations were done in comparison to similar algorithms used by Glowinski et al. [136].

We have adapted CFDEM®coupling code to perform similar experiments using non-Newtonian fluids that follow the fluidity Maxwell model and the Oldroyd-B model. Code implementation details are found in appendix A.2.4.

6.1.1 Governing Equations

The governing equations that include immersed boundary conditions must be defined for the fluid and the body. The total fluid and particle domain is defined as Ω where the fluid part is $\Omega_f = \Omega - \Omega_s$ and Ω_s is the body or particle domain. Boundaries are denoted as $\partial\Omega$ and $\partial\Omega_s$ for the whole domain and particle domain respectively. A schematic diagram of the particle in the fluid with corresponding notation is shown in Fig. 6.1 [7].

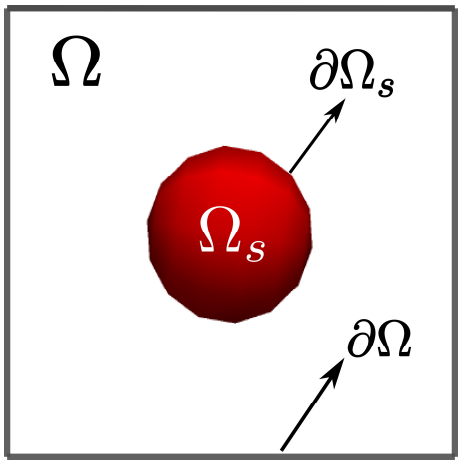


Figure 6.1: Schematic representation used to define immersed boundary conditions.

In the fluid domain the Navier-Stokes and continuity equations are defined as usual together with the immersed body equations [5, 7, 127]:

$$\rho\left(\frac{\partial \boldsymbol{u}}{\partial t} + \boldsymbol{u}\cdot\nabla\boldsymbol{u}\right) = -\nabla p + \nabla\cdot\boldsymbol{\sigma} \quad \text{in } \Omega_f, \tag{6.3}$$

$$\nabla\cdot\boldsymbol{u} = 0 \quad \text{in } \Omega_f. \tag{6.4}$$

As boundary condition on the domain we have

$$\boldsymbol{u} = \boldsymbol{u}_{\partial\Omega} \quad \text{on } \partial\Omega, \tag{6.5}$$

and initial conditions that must satisfy the continuity equation 6.4 would be

$$\boldsymbol{u}(\boldsymbol{x}, t = 0) = \boldsymbol{u}_0(\boldsymbol{x}) \quad \text{in } \Omega \;\; (t = 0). \tag{6.6}$$

At the interface of the solid and particle an unknown velocity $\boldsymbol{u}_i$ arises, which couples the fluid and solid phase as:

$$\boldsymbol{u} = \boldsymbol{u}_i, \tag{6.7}$$

$$\boldsymbol{\pi} \cdot \hat{\boldsymbol{n}} = \boldsymbol{t}_{\partial\Omega_s}. \tag{6.8}$$

This is one key for the method, where $\boldsymbol{t}_{\partial\Omega_s}$ is the traction vector of the fluid acting on the particle defined by $\hat{\boldsymbol{n}}$ as an outward unit vector on the particle surface. This is an interface condition that defines the stress between the fluid and solid. $\boldsymbol{\pi}$ enclosures hydrostatic pressure p, and the deviatoric stress tensor $\boldsymbol{\sigma}$ that we have previously defined as the sum of a Newtonian and non-Newtonian contribution, hence $\boldsymbol{\pi} = -p\mathbf{I} + \boldsymbol{\sigma}$.

The dynamics of the particles follow the equation of motion by accounting all forces acting on them like gravity, pressure and collisions:

$$m_p \frac{d\boldsymbol{u}_p}{dt} = m_p \boldsymbol{g} + f_{p,f} + \sum_{N_p} f_{p,p} + \sum_{N_w} f_{p,w}, \tag{6.9}$$

by defining m_p as particle mass, $\boldsymbol{u}_p$ particle velocity, gravity as $\boldsymbol{g}$, and interactions between particles and fluid, other particles, and walls are denoted as $f_{p,f}$, $f_{p,p}$, and $f_{p,w}$, respectively. As it was mentioned earlier, the tracking of particles is done using a discrete element method (DEM) that treats particles in a Lagrangian frame. Hence, each particle trajectory is solved since an observer follows an individual flow parcel (where particles are set) as it moves through time and space.

The particles occupy a parcel in the system that is treated as another fluid, but with a rigidity constraint defined by their deformation rate tensor, therefore the latter must be written as

$$\mathbf{D}(\boldsymbol{u} - \boldsymbol{u}_f) = 0 \quad \text{in } \Omega_s. \tag{6.10}$$

This equation corresponds to the deformation within the solid: $\boldsymbol{u}_f$ is the velocity field of the body in its reference frame and $\boldsymbol{u} = \boldsymbol{u}_r + \boldsymbol{u}_f$ where $\boldsymbol{u}_r$ is defined as the rigid body motion of the body. Hence, following [5] and [30] the constraint set by Eq. 6.10 is written as

$$\nabla \cdot \mathbf{D}(\boldsymbol{u} - \boldsymbol{u}_f) = 0 \quad \text{in } \Omega_s, \tag{6.11}$$

$$\mathbf{D}(\boldsymbol{u} - \boldsymbol{u}_f) \cdot \hat{\boldsymbol{n}} = 0 \quad \text{on } \partial\Omega_s. \tag{6.12}$$

To account for the particle's presence in the fluid these constraints give rise to a force term that will be non-zero in the particle domain and must be added to the momentum equation 6.3. This is ultimately written for the whole domain as

$$\rho \left(\frac{\partial \boldsymbol{u}}{\partial t} + \boldsymbol{u} \cdot \nabla \boldsymbol{u} \right) = -\nabla p + \nabla \cdot \boldsymbol{\sigma} + \boldsymbol{f} \quad \text{in } \Omega, \tag{6.13}$$

where the density will depend on where in the domain the flow is solved, here it is written as a combined density field.

The force integrated over the particle boundary is calculated using Eq. 6.8 as

$$\int_{\partial\Omega_s} \boldsymbol{\pi} \cdot \hat{\boldsymbol{n}} d\partial\Omega_s = \int_{\partial\Omega_s} \boldsymbol{t}_{\partial\Omega_s} d\partial\Omega_s. \tag{6.14}$$

Within the solid Ω_s the force becomes the divergence of the stress which is set by the pressure and the deviatoric stress tensor as

$$\int_{\Omega_s} \nabla \cdot \boldsymbol{\pi} d\Omega_s = \int_{\Omega_s} -\nabla p + \nabla \cdot \boldsymbol{\sigma} d\Omega_s = \int_{\partial\Omega_s} \boldsymbol{t}_{\partial\Omega_s} d\partial\Omega_s. \tag{6.15}$$

This means the force comes from the liquid as pressure and the deviatoric stress tensor. The force must be discretized within the mesh and the whole domain Ω with a specific number of control volumes "c" with volume of V_c, therefore the force between particles and fluid for a mesh decomposition T_c that covers cells where the solid is in Ω is written as

$$f_{p,f} = \sum_{c \in T_c} \left[-\nabla p + \nabla \cdot \boldsymbol{\sigma} \right] c V_c. \tag{6.16}$$

In summary, to implement immersed boundary conditions in a system where a solid is immersed in a fluid, we must bear in mind:

- Motion of body as sum of rigid body motion and deformation velocity,
- Rigidity constraint of rigid component of the solid velocity field gives rise to force field like incompressibility gives rise to force due to pressure.
- Grid regeneration is not needed since regular grids can also be used for irregular bodies. The solid part is tracked by a collection of Lagrangian particles, and fluid is discretized on a Eulerian grid.

6.1.2 CFDEM®Coupling Algorithm

The algorithm implementation that is used for CFDEM®coupling is based on Shirgaonkar et al. [5] called Fully Resolved Momentum Redistribution for self-propulsion algorithm. A detailed information of this procedure is found on mentioned paper and in Hager et al. CFD-DEM research [127]. Nonetheless, there are three basic steps used in this code that have been summarized by mentioned researchers to perform the IB algorithm we used:

1. The entire domain is regarded as a fluid, hence the momentum equations are solved for the entire domain with the CFD solver ignoring the immersed body. "viscoelasticFluidFoam" was previously introduced and used as solver where the viscoelastic model, fluidity Maxwell model, was chosen to describe the fluid. An intermediate velocity $\hat{\boldsymbol{u}}$ is calculated.

2. Since the solid presence is disregarded in the fluid, now the particle velocity supplied by DEM is introduced, therefore a velocity correction that results in a new velocity $\tilde{\boldsymbol{u}}$. The correction will be as if we add a force $\boldsymbol{f}$ in the Navier-Stokes equations to obtain the corrected velocity $\tilde{\boldsymbol{u}}$:

$$\rho \frac{\tilde{\boldsymbol{u}} - \hat{\boldsymbol{u}}}{\delta t} = \boldsymbol{f}. \tag{6.17}$$

3. The discontinuity in the velocity at the interface leads to non-zero divergence there. To remove the non-divergence of the corrected velocity $\tilde{\boldsymbol{u}}$ a scalar field ϕ is added (Eq. 6.18), which gives the mentioned additional mechanical force. This force $\boldsymbol{f}$ drives the strain rate of the velocity field from $\hat{\boldsymbol{u}}$ to $\boldsymbol{u}_f$.

$$\boldsymbol{u} = \tilde{\boldsymbol{u}} - \nabla\phi. \tag{6.18}$$

Hence the Poisson's equation for ϕ as the correction factor is

$$\nabla^2\phi = \nabla \cdot \tilde{\boldsymbol{u}}. \tag{6.19}$$

New velocity $\tilde{\boldsymbol{u}} = \boldsymbol{u} + \nabla\phi$ is used to define the force in Eq. 6.17, which can be rearranged in the momentum equation, turning the latter into Eq. 6.20 where the pressure is corrected by adding the extra term $\partial\phi/\partial t$:

$$\rho\frac{\partial \boldsymbol{u}}{\partial t} + \rho\left(\tilde{\boldsymbol{u}} \cdot \nabla\right)\tilde{\boldsymbol{u}} = -\left(\nabla p + \rho\frac{\partial \nabla\phi}{\partial t}\right) + \nabla \cdot \boldsymbol{\sigma} + \boldsymbol{f}. \tag{6.20}$$

Notes on the second and third steps: in the second step, since $\hat{\boldsymbol{u}}$ is not the velocity inside of the body (terms like deforming motion $\boldsymbol{u}_f$ is not yet imposed and rigid component $\boldsymbol{u}_r$ must be calculated), the velocity $\hat{\boldsymbol{u}}$ must be corrected by adding a force (Eq. 6.17) in the semidiscrete Navier-Stokes equations to obtain the corrected velocity: constraint force. Note that $\hat{\boldsymbol{u}}$ is divergence-free, hence $\nabla \cdot \boldsymbol{u}_b$ is zero in the solid. The non-divergence is removed by adding $\nabla\phi$ (Eq. 6.18), which gives the additional mechanical force explained earlier. This force $\boldsymbol{f}$ drives the strain rate of the velocity field to $\hat{\boldsymbol{u}}$ to $\boldsymbol{u}_f$.

Non-divergence velocity correction: correction step changes the velocity gradient tensor field inside the solid to target the velocity gradient tensor. The latter is a linear superposition of the gradient of deformation velocity $\boldsymbol{u}_f$ and rigid body motion with zero strain rate and rotation gradient of $\boldsymbol{u}_r$. This process is felt by the fluid as velocity discontinuities at the interface (divergence-free at the interface).

6.2 Particle Sedimentation

6.2.1 Oldroyd-B Fluid

We begin this section by showing the resulting sedimentation behavior of one spherical particle in a fluid that follows the Oldroyd-B model. Let us remember briefly that the stress tensor defined by this model is the sum of a Newtonian and non-Newtonian (solvent) contribution. The non-Newtonian (or so-called polymeric) contribution follows:

$$\tau\overset{\nabla}{\boldsymbol{\sigma}}_p + \boldsymbol{\sigma}_p = \eta_p\mathbf{D}. \tag{6.21}$$

The total stress adds up both contributions as $\boldsymbol{\sigma} = \boldsymbol{\sigma}_s + \boldsymbol{\sigma}_p$, making the viscosity follow the same sum as $\eta = \eta_s + \eta_p$. The Newtonian stress follows the Newton's

law as $\boldsymbol{\sigma}_s = \eta_s \mathbf{D}$. We validated the solver by calculating the correction factor suggested by [10, 106] and the drag force and settling velocity, for small Reynolds and Deborah number $\mathrm{Re} \ll \mathrm{De} \ll 1$. We used a set-up similar to the one suggested by [127, 136] where a container of domain $\Omega = (0, 3) \times (0, 3) \times (0, 6)$ was filled with a viscoelastic fluid with viscosity $\eta_p = 0.75\,\mathrm{g cm^{-1} s^{-1}}$ and $\eta_s = 0.5\,\mathrm{g cm^{-1} s^{-1}}$ and density $\rho = 1\,\mathrm{g\,cm^{-3}}$. The relaxation time was varied as $\tau = 0.01\,\mathrm{s},\ 0.05\,\mathrm{s},\ 0.1\,\mathrm{s}$ to increase the Deborah number. However, for these three cases both Reynolds and Deborah number remained below 1. A spherical particle of diameter $d = 0.167\,\mathrm{cm}$ and density $\rho_s = 1.5\,\mathrm{g\,cm^{-3}}$ whose center was located in the domain centerline {1.5,1.5,5.25} at time $t = 0$ was released with velocity zero and sedimented under the action of gravity $\vec{g} = (0, 0, -981)\,\mathrm{g\,cm\,s^{-2}}$. The blockage ratio, distance between walls to sphere diameter, was therefore 18, substantially bigger than suggested by mentioned authors, since we wanted to reduce any wall effect. We compared the drag

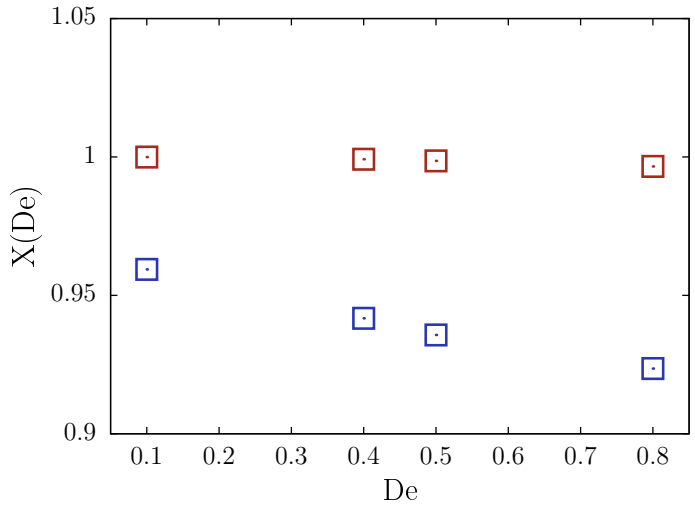


Figure 6.2: Drag correction factor obtained using CFD-DEM (blue) compared to the expansion by Bird et al. (red) [10].

correction factors measured with CFD-DEM calculations to the suggested values using Eq. 6.2 suggested by Bird et al. [10]. Resulting comparison in shown in Fig. 6.2 by displaying correction factors obtained using mentioned equation and the values obtained directly from the viscous forces exerted by the fluid on the particle using the CFDEM code. The latter was calculated as the ratio between gravitational force and the Stokes' drag force for a Newtonian fluid with same viscosity and same settling velocity (see Eq. 6.1). The coupling between CFD and DEM, where particle information is transferred between Lagrangian and Eulerian solvers, creates a small oscillation in the velocity of around 0.01%, which is used and noted to calculate the drag correction factor during settling. Differences between Bird et al. suggested values and our calculations were of around 4%. A mesh compromise was also made to reduce computational cost though representative values are still obtained, since

the settling velocity depends on mesh resolution and time step as well. The latter is related to relaxation time: smaller time step is needed for higher relaxation time since the particle spends more time in each cell therefore better time resolution must be used.

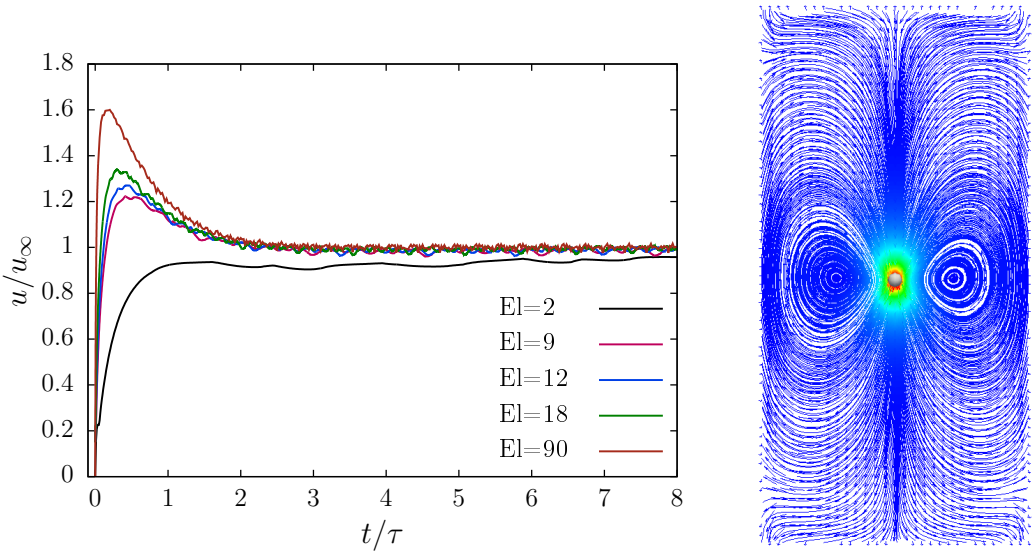


Figure 6.3: Settling velocities for different Elasticity numbers for a sphere sedimenting with gravity in an Oldroyd-B fluid. On the right side streamlines produced by a particle sedimenting in a Newtonian fluid with same zero-shear-rate viscosity.

Elasticity can be defined as the ratio of the Deborah number and Reynolds number, i.e. $\mathrm{El} \equiv \tau\eta/r^2\rho$. When the De number increases, particles will sediment faster reducing the elastic contribution to the drag, therefore the latter is brought by the solvent [106]. Elasticity number is responsible for the initial velocity undershoot found when a particle is sedimenting in viscoelastic fluids: lower Elasticity will induce smaller or no velocity overshoots. Fig. 6.3 shows overshoot effects observed for different Elasticity values when a spherical particle is sedimenting in an Oldroyd-B fluid. Mentioned overshoots seemed to increase with El because more damping and viscous effects are present in the fluid which can translate into velocity oscillations [107]. In fact, it must be said that overshoots are a purely viscoelastic effect which is enhanced by higher El values since the fluid needs to be deformed enough before the elastic effects take over. This means that when the sedimentation starts, at short times, the sphere is seemly falling freely in a fluid with only solvent (Newtonian) viscosity contribution [137]. Becker et al. [137] state that this free fall happens at $\rho r^2/\eta \ll t \ll \tau$ which in our case coincides with the found times for velocity overshoot. They suggest as well that velocity overshoots for high Elasticity values could be estimated as $u/u_\infty \approx \eta/\eta_s \approx 1.69$ which in our case we obtained $u/u_\infty \approx 1.61$ though our set-up was $\eta/\eta_s = 2.5$. Relaxation time increases the elasticity of the fluid which is directly proportional to Deborah number and time resolution, hence a small time

step is needed for higher relaxation times and for higher Elasticity values. Goyal et al. found a linear relationship between the overshoot peaks' time t_p and the Elasticity number for a settling sphere in a viscoelastic fluid (FENE-CR). FENE-CR model is a constant viscosity model like Oldroyd-B model, though the latter's applicability is limited since it allows an infinite extension. However, we got a linear relation of $t_p/\tau \approx 1.2/\sqrt{\text{El}}$ using the Oldroyd-B model to describe the fluid flow.

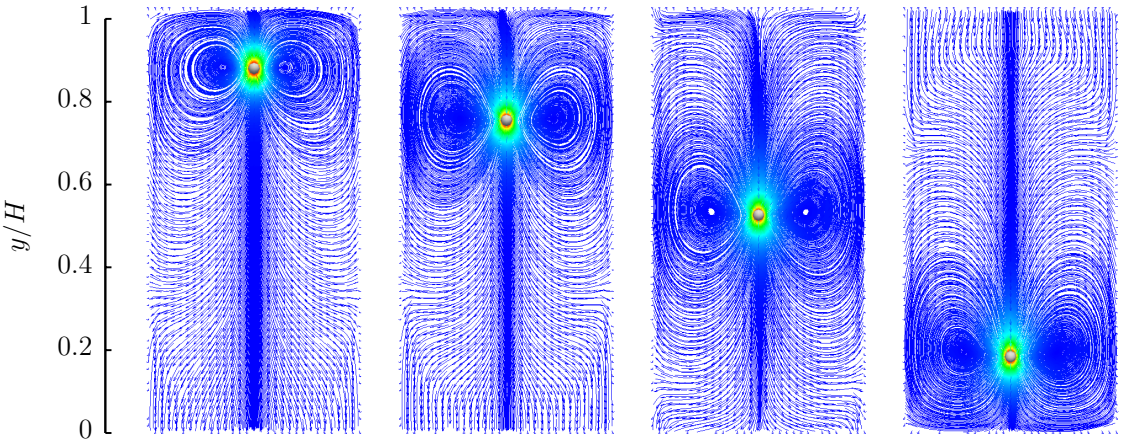


Figure 6.4: Snapshots of colormaps and streamlines found during settling for El = 90 at times $t/\tau = 0.16$ (overshoot), $t/\tau = 2$, 6, 12 of a particle sedimenting in an Oldroyd-B fluid ($\tau = 0.5$). Lines are colored by velocity magnitude: red is for high and blue for low values.

Streamlines gave us useful information regarding how symmetry fore-and-aft the particle in the flow is during sedimentation. Fig. 6.4 shows a series streamlines in time, starting at the overshoot time $t/\tau = 0.2$, for the case of highest El = 90. Particle is denoted by grey color. At the time of the overshoot, asymmetric streamlines are observed before and after the particle which could be induced by the wall presence. Goyal et al. [107] plotted similar streamlines for the viscoelastic fluid they studied and found what they called a "rather stronger asymmetry" at this point of the sedimentation. In their case, the wall effect was stronger on the fluid since their blockage ratio was 4 and in our case 18. Moreover, the top wall is fairly close to the particle location at that point. They also found secondary vortices close to the top wall that might be related to their higher Reynolds number (0.36), which in our case was around 0.08. As we move in time, we observe how the flow is affected by the presence of the particle since the streamlines move along the sedimentation with the particle and even further downstream the particle position as well. The streamlines surrounding the particle during the sedimentation had a fairly constant size. When the particle got close to the bottom wall, the fluid upstream the container seemed to be still affected since there is disrupting of the symmetry along the transverse axis.

6.2.2 Shear Thinning Fluid

We move on now in this section to explain what we have encountered by using the fluidity Maxwell model to describe the flow when a particle is sedimenting in a container with same dimensions as the one used previously. In this case, we increased the relaxation time and viscosities to induce higher shear thinning effects. As it was explained along this thesis the fluidity Maxwell model had a Newtonian and non-Newtonian contribution to the viscosity, which we set in this case to $\eta_p = 2\,\mathrm{gcm^{-1}s^{-1}}$ and $\eta_s = 1\,\mathrm{gcm^{-1}s^{-1}}$ and density $\rho = 1\,\mathrm{g\,cm^{-3}}$. Relaxation time was set to $\tau = 2\,\mathrm{s}$. A spherical particle of diameter $d = 0.167\,\mathrm{cm}$ and density of $\rho = 1.5\,\mathrm{g\,cm^{-3}}$ was released from position $\{0.5,0.5,5.25\}$ at time $t = 0$ with zero velocity. Fluidity Maxwell model parameters as cooperativity length ξ and fluidity relaxation time τ_f were varied. This had an effect on transient velocity behavior and settling velocity as it is plotted in Fig. 6.5.

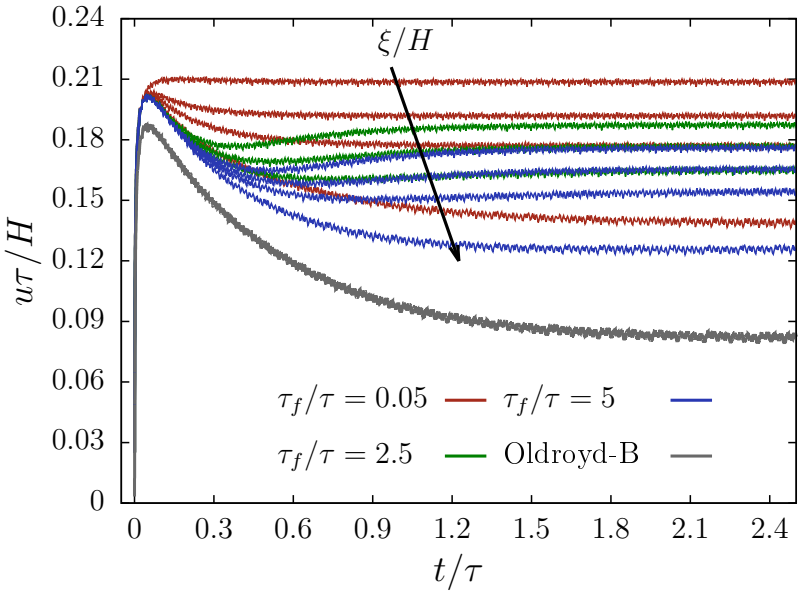


Figure 6.5: Sedimentation transient velocities of one particle in a shear thinning fluid for different τ_f/τ_0 and ξ/H (latter increases with arrow). Sedimenting velocity in Oldroyd-B fluid (grey line).

First, we notice small oscillations in velocity with time that are mostly due to the coupling between the Lagrangian and Eulerian solver. We found overshoots at the approximately same times (at $t/\tau \approx 0.04$) since the Elasticity number is constant for all cases. A settling particle will slow down its velocity when longer time is needed for the fluidity to spread along the neighboring cells, therefore smaller τ_f/τ values speed up the particle and reduce and/or neglect the undershoot found for higher τ_f/τ values. In the same plot, we see distinct lines with the same color, which identify the cooperativity length used. This increases from top to bottom as $\xi/H = 0$, 0.05, 0.08, 0.2.

The uppermost lines for each set of τ_f is set as $\xi/H = 0$. This produced the fastest sedimentation velocity. We included the transient particle sedimentation velocity in an Oldroyd-B fluid as reference which shows a significantly lower sedimentation velocity. In this case, same overshoot time is obtained since the Elasticity number used is the same, but after that, the velocity just decays until the settling is reached. Fluidity profiles along the centerline z-axis of the container are illustrated in Fig. 6.6 at settling time $t/\tau = 2.5$ for similar parameters variation. Smaller ξ will make the process highly localized around the particle which increases the settling velocity and fluidity values around the particle. Increasing ξ in the fluid (indicated by arrow) makes the fluidization process less localized and produces a more spread out and flatter fluidity profiles in the areas surrounding the particle. A wake is formed behind the particle that is enhanced by the fluidity timescale, as denoted by blue lines. Here the profiles become flatter when ξ/H is higher. In fact, the fluidity timescale modifies dramatically the fluidized area shape around the particle while sedimentation occurs. The whole effect along the container can be visualized in more detail in color maps shown in Fig. 6.7 obtained at sedimentation time $t/\tau = 2.5$. An increase of cooperativity length is done from left to right, where the fluidized area surrounding the particle increases with ξ/H. Top figures are obtained using a fluidity timescale $\tau_f/\tau = 0.05$ hence the fluidization is higher at that point in time. If we increase this timescale to $\tau_f/\tau = 5$, as pictured in bottom figures, we notice first a general decrease in fluidity values, but also how wakes enlarge further behind as a trail with the cooperativity in the fluid, spreading and opening more behind the particle for bigger ξ/H values. It is also noted, the fluidity timescale effect, not only in slowing down the sedimentation but we see how areas around the particle are not fluidized enough to let it pass faster.

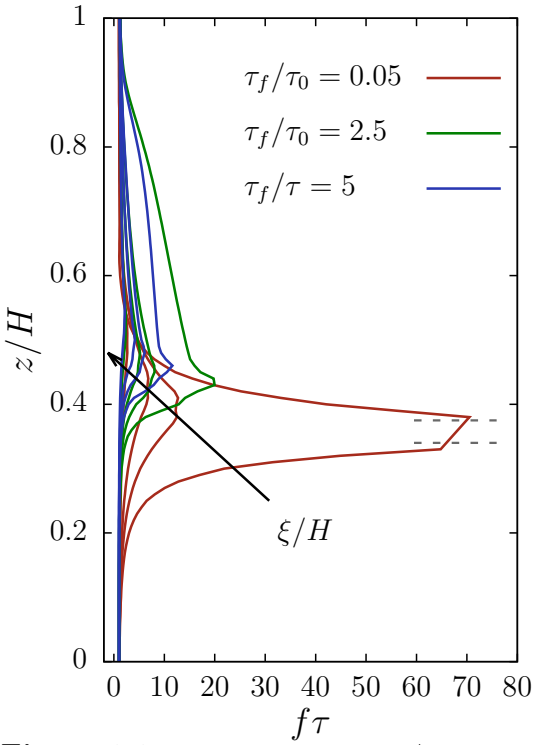


Figure 6.6: Fluidity profiles at $t/\tau = 2.5$ for $\tau_f/\tau = \{0.5, 5\}$ and $\xi/H = \{0, 0.02, 0.05, 0.2\}$ (increasing with arrow).

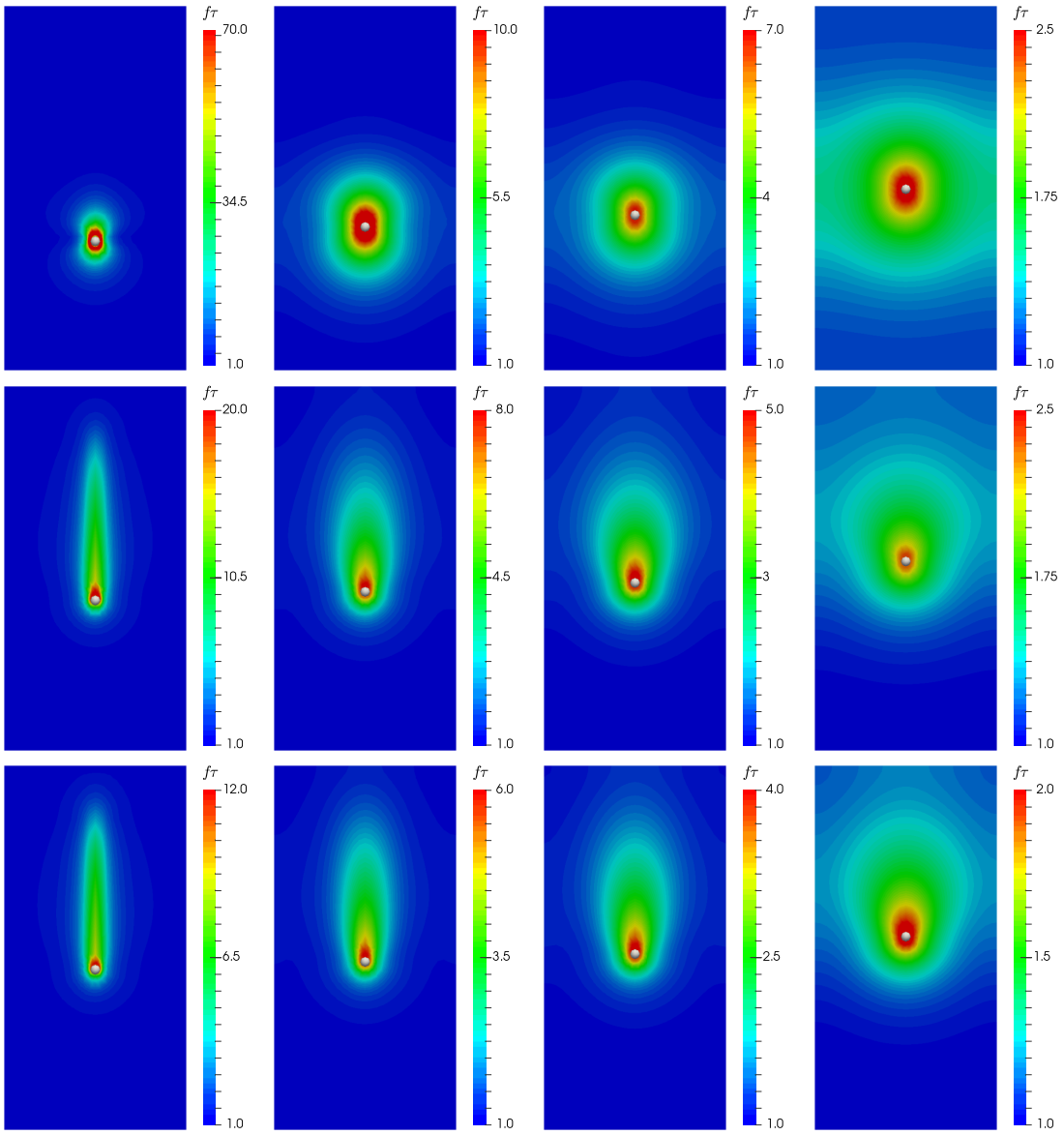


Figure 6.7: Fluidity color maps at sedimentation time $t/\tau = 2.5$ for $\xi/H = 0, 0.05, 0.08, 0.2$ (left to right). Top row corresponds to $\tau_f/\tau = 0.05$, second row to $\tau_f/\tau = 2.5$, and bottom row to $\tau_f/\tau = 5$.

Model parameters change as well the flow lines arrangement along the fluid while sedimentation occurs. A series of snapshots of streamlines at sedimenting time $t/\tau = 2.5$ is displayed in Fig. 6.8 for different τ_f and ξ. At this point, where the particle is fairly close to the middle of the container, an increase in the cooperativity length (in figure from left to right) seems to increase the size of revolving flow area around the particle for the studied values of τ_f/τ. When $\xi/H = 0$ is used, the resulting streamlines do not differ greatly when τ_f/τ increases, which contrasts with the resulting streamlines for higher ξ.

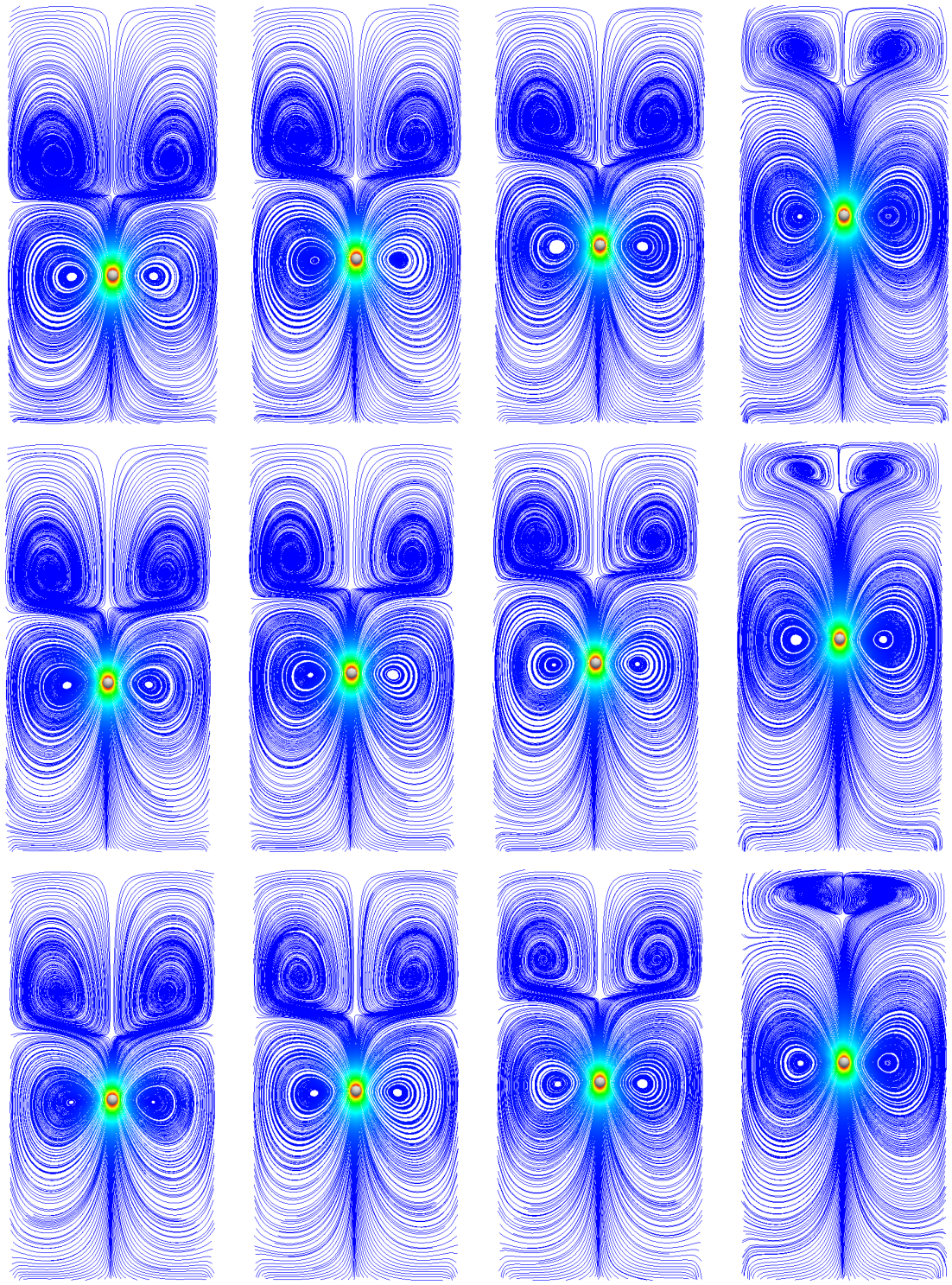


Figure 6.8: Streamlines at sedimentation time $t/\tau = 2.5$ for $\xi/H = 0$, 0.05, 0.08, 0.2 (left to right). Top row corresponds to $\tau_f/\tau = 0.05$, second row to $\tau_f/\tau = 2.5$, and bottom row to $\tau_f/\tau = 5$.

As the matter of fact, we could observe that the lines surrounding the particle seem to form an asymmetric pattern fore and aft the particle position, i.e. if one imagines to fold forward, like an envelope, at the particle position and across the flow, the streamlines seem to be not exactly on the z-axis. Moreover, they are affected by the upper revolving area that is close to the top wall of the container. It important to note that we are still in low Reynolds number regime (Re ≈ 0.015 for all cases). Before this revolving area starts upstream in the channel, a negative wake or flow going upwards is observed for both highly and less fluidized cases, top versus bottom figures. Flow going upwards is observed close to the upstream boundary of the revolving area, although secondary vortices are barely observed close to the walls for higher fluidity timescales. The upward flow forms a smaller secondary revolving area upstream close to the walls of the container whose size seems to decrease with ξ/H. The revolving area around the sedimenting particle is smaller in size when the fluidity timescale increases, but still increases in size with the cooperativity length. In this case, the downstream flow seems not to be as much affected like for the smaller τ_f/τ, as it was denoted in the fluidity profiles.

Drag Coefficient Analysis

As it has been introduced, there is a correction factor suggested by Bird et al. [10] when Oldroyd-B fluids are the matter of study (Eq. 6.2). In the case of a viscoelastic flow with shear thinning effects, we used the fluidity Maxwell model. These effects can substantially modify the behavior of the flow according to the model parameters used. The effect of these parameters is directly related to the settling velocity of the particle. The overall tendency is that the more localized and fast the fluidization process occurs, the sedimentation will be faster. This is because the area where the fluid is deformed by the presence of the particle has higher fluidity which will let the particle fall rapidly. If on the other hand, the fluidization process is slower, or so higher fluidity timescales, and less localized fluidization process i.e. high cooperativity length, the velocity goes through oscillating transient behavior before reaching a lower sedimenting velocity. The particle will be under the action of two forces, drag force exerted by the fluid and gravitational force. From the former, we calculated the drag correction factor by comparing it to what the Stokes's force law (Eq. 6.1) would yield if the particle was falling with the same velocity we obtained for each case in a Newtonian fluid with the same zero-shear-rate viscosity and the gravitational force. Ultimately, the correction factor we calculated using the fluidity model follows the next form:

$$\mathrm{X} = \frac{(4/3)\pi r^3(\rho_s - \rho)g}{6\pi\eta r u_\infty} \tag{6.22}$$

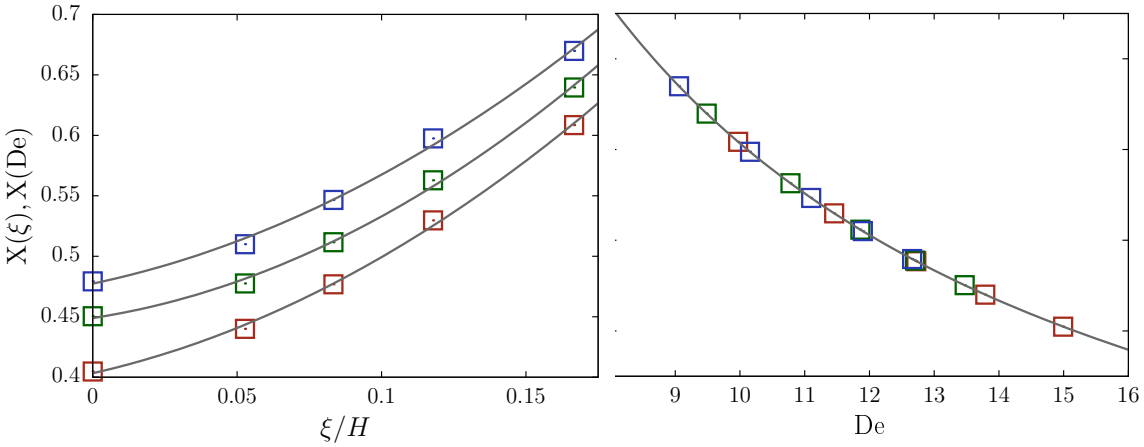


Figure 6.9: a) Drag correction factor in function of cooperativity length for $\tau_f/\tau = 0.05$ (red), 2.5 (green), 5 (blue) and b) drag correction factor versus Deborah number for same τ_f/τ values and all ξ.

This correction factor estimates how deviated the force exerted by the fluid on the particle is with respect to what would be if the fluid followed the Stokes' law in a Newtonian creeping flow. As observed it depends on the sedimentation velocity, therefore, on the Deborah and Reynolds number as well. Deborah number is related directly to settling velocity therefore on ξ and τ_f. On the left side of Fig. 6.9 we show the relation between the correction factor obtained versus cooperativity length for different fluidity timescale τ_f/τ. In all cases, the factor increases with ξ and with τ_f/τ as well. The closer the factor is to 1 the closer the fluid is to behave as a Newtonian fluid. This coincides with what our model predicts for higher cooperativity lengths where the fluid shows a more homogeneous and distributed fluidity. On the right side of the same figure, we can see an overall picture of how the correction factor relates to the Deborah number by collapsing all data for all ξ and τ_f studied. As observed, the correction factor decreases with the Deborah number, with ξ and τ_f. In this right side figure, same colors are used for sets of τ_f values, as in red for $\tau_f/\tau = 0.05$, green for $\tau_f/\tau = 2.5$, and blue for $\tau_f/\tau = 5$. Collapsing all data, for different τ_f and ξ, gave us an overall relation of $\mathrm{X(De)} = 6.0677\mathrm{De}^{-1}$.

6.3 Two Particle Sedimentation

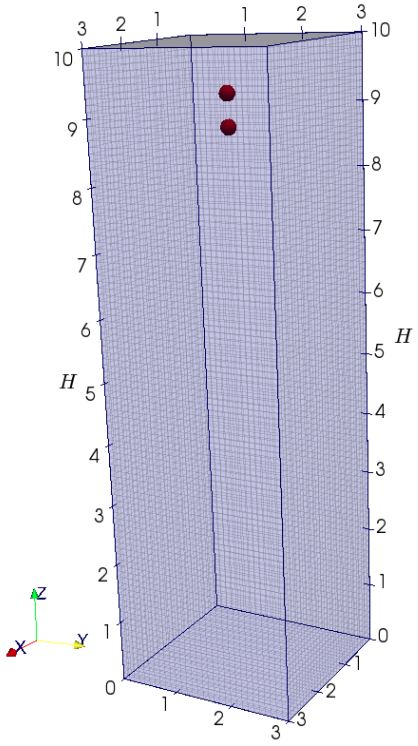


Figure 6.10: Initial position of two particles at time $t = 0$ before sedimenting in a shear thinning fluid.

After discussing the fluidity model parameters influence in the sedimentation of one particle in a shear thinning fluid, we used the same model to reproduce effects found when two particles sediment on top of each other. Following a similar set-up to the suggested by [136] for sedimentation of two disks in an Oldroyd-B fluid, we used the fluidity Maxwell model to describe the fluid and to study how the drafting, kissing and chaining effect phenomena (if present) depends on the model parameters. In mentioned reference, they used two identical disks positioned in the centerline of a container filled with a viscoelastic fluid and, by using a similar fictitious domain method, they were able to assess the sedimentation behavior and mentioned phenomena using an Oldroyd-B fluid. In their setup Deborah and Reynolds numbers were rather low, 1.624 and 0.29 respectively. We used a taller container than what has been used in previous sections as $\Omega = (0, 3) \times (0, 3) \times (0, 10)$ where two spheres were located in the centerline at positions $\{1.5,1.5,9.25\}$ and $\{1.5,1.5,8.75\}$ (Fig. 6.10). Both spheres were identical with a diameter $d = 0.25\,\mathrm{cm}$ and density $\rho_s = 2\,\mathrm{g\,cm^{-3}}$. We used a shear thinning fluid with same properties as in previous section. Reynolds and Deborah number depend directly on particles velocity, particles shape, and fluid properties which ultimately rely on ξ and τ_f. In the cases we studied, Reynolds number was below 0.6 and the maximum Deborah number achieved was in average 33 giving rise to a rather high Elasticity number of 48, which nonetheless only depends on the radius, relaxation time and the fluid viscosity. Figure 6.11 shows a series of snapshots in time after the two particles were released. At the beginning, the leading particle creates a wake behind it with higher fluidity inducing a drafting effect where the following particle is sunk in.

A small corridor is formed between the two particles in time with lower viscosity (higher fluidity) than the steady fluid in the rest of the container. A close-up of this phenomenon is better observed in Fig. 6.12. The existence of such area has been suggested in the literature for particles sedimenting in viscoelastic fluids where fluid

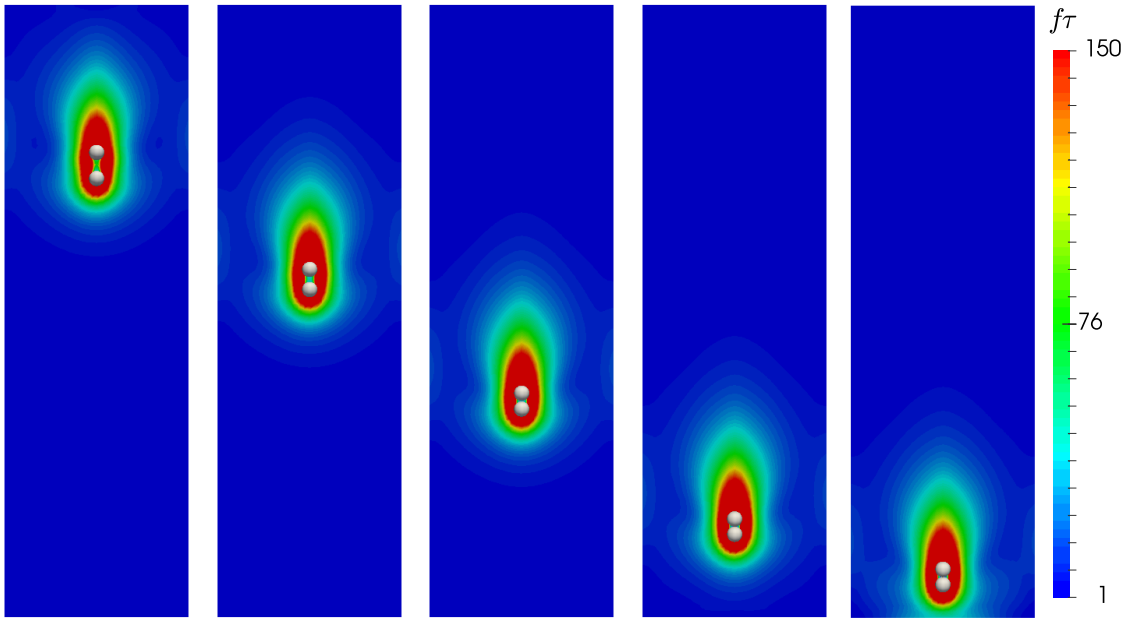


Figure 6.11: Fluidity color map of sedimentation of two particles in a shear thinning fluid at times $t/\tau = 0.25, 0.5, 0.75, 1, 1.1$ for case of $\tau_f/\tau = 0.05$ and $\xi/H = 0$.

viscosity seems to be lower than its bulk value behind trailing particles accelerating the following ones [8]. In the same figure, at time $t/\tau \approx 0.75$, the kissing effect happens after the following particle is accelerated by this corridor and gets to touch the leading one forming a stable pair that remains together "chaining" until they reach the bottom of the container.

Fluidity has been defined as a material property that resembles an inverse viscosity. Along this work, we have varied model parameters enough to describe what happens to the flow when there is more cooperativity in the flow with respect the geometry it is contained, or the effect of a timescale that tells how fast the fluidity will spread along the neighboring sheared or deformed areas. In last section, we saw that when one particle is sedimenting, both ξ and τ_f play a determining role in transient sedimentation velocity behavior and ultimately settling velocity. This tendency prevails when two particles sediment in the shear thinning fluid, where the drafting, kissing, chaining, phenomena is diminished by increasing the cooperativity length, an effect that is at the same time, enhanced by an increment in the fluidity timescale τ_f along the fluid.

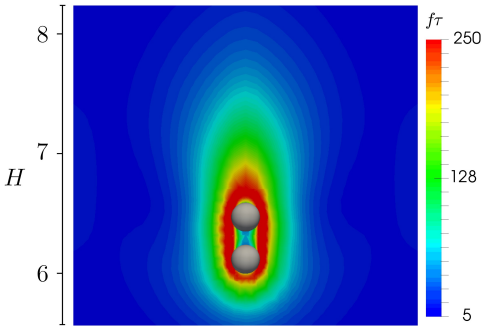


Figure 6.12: Corridor formed between two sedimenting particles before touching at time $t/\tau = 0.4$ ($\tau_f/\tau = 0.05$ and $\xi/H = 0$).

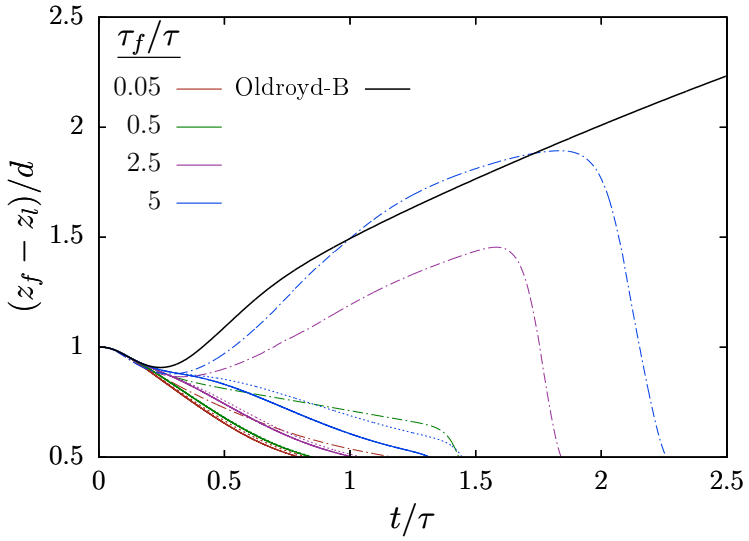


Figure 6.13: Separation distance between particles center normalized by their diameter for τ_f/τ (labeled) and ξ/H as 0 (solid lines), 0.05 (dots), 0.16 (dash-dots). Case Oldroyd-B fluid (black line).

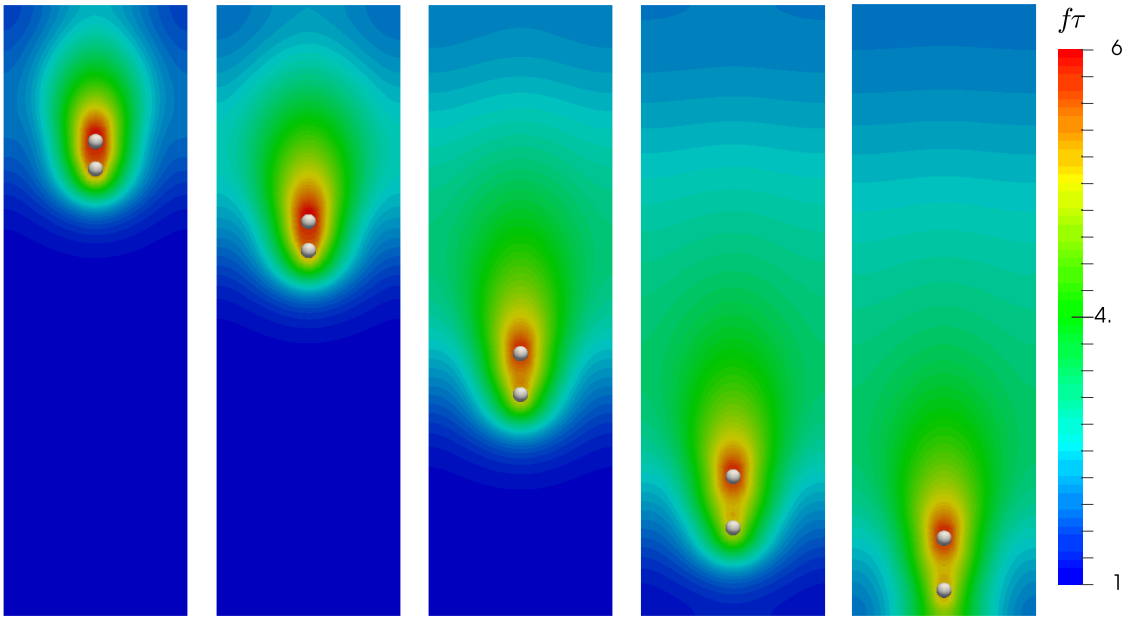


Figure 6.14: Fluidity color map of sedimentation of two particles in a shear thinning fluid at times $t/\tau = 0.25$, 0.5, 1, 1.5, 1.75 for case of $\tau_f/\tau = 2.5$ and $\xi/H = 0.16$.

This effect is more clearly seen in Fig. 6.13, where the distance between the centers of the following and leading particle, normalized by their diameter, is shown in time for the range of parameters we studied. For lower τ_f values, the effect of the cooperativity length is small but still enough to increase the time it takes for particles

to touch after drafting (in plot at separation 0.5). As soon as τ_f starts increasing, the cooperativity length takes longer to spread the fluidity along the system which increases the time it takes for both particles to get in contact. We include the evolution of particle distance between two particles sedimenting in an Oldroyd-B fluid with same viscosity but no shear thinning effect. In this case, the particles tend to separate and the drafting-kissing-chaining effect is absent.

Snapshots taken in time of fluidity color maps are shown in Fig. 6.14 for $\xi/H = 0.16$ and $\tau_f/\tau = 2.5$. In this case, we can observe there is an area between the particles with high fluidity but not so localized like in the previous case. The lack of localized fluidized "corridor" makes the following particle remain in its lower viscosity space than to approach the leading one, since the fluidity starts decreasing between the two of them. Because of this, the particles interaction becomes hindered and no chaining effect was observed. Fig 6.15 shows how the so-called corridor or space between the two particles at time $t/\tau = 0.4$ is not-so-localized but bigger and reaching more distance along the domain. Overall, areas with higher fluidization are localized behind the set of particles which is exemplified by bigger wakes than the ones obtained for lower ξ and τ_f.

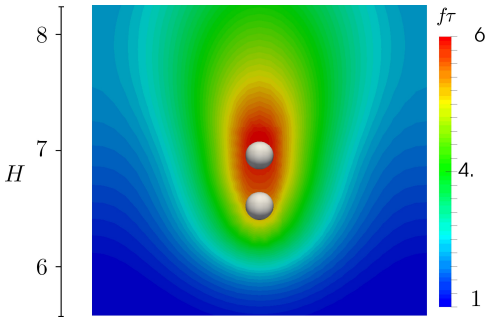


Figure 6.15: Area between two sedimenting particles at time $t/\tau = 0.4$ using $\tau_f/\tau = 2.5$ and $\xi/H = 0.16$.

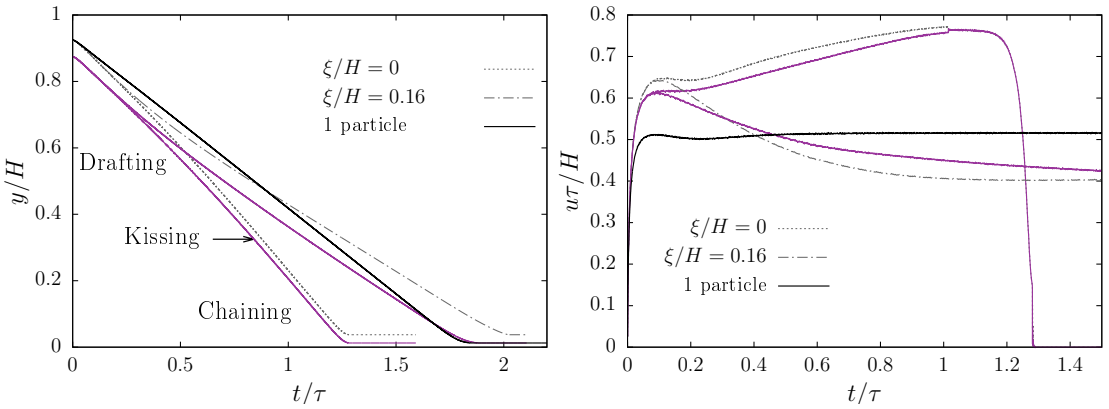


Figure 6.16: Left: position in time of leading (solid) and following particle (dashed/points) (left). Right: corresponding velocity in time, using $\tau_f/\tau = 2.5$ and different ξ/H. Solid black line for one particle sedimenting ($\tau_f/\tau = 2.5$ and $\xi/H = 0$).

This tendency was also shown when one particle was sedimenting in this fluid. As mentioned the drafting, kissing, chaining effect was diminished by an increment in both the cooperativity length and fluidity timescale. For the case of an intermediate

$\tau_f/\tau = 2.5$, mentioned phenomenon was found for smaller ξ. However, particle separation was found for bigger cooperativity along the fluid as it has been shown previously. In this case, Fig. 6.16 illustrates the position of leading and following particles with time (left side) and their corresponding velocity while sedimenting (right side). Regarding positions, we appreciate how the distance between particles increases with ξ which excludes the kissing and chaining effect from the sedimentation. We included the position of one particle sedimenting in time with the same initial set-up as the following particle in the tandem set-up. In this case, we observe how, for lower cooperativity length (dotted line in same figure), one particle takes longer to sediment than the following particle, exemplifying how the presence of the leading particle accelerates the following one. Regarding the sedimentation velocities, an initial overshoot is found at around $t/\tau = 0.1$ for both particles, yet higher velocity values are encountered for the following sphere than for the leading one, which is consistent with Goyal et al. [107] tendencies found for two particles sedimenting in a viscoelastic fluid. Nonetheless, they mentioned repulsion between spheres induced by a negative wake after the overshoot, which was not present in our calculations. In our case, the separation in time found between particles was related to the model parameters used.

We also noted in Fig. 6.16, that the transient velocity of one particle sedimenting after being released from the same position of the following particle in the tandem set-up, interestingly showed no overshoot even though the Elasticity number is about 192 and, in the two particles case, it reduces to 48 and overshoots are present. This might be due to the fast initial acceleration of the following particle which is enhanced by the solvent contribution to the viscosity. Streamlines for both extreme sedimentation cases studied, attraction and separation, are shown in Fig. 6.17 and 6.18 respectively. These figures allow us to exemplify how before and after the tandem particles, streamlines symmetry (fore-and-aft) is disturbed when separation occurs (see central figure of Fig. 6.18) while vortices are formed upstream the spheres that push and deform the streamlines surrounding the particles. This happens for overall low sedimentation velocities i.e. Reynolds number. Upper vortices formed during attraction, indeed affected and bent the surrounding particles streamlines, but in a "softer" way, since they are less affected and distorted by them.

As closure, we would like to add that multiple research about particles sedimenting in Oldroyd-B fluids, especially the ones done by Joseph et al. as in [111, 138] have established how important elastic and inertial effects are while particles (not only spherical) sediment. Even though we only studied spherical particles, other shapes when sedimenting in viscoelastic fluids, tend to do it broadside parallel to the stream. The kissing and chaining effect often found in these fluids is affected by how high the inertia is while sedimentation, which is ultimately related to fluid properties and particle(s) size. In the Oldroyd-B case we used as a comparison, even though we use

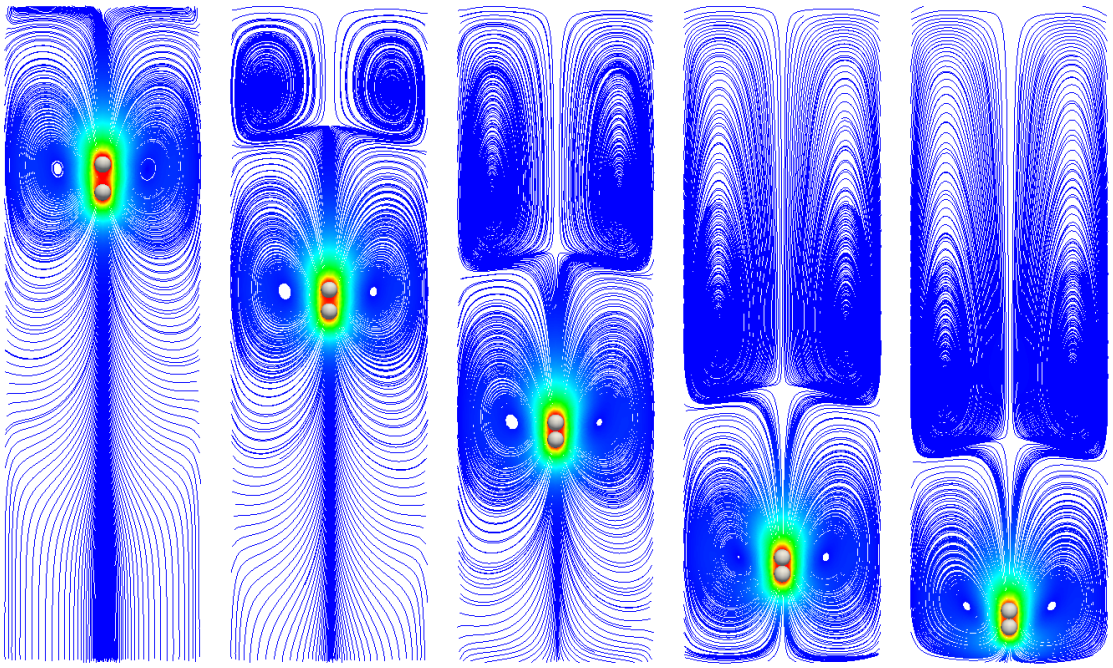


Figure 6.17: Streamlines during two particle sedimentation in a shear thinning fluid at times $t/\tau = 0.25$, 0.5, 0.75, 1, 1.1 ($\tau_f/\tau = 0.05$ and $\xi/H = 0$). Red indicates high velocities and blue lower ones.

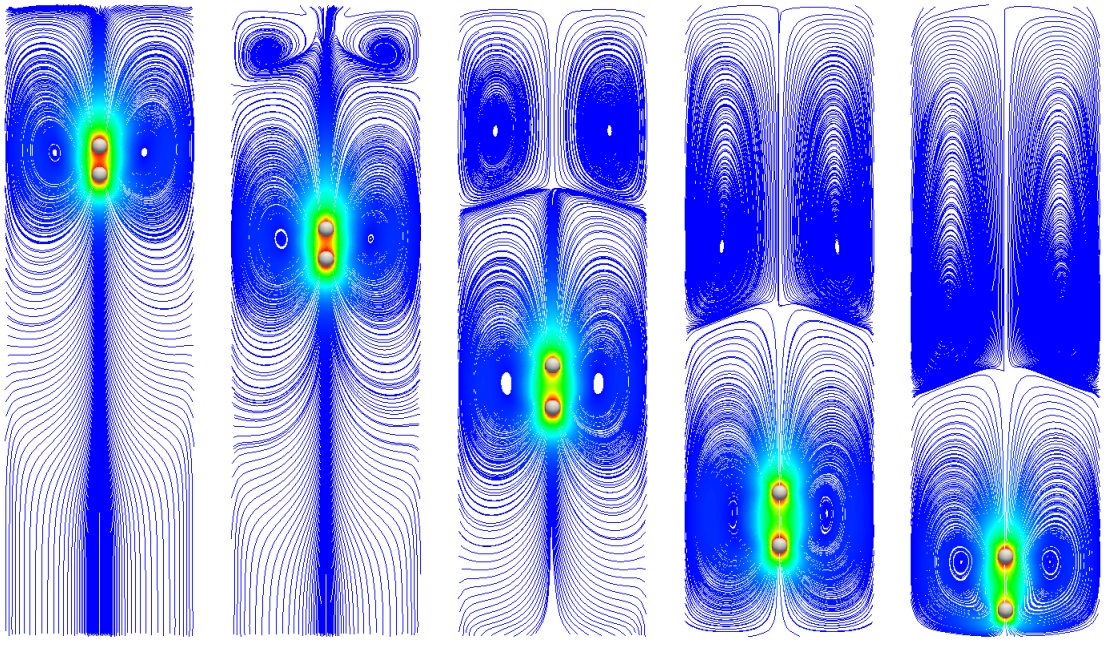


Figure 6.18: Streamlines during two particle sedimentation in a shear thinning fluid at times $t/\tau = 0.25$, 0.5, 1, 1.5, 1.75 for case of $\tau_f/\tau = 2.5$ and $\xi/H = 0.16$. Red indicates high velocities and blue lower ones.

same fluid properties as for the fluidity model, the inertia is lower than in the shear thinning case. Inertial effects can be measured in terms of the viscoelastic Mach number which relates the sedimentation velocity to the shear waves speed in the fluid as

$$M = \sqrt{\mathrm{ReDe}} = \frac{u}{\sqrt{\eta/(\tau\rho)}}. \tag{6.23}$$

Mach number enhances the attraction between particles until they eventually touch and then drag as doublets parallel to the stream. For the shear thinning studied cases and corresponding model parameter variations, we found three regimes in terms of the Mach number. First, Mach number is directly proportional to the sedimentation velocity which is affected as well by the cooperativity length. When ξ is increased for higher τ_f, we found a regime $M \leqslant 1.72$ where particles start separating as soon as they are released and the whole drafting, kissing, chaining phenomena does not occur: they separate during sedimentation for more than 1 particle distance until they reach the bottom of the container. Second, attraction happened between particles for $1.72 < M \leqslant 2.57$, though they did not necessarily touch, probably because the container was not long enough. The third regime corresponded to Mach numbers bigger than 2.57 where the complete kissing and chaining effect was observed. To summarize, we should say that when we used an Oldroyd-B fluid and let two particles sediment on top of each other with same flow parameters as in the shear thinning fluid case, the separation was prominent because the Mach number was below 1, thus the body did not fall faster or comparable than the shear waves speed in the fluid. This means that the inertial effects were not high enough to promote the attraction. Nonetheless, we validated the phenomena for higher Mach numbers using both the Oldroyd-B and shear thinning fluidity model where we set lower viscosities, and the whole drafting, kissing, and chaining effect was observed for both models, though enhanced in the shear thinning fluid case.

6.3.1 Side by Side Configuration

As an outlook, we used same container and shear thinning fluid, but released the two spheres in a side by side arrangement, as shown in Fig. 6.19. Here we found that spheres will ultimately repel each other for initial separations of $\Delta = d/2$, $\Delta = d$ and $\Delta = 2d$. This behavior might be because the Mach number was higher than the unity and dispersion is found, as suggested by Joseph et al. [112, 138], who claim that because of the supercritical speed objects tend to form long bodies perpendicular to the stream when they are released side by side, otherwise alignment parallel to the stream would be expected. Figure 6.20 shows the transient positions and velocities across the stream of each particle for each of the initial distances studied. It is noticeable that for our fluid setup, as it was mentioned, spheres repel until they reach a steady position in the container while sedimenting. The bigger the distance, the slower the repulsion since each other presence is not as acknowledged as with smaller distances. In this case, we use as model parameters no cooperativity length and smaller fluidity timescale as $\tau_f/\tau = 0.05$. We can observe how streamlines across the container are developed in time in the bottom part of the container in see Fig. 6.21.

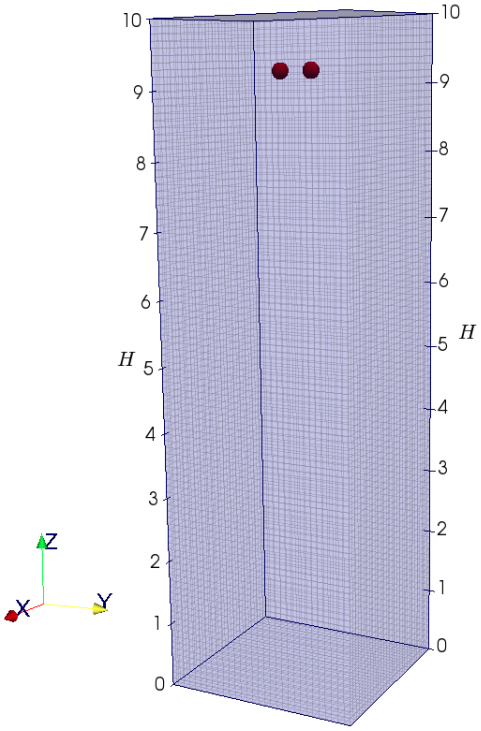


Figure 6.19: Two particles side by side initial position at time $t = 0$ before sedimenting in a shear thinning fluid.

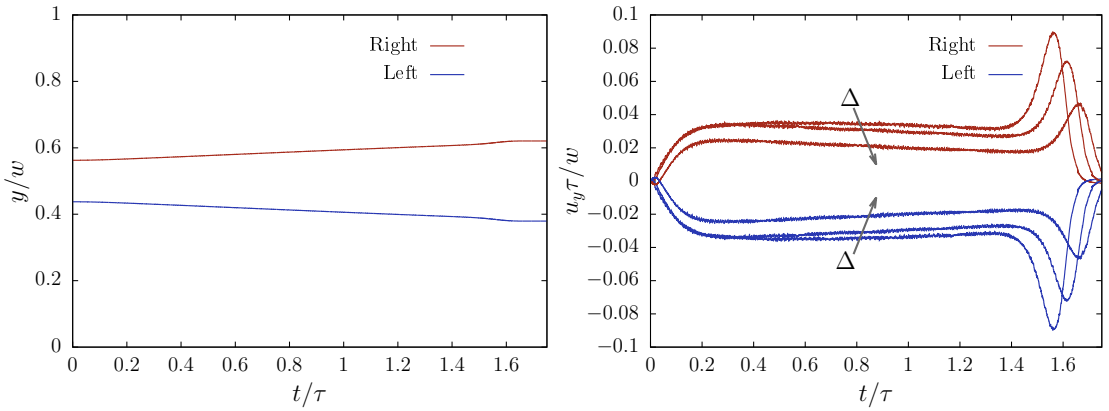


Figure 6.20: Transient position of each particle in the y-direction (left) and corresponding velocities (right) for sedimenting side by side particles.

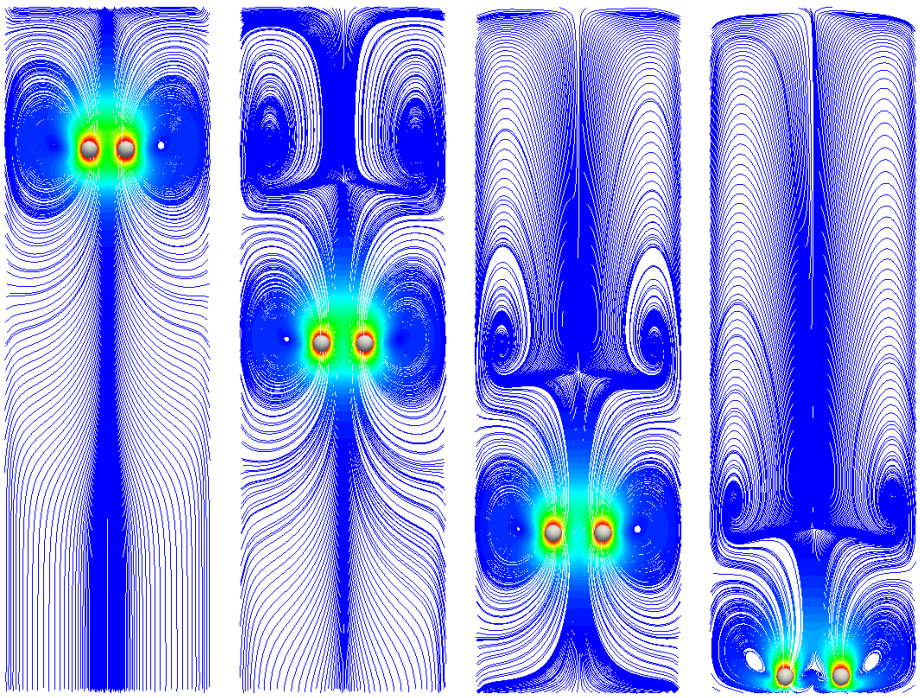


Figure 6.21: Streamlines found during two-particle side by side sedimentation in a shear thinning fluid following fluidity model using $\xi/H = 0$ and $\tau_f/\tau = 0.05$ in time at $t/\tau = 0.25, 0.75, 1.25, 1.65$.

The interaction between sedimenting spheres depends strongly on the inertia and normal stresses developed in the fluid. In our fluid setup we stayed in the low Reynolds number region, Mach number bigger than 1, and high Deborah number (around 30). Inertial effects played a role during sedimentation, which may enhance attraction and chaining behavior when particles were released vertically, but not quite enough for horizontal initial configuration. The latter case showed horizontal separation among the spheres while sedimenting until they reach the bottom of the container. Nonetheless, when inertial effects were increased by using smaller Deborah number and viscosity, the attraction between the spheres was found as suggested by authors like [139] and [112]. They based their assumptions seemly on a critical distance that separates attraction and spheres divergence. Moreover, we observed attraction at the beginning of the sedimentation, but not throughout the whole process. However, there are studies where this critical distance does not appear to be deterministic on the attraction or repulsion behavior like [140] and [113]. We must say as well, that these two particles, by means of our code, were "perfectly" set next to each other, hence if there are no fluctuations they indeed just fall without much interaction in this set-up. A suggestion for future research would be to set the particles next to each other but offset in order to find how distance and initial configuration might affect their sedimentation behavior.

Chapter 7

Summary and Conclusions

We have developed and extended a fluidity model based on features of the schematic model from a microscopic theory that is useful to study the non-local rheology of glass-forming liquids. This rather simple model, could describe a variety of microscopic phenomenology that is typical of dense liquids, including yield stress and shear thinning behavior. There are other models able to describe this kind of features, but the schematic model starts from a first-principle theory which we used to connect microscopic aspects to macroscopic performance. By means of this model, we could apply this knowledge in robust and traditional finite volume methodology and reproduce memory effects such as long-lasting stresses remaining in glassy systems after flow cessation.

The rheological model we used in this work brings in a term that has been around in the scientific environment for a few years, called "fluidity". This term might be seen as a non-local inverse viscosity, which has allowed us to study heterogeneities in the flow due to cooperativity. These effects have been found to be relevant in dense liquids, jammed emulsions, and overall glass liquid flow, especially in confinement. Heterogeneities in the flow can be accounted for by using this model, where cooperativity plays a decisive role in defining transient and final macroscopic behavior. Fluidity field will spread in the system by diffusion depending on two main parameters: cooperativity length ξ, which tells us how far a system can be fluidized, and its timescale τ_f which tells us how fast this process happens. As an example we can refer to how a plug flow profile, expected in pressure driven yield-stress liquids, turns into a parabolic-like profile resembling Newtonian behavior by means of cooperativity in the flow.

We have studied how heterogeneities in the flow produce shear bands in a system using this model. Transient and long-lasting banding phenomena was described. Bands were defined as distinct velocity profiles from what is expected in a simple shear

setup (linear profiles). Bent velocity profiles appeared transiently when monotonic flow curves were used together with an initial heterogeneous fluidity field. Fluidity diffusion played a role in the transient size banding. The more time was given to the system to spread heterogeneities, bending of the velocity profile was bigger. Size and shape of the initial perturbation were related to band size, even when we used random initial fluidity fields. Banding happened transiently at a clear undershoot (or overshoot) in the velocity with time. Corresponding stress versus deformation showed overshoots depending on τ_f regardless of the transient banding presence. Long-lasting banding was also obtained in steady state when a fixed fluidity value was set at the wall. Size of the bands in this case depended increased with shear rate and cooperativity length up to a saturation value for each of both parameters.

Stress remaining after flow cessation was also part of our studies. Model parameters allowed us to tailor the shape and values of remaining stresses in trivial and non-trivial geometries like: lid-driven cavity flow, abrupt 4:1 contraction, and flow through obstacles. Presence of residual stresses has been previously studied through experiments and simulations in glass forming systems. In simple geometries, we found similar tendencies regarding shear rate influence on remaining stresses, where higher values were obtained for lesser pre-stressed systems. If the fluidity diffusion happened faster, the stresses have less time to relax hence higher residual stresses remained present. Cooperativity length allowed us to see how fluidization affected a system after cessation. We have found that when the initial protocol to induce stress in steady state was done through pressure-driven flow, stress patterns after cessation would be smoother and more symmetrical with an increase of ξ. However, when the initial stresses in steady state were induced via shear, the final stress patterns after cessation would become less symmetrical for larger cooperativity length. Final mechanical properties of studied systems were also affected by the presence of residual stresses, where an increasing shear modulus was found for rather lower initial driving velocities.

The stress advection term influence in constitutive models was studied in two different geometries for low and high Deborah numbers. The term becomes relevant for linear models like the linear Maxwell model, mainly at high Deborah numbers, otherwise, the difference regarding its presence is negligible. The effect is even less noticeable for shear thinning fluids, as we call non-linear Maxwell model and fluidity models, where shear-dependence of the relaxation time weakens the effect of the missing term for either low and high Deborah numbers. This statement corroborates LB methodology implemented by Papenkort [65], where the integral form of the schematic model (Eq. 3.12) was implemented without the presence of the advection term in calculations, hence its use in non-trivial geometries is advised and encouraged at best with shear thinning models.

After being able to implement the fluidity model in diverse configurations and

ultimately reproduce glass-forming liquids behavior in macroscopic state, we found ourselves interested in applications like sedimenting particles in viscoelastic fluids. In this regard, we can conclude that there is a delicate connection between inertial effects and what happens when more than one sphere sediments in a viscoelastic fluid with or without shear thinning effect. First of all, when two spheres sediment on top of each other, inertia will enhance the otherwise expected drafting, kissing, chaining effect.

As we saw, model parameters and fluid characteristics are responsible for this behavior together with particles properties. Nonetheless, the mentioned phenomenon is expected generally in viscoelastic fluids which differs greatly from what would happen in a Newtonian fluid. Particles sedimenting in the latter go through a drafting, kissing and tumbling effect which is also enhanced by the inertia, i.e. Mach number. Even though our focus was to study viscoelastic fluids, in the Newtonian case we found that mentioned phenomenon is not necessarily fully achieved for highly viscous fluids where the Mach number is indeed low. In the latter case, we must say as a general statement that particles sedimenting on top of each other would go intro drafting but touching might be hindered. This and subsequently tumbling was prominent for higher Mach numbers. We recall again how Joseph et al. [112, 138] described that in the case of side by side sedimentation of particles in viscoelastic fluids spheres would attract, touch, and chain, preferably for low Mach numbers where the side by side configuration would be otherwise unstable.

Fully resolved methods can be powerful tools to solve the dynamics of swimming objects either by inputting detailed characteristics of the object, i.e. muscles physiology and elastic properties, or by using a hydrodynamic approach where the body deformation is known and swimming speed can be calculated. Applied research describes specific swimming organisms using body specifications by making assumptions of swimming velocities or calculating the latter based on the hydrodynamic forces on the body. Examples of these calculations on self-driven organisms have been done by [141, 142] for anguilliform swimmers where even swimming efficiency across various swimming styles can be compared. Similar studies have been done by [143] where fish dynamics of zebrafish larvae was assessed using the morphology of the organisms and specific swimming styles are used either as input or obtained. Having this in mind, we suggest as an appealing addition to this last part of our research to make the particles active and study their behavior in viscoelastic fluids by means of this type of simulation, where different shapes and initial configurations could be tested.

Appendix A

Supplementary Information

A.1 Simulation Basics

OpenFOAM is an open source software that permitted us to perform finite volume calculations. An integrated transient solver called "viscoelasticFluidFoam" was used to perform viscoelastic fluid flow analyses using different constitutive models in different geometries. This package allows the user not only to implement the desired constitutive equation or viscoelastic model but to use it in complex geometries, meshes that could be fixed, moving or unstructured, wide discretization solvers availability, interpolation schemes, data processing and post-processing.

Continuity and momentum equations were already implemented in the solver using OpenFOAM C++ resources by Favero et. al in addition to a list of mostly used solvers in viscoelastic flows [9, 37], based on a PISO solver. A DEVSS approach was used, which was previously introduced in section 2.3.4.

The material parameters used across our research were: $\eta_s = 1$ Pa $\cdot$ s, $\eta_p = 10$ Pa $\cdot$ s, $\tau_s = 1\ s$, $\tau = 10\ s$, $\rho = 1360\,\mathrm{kg\,m^{-3}}$, unless said otherwise.

A.2 Code Implementation

A.2.1 Material Models

Different constitutive equations were implemented or modified in the original "viscoelasticFluidFoam" package, including the model variations that were studied in Chapter 2 (see section 2.4) were the upper convected time derivative of the stress tensor was modified. So-called model-ac variation (for the linear and non-linear

Maxwell model) was done by changing the mentioned derivative (see Eq. 2.58) by an incomplete one as:

$$\overset{\nabla}{\boldsymbol{\sigma}}_{ac}(t) = \frac{\partial \boldsymbol{\sigma}}{\partial t} - [\boldsymbol{\sigma} \cdot \nabla \boldsymbol{u}]^T - [\boldsymbol{\sigma} \cdot \nabla \boldsymbol{u}] \tag{A.1}$$

The viscoelastic models that were either modified or newly created were done directly in the OpenFOAM solver implementation by following its instructions [33, 35].

- Linear Maxwell model and model-ac variation: the implementation of the linear Maxwell model (see Eq. 2.59 for a constant relaxation time τ_M) was already in the solver package, which was found within the models as "Oldroyd-B" ($FOAM_SRC/transportModels/viscoelastic/ viscoleasticLaws/Oldroyd-B/Oldroyd_B.C). The code defining the stress tensor was originally written as:

```
// Stress transport equation
fvSymmTensorMatrix tauEqn
(
    fvm::ddt(tau_)
  + fvm::div(phi(), tau_)
  ==
    etaP_/lambda_*twoD
  + twoSymm(C)
  - fvm::Sp(1/lambda_, tau_)
);
```

  In this code `tau_` defines the stress tensor $\boldsymbol{\sigma}$, `phi()` the flux normal to the control volume, and constants `etaP_` and `lambda_` are the non-Newtonian viscosity η_p and relaxation time τ respectively.

$$\texttt{fvm::ddt(tau_)} = \frac{\partial \boldsymbol{\sigma}}{\partial t} \tag{A.2}$$

$$\texttt{fvm::div(phi(), tau_)} = (\boldsymbol{u} \cdot \nabla \boldsymbol{\sigma}) \tag{A.3}$$

$$\texttt{twoSymm(C)} \;\; = [\boldsymbol{\sigma} \cdot \nabla \boldsymbol{u}]^T + [\boldsymbol{\sigma} \cdot \nabla \boldsymbol{u}] \tag{A.4}$$

$$\texttt{etaP_/lambda_*twoD} = \frac{\eta_p}{\tau}\mathbf{D} \tag{A.5}$$

$$\texttt{fvm::Sp(1/lambda_, tau_)} = \frac{\boldsymbol{\sigma}}{\tau} \tag{A.6}$$

Furthermore, the model-ac version of the linear Maxwell model was implemented by changing the definition of the stress tensor to:

```
// Stress transport equation
fvSymmTensorMatrix tauEqn
(
    fvm::ddt(tau_)
    ==
    etaP_/lambda_*twoD
  + twoSymm(C)
  - fvm::Sp(1/lambda_, tau_)
);
tauEqn.relax();
tauEqn.solve();
```

- Non-linear Maxwell model and model-ac variation

For the non-linear Maxwell model the relaxation time τ_M was defined following eq. 2.60 as `lambdaM` and written in the code as:

```
volScalarField lambdaM =
(lambda_*gammaC_/(gammaC_+lambda_*sqrt(0.5)*mag(twoD)));

// Stress transport equation
fvSymmTensorMatrix tauEqn
(
fvm::ddt(tau_)
+ fvm::div(phi(), tau_)
==
etaP_/lambda_*twoD
+ twoSymm(C)
- fvm::Sp(1/lambdaM, tau_)
);
tauEqn.relax();
tauEqn.solve();
```

where `gammaC_` is γ_c, and `lambdaM` definition is written as:

$$\texttt{(lambda_*gammaC_/(gammaC_+lambda_*sqrt(0.5)*mag(twoD)))} = \tau_M \tag{A.7}$$

Corresponding model-ac version will follow the same code but without the `fvm::div(phi(), tau_)` line as in the linear Maxwell model case.

- Fluidity Maxwell model: in order to develop this model, we started by defining the new term fluidity `flu_` and its corresponding definition, following Eq. 3.15, part of the code in the model definition looks as

```
volScalarField lambdaM =
(lambda_*gammaC_/(gammaC_+lambda_*sqrt(0.5)*mag(twoD)));

fvScalarMatrix fluEqn
(
fvm::ddt(flu_)
+ fvm::div(phi(), flu_)
==
- (flu_/lambdaFlu_) + 1/(lambdaFlu_*lambdaM)
+ fvm::laplacian((D_/lambdaFlu_),flu_, "laplacian(D,flu)")
);
fluEqn.solve();

// Stress transport equation
fvSymmTensorMatrix tauEqn
(
fvm::ddt(tau_)
+ fvm::div(phi(), tau_)
==
etaP_/lambda_*twoD
+ twoSymm(C)
- fvm::Sp(flu_, tau_)
);
tauEqn.relax();
tauEqn.solve();
```

τ_M definition was the same one used in the non-linear Maxwell model. The first couple of terms in the fluidity equation disclosure as the "material derivative" of the fluidity $f(\vec{x}, t)$ as:

$$\texttt{fvm::ddt(flu_)+fvm::div(phi(), flu_)} = \frac{\partial f(\vec{x},t)}{\partial t} + (\boldsymbol{u} \cdot \nabla f(\vec{x},t)) \tag{A.8}$$

The rest of the fluidity equation follows the next expressions, where `lambdaFlu_` is the fluidity timescale τ_f

$$\texttt{- (flu_/lambdaFlu_) + 1/(lambdaFlu_*lambdaM)} = -\left(\frac{f(\vec{x},t)}{\tau_f} - \frac{1}{\tau_f \tau_M(\mathrm{II}_D)}\right) \tag{A.9}$$

The diffusion part of the fluidity equation is written in the code using `D_` as the squared cooperativity length ξ^2, hence

$$\texttt{fvm::laplacian((D_/lambdaFlu_),flu_)} = \frac{\xi^2}{\tau_f}\nabla^2 f(\vec{x},t) \tag{A.10}$$

- Fluidity Glass model: this is a variation of the fluidity Maxwell model, but the relaxation time is set to infinity, $1/\tau_M = \sqrt{\mathrm{II}_D}/\gamma_c$ as it was defined in section 3.3.1, therefore we redefined `lambdaM` as

```
volScalarField lambdaM =
gammaC_/(sqrt(0.5)*mag(twoD));
```

To solve the partial differential equations, OpenFOAM uses diverse libraries that have the required discretization methods to handle each field. As it was seen in previous parts of the constitutive equations codes, each term is labeled and solved either explicitly or implicitly. OpenFOAM makes this difference by using `fvc` and `fvm` libraries: "*finiteVolumeMethod*" and "*finiteVolumeCalculus*", respectively. Both libraries have functions to discretize differential operators like gradient, laplacians and time derivative. `fvc` calculates explicit derivatives without storing solutions but rather producing them immediately as a geometric field, and `fvm` solves the equations iteratively producing a matrix to be solved and storing it [33].

A.2.2 Under-relaxation

It was mentioned in Section 2.3.3, under-relaxation factors can be included and used in the equation discretization to perform calculations that reach directly a stable steady state in the transient solver. This option is added in the solver to the stress,

pressure and velocity equation after each equation is solved, i.e. `tauEqn.relax()`, `pEqn.relax()`, and `tauEqn.relax()`. The under-relaxation factors values must be chosen between 0 and 1, where 0 is the strongest under-relaxation and 1 is no under-relaxation [35]. We used next values, as suggested by Favero et. al [9, 37] and set them up in the "fvSolution" dictionary that will be introduced in next part:

```
relaxationFactors
{p 0.3;
U 0.5;
tau 0.3;}
```

A.2.3 OpenFOAM Case Setup

There has to be a basic directory structure to setup any case using OpenFOAM, which is well explained in the OpenFOAM user guide [35]. However, in Fig. A.1 we introduced how our directories and setups were organized to show the specific configurations we used to run the solvers using different constitutive equations in the geometries studied. The time directory name is usually the time when the simulation starts (e.g. "0"), and it contains the variables needed by the solver like velocity, pressure, stress, and fluidity (when the fluidity models are used). System folder contains indispensable dictionaries as: "controlDict" where time step is set and reading and writing solution is specified. In the "fvSolution" file we set the specific linear equations solvers to be used, and in "fvSchemes" the finite volume schemes to discretize the differential equations [35]. In the case of "fvSolution" we chose preconditionated solvers to deal with the velocity, pressure, fluidity and stress equations. For the pressure PCG preconditioned solver was used, which is a gradient solver for symmetric matrices, and for the rest of variables we used a PBiCG, preconditioned bi-conjugate gradient solver. "fvSchemes" file contained discretization schemes for time differentiation, and other terms like derivative, laplacians, and gradients. For time differentiation we used a Crank Nicolson method. For gradient, divergences, and laplacians we used

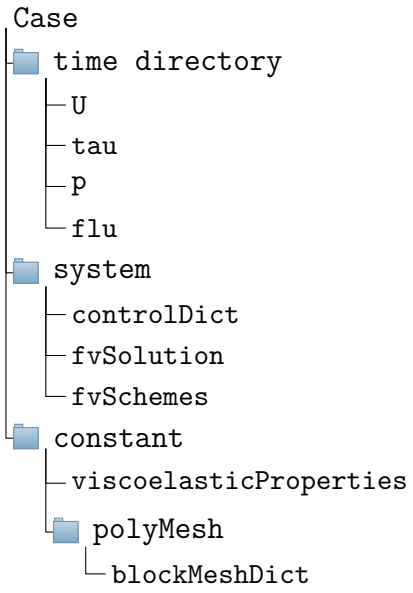


Figure A.1: Schematic representation of OpenFOAM directories used to run viscoelastic solver.

Gauss linear methodology which is the standard finite volume discretization where linear interpolation is done from cell center values to face centers.

In the constant directory we specified the viscoelastic properties of the flow problem, where the used solver is chosen together with flow properties like density `rho`, Newtonian viscosity `etaS`, non-Newtonian viscosity `etaP`, relaxation time `lambda`, model parameter `gammaC`, fluidity timescale `lambdaFlu`, squared cooperativity length `D`. These properties are set up in the "viscoelasticProperties" dictionary as:

```
rheology
{
type            fluidityMaxwellDiffusion;
rho             rho [1 -3 0 0 0 0 0] 1360;
etaS            etaS [1 -1 -1 0 0 0 0] 1;
etaP            etaP [1 -1 -1 0 0 0 0] 10;
lambda          lambda [0 0 1 0 0 0 0] 10;
gammaC          gammaC [0 0 0 0 0 0 0] 0.1;
lambdaFlu       lambdaFlu [0 0 1 0 0 0 0] 1;
D               D [0 2 0 0 0 0 0] 1e-2;
}
```

Subdirectory "polyMesh" includes a file called "blockMeshDict" which is where the geometry and mesh are defined. This allowed us to set boundary conditions for each variable in the time directory.

A.2.4 Particles Sedimentation

We modified a preexisting CFD-DEM solver using the previously learned CFD (OpenFOAM) knowledge in a package called CFDEM®project. The available code was a PISO solver "cfdemSolverIB" for transient calculations with the capability of include immersed boundary conditions for solids present in fluids. The adaptation named "cfdemSolverIBVisco" allowed us to use the viscoelastic models we used along this thesis.

This solver can resolve a viscoelastic fluid as usual and requires a dictionary where the force acting on the particle is calculated. This force boundary condition was implemented based on Shirgaonkar et. al algorithm (shirgaonkarIB.C) that was previously done for Newtonian fluids. We modified this code and called it "viscoelasticIB.C" where the force that is needed in the intermediate step to close the momentum equation is introduced. The calculation of this force is done after the fluid is resolved as the gradient of pressure and stress divergence on the surface of the particle. "viscoelasticIB.C" calculates the volumetric force on the particle by

accounting the volumetric space is occupied by the particles. This information is read in "forceSubModels" as "IBViscoDragPerV":

```
const volVectorField&
forceSubModel::IBViscoDragPerV(const volVectorField& U,
const volVectorField& divStress, const volScalarField& p) const

{
IBViscoDragPerV_ = rhoField()*(divStress-fvc::grad(p));
return IBViscoDragPerV_;
}
```

The force obtained is volumetric hence the viscous forces are multiplied by the density of the fluid to be consistent. The viscous forces are the sum of the pressure gradient and the stress divergence obtained with the "cfdemSolverIBVisco". This sum is different from zero where the solid is. The pressure gradient and "divStress" (stress divergence) is extracted from the viscoelastic solver for each time step.

Location of needed and modified files:

- cfdemSolverIBVisco:
  /CFDEM/CFDEMcoupling-PUBLIC-3.0.x/applications/solvers/
  cfdemSolverIBVisco

- forceSubModel:
  /CFDEM/CFDEMcoupling-PUBLIC-3.0.x/src/lagrangian/
  cfdemParticle/subModels/forceModel/forceSubModels/forceSubModel
- viscoelasticIB: /CFDEM/CFDEMcoupling-PUBLIC-3.0.x/src/lagrangian/
  cfdemParticle/subModels/forceModel/viscoelasticIB

The basic steps of the CFD-DEM coupling are explained in [7,127], which in summary are:

- Particle positions, ratio, and velocity of each particle is obtained. This information is assigned to cells across the previously meshed geometry. A void fraction is assigned that differentiates where the fluid and solid covers the cells in the domain.
- The drag force is calculated using the void fraction information and are used as input in the DEM solver to update particles velocities.
- DEM solver updates particles positions with previous information while the CFD solves the momentum equations on the whole domain.

- New velocity and pressure field are corrected since the particles velocities are introduced in the void regions and correction of continuity equation is performed. Pressure is corrected as well.

A.3 Mesh Analysis: Abrupt 4:1 Contraction

Time step in our model is very much dependent on the relaxation time and mesh size. In fact choosing the time step needs a compromise between the smallest cell in the mesh and the relaxation time, especially since the latter is chosen high along our research, making transient simulations become very lengthy. In order to chose the most appropriate mesh size we compared steady state profiles obtained with different meshes using the Linear Maxwell model. Profiles are normalized by the width of the downstream channel $2h$. Main features of compared meshes are summarized in table A.1. N_x and N_y are the number of cells in x and y-direction respectively, NC is the number of cells, f_x and f_y define a percentile ratio between the smallest cell and h, since cells were made smaller close to the contraction. δt is the time step, and L_v is the corner vortex length.

Table A.1: Main meshes' characteristics.

	Upstream		Downstream						
	N_x	N_y	N_x	N_y	NC	$\%f_x$	$\%f_y$	$\delta t(s)$	L_v/h
Mesh 1	75	80	50	20	7000	4.87	5.00	10^{-6}	1.34
Mesh 2	75	95	50	25	8375	1.29	2.05	10^{-7}	1.41
Mesh 3	150	120	90	30	20700	0.65	1.71	10^{-8}	1.45

Figures A.2 and A.3 show comparisons between velocity, normal stress difference, and shear stress profiles in steady state obtained for the three meshes studied using the linear Maxwell model. Differences between mesh 1 (coarser) and the mesh 3 (finer) regarding velocity profiles (at position $x/h = -0.5$) were smaller than 1.9 %. Normal stress and shear stress show more pronounced differences ($\approx 12\%$) between coarser and finer mesh close to the lower corner of the contraction next to the wall, though through the rest of the y-profile differences for both variables are around 5 %. Mesh 1 was the chosen one because it converged at the fastest computational speed, which is desirable for lengthy transients calculations. There are two reasons behind this result: first, the smallest cells allow choosing a higher time steps due to Courant number convergence criterion, second, less cells are used hence less calculating points.

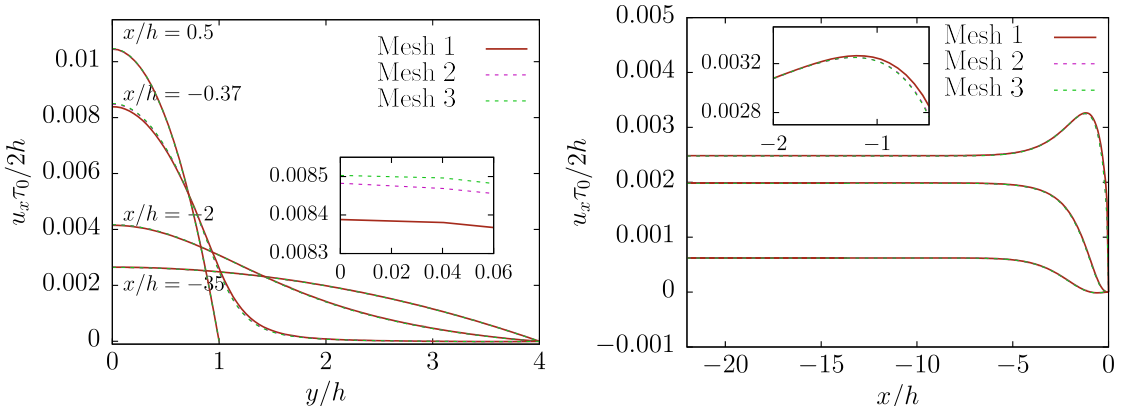


Figure A.2: Velocity $u_x\tau_0/2h$ (left) y-profiles at different x-positions in the channel, and (right) x-profiles at different y-positions in the channel for the three meshes.

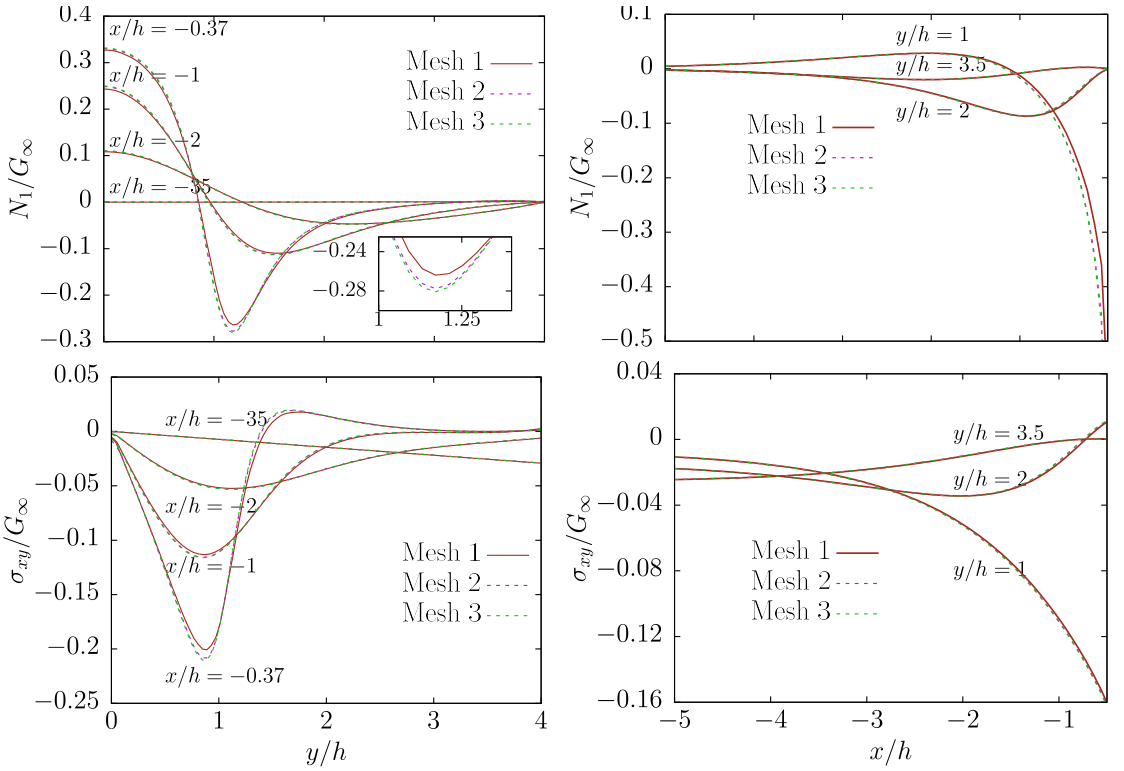


Figure A.3: Top figures: steady state normal stress difference, and bottom figures: steady state shear stress profiles. Left: y-profiles, and rigth side: x-profiles upstream the channel for the 3 studied meshes.

Courant number, $C_o = u_x\delta t/\delta x$, relates the time step δt, smallest cell size δx, and mean velocity in that cell u_x, making it a convergence criterion for transient explicit calculations. This means we could obtain the time step needed to reach convergence

and have stable calculations by ensuring the fluid moves from one cell to another within one-time step.

Contraction flows are very sensitive to fluid viscosity, contraction ratio, elasticity of the fluid (We/Deborah number), and Reynolds number. A fine mesh is necessary to enhance the quality of the vortex formed at the upper corner. Despite the use of a coarse mesh, main features like the corner vortex are reproduced as observed in figure A.4. The length of the vortex was measured in x-direction and normalized by h (L_v/h in table A.1), where the difference between Mesh 1 and Mesh 3 is roughly 7 %.

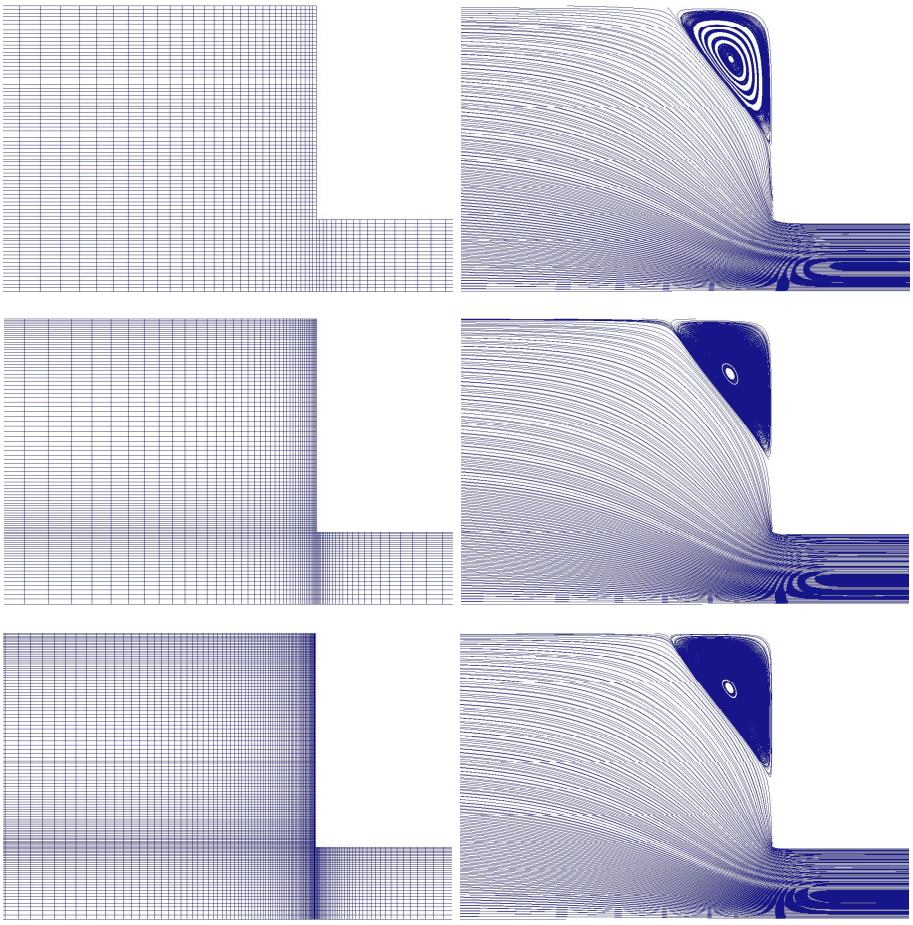


Figure A.4: Top to bottom: mesh 1, mesh 2, and mesh 3 next to corresponding streamlines in steady state showing corner vortices.

A.4 Supplementary Plots

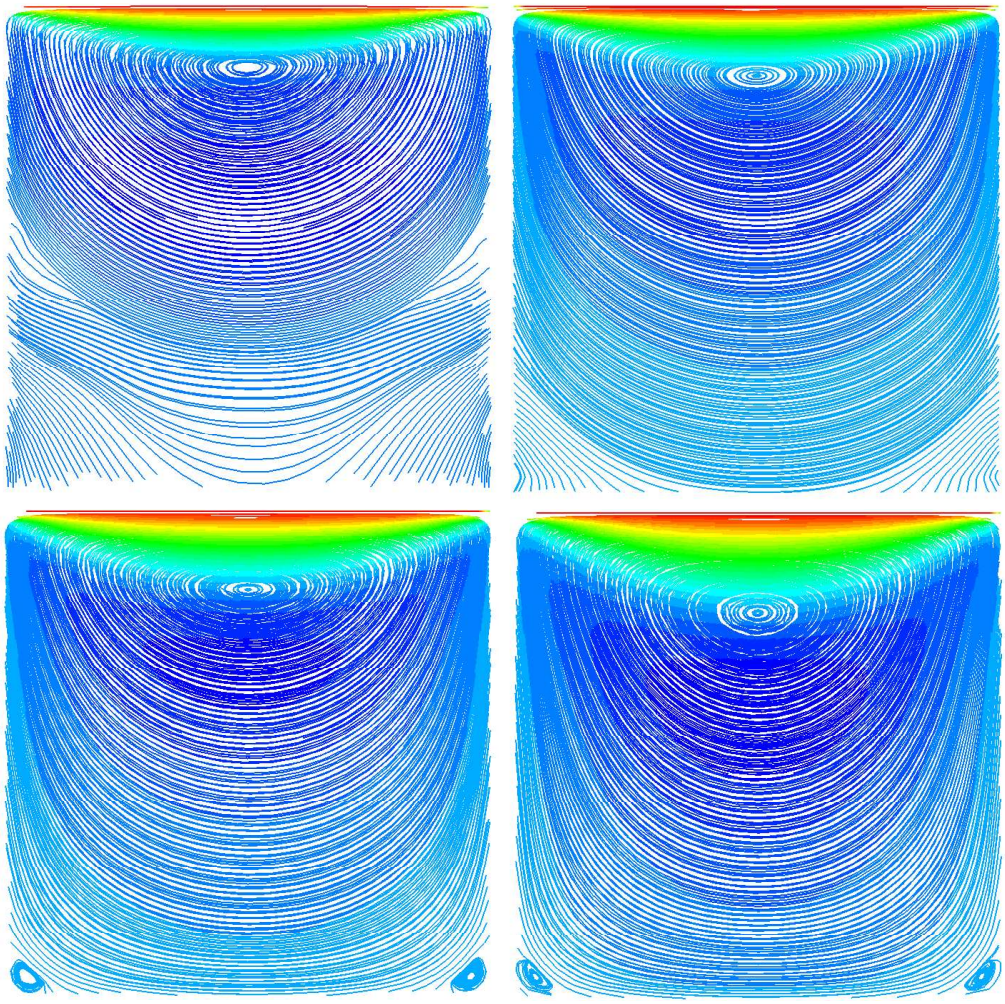


Figure A.5: Steady state streamlines for $u_l = 0.01$ using $\tau_f/\tau_0 = 0.1$ for ξ/h: 0 (top left), 0.03 (top right), 0.1 (bottom left), and 0.3 (bottom right). Red for high velocity values, blue for low values.

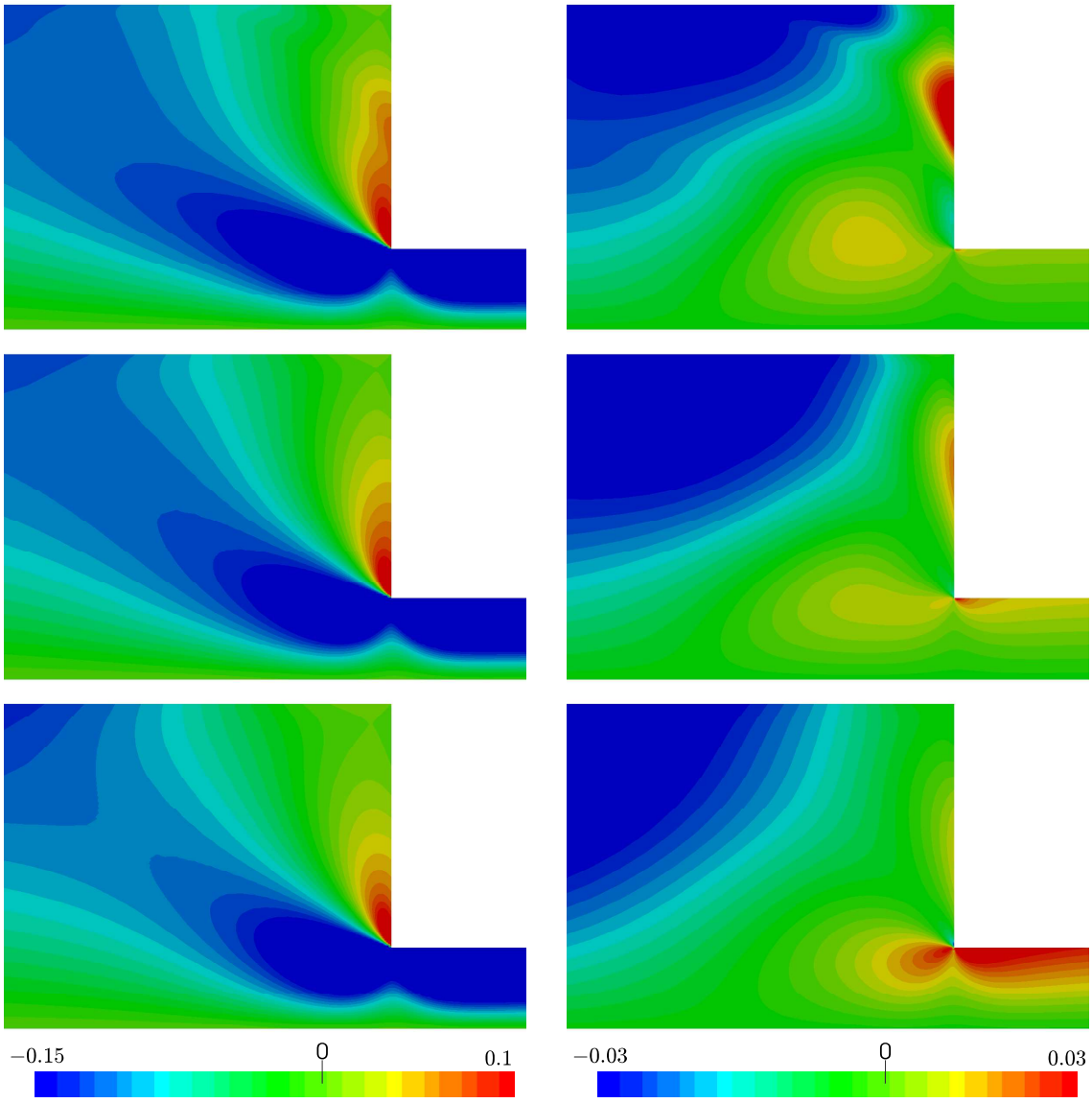


Figure A.6: Shear stress color maps found in steady state (left panel) and after cessation of flow (right panel) for $\tau_f/\tau_0 = 10$ and cooperativity length $\xi/4h$ values from top to bottom of 0, 0.1 and 0.2.

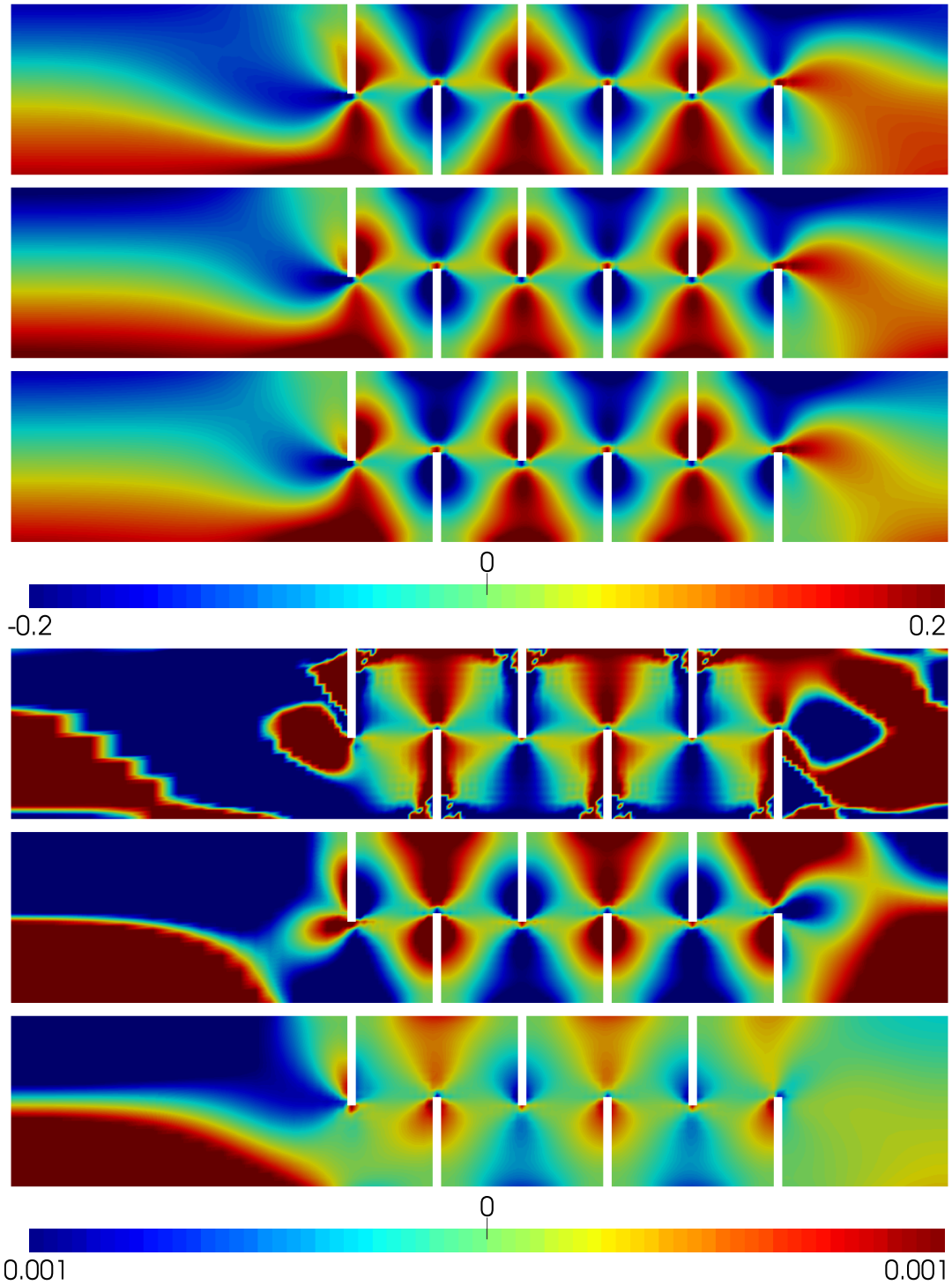


Figure A.7: Top three figures correspond to steady state shear stress color maps obtained using for $\xi/h = 0$, 0.3, 10 from top to bottom and $\tau_f/\tau_0 = 10$. Bottom three figures show corresponding residual shear stress color maps obtained for $\xi/h = 0$, 0.3, 1 from top to bottom as well.

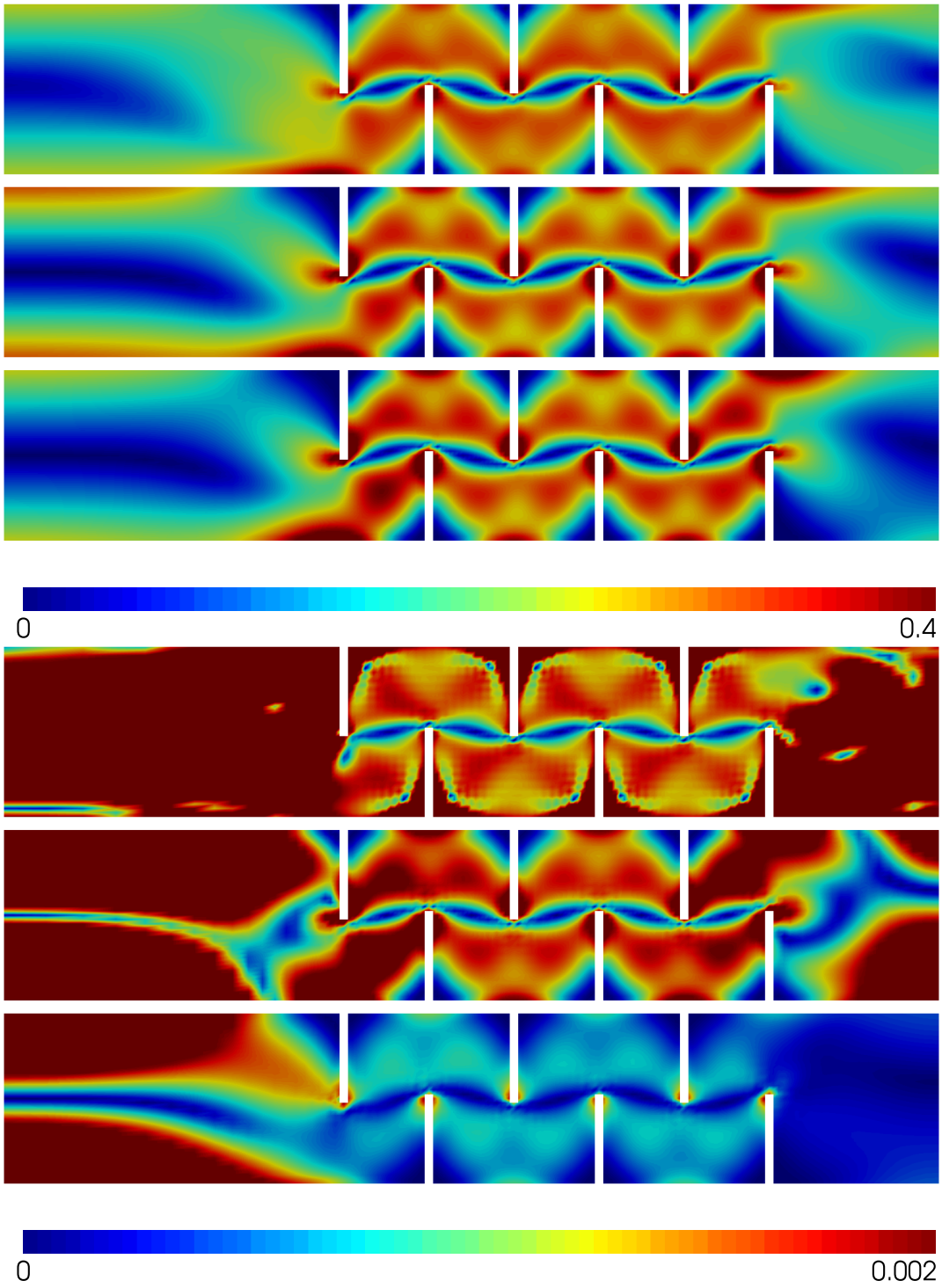


Figure A.8: Top three figures correspond to steady state stress magnitude color maps obtained using for $\xi/h = 0$, 0.3, 1 from top to bottom and $\tau_f/\tau_0 = 10$. Bottom three figures show corresponding residual stress magnitude color maps obtained for $\xi/h = 0$, 0.3, 1 from top to bottom as well.

Bibliography

[1] Thomas Voigtmann. Nonlinear glassy rheology. *Current Opinion in Colloid & Interface Science*, 19(6):549–560, 2014.

[2] Julie Goyon, Annie Colin, and Lyderic Bocquet. How does a soft glassy material flow: finite size effects, non local rheology, and flow cooperativity. *Soft Matter*, 6:2668–2678, 2010.

[3] Lydéric Bocquet, Annie Colin, and Armand Ajdari. Kinetic theory of plastic flow in soft glassy materials. *Phys. Rev. Lett.*, 103:036001, Jul 2009.

[4] J. Goyon, A. Colin, G. Ovarlez, A. Ajdari, and L. Bocquet. Spatial cooperativity in soft glassy flows. *Nature*, 454(7200):84–87, Jul 2008.

[5] Anup Shirgaonkar, Malcolm A. MacIver, and Neelesh A. Patankar. A new mathematical formulation and fast algorithm for fully resolved simulation of self-propulsion. *Journal of Computational Physics*, 228(7):2366–2390, 2009.

[6] Alice Hager, Christoph Kloss, Stefan Pirker, and Christoph Goniva. Parallel open source CFD-DEM for resolved particle-fluid interaction. *Ninth International Conference on CFD in the Minerals and Process Industries*, October 2012.

[7] Alice Hager. *An Extensive Investigation of Particle-Fluid Interactions*. PhD thesis, Johannes Kepler Universität Linz, April-2014.

[8] G. D'Avino and P.L. Maffettone. Particle dynamics in viscoelastic liquids. *Journal of Non-Newtonian Fluid Mechanics*, 215:80–104, 2015.

[9] J.L. Favero, A.R. Secchi, N.S.M. Cardozo, and H. Jasak. Viscoelastic flow analysis using the software OpenFOAM and differential constitutive equations. *Journal of Non-Newtonian Fluid Mechanics*, 165(23-24):1625–1636, 2010.

[10] R.B. Bird, R.C. Armstrong, and O. Hassager. *Dynamics of Polymeric Liquids. 2nd ed.* New York: John Wiley & Sons, 1987.

[11] Masao Doi and S. F. Edwards. Dynamics of concentrated polymer systems. part 4.-rheological properties. *J. Chem. Soc., Faraday Trans. 2*, 75:38–54, 1979.

[12] J. M. Brader, M. E. Cates, and M. Fuchs. First-principles constitutive equation for suspension rheology. *Physical Review Letters*, 101(13), Sep 2008.

[13] J. M. Brader, Th. Voigtmann, M. E. Cates, and M. Fuchs. Dense colloidal suspensions under time-dependent shear. *Physical Review Letters*, 98(5), Jan 2007.

[14] J M Brader. Nonlinear rheology of colloidal dispersions. *Journal of Physics: Condensed Matter*, 22(36):363101, 2010.

[15] L. D. Landau. *Fluid mechanics*. Pergamon Press, Oxford, England New York, 1987.

[16] George Mase. *Continuum mechanics for engineers*. CRC Press, Boca Raton, Fla, 1999.

[17] Yasuki Nakayama, Kazuyasu Izawa, and Robert Boucher. *Introduction to Fluid Mechanics*. Butterworth-Heinemann, 1999.

[18] Alfred Leder. *Abgelöste Strömungen Physikalische Grundlagen (Grundlagen und Fortschritte der Ingenieurwissenschaften) (German Edition)*. Vieweg+Teubner Verlag, 1992.

[19] H. Jasak. *Error Analysis and Estimation for the Finite Volume Method with Applications to Fluid Flows*. PhD thesis, Imperial College of Science, Technology and Medicine, University of London, 1996.

[20] J.H. Ferziger and M. Peric. *Computational Methods for Fluid Dynamics*. Springer Berlin Heidelberg, 2002.

[21] H.K. Versteeg and W. Malalasekera. *An Introduction to Computational Fluid Dynamics: The Finite Volume Method*. Pearson Education Limited, 2007.

[22] Ronald G. Larson. Front matter. In *Constitutive Equations for Polymer Melts and Solutions*, Butterworths Series in Chemical Engineering, pages iii–. Butterworth-Heinemann, 1988.

[23] J. G. Oldroyd. On the formulation of rheological equations of state. *Proceedings of the Royal Society of London A: Mathematical, Physical and Engineering Sciences*, 200(1063):523–541, 1950.

[24] H.A. Barnes, J.F. Hutton, and K. Walters. *An Introduction to Rheology*. Annals of Discrete Mathematics. Elsevier, 1989.

[25] Yoshiyuki Einaga, Kunihiro Osaki, Michio Kurata, Shin-ichi Kimura, and Mikio Tamura. Stress relaxation of polymer solutions under large strain. *Polym J*, 2(4):550–552, Jul 1971.

[26] J. L. White and A. B. Metzner. Development of constitutive equations for polymeric melts and solutions. *Journal of Applied Polymer Science*, 7(5):1867–1889, 1963.

[27] Yoshiaki Ide and James L. White. Investigation of failure during elongational flow of polymer melts. *Journal of Non-Newtonian Fluid Mechanics*, 2(3):281–298, May 1977.

[28] P. W. McDonald. The computation of transonic flow through two-dimensional gas turbine cascades. In *ASME 1971 International Gas Turbine Conference and Products Show*. ASME International, Mar 1971.

[29] R. MacCormack and A. Paullay. Computational efficiency achieved by time splitting of finite difference operators. In *10th Aerospace Sciences Meeting*. American Institute of Aeronautics and Astronautics (AIAA), Jan 1972.

[30] Suhas Patankar. *Numerical Heat Transfer and Fluid Flow (Hemisphere Series on Computational Methods in Mechanics and Thermal Science)*. CRC Press, 1 edition, 1 1980.

[31] Michael Schäfer. *Computational Engineering - Introduction to Numerical Methods*. Springer, 2006 edition, 10 2008.

[32] OpenFOAM The OpenFOAM Foundation, 2014.

[33] OpenCFD. *OpenFOAM - The Open Source CFD Toolbox Programer's Guide*. OpenCFD Ltd., United Kingdom, 2.2.0 edition, 02- 2013.

[34] P.J. Oliveira and F.T. Pinho. Plane contraction flows of upper convected maxwell and phan-thien-tanner fluids as predicted by a finite-volume method. *Journal of Non-Newtonian Fluid Mechanics*, 88(1-2):63–88, 1999.

[35] OpenCFD. *OpenFOAM - The Open Source CFD Toolbox User's Guide*. OpenCFD Ltd., United Kingdom, 2.2.2 edition, 09- 2013.

[36] R. A. Brown, M. J. Szady, P. J. Northey, and R. C. Armstrong. On the numerical stability of mixed finite-element methods for viscoelastic flows governed by differential constitutive equations. *Theoretical and Computational Fluid Dynamics*, 5(2-3):77–106, Oct 1993.

[37] Jovani Favero. Simulação de escoamentos viscoelásticos: Desenvolvimento de uma metodologia de análise utilizando o software OpenFOAM e equações

constitutivas diferenciais. Master's thesis, Universidade Federal Do Rio Grande Do Sul, Porto Alegro, RS, 2009.

[38] Robert Guénette and Michel Fortin. A new mixed finite element method for computing viscoelastic flows. *Journal of Non-Newtonian Fluid Mechanics*, 60(1):27–52, 1995.

[39] R.I Issa. Solution of the implicitly discretised fluid flow equations by operator-splitting. *Journal of Computational Physics*, 62(1):40–65, 1986.

[40] S. J. Muller, R. G. Larson, and E. S. G. Shaqfeh. A purely elastic transition in taylor-couette flow. *Rheologica Acta*, 28(6):499–503, Nov 1989.

[41] A. Groisman and V. Steinberg. Elastic turbulence in a polymer solution flow. *Nature*, 405(6782):53–55, May 2000.

[42] Alexandre Nicolas and Matthias Fuchs. Shear-thinning in dense colloidal suspensions and its effect on elastic instabilities: from the microscopic equations of motion to an approximation of the macroscopic rheology, 2015.

[43] G. I. Taylor. The formation of emulsions in definable fields of flow. *Proceedings of the Royal Society A: Mathematical, Physical and Engineering Sciences*, 146(858):501–523, Oct 1934.

[44] G. G. Fuller and L. G. Leal. Flow birefringence of concentrated polymer solutions in two-dimensional flows. *Journal of Polymer Science: Polymer Physics Edition*, 19(4):557–587, 1981.

[45] G. I. Taylor and A. E. Green. Mechanism of the production of small eddies from large ones. *Proceedings of the Royal Society A: Mathematical, Physical and Engineering Sciences*, 158(895):499–521, Feb 1937.

[46] L.G. Leal, M.M. Denn, and R. Keunings. Lake arrowhead workshop special issue papers-introduction. *Journal of Non-Newtonian Fluid Mechanics*, 29:1–8, 1988.

[47] D V Boger. Viscoelastic flows through contractions. *Annual Review of Fluid Mechanics*, 19(1):157–182, Jan 1987.

[48] R.E. Evans and K. Walters. Flow characteristics associated with abrupt changes in geometry in the case of highly elastic liquids. *Journal of Non-Newtonian Fluid Mechanics*, 20:11–29, 1986.

[49] Wei Wang, Xuanping Wang, and Changxu Hu. A comparative study of viscoelastic planar contraction flow for polymer melts using molecular constitutive models. *Korea-Australia Rheology Journal*, 26(4):365–375, Nov 2014.

[50] Jonathan P. Rothstein and Gareth H. McKinley. Extensional flow of a polystyrene Boger fluid through a 4:1:4 axisymmetric contraction/expansion. *Journal of Non-Newtonian Fluid Mechanics*, 86(1-2):61–88, 1999.

[51] Mónica S.N. Oliveira, Paulo J. Oliveira, Fernando T. Pinho, and Manuel A. Alves. Effect of contraction ratio upon viscoelastic flow in contractions: The axisymmetric case. *Journal of Non-Newtonian Fluid Mechanics*, 147(1-2):92–108, 2007.

[52] Jonathan P. Rothstein and Gareth H. McKinley. The axisymmetric contraction-expansion: the role of extensional rheology on vortex growth dynamics and the enhanced pressure drop. *Journal of Non-Newtonian Fluid Mechanics*, 98(1):33–63, 2001.

[53] Phillip Coussot. *Rheophysics: Matter in all its states*. Spinger, 2014.

[54] J Jackle. Models of the glass transition. *Reports on Progress in Physics*, 49(2):171–231, Feb 1986.

[55] W. van Megen and S. M. Underwood. Glass transition in colloidal hard spheres: Measurement and mode-coupling-theory analysis of the coherent intermediate scattering function. *Phys. Rev. E*, 49:4206–4220, May 1994.

[56] W. van Megen and P. N. Pusey. Dynamic light-scattering study of the glass transition in a colloidal suspension. *Phys. Rev. A*, 43:5429–5441, May 1991.

[57] W. van Megen and S. M. Underwood. Glass transition in colloidal hard spheres: Mode-coupling theory analysis. *Phys. Rev. Lett.*, 70:2766–2769, May 1993.

[58] Jean-Pierre Hansen and I.R. McDonald. *Theory of Simple Liquids: with Applications to Soft Matter*. Academic Press, 2013.

[59] Umberto Balucani and Marco Zoppi. *Dynamics of the Liquid State (Oxford Series on Neutron Scattering in Condensed Matter)*. Clarendon Press, 1995.

[60] Stephen W. Lovesey. *The Theory of Neutron Scattering from Condensed Matter: Volume II (International Series of Monographs on Physics)*. Clarendon Press, 1986.

[61] R. Zorn, D. Richter, B. Frick, and B. Farago. Neutron scattering experiments on the glass transition of polymers. *Physica A: Statistical Mechanics and its Applications*, 201(1):52–66, 1993.

[62] David R Reichman and Patrick Charbonneau. Mode-coupling theory. *Journal of Statistical Mechanics: Theory and Experiment*, 2005(05):P05013, May 2005.

[63] Thomas Voigtmann. Slow dynamics in external forces: Creep and microrheology. *AIP Conference Proceedings*, 1518(1):94–103, 2013.

[64] Joseph M. Brader, Thomas Voigtmann, Matthias Fuchs, Ronald G. Larson, and Michael E. Cates. Glass rheology: From mode-coupling theory to a dynamical yield criterion. *Proceedings of the National Academy of Sciences*, 106(36):15186–15191, 9 2009.

[65] Simon Papenkort. *Flow of yield-stress fluids through channels*. PhD thesis, University of Konstanz, Deutsches zentrum für Luft und Raumfahrt, 2013.

[66] Matthias Fuchs and Michael E. Cates. Schematic models for dynamic yielding of sheared colloidal glasses. *Faraday Discuss.*, 123:267–286, 2003.

[67] Matthias Fuchs and Michael E. Cates. Theory of nonlinear rheology and yielding of dense colloidal suspensions. *Physical Review Letters*, 89(24), Nov 2002.

[68] Wolfgang Götze. *Complex Dynamics of Glass-Forming Liquids: A Mode-Coupling Theory (International Series of Monographs on Physics)*. Oxford University Press, 2009.

[69] J. M. Brader, M. E. Cates, and M. Fuchs. First-principles constitutive equation for suspension rheology. *Phys. Rev. E*, 86:021403, Aug 2012.

[70] Matthias Fuchs and Matthias Ballauff. Nonlinear rheology of dense colloidal dispersions: A phenomenological model and its connection to mode coupling theory. *Colloids and Surfaces A: Physicochemical and Engineering Aspects*, 270-271:232–238, 2005. Liquids and MesoScience.

[71] S. Papenkort and Th. Voigtmann. Channel flow of a tensorial shear-thinning maxwell model: Lattice Boltzmann simulations. *The Journal of Chemical Physics*, 140(16):164507, 2014.

[72] S. Papenkort and Th. Voigtmann. Lattice Boltzmann simulations of a viscoelastic shear-thinning fluid. *The Journal of Chemical Physics*, 143(4):044512, 2015.

[73] C. Derec, A. Ajdari, and F. Lequeux. Rheology and aging: A simple approach. *The European Physical Journal E*, 4(3):355–361, Mar 2001.

[74] Guillemette Picard, Armand Ajdari, Lydéric Bocquet, and François Lequeux. Simple model for heterogeneous flows of yield stress fluids. *Phys. Rev. E*, 66:051501, Nov 2002.

[75] P. Hébraud, F. Lequeux, J. P. Munch, and D. J. Pine. Yielding and rearrangements in disordered emulsions. *Phys. Rev. Lett.*, 78:4657–4660, Jun 1997.

[76] P. Schall, D. A. Weitz, and F. Spaepen. Structural rearrangements that govern flow in colloidal glasses. *Science*, 318(5858):1895–1899, Dec 2007.

[77] L. Berthier, G. Biroli, J.-P. Bouchaud, L. Cipelletti, D. El Masri, D. L'Hôte, F. Ladieu, and M. Pierno. Direct experimental evidence of a growing length scale accompanying the glass transition. *Science*, 310(5755):1797–1800, 2005.

[78] S. Fritschi, M. Fuchs, and Th. Voigtmann. Mode-coupling analysis of residual stresses in colloidal glasses. *Soft Matter*, 10:4822–4832, 2014.

[79] N. Koumakis, M. Laurati, S. U. Egelhaaf, J. F. Brady, and G. Petekidis. Yielding of hard-sphere glasses during start-up shear. *Phys. Rev. Lett.*, 108:098303, Mar 2012.

[80] Jaime Wisniak. Frederick thomas trouton: The man, the rule, and the ratio. *The Chemical Educator*, 6(1):55–61, Feb 2001.

[81] P. Scheidler, W. Kob, and K. Binder. Cooperative motion and growing length scales in supercooled confined liquids. *EPL (Europhysics Letters)*, 59(5):701, 2002.

[82] Lidia M. Quinzani, Robert C. Armstrong, and Robert A. Brown. Birefringence and laser-doppler velocimetry (ldv) studies of viscoelastic flow through a planar contraction. *Journal of Non-Newtonian Fluid Mechanics*, 52(1):1–36, 1994.

[83] Gaurav Prakash Shrivastav, Pinaki Chaudhuri, and Jürgen Horbach. Yielding of glass under shear: A directed percolation transition precedes shear-band formation. *Physical Review E*, 94(4), Oct 2016.

[84] T. Sentjabrskaja, P. Chaudhuri, M. Hermes, W. C. K. Poon, J. Horbach, S. U. Egelhaaf, and M. Laurati. Creep and flow of glasses: strain response linked to the spatial distribution of dynamical heterogeneities. *Scientific Reports*, 5(1), Jul 2015.

[85] T. W. Wright. *The physics and mathematics of adiabatic shear bands.* Cambridge University Press, Cambridge, UK New York, 2002.

[86] Thibaut Divoux, Marc A. Fardin, Sebastien Manneville, and Sandra Lerouge. Shear banding of complex fluids. *Annual Review of Fluid Mechanics*, 48(1):81–103, 2016.

[87] Pierre-Gilles de Gennes. Soft matter (nobel lecture). *Angewandte Chemie International Edition in English*, 31(7):842–845, 1992.

[88] A.L. Greer, Y.Q. Cheng, and E. Ma. Shear bands in metallic glasses. *Materials Science and Engineering: R: Reports*, 74(4):71–132, 2013.

[89] Robyn L. Moorcroft, Michael E. Cates, and Suzanne M. Fielding. Age-dependent transient shear banding in soft glasses. *Phys. Rev. Lett.*, 106:055502, Feb 2011.

[90] S M Fielding. Shear banding in soft glassy materials. *Reports on Progress in Physics*, 77(10):102601, 2014.

[91] S. M. Fielding, M. E. Cates, and P. Sollich. Shear banding, aging and noise dynamics in soft glassy materials. *Soft Matter*, 5:2378–2382, 2009.

[92] Fabian Frahsa, Amit Kumar Bhattacharjee, Juergen Horbach, Matthias Fuchs, and Thomas Voigtmann. On the Bauschinger effect in supercooled melts under shear: Results from mode coupling theory and molecular dynamics simulations. *The Journal of Chemical Physics*, 138(12), 2013.

[93] Smarajit Karmakar, Edan Lerner, and Itamar Procaccia. Plasticity-induced anisotropy in amorphous solids: The Bauschinger effect. *Phys. Rev. E*, 82:026104, Aug 2010.

[94] S. Chandrasekar and M. M. Chaudhri. The explosive disintegration of Prince Rupert's drops. *Philosophical Magazine Part B*, 70(6):1195–1218, Dec 1994.

[95] L. Brodsley, C. Frank, and J. W. Steeds. Prince Rupert's drops. *Notes and Records of the Royal Society*, 41(1):1–26, Oct 1986.

[96] Lavanya Mohan, Roger T. Bonnecaze, and Michel Cloitre. Microscopic origin of internal stresses in jammed soft particle suspensions. *Physical Review Letters*, 111(26), Dec 2013.

[97] M. Ballauff, J. M. Brader, S. U. Egelhaaf, M. Fuchs, J. Horbach, N. Koumakis, M. Krüger, M. Laurati, K. J. Mutch, G. Petekidis, M. Siebenbürger, Th. Voigtmann, and J. Zausch. Residual stresses in glasses. *Phys. Rev. Lett.*, 110:215701, May 2013.

[98] P J Withers. Residual stress and its role in failure. *Reports on Progress in Physics*, 70(12):2211, 2007.

[99] CORNING INCORPORATED, Matthew John Dejneka, Adam James Ellison, and John Christopher Mauro. *Ion exchangeables glass with high compressive stress*, 2013.

[100] M. E. Cates and P. Sollich. Tensorial constitutive models for disordered foams, dense emulsions, and other soft nonergodic materials. *Journal of Rheology*, 48(1):193–207, Jan 2004.

[101] Shuling Hou, Qisu Zou, Shiyi Chen, Gary Doolen, and Allen C. Cogley. Simulation of cavity flow by the Lattice Boltzmann method. *Journal of Computational Physics*, 118(2):329–347, May 1995.

[102] Shun Zou, Xinhai Xu, Juan Chen, Xiaowei Guo, and Qian Wang. Benchmark numerical simulations of viscoelastic fluid flows with an efficient integrated Lattice Boltzmann and finite volume scheme. *Advances in Mechanical Engineering*, 7(2):805484, Feb 2015.

[103] Odus R. Burggraf. Analytical and numerical studies of the structure of steady separated flows. *Journal of Fluid Mechanics*, 24(1):113–151, 1966.

[104] Simon Haque, Iman Lashgari, Flavio Giannetti, and Luca Brandt. Stability of fluids with shear-dependent viscosity in the lid-driven cavity. *Journal of Non-Newtonian Fluid Mechanics*, 173-174(1):49–61, 2012.

[105] J.F. Richardson and W.N. Zaki. The sedimentation of a suspension of uniform spheres under conditions of viscous flow. *Chemical Engineering Science*, 3(2):65–73, Apr 1954.

[106] D. De Kee R.P. Chhabra. *Transport processes in bubbles, drops and particles.* Taylor & Francis, New York, 2002.

[107] N. Goyal and J.J. Derksen. Direct simulations of spherical particles sedimenting in viscoelastic fluids. *Journal of Non-Newtonian Fluid Mechanics*, 183-184:1–13, Sep 2012.

[108] M. Stimson and G. B. Jeffery. The motion of two spheres in a viscous fluid. *Proceedings of the Royal Society A: Mathematical, Physical and Engineering Sciences*, 111(757):110–116, May 1926.

[109] R H Davis and A Acrivos. Sedimentation of noncolloidal particles at low Reynolds numbers. *Annual Review of Fluid Mechanics*, 17(1):91–118, Jan 1985.

[110] A. F. Fortes, D. D. Joseph, and T. S. Lundgren. Nonlinear mechanics of fluidization of beds of spherical particles. *Journal of Fluid Mechanics*, 177:467–483, 1987.

[111] J. Feng, P.Y. Huang, and D.D. Joseph. Dynamic simulation of sedimentation of solid particles in an Oldroyd-b fluid. *Journal of Non-Newtonian Fluid Mechanics*, 63(1):63–88, 1996.

[112] D.D. Joseph, Y.J. Liu, M. Poletto, and J. Feng. Aggregation and dispersion of spheres falling in viscoelastic liquids. *Journal of Non-Newtonian Fluid Mechanics*, 54:45–86, Aug 1994.

[113] A. M. Ardekani, R. H. Rangel, and D. D. Joseph. Two spheres in a free stream of a second-order fluid. *Physics of Fluids*, 20(6):063101, 2008.

[114] Daniel D. Joseph and Yaoqi Joe Liu. Orientation of long bodies falling in a viscoelastic liquid. *Journal of Rheology*, 37(6):961–983, Nov 1993.

[115] Michael J. Riddle, Carlos Narvaez, and R. Byron Bird. Interactions between two spheres falling along their line of centers in a viscoelastic fluid. *Journal of Non-Newtonian Fluid Mechanics*, 2(1):23–35, Jan 1977.

[116] P. Brunn. Interaction of spheres in a viscoelastic fluid. *Rheologica Acta*, 16(5):461–475, Sep 1977.

[117] E.T.G Bot, M.A Hulsen, and B.H.A.A van den Brule. The motion of two spheres falling along their line of centres in a Boger fluid. *Journal of Non-Newtonian Fluid Mechanics*, 79(2-3):191–212, Nov 1998.

[118] Abbas H. Sulaymon, Catherine A.M.E. Wilson, and Abeer I. Alwared. An experimental investigation of the settling behavior of two spheres in a power law fluid. *Journal of Non-Newtonian Fluid Mechanics*, 192:29–36, Feb 2013.

[119] Oliver G. Harlen. The negative wake behind a sphere sedimenting through a viscoelastic fluid. *Journal of Non-Newtonian Fluid Mechanics*, 108(1-3):411–430, Dec 2002.

[120] D.D. Joseph and J. Feng. A note on the forces that move particles in a second-order fluid. *Journal of Non-Newtonian Fluid Mechanics*, 64(2-3):299–302, Jun 1996.

[121] D. A. Eisenberg, I. M. Klink, and R. J. Phillips. Axisymmetric sedimentation of spherical particles in a viscoelastic fluid: Sphere-wall and sphere-sphere interactions. *Journal of Rheology*, 57(3):857–880, May 2013.

[122] Housam Binous and Ronald J. Phillips. Dynamic simulation of one and two particles sedimenting in viscoelastic suspensions of FENE dumbbells. *Journal of Non-Newtonian Fluid Mechanics*, 83(1-2):93–130, Jun 1999.

[123] Y.I. Cho and J.P. Hartnett. The falling ball viscometer- a new instrument for viscoelastic fluids. *Letters in Heat and Mass Transfer*, 6(4):335–342, Jul 1979.

[124] Mariappan Hariharaputhiran, R.Shankar Subramanian, Gregory A Campbell, and Raj. P Chhabra. The settling of spheres in a viscoplastic fluid. *Journal of Non-Newtonian Fluid Mechanics*, 79(1):87–97, Sep 1998.

[125] M. M. Gumulya, R. R. Horsley, and V. Pareek. Numerical simulation of the settling behaviour of particles in thixotropic fluids. *Physics of Fluids*, 26(2):023102, Feb 2014.

[126] D. Rodrigue, D. De Kee, and C. F. Chan Man Fong. The slow motion of a slow motion of a spherical particle in a Carreau fluid. *Chemical Engineering Communications*, 154(1):203–215, Nov 1996.

[127] A. Hager, C. Kloss, S. Pirker, and C. Goniva. Parallel resolved open source CFD-DEM: Method, validation and application. *The Journal of Computational Multiphase Flows*, 6(1):13–28, Mar 2014.

[128] Xin Yang, Haibo Huang, and Xiyun Lu. The motion of a neutrally buoyant ellipsoid inside square tube flows. *Advances in Applied Mathematics and Mechanics*, 9(02):233–249, Jan 2017.

[129] J. Feng, H. H. Hu, and D. D. Joseph. Direct simulation of initial value problems for the motion of solid bodies in a newtonian fluid part 1. sedimentation. *Journal of Fluid Mechanics*, 261(-1):95, Feb 1994.

[130] Mehdi Niazi Ardekani, Pedro Costa, Wim Paul Breugem, and Luca Brandt. Numerical study of the sedimentation of spheroidal particles. *International Journal of Multiphase Flow*, 87:16–34, Dec 2016.

[131] Sudeshna Ghosh and John M. Stockie. Numerical simulations of particle sedimentation using the immersed boundary method. *Communications in Computational Physics*, 18(02):380–416, Jul 2015.

[132] Charles S. Peskin. The immersed boundary method. *Acta Numerica*, 11, Jan 2002.

[133] Rajat Mittal and Gianluca Iaccarino. Immersed boundary methods. *Annual Review of Fluid Mechanics*, 37(1):239–261, Jan 2005.

[134] N.A. Patankar, P. Singh, D.D. Joseph, R. Glowinski, and T.-W. Pan. A new formulation of the distributed Lagrange multiplier/fictitious domain method for particulate flows. *International Journal of Multiphase Flow*, 26(9):1509–1524, Sep 2000.

[135] N. A. Patankar. A formulation for fast computations of rigid particulate flows. *Center for Turbulence Research Annual Research Briefs*, 2001.

[136] R. Glowinski, T.W. Pan, T.I. Hesla, D.D. Joseph, and J. Périaux. A fictitious domain approach to the direct numerical simulation of incompressible viscous flow past moving rigid bodies: Application to particulate flow. *Journal of Computational Physics*, 169(2):363–426, 2001.

[137] L. E. Becker, G. H. McKinley, H. K. Rasmussen, and O. Hassager. The unsteady motion of a sphere in a viscoelastic fluid. *Journal of Rheology*, 38(2):377–403, Mar 1994.

[138] P. Y. Huang, H. H. Hu, and D. D. Joseph. Direct simulation of the sedimentation of elliptic particles in Oldroyd-b fluids. *Journal of Fluid Mechanics*, 362:297–326, 1998.

[139] M.M. Gumulya, R.R. Horsley, V. Pareek, and D.D. Lichti. The effects of fluid viscoelasticity on the settling behaviour of horizontally aligned spheres. *Chemical Engineering Science*, 66(23):5822–5831, 2011.

[140] Ronald J. Phillips. Dynamic simulation of hydrodynamically interacting spheres in a quiescent second-order fluid. *Journal of Fluid Mechanics*, 315:345–365, 1996.

[141] S. Kern and P. Koumoutsakos. Simulations of optimized anguilliform swimming. *Journal of Experimental Biology*, 209(24):4841–4857, Dec 2006.

[142] J. Carling, T. L. Williams, and G. Bowtell. Self-propelled anguilliform swimming: simultaneous solution of the two-dimensional Navier-Stokes equations and Newton's laws of motion. *Journal of Experimental Biology*, 201(23):3143–3166, 1998.

[143] G. Li, U. K. Muller, J. L. van Leeuwen, and H. Liu. Body dynamics and hydrodynamics of swimming fish larvae: a computational study. *Journal of Experimental Biology*, 215(22):4015–4033, Oct 2012.